Distribution Agreement

In presenting this thesis or dissertation as a partial fulfillment of the requirements for an advanced degree from Emory University, I hereby grant to Emory University and its agents the non-exclusive license to archive, make accessible, and display my thesis or dissertation in whole or in part in all forms of media, now or hereafter known, including display on the world wide web. I understand that I may select some access restrictions as part of the online submission of this thesis or dissertation. I retain all ownership rights to the copyright of the thesis or dissertation. I also retain the right to use in future works (such as articles or books) all or part of this thesis or dissertation.

Signature:

Qi Yu	Date

Vibrational Dynamics of Hydrated Proton based on High-level *Ab Initio* Potential Energy Surface and Dipole Moment Surface

By

Qi Yu
Doctor of Philosophy
Chemistry

Joel M. Bowman, Ph.D
Advisor

James T. Kindt, Ph.D
Committee Member

Francesco A. Evangelista, Ph.D
Committee Member

Accepted:

Lisa A. Tedesco, Ph.D
Dean of the James T. Laney School of Graduate Studies

Date

Vibrational Dynamics of Hydrated Proton based on High-level *Ab Initio* Potential Energy Surface and Dipole Moment Surface

By

Qi Yu
B.S., University of Science and Technology of China, 2014

Advisor: Joel M. Bowman, Ph.D

An abstract of
A dissertation submitted to the Faculty of the
James T. Laney School of Graduate Studies of Emory University
in partial fulfillment of the requirements for the degree of
Doctor of Philosophy
in Chemistry
2019

Abstract

Vibrational Dynamics of Hydrated Proton based on High-level *Ab Initio* Potential Energy Surface and Dipole Moment Surface

By Qi Yu

The hydrated excess proton is a common species in both aqueous chemistry and gas-phase chemistry which complexes with water in a variety of structures. Previous theoretical tools are limited in investigating the structure, dynamics and vibrational spectra of hydrated proton with both accuracy and computational efficiency. In our work, an accurate *ab initio* potential energy surface (PES) and dipole moment surface (DMS) is developed. This PES/DMS, based on a many-body representation, accurately describe the electronic energy of the hydrated proton system including one excess proton and arbitrary number of water monomers. Each term of the many-body representation is fitted using linear least square fitting method with thousands of high-level *ab initio* electronic energies. Part 1 and Part 2 of the dissertation will review the PES/DMS fitting methods and introduce how the PES/DMS for hydrated proton is constructed.

The accuracy of constructed PES/DMS is verified in properties of small protonated water cluster, $H_3O^+(H_2O)n$, n=0-5. We carry out detailed comparison with high-level benchmark electronic structure calculations for all current known low-lying isomers of those clusters in terms of structures, energetics and harmonic spectra. Taking advantage of the PES/DMS, we report fully quantum studies of the vibrational spectra of different protonated water clusters. This includes the infrared spectra of $H_7O_3^+$, four isomers of $H_9O_4^+$, Zundel and Eigen isomer of $H^+(H_2O)_6$.

We also apply the PES/DMS to infrared spectra calculation of aqueous proton system. We obtain hundreds of protonated water clusters, $H^+(H_2O)_6$, from reactive molecular dynamics trajectories. Anharmonic vibrational spectra are conducted for all selected clusters combining extended local monomer approach and quantum vibrational self-consistent and virtual state configuration interaction approach (VSCF/VCI).

Vibrational Dynamics of Hydrated Proton based on High-level *Ab Initio* Potential Energy Surface and Dipole Moment Surface

By

Qi Yu
B.S., University of Science and Technology of China, 2014

Advisor: Joel M. Bowman, Ph.D

A dissertation submitted to the Faculty of the
James T. Laney School of Graduate Studies of Emory University
in partial fulfillment of the requirements for the degree of
Doctor of Philosophy
in Chemistry
2019

Acknowledgement

Of the many people who supported and encouraged me over the past five years, I would like to express my deepest gratitude to my advisor, Dr. Joel M. Bowman, for his patient guidance. His attitude towards science strengthened my understanding of what good science is and he continues to serve as an important role-model for me. Under his instructions, I learned how to become an in-depth thinker, how to conduct independent research, how to deal with oral presentation and how to write scientific paper.

I would like to thank Dr. James T. Kindt and Dr. Francesco A. Evangelista for their time to be committee members of my graduate studies and their helpful suggestions. I would also like to thank Dr. Stuart Carter for his guidance in using "MULTIMODE" software.

I must also express my gratitude to all the current and past members of the Bowman group: Dr. Yimin Wang, Dr. Hanchao Liu, Dr. Xiaohong Wang, Dr. Chen Qu, Apurba Nandy, especially Dr. Yimin Wang and Dr. Chen Qu, for all their support and all valuable discussions. I am also grateful to Susan Browne for her coordination work during my graduate studies.

Last but not least, I want to deliver the deepest appreciation to my family, my father Zhaobiao Yu, my mother Yan Shen and my sister Li Yu. They gave me continuous encouragement and unconditional love. I also want to thank my new family member, Yun Jiang, my wife! She always gives me unconditional support and chooses to be accompany with me during any difficult times. I would also thank all my friends for their suggestions and encouragements. Because of all my friends and my family, my Ph.D study becomes smooth and enjoyable.

Table of Contents

List of Figures

List of Tables

Chapter 1 Introduction

Hydrated excess proton is a common species in aqueous chemistry which complexes with water in a variety of structures. It is well known that proton in aqueous solution plays essential role in different aspects of chemical, biological and industrial fields.[1–4]The molecular formula of hydrated proton is not complex, written as $H^+(H_2O)n$, which is one excess proton plus certain number of water monomers. However, the molecular-level understanding of properties of hydrated proton is not fully clear even though people have made a lot of experimental and theoretical efforts in investigating the structure, proton transport process and associated vibrational signatures.[5–23]One unusual feature of hydrated proton is its anomalously high mobility in water as compared to other ions. Experiments have been done during the first half of the last century.[24–26] For example, the mobilities of Rb^+ and Cs^+ are just 22% that of the proton.[27] Another unusual feature of hydrated proton is its vibrational spectra. The vibrational spectra of aqueous proton expands an extremely broad band starting from 1000 cm^{-1} and ending at 3000 cm^{-1}. This diffuse background absorption band provide little structural information about the local environment of the excess proton and is often referred as “Zundel continuum".[28,29]

To explain the anomalously mobility of proton transfer process in water, a structural process, called Grotthuss mechanism,[30] is widely used for proton-hopping process. In this mechanism, an “Eigen" structure is identified as resting state where a hydronium cation, H_3o^+ exists in the first solvations shell. One O-H colvent bond in the hydronium can break and the proton starts to connect to adjacent water. This forms a “Zundel" intermediate where the proton sits between two water monomers. Next, a new O-H bond forms and this results to a new “Eigen" structure. As to the vibrational spectrum of aqueous proton, two structural models has been widely

used to help interpret the spectra and provide structural information. On one end, the excess proton localizes on one water to form a hydronium ion with a particularly tight first solvation shell, known as the Eigen species $H_9O_4^+$.[31,32]The gas-phase Eigen cluster $H_9O_4^+$ displays a signature band at 2650 cm^{-1}.[12,13,23]On the other extreme, the proton is equally shared between two flanking waters, behaving collectively as the Zundel complex $H_5O_2^+$.[33]The gas-phase Zundel molecule $H_5O_2^+$ has the signature band at 1000 cm^{-1}.[12,23,34]Even though many success has reached in investigating the proton dynamics and vibration spectra of hydrated proton, the ultrafast dynamics of proton and broad featureless vibrational spectrum of the excess proton eludes straightforward interpretation.

Theoretical investigations of the structure, infrared (IR) spectra and dynamical properties have been mainly based on two approaches. One approach relies on on-the-fly evaluation of electronic energies, using a fast electronic structure method, predominantly density functional theory (DFT). Early work of *ab initio* molecular dynamics simulation (AIMD) of excess proton in liquid water started from early 1990s.[35,36]These work provides evidence of two dominant structures of the excess proton in water, Eigen and Zundel structures. Series of AIMD simulation were conducted in the past 20 year and shows rich information of the proton dynamics in water.[14,17,37]Recent examples include DFT-based molecular dynamics simulations used to model the speciation of hydronium and hydroxide in aqueous system.[21] This group reported that the difference between the diffusivities of hydronium and hydroxide originates from their different solvation structure according to their AIMD simulations. On-the-fly evaluation of electronic energies with direct electronic structure method is also used to calculate both harmonic and anharmonic vibrational spectra of gas-phase protonated water clusters. in a recent feature article[23] focusing on the vibrational spectra of $H^+(H_2O)_n$, n=2-28, the theoretical analyses mainly relied on vibrational second order perturbation theory (VPT2) with the electronic energies typically obtained at

the B3LYP DFT level. The calculated spectra provided assignments of several important vibration bands in different protonated water clusters, which are clearly valuable to interpret the experimentally recorded IR spectra. Agmon and coworkers applied both AIMD and VPT2 approaches in calculating the vibrational spectra of small protonated water clusters based on B3LYP DFT and second order perturbation theory (MP2) level of method.[38–40] Accurate approaches of accounting for electron correlation like MP2 are usually used for geometry optimization, such as the study of the various isomers of the various isomers of $H_3O^+(H_2O)_{20}$,[41] while coupled-cluster (CC) methods are far more computationally intensive and have not been extensively applied to the calculations of the structures of larger protonated water clusters.

Another approach to probe the structure and dynamics of extended aqueous systems is to develop empirical or semi-empirical potentials that can describe proton transfer processes. For example, a Multi-State Empirical Valence Bond (MS-EVB) force field for the hydrated proton has been developed by Voth and coworkers.[42–44] This model yields the potential of a protonated water system from the ground-state energy of an effective EVB Hamiltonian. The diagonal term in the Hamiltonian includes the H_3O^+ 1-body, H_2O 1-body, H_3O^+-H_2O 2-body interaction and H_2O-H_2O 2-body interactions, while the off-diagonal term considers the electrostatic interaction between the “Zundel" species involved in two EVB states and the remaining water molecules. The MS-EVB model has been used successfully to model proton transfer processes[18,45] and in the calculation of the vibrational spectra[46–48] using dynamics simulations. Recently, Voth and co-workers used MS-EVB (version 3.2) in MD simulations to obtain a large sample of protonated water clusters which were analyzed at the harmonic level, using DFT to investigate the importance of Zundel vs Eigen structure in 2D IR experiments.[49] Jordan and co-workers developed a modified MS-EVB force field (MSEVB4P), which incorporates the TIP4P water model and a new set of parameters.[50] When compared to the MP2 *ab initio* calculations, this modified

MS-EVB model was proved to be relatively accurate in describing the structures of different sizes of protonated water clusters. In spite of the many successes of the MSEVB model, errors still exist in the potential curves along the proton transfer in different protonated water clusters when compared to the results of high level *ab initio* calculations. More introduction of theoretical investigations of hydrated proton can be referred to a review paper by Agmon and coworkers.[22]

To obtain a balance between accuracy and computational cost for the description of the dynamic properties of the hydrated proton, a high level *ab initio* potential energy surface is the obvious choice. Previously, an accurate *ab initio* potential energy surface for water based on many-body representation (WHBB model) has been reported.[51–53]This WHBB potential model can be used to calculate potential energy of water with arbitrary number water monomers. The many-body representation is written as:

$$E = \sum_{i}^{N} V_{1-body}(i) + \sum_{i<j}^{N} V_{2-body}(i,j) + \sum_{i<j<k}^{N} V_{3-body}(i,j,k) + \sum_{n\geq 4}^{n} V_{n-body}$$

In this expression, V_{1-body} is the 1-body potential for each water monomer which uses a spectroscopically accurate model.[54] The V_{2-body} and V_{3-body} parts are 2-body and 3-body interactions between water monomers and they are fitted from thousands of high-level *ab initio* electronic energies using permutationally invariant polynomial method. The V_{n-body} represents the 4- and higher-body terms which are polarization energies adopted from TTM3-F water model. The accuracy of constructed WHBB water model has been verified in structures, binding energies and vibrational spectra of water from gas-phase cluster to liquid and ice model. Another accurate *ab initio* many-body potential energy model of water is the MB-pol potential energy surface (PES). This PES uses the similar strategy of many-body representation but with polarization terms included. The MB-pol water model also receives many success in describing water properties from dimer to condensed phase and has already been applied in different molecular dynamics investigation of water system.

Inspired by the success of constructing accurate potential model of water with many-body representation, we proceed to a more complex but important system, hydrated proton, with the same many-body concept. Chapter 2 and 3 of this dissertation will introduce the main theories and methods in constructing *ab initio* many-body potential energy surface and variational methods for vibrational spectrum calculations.

Chapter 4 will main focus on the details of constructing many-body potential energy surface (PES) and dipole moment surface (DMS) of hydrated proton. This chapter covers all contents of the many-body PES/DMS from 1-body terms to 4-body terms. Tests of constructed PES/DMS in structure, binding energy and harmonic frequencies of small gas-phase clusters will also be included in this chapter. In Chapter 5, we report the vibrational analysis of bare hydronium H_3O^+ ion. In Chapter 6, we report the vibrational spectra of two important protonated water clusters, $H_7O_3{}^+$ and $H_9O_4{}^+$ and their fully deuterated Isotopologues. Chapter 7 will focus on the details and results of fully-quantum anharmonic vibrational spectra of aqueous proton using constructed PES/DMS. We will also show the vibrational spectra calculation of two low-energy isomers of protonated water hexamer

Bibliography

[1] Heberle, J.; Riesle, J.; Thiedemann, G.; Oesterhelt, D.; Dencher, N. A. *Nature* **1994**, *370*, 379.

[2] Stowell, M. H. B.; McPhillips, T. M.; Rees, D. C.; Soltis, S. M.; Abresch, E.; Feher, G. *Science* **1997**, *276*, 812–816.

[3] Luecke, H.; Richter, H.-T.; Lanyi, J. K. *Science* **1998**, *280*, 1934–1937.

[4] Rini, M.; Magnes, B.-Z.; Pines, E.; Nibbering, E. T. J. *Science* **2003**, *301*, 349–352.

[5] Begemann, M. H.; Gudeman, C. S.; Pfaff, J.; Saykally, R. J. *Phys. Rev. Lett.* **1983**, *51*, 554.

[6] Yeh, L. I.; Okumura, M.; Myers, J. D.; Price, J. M.; Lee, Y. T. *J. Chem. Phys.* **1989**, *91*, 7319.

[7] Jiang, J.-C.; Wang, Y.-S.; Chang, H.-C.; Lin, S. H.; Lee, Y. T.; Niedner-Schatteburg, G.; Chang, H.-C. *J. Am. Chem. Soc.* **2000**, *122*, 1398.

[8] Yeh, L. I.; Lee, Y. T.; Hougen, J. T. *J. Mol. Spectrosc.* **1994**, *164*, 473.

[9] Douberly, G. E.; Ricks, A. M.; Duncan, M. A. *J. Phys. Chem. A* **2009**, *113*, 8449.

[10] Douberly, G. E.; Walters, R. S.; Cui, J.; Jordan, K. D.; Duncan, M. A. *J. Phys. Chem. A* **2010**, *114*, 4570.

[11] Shin, J.-W.; Hammer, N. I.; Diken, E. G.; Johnson, M. A.; Walters, R. S.; Jaeger, T. D.; Duncan, M. A.; Christie, R. A.; Jordan, K. D. *Science* **2004**, *304*, 1137.

[12] Headrick, J. M.; Diken, E. G.; Walters, R. S.; Hammer, N. I.; Christie, R. A.; Cui, J.; Myshakin, E. M.; Duncan, M. A.; Johnson, M. A.; Jordan, K. D. *Science* **2005**, *308*, 1765.

[13] Wolke, C. T.; Fournier, J. A.; Dzugan, L. C.; Fagiani, M. R.; Odbadrakh, T. T.; Knorke, H.; Jordan, K. D.; McCoy, A. B.; Asmis, K. R.; Johnson, M. A. *Science* **2016**, *354*, 1131.

[14] Marx, D.; Tuckerman, M. E.; Hutter, J.; Parrinello, M. *Nature* **1999**, *397*, 601.

[15] Xantheas, S. S. *Nature* **2009**, *457*, 673.

[16] Tuckerman, M. E.; Marx, D.; Parrinello, M. *Nature* **2002**, *417*, 925.

[17] Berkelbach, T. C.; Lee, H. S.; Tuckerman, M. E. *Phys. Rev. Lett.* **2009**, *103*, 238302.

[18] Day, T. J. F.; Schmitt, U. W.; Voth, G. A. *J. Am. Chem. Soc.* **2000**, *122*, 12027.

[19] Yu, Q.; Bowman, J. M. *J. Am. Chem. Soc.* **2017**, *139*, 10984–10987.

[20] Xantheas, S. S. *Science* **2016**, *354*, 1101.

[21] Chen, M.; Zheng, L.; Santra, B.; Ko, H.-Y.; DiStasio Jr, R. A.; Klein, M. L.; Car, R.; Wu, X. *Nat. Chem* **2018**,

[22] Agmon, N.; Bakker, H. J.; Campen, R. K.; Henchman, R. H.; Pohl, P.; Roke, S.; Thämer, M.; Hassanali, A. *Chem. Rev.* **2016**, *116*, 7642–7672.

[23] Fournier, J. A.; Wolke, C. T.; Johnson, M. A.; Odbadrakh, T. T.; Jordan, K. D.; Kathmann, S. M.; Xantheas, S. S. *J. Phys. Chem. A* **2015**, *119*, 9425–9440.

[24] Noyes, A. A.; Kato, Y. *J. Am. Chem. Soc.* **1908**, *30*, 318–334.

[25] Johnston, J. *J. Am. Chem. Soc.* **1909**, *31*, 1010–1020.

[26] Gierer, A.; Wirtz, K. *Ann. Phys.* **1950**, *441*, 257.

[27] Robinson, R. H., R. A.; Stokes *Electrolyte Solutions; 2nd ed.*; Butterworths: London, 1959.

[28] Vener, M. V.; Librovich, N. B. *Int. Rev. Phys. Chem.* **2009**, *28*, 407.

[29] Yukhnevich, G. V.; Tarakanova, E. G.; Mayorow, V. D.; Librovich, N. B. *J. Mol. Struct.* **1992**, *265*, 237.

[30] de Grotthuss,; T., C. J. *Ann. Chim.* **1806**, *58*, 54.

[31] Wicke, E.; Eigen, M.; Ackermann, T. *Z. für Phys. Chem.* **1954**, *1*, 340.

[32] Eigen, M. *Angew. Chem., Int. Ed. Engl.* **1964**, *3*, 1.

[33] Zundel, G.; Metzger, H. *Z. Phys. Chem.* **1968**, *58*, 225.

[34] Asmis, K. R.; Pivonka, N. L.; Santambrogio, G.; Brummer, M.; Kaposta, C.; Newmark, D. M.; Woste, L. *Science* **2003**, *299*, 1375–1377.

[35] Tuckerman, M. E.; Laasonen, K.; Sprik, M.; Parrinello, M. *J. Phys.: Condens. Matter* **1994**, *6*, A93.

[36] Tuckerman, M. E.; Laasonen, K.; Sprik, M.; Parrinello, M. *J. Chem. Phys.* **1995**, *103*, 150.

[37] Marx, D. *ChemPhysChem* **2006**, *7*, 1848.

[38] Kulig, W.; Agmon, N. *J. Phys. Chem. B* **2014**, *118*, 278–286.

[39] Wang, H.; Agmon, N. *J. Phys. Chem. A* **2017**, *121*, 3056.

[40] Samala, N. R.; Agmon, N. *Chemical Physics* **2018**,

[41] Xantheas, S. S. *Can. J. Chem. Eng.* **2012**, *90*, 843.

[42] Schmitt, U. W.; Voth, G. A. *J. Phys. Chem. B* **1998**, *102*, 5548.

[43] Day, T. J. F.; Soudackov, A. V.; Cuma, M.; Schmitt, U. W.; Voth, G. A. *J. Chem. Phys.* **2002**, *117*, 5839.

[44] Wu, Y.; Chen, H.; Wang, F.; Paesani, F.; Voth, G. A. *J. Phys. Chem. B* **2008**, *112*, 467.

[45] Knight, C.; Voth, G. A. *Accounts of Chemical Research* **2011**, *45*, 101.

[46] Xu, J.; Zhang, Y.; Voth, G. A. *J. Phys. Chem. Lett.* **2011**, *2*, 81–86.

[47] Agostini, F.; Vuilleumier, R.; Ciccotti, G. *J. Chem. Phys.* **2011**, *134*.

[48] Kulig, W.; Agmon, N. *Nat. Chem.* **2013**, *5*, 29.

[49] Biswas, R.; Carpenter, W.; Fournier, J. A.; Voth, G. A.; Tokmakoff, A. *J. Chem. Phys.* **2017**, *146*, 154507.

[50] Kumar, R.; Christie, R. A.; Jordan, K. D. *J. Phys. Chem. B* **2009**, *113*, 4111–4118.

[51] Wang, Y.; Shepler, B. C.; Braams, B. J.; Bowman, J. M. *J. Chem. Phys.* **2009**, *131*, 054511.

[52] Wang, Y.; Huang, X.; Shepler, B. C.; Braams, B. J.; Bowman, J. M. *J. Chem. Phys.* **2011**, *134*, 094509.

[53] Wang, Y.; Bowman, J. M. *J. Chem. Phys.* **2011**, *134*, 154510.

[54] Partridge, H.; Schwenke, D. W. *J. Chem. Phys.* **1997**, *106*, 4618.

Part I

Theories and Methods

Chapter 2 Potential Energy Surface

2.1 Born-Oppenheimer Approximation

In the world of quantum chemistry, Born-Oppenheimer approximation is a broadly used assumption that separates the motions of atomic nuclei and electrons. This assumption states that the electrons move much faster than the nuclei and the electrons respond to the nuclei motion instantaneously. Thus, in the time independent Schrödinger equation, degrees of freedom associated with electrons and nuclei are separated and solved independently for the energies and wavefunction. For a molecule, its exact non-relativistic, time-independent Hamiltonian is:

$$\begin{aligned}\hat{H} &= \hat{H}_e + \hat{T}_n \\ &= -\sum_i \frac{1}{2}\nabla_i^2 - \sum_{i,A}\frac{Z_A}{r_{iA}} + \sum_{i>j}\frac{1}{r_{ij}} + \sum_{B>A}\frac{Z_A Z_B}{R_{AB}} - \sum_A \frac{1}{2M_A}\nabla_A^2\end{aligned} \tag{2.1}$$

where A, B refer to nuclei and i,j refer to the electrons. Z_A and M_A are the charge and mass of nucleus A. $\hat{T}_n$ is the kinetic energy operator of the nuclei with

$$\hat{T}_n = -\sum_A \frac{1}{2M_A}\nabla_A^2. \tag{2.2}$$

The operator $\hat{H}_e$ includes all the remaining parts in Equation 2.1 and can be rewritten as

$$\hat{H}_e = \hat{T}_e(\mathbf{r}) + \hat{V}_{eN}(\mathbf{r},\mathbf{R}) + \hat{V}_{ee}(\mathbf{r}) + \hat{V}_{NN}(\mathbf{R}) \tag{2.3}$$

with $\hat{T}$ as kinetic energy operator and $\hat{V}$ as potential operator.

Under the Born-Oppenheimer approximation, the nuclei can be treated as fixed and the electronic function can be formulated as

$$\hat{H}_e\Psi(\mathbf{r};\mathbf{R}) = E_e\Psi(\mathbf{r};\mathbf{R}) \tag{2.4}$$

In Equation 2.4, the total electronic energy E_e equals to $E_{el} + V_{NN}$ and is termed as potential energy of the molecule. Through changing the nuclei position $\mathbf{R}$ and

solving Equation 2.4 correspondingly, we construct an one-to-one connection between nuclei geometry and its potential energy. This is known as the poential energy surface (PES).

2.2 Permutationally Invariant Potential Energy Surface

In principle, we could solve the Schrödinger equation, Equation 2.4, of the electrons for a variety of nuclear configuration. However, it is extremely computationally expensive and may not be feasible even when a low-level *abinitio* method is used. Therefore, a practical way is to find a functional representation of the potential energy in terms of the nuclei geometry. Many efforts have been made in developing molecular potential energy surface in the last 50 years. The developed methods include Shepard-interpolation approach, interpolated moving least-square methods, neural network fitting, Gaussian process fitting and permutationally invariant polynomials (PIP) etc.[1–20]The goal of all of these approaches is to provide a precise mathematical fit to of order 10^3 – 10^5s "scattered" electronic energies (and possibly also gradients). The term "scattered" is vague, but is used to indicate that the distribution is not on grids, as for example it would be for a spline. Clearly, the dataset using a direct-product grid has exponential growth with the dimensionality, whereas from the experience with many PESs, scattered data can remain in the range given above, almost independent of the dimensionality, at least up to 10 atoms, where the PES dimensionality is 45. Explicitly incorporating permutational symmetry, which is discussed in detail below, greatly reduces the size of the dataset.

The invariance of the molecular PES with respect to overall translation and rotation is automatic if the PES is represented in terms of internal coordinates, which it generally is. For many years, the community that developed analytical expression for PESs using $3N-6$ internal coordinates instead of say all the internuclear distances.

This becomes an issue for systems with more than four atoms where the number of corresponding variable first differs.

Clearly, it would be desirable to directly incorporate the permutational symmetry into the fitting basis. The methodology that does this, using a fitting basis of polynomials in all the internuclear distances, was reviewed in papers in 2009,[16] 2010[17] and 2018.[21] Here, two techniques we developed to incorporate the permutational invarance will be briefly presented in the following section.

2.3 Permutational Symmetry

The first issue to be addressed in PES fitting is the choice of coordinates. The choice of variables turns out to be related to the number of coordinates needed to represent the PES. Historically, this was assumed to be $3N-6$, i.e., the number of vibrational modes of a non-linear molecule of N atoms. Indeed many PESs, especially those based on models, depend on this number of variables. As a result, the choice of coordinates are typically bond stretches, valence and dihedral angles, or other curvilinear coordinates such as Jacobi coordinates, polyspherical coordinates. For local representations of the PES, normal coordinates or point-group symmetry adapted coordinates have typically been used. There are advantages of course to each of these choices; however, clearly none is truly general and universal. In the permutationally invariant polynomial approach, the $N(N-1)/2$ internuclear distances (typically transformed to so-called Morse variables) are used. Interestingly, this number of variables is equal to $3N-6$ (or $3N-5$ for diatomics) for N equal to 2, 3 and 4 and then differs for N greater than or equal to 5. Thus, $N=5$ is an important boundary that affects the choice of coordinates. Clearly, using all the internuclear distances or Morse variables is general and universal for all PESs. An additional benefit of this set of variables is that it is closed under all permutations of atoms. That is, any permutation of atoms leads to the same set of variables. Of course, the

interest is on permutations of like atoms, as the PES is invariant with respect to these permutations.

Morse variables are given by $y_{ij} = \exp(-r_{ij}/a)$, where r_{ij} is the internuclear distance between atom i and j, and a is a range parameter. These variables have been used in numerous global PESs for roughly twenty years and it is worth explaining why. To make this point clear, we show fits to a Morse and LJ(8,6) potentials using a Morse variable $y = \mathrm{e}^{-r}$ and the internuclear distance r. For the former the range parameter a was taken as 1 Bohr and was not optimized. The results are shown in Figs. 2.1 and 2.2. Clearly, the fits in terms of the Morse variable are superior to the ones in r in two key ways. First, the Morse variable goes to zero as r goes to infinity and this leads to qualitatively correct asymptotic behavior of the fits, while the two potentials using r are qualitatively incorrect, and have diverging asymptotic behavior in r. (A discussion of the quantitative accuracy of the long-range behavior of the PES is deferred to the end of this section.) Second, the fitting precision of polynomials in y is superior to polynomials in r. This may appear to be obvious since the Morse variable is itself infinite order in r; however, it should be stressed that the number of linear fitting coefficient is the same in the two fits for a given polynomial order.

Morse variables were used by our group to develop a PES for C_2H_2 that describes the acetylene/vinylidene isomerization, using the following multinomial expression:[22]

$$V = \sum_{a,b,c,d,e,f} C_{abcdef} \left[y_{12}^a y_{13}^b y_{14}^c y_{23}^d y_{24}^e y_{34}^f \right], \tag{2.5}$$

where the powers varied from zero to 4, subject to the constraint that the sum of the powers is less than or equal to this maximum. The H atoms are labeled 1, 2, and the C atoms are labeled 3 and 4. Internuclear distances (and also the y_{ij}) are given using the normal order. The linear coefficients C_{abcdef} were determined using a standard linear least-squares fit to *ab initio* (in this C_2H_2 example, CCSD(T)/aug-cc-pVTZ) energies. Three-quarters of the data set was obtained by replicating 2430 energies upon interchanging the two groups of identical atoms. The resulting data

set contained 9720 energies and the least-squares fitting effort was trivial with only 210 linear coefficients to determine. Later, we recognized that a large number of coefficients were numerically equal and this was a direct consequence of taking account of the permutational symmetry numerically, i.e., by replicating the data.

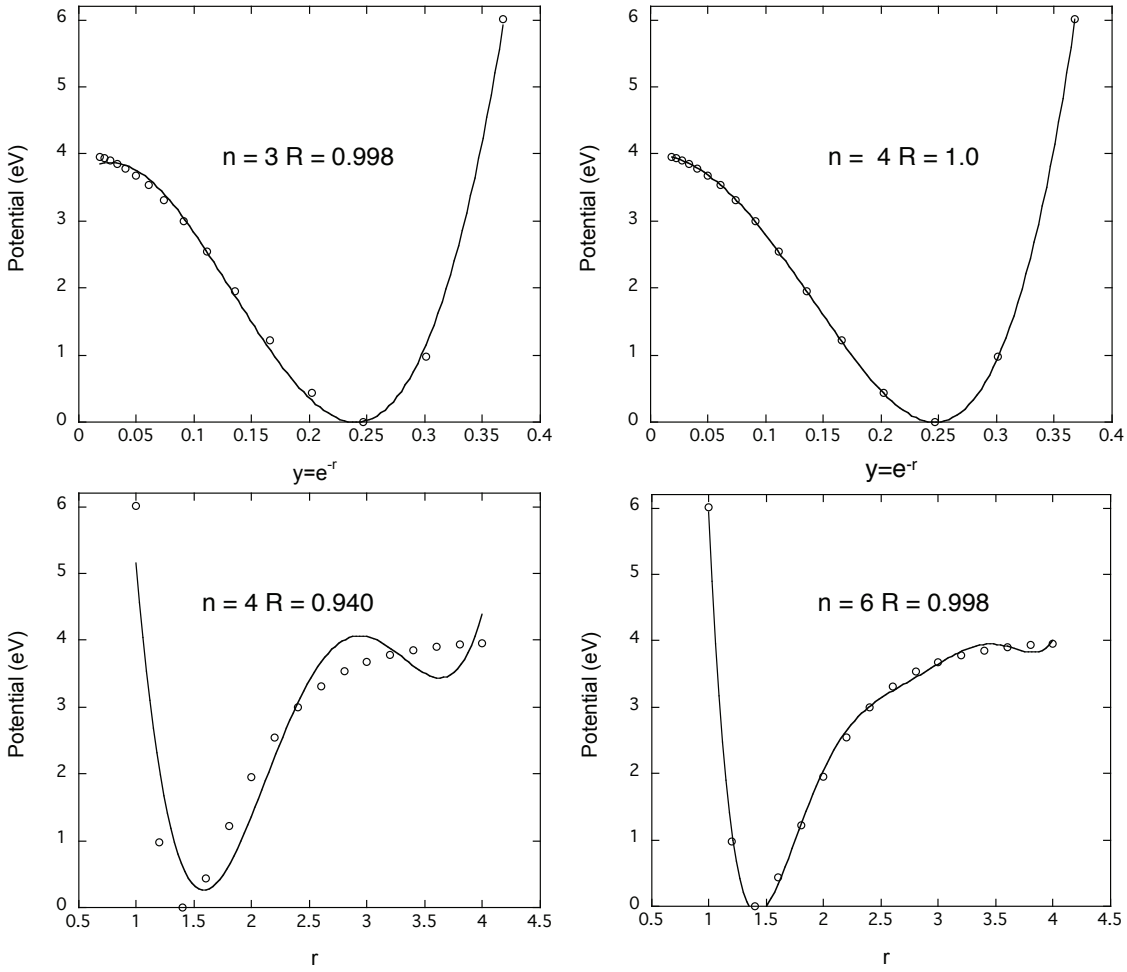

Figure 2.1 Linear least-squares polynomial fits of order n and R-value in the variables r and y to a Morse potential.

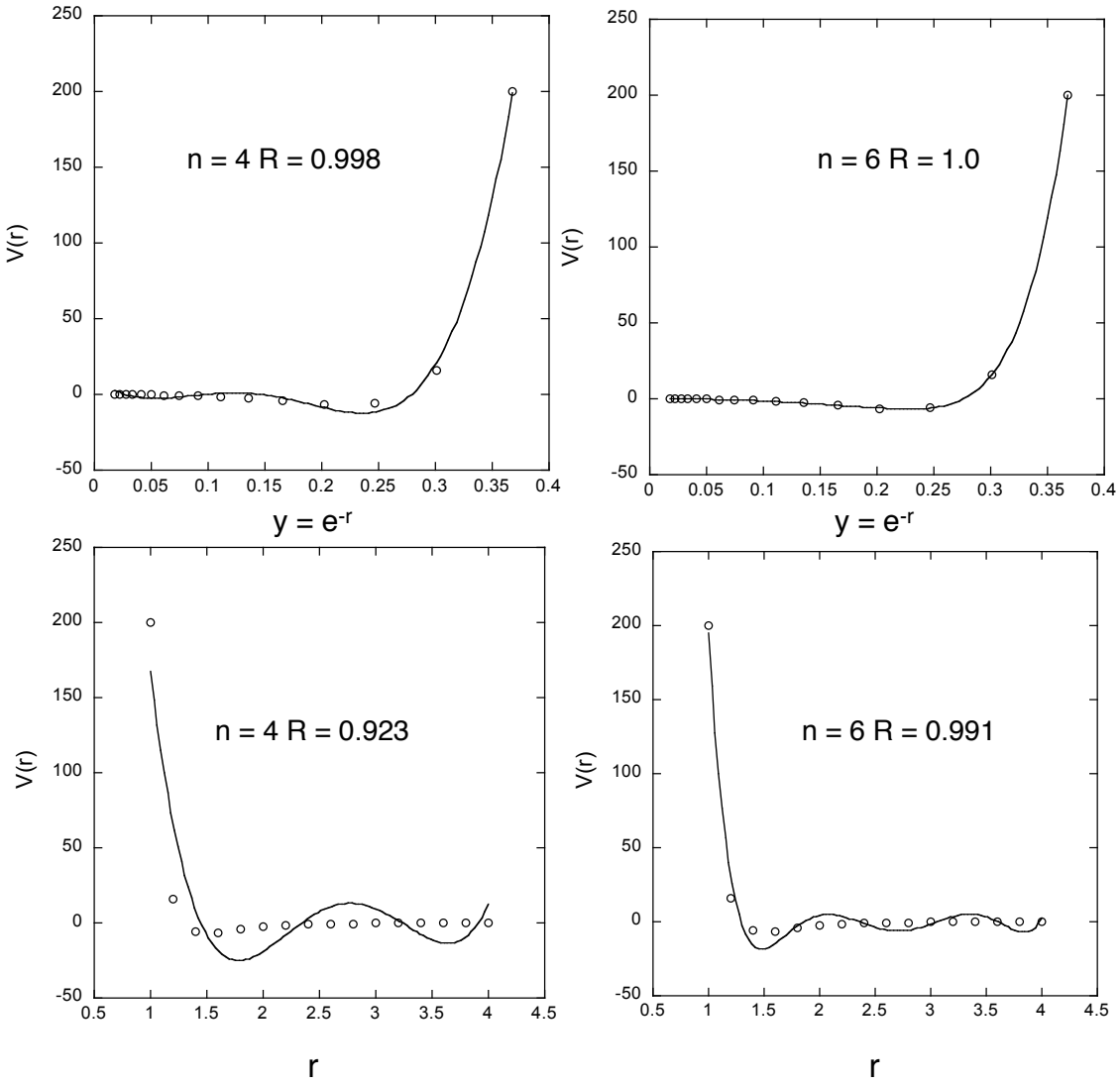

Figure 2.2 Linear least-squares polynomial fits of indicated n and R-value in the variables r and y to an LJ(8,6) potential.

Clearly, the approach of replicating data is limited to small molecules with low-order permutational symmetry. It would be infeasible for the notoriously fluxional cation, CH_5^+, which has 120 equivalent structures, all of which are feasible even for the zero-point state. In fact this was the first PES developed by our group using a fitting basis that was explicitly invariant with respect to the 120 permutations of the five H atoms.[23,24] Before we review the approach taken for this challenging example, we illustrate how the above monomial representation can by symmetrized

to incorporate permutational symmetry. For simplicity, this is shown for H_2CO in Fig. 2.3. As shown, the permutation of the two H atoms results in a mapping of the original six internuclear distances onto six new ones, two of which are the same. The monomial basis shown at the top is not invariant with respect to the permutation; however, the symmetrized basis at the bottom of the figure is.

$$V(r_1,r_2,r_3,r_4,r_5,r_6) = \sum_{n_1,n_2\cdots n_5,n_6} C_{n_1,n_2,n_3,n_4,n_5,n_6} y_1^{n_1} y_2^{n_2} y_3^{n_3} y_4^{n_4} y_5^{n_5} y_6^{n_6}$$

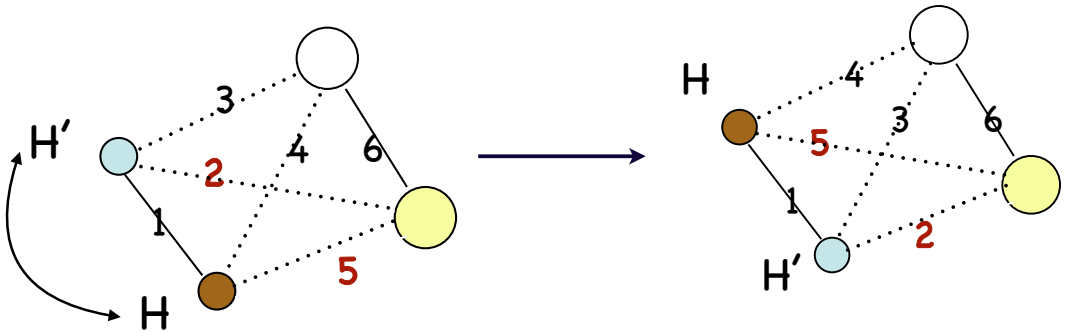

$$V(r_1,r_2,r_3,r_4,r_5,r_6) = \sum_{n_1,n_2\cdots n_5,n_6} C_{n_1,n_2,n_3,n_4,n_5,n_6} y_1^{n_1} y_6^{n_6} (y_2^{n_2} y_3^{n_3} y_4^{n_4} y_5^{n_5} + y_2^{n_5} y_3^{n_4} y_4^{n_3} y_5^{n_2})$$

Figure 2.3 Symmetrized monomial representation of the potential for H_2CO

This straightforward symmetrization was discussed in detail in the 2009 review,[16] and to illustrate it briefly here, we show the procedure for A_3B_2 molecules in the Table 2.1 below. In the first row, the first column lists the numerical labels of all atoms starting with the largest group of identical atoms, followed by the next group of identical atoms. The next column in this row gives the monomial resulting from the given order of atoms and the third column gives the monomial in the normal order. The subsequent rows in the table gives the atom labels for all permutations of like atoms followed by the permutation of the original monomial followed by the monomial in normal order, i.e, with the y_{ij} arranged with permuted powers. Summing these 12 monomials gives the complete symmetrized monomial that is invariant with

Table 2.1 Symmetrized monomials for A_3B_2 molecules

Atom Labels	Monomial	Normal Order
1 2 3 4 5	$y_{12}^a y_{13}^b y_{14}^c y_{15}^d y_{23}^e y_{24}^f y_{25}^g y_{34}^h y_{35}^i y_{45}^j$	$y_{12}^a y_{13}^b y_{14}^c y_{15}^d y_{23}^e y_{24}^f y_{25}^g y_{34}^h y_{35}^i y_{45}^j$
2 1 3 4 5	$y_{12}^a y_{23}^b y_{24}^c y_{25}^d y_{13}^e y_{14}^f y_{15}^g y_{34}^h y_{35}^i y_{45}^j$	$y_{12}^a y_{13}^e y_{14}^f y_{15}^g y_{23}^b y_{24}^c y_{25}^d y_{34}^h y_{35}^i y_{45}^j$
3 2 1 4 5	$y_{23}^a y_{13}^b y_{34}^c y_{35}^d y_{12}^e y_{24}^f y_{25}^g y_{14}^h y_{15}^i y_{45}^j$	$y_{12}^e y_{13}^b y_{14}^h y_{15}^i y_{23}^a y_{24}^f y_{25}^g y_{34}^c y_{35}^d y_{45}^j$
1 3 2 4 5	$y_{13}^a y_{12}^b y_{14}^c y_{15}^d y_{23}^e y_{34}^f y_{35}^g y_{24}^h y_{25}^i y_{45}^j$	$y_{12}^b y_{13}^a y_{14}^c y_{15}^d y_{23}^e y_{24}^h y_{25}^i y_{34}^f y_{35}^g y_{45}^j$
3 1 2 4 5	$y_{13}^a y_{23}^b y_{34}^c y_{35}^d y_{12}^e y_{14}^f y_{15}^g y_{24}^h y_{25}^i y_{45}^j$	$y_{12}^e y_{13}^a y_{14}^f y_{15}^g y_{23}^b y_{24}^h y_{25}^i y_{34}^c y_{35}^d y_{45}^j$
2 3 1 4 5	$y_{23}^a y_{12}^b y_{24}^c y_{25}^d y_{13}^e y_{34}^f y_{35}^g y_{14}^h y_{15}^i y_{45}^j$	$y_{12}^b y_{13}^e y_{14}^h y_{15}^i y_{23}^a y_{24}^c y_{25}^d y_{34}^f y_{35}^g y_{45}^j$
1 2 3 5 4	$y_{12}^a y_{13}^b y_{15}^c y_{14}^d y_{23}^e y_{25}^f y_{24}^g y_{35}^h y_{34}^i y_{45}^j$	$y_{12}^a y_{13}^b y_{14}^d y_{15}^c y_{23}^e y_{24}^g y_{25}^f y_{34}^i y_{35}^h y_{45}^j$
2 1 3 5 4	$y_{12}^a y_{23}^b y_{25}^c y_{24}^d y_{13}^e y_{15}^f y_{14}^g y_{35}^h y_{34}^i y_{45}^j$	$y_{12}^a y_{13}^e y_{14}^g y_{15}^f y_{23}^b y_{24}^d y_{25}^c y_{34}^i y_{35}^h y_{45}^j$
3 2 1 5 4	$y_{23}^a y_{13}^b y_{35}^c y_{34}^d y_{12}^e y_{25}^f y_{24}^g y_{15}^h y_{14}^i y_{45}^j$	$y_{12}^e y_{13}^b y_{14}^i y_{15}^h y_{23}^a y_{24}^g y_{25}^f y_{34}^d y_{35}^c y_{45}^j$
1 3 2 5 4	$y_{13}^a y_{12}^b y_{15}^c y_{14}^d y_{23}^e y_{35}^f y_{34}^g y_{25}^h y_{24}^i y_{45}^j$	$y_{12}^b y_{13}^a y_{14}^d y_{15}^c y_{23}^e y_{24}^i y_{25}^h y_{34}^g y_{35}^f y_{45}^j$
3 1 2 5 4	$y_{13}^a y_{23}^b y_{35}^c y_{34}^d y_{12}^e y_{15}^f y_{14}^g y_{25}^h y_{24}^i y_{45}^j$	$y_{12}^e y_{13}^a y_{14}^g y_{15}^f y_{23}^b y_{24}^i y_{25}^h y_{34}^d y_{35}^c y_{45}^j$
2 3 1 5 4	$y_{23}^a y_{12}^b y_{25}^c y_{24}^d y_{13}^e y_{35}^f y_{34}^g y_{15}^h y_{14}^i y_{45}^j$	$y_{12}^b y_{13}^e y_{14}^i y_{15}^h y_{23}^a y_{24}^d y_{25}^c y_{34}^g y_{35}^f y_{45}^j$

respect to all 12 permutations. Note however, that the actual symmetrized monomial basis rarely contains all of these monomials. This is because the summation must truncate at some reasonable value of the total polynomial order. Typically, we limit the total polynomial order to a value between 5 and 8 (higher values are used for smaller systems, e.g., 12 or more for triatomics). Thus, for the A_3B_2 example with a maximum total polynomial order of say 6 there are no monomials with seven or more Morse variables.

A compact expression that expresses this symmetrization approach is the following one, specifically for a tetraatomic.

$$V = \sum_{a,b,c,d,e,f} C_{abcdef} \hat{S} \left[y_{12}^a y_{13}^b y_{14}^c y_{23}^d y_{24}^e y_{34}^f \right], \tag{2.6}$$

where "$\hat{S}$" is a symmetrization operator that produces the appropriate sum of monomials.

An important point, as mentioned above, is that all the internuclear distances (Morse variables) are used in the monomials. For N atoms this number is $N(N-1)/2$. This is a general and convenient (if not necessary) feature of the fitting using permutationally invariant polynomials, since this set of variables is closed under all

permutations of like atoms. (This use of all internuclear distances/Morse variables has been used by other groups, who employ neural network fitting.[8–10])

To summarize thus far, permutationally invariant polynomials in all Morse variables provide a general approach to mathematically represent high-dimensional PESs. For a given range parameter, a, in the Morse variable, the PES is determined by straightforward linear least-squares fitting tens of thousands to hundreds of thousands of electronic energies.

Next, we need to mention that the above presentation of symmetrized monomials, while correct and usable, is mainly pedagogical, because the monomial symmetrization method is not the one we employ in numerical work, except in simple cases where the order of the permutation group is small. The two approaches we use, which are more computationally efficient, are briefly described next. They are mathematically equivalent to monomial symmetrization. One uses an efficient recursive method to generate the symmetrized monomials and does makes use of factorization. This is called the Monomial Symmetrization Approach (MSA) and is described in detail in paper by Xie and Bowman.[17]

The other approach, which is the one that has been used to generate most of the PESs, makes use of powerful theorems from invariant polynomial theory[25] to provide efficient factorization of the symmetrized monomial basis. Details of the implementation along with the relevant theory are given in the review by Braams and Bowman[16] and also in an earlier paper reporting a PES for $H_5O_2^+$.[26] The expression for the PES using this approach is

$$V(\boldsymbol{y}) = \sum_{\alpha=1}^{M} c_\alpha \mathrm{poly}_\alpha(p(\boldsymbol{y}))q_\alpha(\boldsymbol{y}), \tag{2.7}$$

where $\boldsymbol{y}$ represents all Morse variables, $p(\boldsymbol{y})$ and $q_\alpha(\boldsymbol{y})$ are *primary* and *secondary* invariant polynomials. That is, they are polynomials that are invariant over the direct-product symmetry group for the present application.

A theorem states that the number of *primary* polynomials is equal to the number

of arguments of V, i.e., the number of internuclear distances, $N(N-1)/2$ for an N-atom system. The number of *secondary* polynomials (which are similar in structure to symmetrized monomials) is unbounded; however, for a finite maximum total polynomial order, indicated in Eq. 2.7 to be M, the maximum order of $q_\alpha(\boldsymbol{y})$ is M. Finding these polynomials for direct-product groups $S_n \times S_m \cdots \times S_p$ (for $A_nB_m \cdots X_p$ molecules) is non-trivial and so computational algebra software was employed. Specifically, the code MAGMA[27] was used to generate a library of primary and secondary invariant polynomials for many molecule types.

Also, it should be noted that permutationally covariant expressions for the dipole moment have also been developed[16,26] and used in numerous fits to full-dimensional dipole moment surfaces.

2.4 Many-body Expansion

The current fitting software is limited to roughly 10 atoms. Extending the global fitting method to more than 10 atoms is certainly a worthy research direction; however, another approach, especially for non-covalent interactions, is already in use. This is the many-body approach, which has been used, for example to develop an *ab initio* PES for water.[28] This many-body approach has been used to develop PESs for hydrated HCl,[29] CH_4,[30] H_2,[31] CO_2,[32] Na^+, F^-, Cl^- [33] and H_3O^+.[34–37]

For a molecular cluster, by defining monomers which is the single molecule in the cluster, the total potential energy of the cluster can be represented as a sum of one-body, intrinsic two-body, three-body energies, etc.

$$V = \sum_i V_i^{(1)} + \sum_{i<j} V_{i,j}^{(2)} + \sum_{i<j<k} V_{i,j,k}^{(3)} + \cdots \tag{2.8}$$

where

$$\begin{aligned} V_i^{(1)} &= V_i \\ V_{i,j}^{(2)} &= V_{i,j} - V_i^{(1)} - V_j^{(1)} \\ V_{i,j,k}^{(3)} &= V_{i,j,k} - V_{i,j}^{(2)} - V_{i,k}^{(2)} - V_{j,k}^{(2)} - V_i^{(1)} - V_j^{(1)} - V_k^{(1)} \end{aligned} \tag{2.9}$$

In Equation 2.8 and 2.9, $V_i^{(1)}$,$V_{i,j}^{(2)}$ and $V_{i,j,k}^{(3)}$ are one-body, two-body and 3-body energies of the clusters. In principal, for a system with n monomers, the many-body expansion should extend to n-body to make the summation compact. However, for weakly bonded monomers, the interactions decay quickly and most of the higher-body (>3) terms can be neglected. For example, in water clusters, it has been investigated that the one, two and three-body terms contribute to more than 98% of the total energy of the whole system. Using the many-body expansion, the potential energy of the cluster system with arbitrary number of monomers can be calculated easily.

Bibliography

[1] Schatz, G. C. *Rev. Mod. Phys.* **1989**, *61*, 669–688.

[2] Dawes, R.; Thompson, D. L.; Guo, Y.; Wagner, A. F.; Minkoff, M. *J. Chem. Phys.* **2007**, *126*, 184108.

[3] Dawes, R.; Passalacqua, A.; Wagner, A.; Sewell, T. D.; Minkoff, M.; Thompson, D. L. *J. Chem. Phys.* **2009**, *130*, 144107.

[4] Guo, Y.; Harding, L. B.; Wagner, A. F.; Minkoff, M.; Thompson, D. L. *J. Chem. Phys.* **2007**, *126*, 104105.

[5] Raff, L. M.; Malshe, M.; Hagan, M.; Doughan, D. I.; Rockley, M. G.; Komanduri, R. *J. Chem. Phys.* **2005**, *122*, 084104.

[6] Doughan, D. I.; Raff, L. M.; Rockley, M. G.; Hagan, M.; Agrawal, P. M.; Komanduri, R. *J. Chem. Phys.* **2006**, *124*, 054321.

[7] Manzhos, S.; Carrington, T. *J. Chem. Phys.* **2006**, *125*, 084109.

[8] Chen, J.; Xu, X.; Xu, X.; Zhang, D. H. *J. Chem. Phys.* **2013**, *138*, 221104.

[9] Jiang, B.; Guo, H. *J. Chem. Phys.* **2013**, *139*, 054112.

[10] Jiang, B.; Li, J.; Guo, H. *Int. Rev. Phys. Chem.* **2016**, *35*, 479–506.

[11] Manzhos, S.; Dawes, R.; Carrington, T. *Int. J. Quant. Chem.* **2015**, *115*, 1012–1020.

[12] Behler, J. *Int. J. Quant. Chem.* **2015**, *115*, 1032–1050.

[13] Behler, J. *J. Chem. Phys.* **2016**, *145*, 170901.

[14] Bartók, A. P.; Csányi, G. *Int. J. Quant. Chem.* **2015**, *115*, 1051–1057.

[15] Cui, J.; Krems, R. V. *J. Phys. B* **2016**, *49*, 224001.

[16] Braams, B. J.; Bowman, J. M. *Int. Rev. Phys. Chem.* **2009**, *28*, 577–606.

[17] Xie, Z.; Bowman, J. M. *J. Chem. Theory Comput.* **2010**, *6*, 26–34.

[18] Bowman, J. M.; Braams, B. J.; Carter, S.; C., C.; Czakó, G.; Fu, B.; Huang, X.; Kamarchik, E.; Sharma, A. R.; C., S. B.; Wang, Y.; Xie, Z. *J. Phys. Chem. Lett.* **2010**, *1*, 1866–1874.

[19] Bowman, J. M.; Czakó, G.; Fu, B. *Phys. Chem. Chem. Phys.* **2011**, *13*, 8094–8111.

[20] Shao, K.; Chen, J.; Zhao, Z.; Zhang, D. H. *J. Chem. Phys.* **2016**, *145*, 071101.

[21] Qu, C.; Yu, Q.; Bowman, J. M. *Annu. Rev. Phys. Chem.* **2018**, *69*, 6.1–6.25.

[22] Zou, S. L.; Bowman, J. M. *Chem. Phys. Lett.* **2003**, *368*, 421–424.

[23] Brown, A.; Braams, B. J.; Christoffel, K.; Jin, Z.; Bowman, J. M. *J. Chem. Phys.* **2003**, *119*, 8790–8793.

[24] Jin, Z.; Braams, B. J.; Bowman, J. M. *J. Phys. Chem. A* **2006**, *110*, 1569–1574.

[25] Derksen, H.; Kemper, G. *Computational Invariant Theory*; Springer Verlag: Berlin, Heidelberg, New York, 2002.

[26] Huang, X.; Braams, B. J.; Bowman, J. M. *J. Chem. Phys.* **2005**, *122*, 044308.

[27] Bosma, W.; Cannon, J.; Playoust, C. *J. Comp. Symb. Comp.* **1997**, *24*, 235–245.

[28] Wang, Y.; Huang, X.; Shepler, B. C.; Braams, B. J.; Bowman, J. M. *J. Chem. Phys.* **2011**, *134*, 094509.

[29] Mancini, J. S.; Bowman, J. M. *J. Phys. Chem. A* **2014**, *118*, 7367–7374.

[30] Conte, R.; Qu, C.; Bowman, J. M. *J. Chem. Theory Comput.* **2015**, *11*, 1631–1638.

[31] Homayoon, Z.; Conte, R.; Qu, C.; Bowman, J. M. *J. Chem. Phys.* **2015**, *143*, 084302.

[32] Wang, Q.; Bowman, J. M. *J. Chem. Phys.* **2017**, *147*, 161714.

[33] Wang, Y.; Bowman, J. M.; Kamarchik, E. *J. Chem. Phys.* **2016**, *144*, 114311.

[34] Yu, Q.; Bowman, J. M. *J. Chem. Theory Comput.* **2016**, *12*, 5284–5290.

[35] Yu, Q.; Bowman, J. M. *J. Chem. Phys.* **2017**, *146*, 121102.

[36] Heindel, J. P.; Yu, Q.; Bowman, J. M.; Xantheas, S. S. *J. Chem. Theory Comput.* **2018**, *14*, 4553–3566.

[37] Yu, Q.; Bowman, J. M. *J. Am. Chem. Soc.* **2017**, doi: 10.1021/jacs.7b05459.

Chapter 3 Molecular Vibrations

Vibrational properties of molecular system provide invaluable insight of its structure and dynamics. Advanced methods mainly focus on solving the nuclear Schrödinger equation which is a challenging problem for polyatomic system. In this chapter, we will introduce the fully quantum mechanical approaches to solve the nuclear Schrödinger equation, vibrational self-consistent field (VSCF) and virtual-state configuration interaction (VCI) methods. These methods are implemented in the software MULTIMODE which has been used in vibrational analysis of many molecular systems. Another approach to be introduced in this chapter is diffusion Monte Carlo (DMC) method. This method is mainly applied to investigate the ground state vibrational properties of molecular system.

3.1 Vibrational Self-Consistent Field and Virtual-state Configuration Interaction

First, we write the molecular Hamiltonian of a nonlinear molecule in normal mode coordinates:

$$\hat{H} = \sum_{i=1}^{3N-6} \hat{T}_i + V(\mathbf{Q}) \tag{3.1}$$

where $\mathbf{Q} = [Q_1 \cdots Q_{3N-6}]$ and $\hat{T}_i$ is the kinetic energy operator of the i-th normal mode where $V(\mathbf{Q})$ is the potential energy for the molecule.

In the self-consistant field (SCF) method,[1–3] the total wavefunction for the quantum state $(k_1, k_2, \cdots, k_N)$ can be expanded as a direct product of one-mode wavefunctions:

$$\Phi_K = \prod_{i=1}^{3N-6} \phi_i(Q_i) \tag{3.2}$$

To find out a set of optimal one-mode wavefunctions $\phi_i(Q_i)$, the Lagrange multipliers

method is applied:

$$\mathcal{L} = \langle \Phi_K | \hat{H} | \Phi_K \rangle - \lambda(\langle \Phi_K | \Phi_K \rangle) - 1) \tag{3.3}$$

$$\delta\mathcal{L} = \delta\langle \Phi_K | \hat{H} | \Phi_K \rangle - \lambda\delta\langle \Phi_K | \Phi_K \rangle) = 0 \tag{3.4}$$

The variation procedure from Equation 3.3 and 3.4 results in a set of coupled SCF equations.

$$\Big[\hat{T}_i + \Big\langle \prod_{l\neq i}^{3N-6} \phi_l(Q_l) \Big| V(\mathbf{Q}) \Big| \prod_{l\neq i}^{3N-6} \phi_l(Q_l) \Big\rangle - \lambda_i \Big] \phi_i(Q_i) = 0 \tag{3.5}$$

These coupled equations are then solved iteratively for each model wave-function until self-consistency is reached. Each modal function $\phi_i(Q_i)$ is expressed as a linear summation of a finite set of basis functions multiplied by unknown coefficients

$$\phi_i(Q_i) = \sum_{n_i}^{F_i} C_{n_i} \psi^{(n_i)}(Q_i) \tag{3.6}$$

where F_i is the number of basis functions for the i_{th} mode. The coefficients can be determined by diagonalizing the Hamiltonian matrix.

The VSCF approach is analogous to the Hartree-Fock self-consistent Field (HF-SCF) approach in the electronic structure theory. The VSCF method treats the coupling between one mode and all other modes as an averaged potential over all remaining coordinates. Similar to the configuration interaction (CI) concept in electronic structure problem, the result of VSCF calculation can be further implemented in configuration interaction calculation, which is termed as virtual state configuration interaction method (VCI).[4]

Recall that in the VSCF calculation, for each mode, we obtain the eigenfunction $\phi_i^{\nu_i}(Q_i)$ with different excitations ν_i. Then, the ground state and other virtual state wavefunctions from VSCF method can be expressed as:

$$\Phi_K = \prod_{i=1}^{3N-6} \phi_i^{\nu_i}(Q_i), (\nu_i = 0, 1, 2, \cdots) \tag{3.7}$$

where K is the index of ground and excited VSCF states. In the VCI expression, the wavefunction is expanded in terms of the VSCF ground and virtual states.

$$\Psi = \sum_K C_K \Phi_K \tag{3.8}$$

where coefficients C_K can be obtained through diagonalizing the Hamiltonian matrix.

3.2 MULTIMODE

The VSCF and VCI methods are implemented in the software "MULTOMODE".[5] This code is based on the rigorous Watson Hamiltonian for non-linear molecule. With a n-mode representation of the full potential energy, MULTIMODE has been widely applied to a variety of molecular systems.

3.2.1 Watson Hamiltonian

For a nonlinear polyatomic molecule, the Watson Hamiltonian is used in MULTIMODE, which is represented in normal coordinates

$$\hat{H} = \frac{1}{2}\sum_{\alpha\beta}(\hat{J}_\alpha - \hat{\pi}_\alpha)\mu_{\alpha\beta}(\hat{J}_\beta - \hat{\pi}_\beta) - \frac{1}{2}\sum_k^{3N-6}\frac{\partial^2}{\partial Q_k^2} - \frac{1}{8}\sum_\alpha \mu_{\alpha\alpha} + V(\mathbf{Q}) \tag{3.9}$$

where α, β are x,y and z component of the Cartesian coordinates, $\hat{j}_\alpha$ and $\hat{\pi}_\alpha$ are the Cartesian component of the total and vibrational angular momenta. $\mu_{\alpha\beta}$ is the inverse effective moment of the inertia tensor and $V(\mathbf{Q})$ is the full potential in terms of the N normal coordinates, denoted as $\mathbf{Q}$. In most cases, we solve the $J = 0$ Schrödinger equation. Equation 3.9 can be simplified as

$$\hat{H} = \frac{1}{2}\sum_{\alpha\beta}\hat{\pi}_\alpha\mu_{\alpha\beta}\hat{\pi}_\beta - \frac{1}{2}\sum_k^{3N-6}\frac{\partial^2}{\partial Q_k^2} - \frac{1}{8}\sum_\alpha \mu_{\alpha\alpha} + V(\mathbf{Q}) \tag{3.10}$$

where the fist term is the vibration-rotation (Coriolis) coupling term, second term is the kinetic opetrator and third term is the Watson correction term.

3.2.2 n-Mode Representation of the Potential

In MULTIMODE, the full-dimensional potential is represented in a hierarchical n-mode representation (nMR)

$$V(Q_1, Q_2, \cdots, Q_m) \approx \sum_i V_i^{(1)}(Q_i) + \sum_{ij} V_{ij}^{(2)}(Q_i, Q_j) + \sum_{ijk} V_{ijk}^{(3)}(Q_i, Q_j, Q_k) + \sum_{ijkl} V_{ijkl}^{(4)}(Q_i, Q_j, Q_k, Q_l) + \cdots + \sum_{ijkl\cdots} V_{ijkl\cdots}^{(n)}(Q_i, Q_j, Q_k, Q_l, \cdots) \tag{3.11}$$

In this representation, the one-mode representation of the potential is $V_i^{(1)}(Q_i)$ where just one specific mode coordinate,Q_i, varies with all remaining coordinates set as zero. The two-mode representation contains the one-mode representation plus the two-mode terms, $V_{ij}^{(2)}(Q_i, Q_j)$, which is

$$V_{ij}^{(2)} = V(Q_i, Q_j, Q_{l,j} = 0) - V_i^{(1)}(Q_i) - V_j^{(1)}(Q_j) \tag{3.12}$$

The 3-mode, 4-mode,$\cdots$,n-mode terms are then expressed accordingly. Due to the computational resources, in MULTIMODE, this expansion is truncated at maximum level of six. Thus, the multidimensional integration over the potential can be greatly reduced to six rather than 3N-6.

3.2.3 Infrared Intensity

Upon VSCF/VCI calculation is finished using MULTOMODE, the VCI wavefunctions can be written to the disk and they will be used for property calculation, especially here, infrared intensity calculation. Using the provided dipole moment surface (DMS), the transition dipole matrix element is calculated by

$$R_{\nu\nu'}^{\alpha} = \langle \Psi_\nu(\mathbf{Q}) | \mu^\alpha(\mathbf{Q}) | \Psi_{\nu'}(\mathbf{Q}) \rangle \tag{3.13}$$

where Ψ_ν and $\Psi_{\nu'}$ are vibrational wavefunction for vibration state ν and ν'. $\mu^\alpha(\mathbf{Q})$ is the α component ($\alpha = x, y, z$) of the dipole moment which is also expressed in a n-mode representation.

According to the calculated transition dipole matrix, the infrared intensity for the associated transition $\nu \rightarrow \nu'$ is calculated

$$I_{\nu\nu'} = \frac{8\pi^3 N_A}{3hc \times 4\pi\epsilon_0} E_{\nu\nu'} \sum_{\alpha} |R^{\alpha}_{\nu\nu'}|^2 (N_\nu - N_{\nu'}) \tag{3.14}$$

where N_A is the Avogadro's number, $E_{\nu\nu'}$ is the transition energy between two states, N_ν is the number of molecules in state ν. Considering the transitions from vibrational ground state to other excited states, the term $N_\nu - N_{\nu'}$ is approximately 1.

3.3 Quantum Local Monomer Model

The large dimensionality in a large molecular cluster or in condensed phase matters makes it very difficult to conduct vibrational calculations, especially using quantum methods like VSCF/VCI. To reduced the dimensionality in calculation, the local monomer model is introduced for systems including weakly bounded molecules and intramolecular vibrations are of interest. This method has been successfully applied in anharmonic vibrational spectra calculations of different systems like water clusters,[6,7] ice and liquid water,[8,9] HCl clusters,[10] protonated water clusters.[11,12]

In the Local-Monomer model, only one monomer's vibrational contribution is calculated at each time with structure of all other monomers fixed (assuming that the interaction between this monomer with other monomers can be neglected). This basic concept is adopted from harmonic analysis and also the anharmonic analysis (VSCF/VCI for example). Thus, the Schrödinger equation for the embedded monomer i can be written as

$$[\hat{T}_i + V_i(\mathbf{Q_i})]\Psi_i(\mathbf{Q}_i) = E_i \Psi_i(\mathbf{Q}_i) \tag{3.15}$$

where $\hat{T}_i$ is the kinetic energy operator for monomer i, $\mathbf{Q}_i$ is the set of local normal mode of monomer i and $V_i(\mathbf{Q_i})$ is the potential energy of the whole cluster system which is calculated from perturbed structure of monomer i and fixed structure of all remaining monomers.

Bibliography

[1] Bowman, J. M. *J. Chem. Phys.* **1978**, *68*, 608.

[2] Bowman, J. M. *Acc. Chem. Res.* **1986**, *19*, 202–208.

[3] Carter, S.; Culik, J. S.; Bowman, J. M. *J. Chem. Phys.* **1997**, *107*, 10458.

[4] Christoffel, K. M.; Bowman, J. M. *Chem. Phys. Lett.* **1982**, *85*, 220–224.

[5] Bowman, J. M.; Carter, S.; Huang, X. *Int. Rev. Phys. Chem.* **2003**, *22*, 533–549.

[6] Wang, Y.; Huang, X.; Shepler, B. C.; Braams, B. J.; Bowman, J. M. *J. Chem. Phys.* **2011**, *134*, 094509.

[7] Wang, Y.; Bowman, J. M. *J. Chem. Phys.* **2011**, *134*, 154510.

[8] Liu, H.; Wang, Y.; Bowman, J. M. *J. Chem. Phys.* **2015**, *142*, 194502.

[9] Liu, H.; Wang, Y.; Bowman, J. M. *J. Phys. Chem. B* **2016**, *120*, 2824–2828.

[10] Mancini, J. S.; Bowman, J. M. *J. Phys. Chem. A* **2014**, *118*, 7367–7374.

[11] Yu, Q.; Bowman, J. M. *J. Chem. Phys.* **2017**, *146*, 121102.

[12] Yu, Q.; Bowman, J. M. *J. Am. Chem. Soc.* **2017**, doi: 10.1021/jacs.7b05459.

Part II

Many-body Potential Model for Hydrated Proton

Chapter 4 Many-body Potential Energy Surface and Dipole Moment Surface

As introduced in Chapter 1, an *ab initio* many-body potential energy surface (PES) is needed to accurately describe the potential energy of the molecular system with proton plus an arbitrary number of water monomers. The vibrational spectra and molecular dynamics calculations of different hydrated proton systems can then be conducted. We report the first version of this PES in the format of communication when we calculate the VSCF/VCI spectra of two important protonated water clusters, $H_7O_3^+$ and $H_9O_4^+$.[1] In this version, the PES is truncated at three body level and the hydronium-water-water 3-body interaction is represented in a simple expression, suggested by Skinner and coworkers' work to represent the water 3-body interaction.[2,3] Later, to generate a more accurate and general PES for hydrated proton system, we conduct a mathematical fit to the hydronium-water-water 3-body term based on Monomial Symmetrization approach using thousands of CCSD(T)-F12/aVDZ electronic energies.[4] We also address the issue of defining monomers in hydrated proton system especially the hydronium core. This is done through considering different assignments of hydronium core (pivot hydronium and non-pivot hydronium in the first solvation shell). This PES has been successfully tested in different vibrational calculations on different protonated water clusters.[4–6] A final version of hydroted proton PES is reported in 2018 where we compared the PES results with benchmark calculation of series of small protonated water clusters in terms of structure, binding energies and harmonic frequencies.[7]In this version, we refit the hydronium-water-water 3-body interaction through adding more *ab initio* electronic energies sampled from larger protonated water clusters. We also added a simple expression of hydronium-water 4-body terms to correct the binding energies of different protonated water clusters. In this

chapter, all the terms in the many-body representation will be discussed in detail.

4.1 Assignment of Monomers

The many-body representation of the potential energy of hydrated proton requires an identification of the hydronium and water monomers. This is a well-known issue in all many-body representations of the proton-water potential. This is especially important for “Zundel" structures or geometries during proton transfer process. For example, in $H_5O_2^+$ the proton sits equidistant between two water monomers at equilibrium and thus then proton can be arbitrarily assigned to either one of the two water monomers to form the hydronium monomer. To deal with this issue, we proposed a monomer assignment approach based on the nuclear positions, stimulated by previous work.[8]

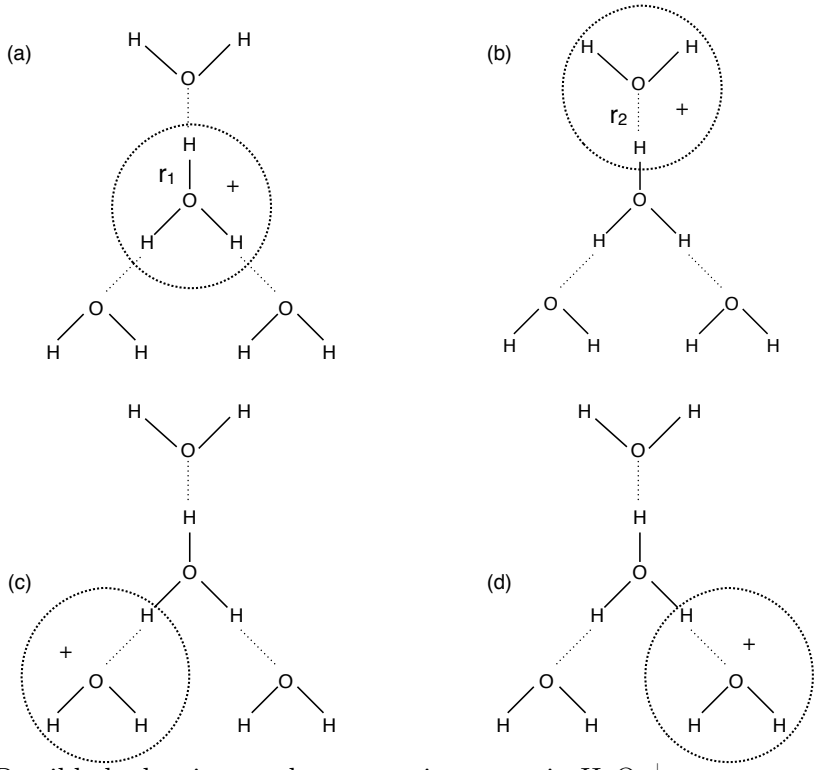

Figure 4.1 Possible hydronium and water assignments in $H_9O_4^+$

We demonstrate this assignment approach with an Eigen structure as a simple

example, shown in Figure 4.1.

In Eigen structure, since the proton is essentially localized at the center, the central hydronium is defined as the pivot hydronium core, as shown in panel (a). However, either one of the three hydrogen atoms in the pivot hydronium ion could act as a proton and transfers to a surrounding water molecule, three non-pivot hydronium core assignments should also be considered, as indicated in panels (b), (c), and (d) in Figure 4.1. In a general case, among all the possible assignments, we pick the hydronium that has the smallest sum of three OH distances as the pivot hydronium core. Unlike the earlier assignment protocol,[8] where all the possible monomer assignment are considered, we only considered the first solvation shell of the pivot hydronium core. The final potential is a weighted average of the four potential values of the four assignments. The pivot assignment usually has the largest weight in the average. For each non-pivot hydronium core assignment, the weight is calculated based on the distances between the proton and oxygen atoms. Take assignment (b) as an example, and let r_1 be the distance between the proton and the oxygen in the pivot hydronium core and r_2 be the distance between the proton and the oxygen in non-pivot hydronium core (shown in the figure). The weight of this non-pivot assignment can be obtained based on the difference between r_1 and r_2, denoted $r = r_1 - r_2$. The weighting function is basically the same as the switching function introduced above, given by

$$\begin{aligned} s_i(r) &= 0.0, && r < -0.5 \text{ Å} \\ &= 10(r+0.5)^3 - 15(r+0.5)^4 + 6(r+0.5)^5, && -0.5 \text{ Å} \leq r \leq 0.5 \text{ Å} \\ &= 1.0, && r > 0.5 \text{ Å} \end{aligned} \tag{4.1}$$

We determined the switching range (-0.5 to 0.5 Å) from $H_7O_3^+$ and $H_9O_4^+$ minimum structures where all the values of defined r are smaller than -0.5 Å. It is clear that for an Eigen structure where all the H nuclei are closer to the central oxygen atom, r is smaller than -0.5 Å and the contribution of all three non-pivot hydronium assignment

is 0. For the bare Zundel structure $H_5O_2^+$, the proton is equally shared by two water molecules so r is 0, and therefore two possible hydronium assignments have the same weight of 0.5. In the weighted average for the final potential, the contribution of a non-pivot hydronium core assignment is $\frac{s_i}{1-s_i}V_i$. Thus, the final potential energy for a given cluster is

$$V_{total} = \frac{V_{pivot} + \sum_i^3 \frac{s_i}{1-s_i} V_i}{1 + \sum_i^3 \frac{s_i}{1-s_i}} \tag{4.2}$$

with proper normalization. Similarly, the total dipole moment of the system is also calculated as,

$$\mu_{total} = \frac{\mu_{pivot} + \sum_i^3 \frac{s_i}{1-s_i} \mu_i}{1 + \sum_i^3 \frac{s_i}{1-s_i}}, \tag{4.3}$$

Next, we will demonstrate each component in the many-body representation of the potential truncated at 4-body level, along with the many-body representation of the total dipole moment truncated at 2-body level.

$$\begin{aligned} V =& V_h^{(1)} + \sum_i V_{w_i}^{(1)} + \sum_i V_{h,w_i}^{(2)} + \sum_{i,j} V_{w_i,w_j}^{(2)} \\ &+ \sum_{i,j,k} V_{w_i,w_j,w_k}^{(3)} + \sum_{i,j} V_{h,w_i,w_j}^{(3)} + \sum_{i,j,k} V_{h,w_i,w_j,w_k}^{(4)}. \end{aligned} \tag{4.4}$$

$$\mu = \mu_h^{(1)} + \sum_i \mu_{w_i}^{(1)} + \sum_i \mu_{h,w_i}^{(2)} + \sum_{i,j} \mu_{w_i,w_j}^{(2)}. \tag{4.5}$$

4.2 H_3O^+ Potential Energy Surfaces

Hydronium is among the most important cations in chemistry. It has been extensively studied in the gas phase, spectroscopically, where large tunneling splittings for the ground and excited vibrational states have been observed, due to the low (planar) barrier (roughly 700 cm^{-1}) separating equivalent minima of C_{3v} symmetry.[9–16] It has also been observed in the interstellar medium.[17]

Theoretically, there have been a number of full-dimensional quantum calculations of the vibrational energies of hydronium, using *ab initio* potential energy surfaces.[18–20] These are based on fitting many high-level, CCSD(T) energies, but restricted to

the region of the equivalent minima and saddle-point separating them. The PESs do produce vibrational energies and splittings in good agreement with experiment, especially the 2003-PES of Halonen and co-workers.[20] However, these PESs are semi-global, which means that while they are full-dimensional, they are restricted to regions around the two equivalent minima and saddle point separating them and thus do not describe dissociation.

In condensed phase, hydronium is even more well known as the hydrated proton, which, in elementary descriptions, is simply the association of the proton with H_2O. However, the dissocation/association of the proton with H_2O is not a simple process.[21] In fact the adiabatic dissociation of H_3O^+ correlates with $H_2O^+ + H$ with the dissociation products $H^+ + H_2O$ being roughly 1 eV higher. However, in condensed phase the energy ordering switches, even with a single H_2O molecule. Indeed, the so-called Zundel cation, $H_5O_2^+$, has the proton equidistant between two water molecules, at the equilibrium configuration, see ref.,[22] which reported a full-dimensional *ab initio* potential for $H_5O_2^+$, and references therein.

Clearly, a PES for H_3O^+ that (diabatically) dissociates to $H^+ + H_2O$ and which could possibly be used in studies of hydration of the proton would be of interest. (It could also be used in appropriate scattering calculations, where the charge-transfer probability is negligible.) We present such a PES here, which is also of unprecedented accuracy in describing the vibrational energies and splittings of H_3O^+.

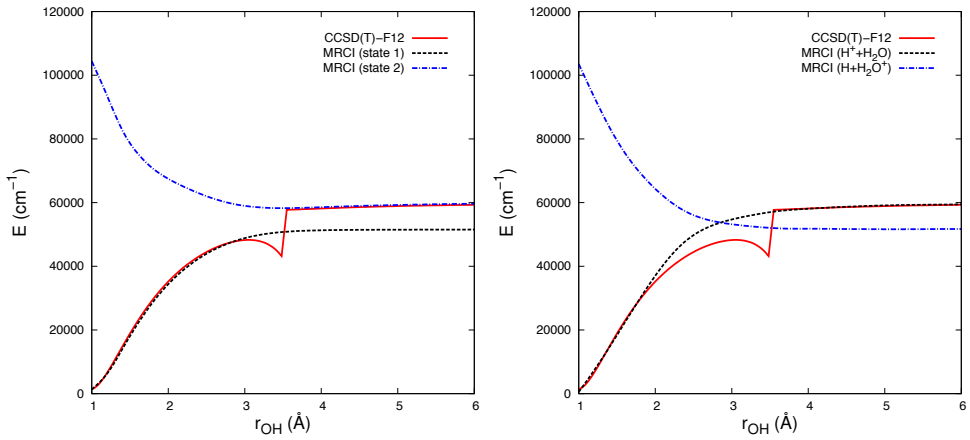

Figure 4.2 Potential cuts (no relaxation) of H_3O^+ as one H is removed along an OH bond. Adiabatic and diabatic MRCI energies are shown in the left and right panels, respectively and CCSD(T)-F12 ones are shown in both panels.

To motivate the computational approach, which is somewhat unusual, Figure 4.2 shows potential cuts of CCSD(T)-F12b/aug-cc-pVQZ(aVQZ),[23–25] and adiabatc and diabatic MRCI/aVTZ energies, relative to the corresponding energies at the global minimum as one H atom is removed (no relaxation). All calculations were done with MOLPRO 2010.[26] As seen, the CCSD(T)-F12/aVQZ cut shows the familiar signature of breakdown involving open shell fragments, in this case the doublets H_2O^+ and H, but then a recovery at longer OH distances to the closed-shell H_2O + H^+ fragments. This behavior is due to the single reference RHF wavefunction used in the CCSD(T) method. In contrast, the MRCI adiabatic energies, show a classic and correct avoided crossing where the CCSD(T)-F12b/aVQZ failure occurs. The two diabatic MRCI potentials describe $H_3O^+(\widetilde{X}\ ^1A) \longrightarrow H(^2S) + H_2O^+(\widetilde{X}\ ^2B_1)$ and $H_3O^+(\widetilde{X}\ ^1A) \longrightarrow H^+(^1S) + H_2O(\widetilde{X}\ ^1A_1)$. At large OH distance, $H(^2S) + H_2O^+(\widetilde{X}\ ^2B_1)$ is the elec-

tronic ground state while $H^+(^1S) + H_2O(\widetilde{X}\ ^1A_1)$ is the first excited state. The relaxed asymptotic energy difference of these two states is just the difference in the ionization energies of H and H_2O, roughly 1 eV.

Since the goal is to obtain a global fit that dissociates to $H^+ + H_2O$, we initially discarded the failed CCSD(T) energies and performed least-squares fits of the remaining data and, thereby, to "interpolate through" the problematic region. However, the resulting fits did show a small oscillation in this region. So, we decided to add MRCI diabatic energies to the dataset. These were obtained using the standard option in MOLPRO. As seen in the figure, these energies are smooth and are quite close to the CCSD(T)-F12 energies away from the point of crossing. However, these absolute energies are not equal, and so we applied a small shift to the diabatic energies. This was done by simply interpolating between the CCSD(T)-F12 and MRCI diabatic energy differences at 2.2 and 4 Å, which are nearly the same, and the distance-dependent shift was applied to the MRCI diabatic energies as a function of the OH distance.

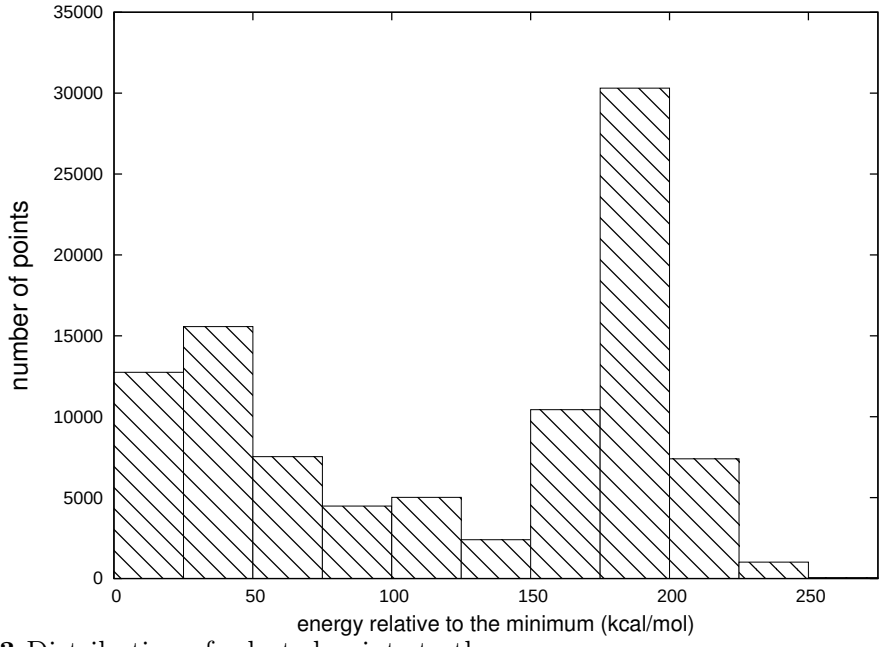

Figure 4.3 Distribution of selected points to the energy

In detail, 79 213 CCSD(T)-F12b/aVQZ energies were obtained over a large range of configurations and also orientations of the H^+ and H_2O fragments in the near asymptotic region. The distribution of these points is shown in Figure 4.7. Configurations for the MRCI energies were obtained from classical trajectories, using preliminary fits, which were initiated from the H_3O^+ minimum then let H^+ dissociates until r_{OH} is about 7 Å. Configurations in the range r_{OH} between 2.2 and 4Å were selected for the MRCI calculations. In these calculations, the 1s orbital of oxygen is set as closed so that there are 7 active orbitals and 1 closed orbital for H_3O^+. This means the 1s orbital of oxygen is kept doubly occupied and excluded from active space but this 1s orbital is still optimized during the MCSCF calculation. Three adiabatic states are calculated first at each configuration and then the lowest two diabatic states were obtained from the first two adiabatic states. Finally, we obtained 2 284 MRCI-aVTZ diabatic energies in the region r_{OH} between 2.2 and 4 Å. These MRCI diabatic energies are shifted to CCSD(T)-F12b energies through a switching function.

$$\Delta E = \Delta E_1 \times S + \Delta E_2 \times (1 - S) \tag{4.6}$$

Where ΔE_1=-0.038037 a.u., ΔE_2=-0.042082 a.u. and S, ranging from 0 to 1, is a function of OH distance.

$$S = 10(\frac{r - 2.2}{4.0 - 2.2})^3 - 15(\frac{r - 2.2}{4.0 - 2.2})^4 + 6(\frac{r - 2.2}{4.0 - 2.2})^6 \tag{4.7}$$

To improve the fit in this region, these points were replicated, effectively doubling their weight. Also, CCSD(T)-F12/aVQZ energies were replicated in the near asymptotic region 4.4 to 5.2 Å. Finally, the data set consists of 96 955 energies. The fit was done using permutationally invariant polynomials, factored as products of polynomials of primary and secondary invariant polynomials.[27]

$$V(y) = \sum_{n=0}^{10} h_n[p(y)]q_n(y) \tag{4.8}$$

where h_n is a polynomial of $p(y)$, a set of primary invariant polynomials, $q_n(y)$ are secondary invariant polynomials, and y is a set of Morse-like variables y_i. Each y_i is a Morse-type function of the form $y_{ij} = \exp(-r_{ij}/\alpha)$. The α value is fixed at 2.0 bohr, and r_{ij} is the internuclear distance between two atoms i and j. With such a large data set, the maximum polynomial order was set to 10, resulting in 1506 linear coefficients. The RMS fitting error for the entire data set, which includes energies as high as 200 kcal/mol (69 800 cm^{-1}) above the global minimum, is 6.7 cm^{-1}. We note that owing to the permutational symmetry each H atom dissociates identically to the products $H^+ + H_2O$.

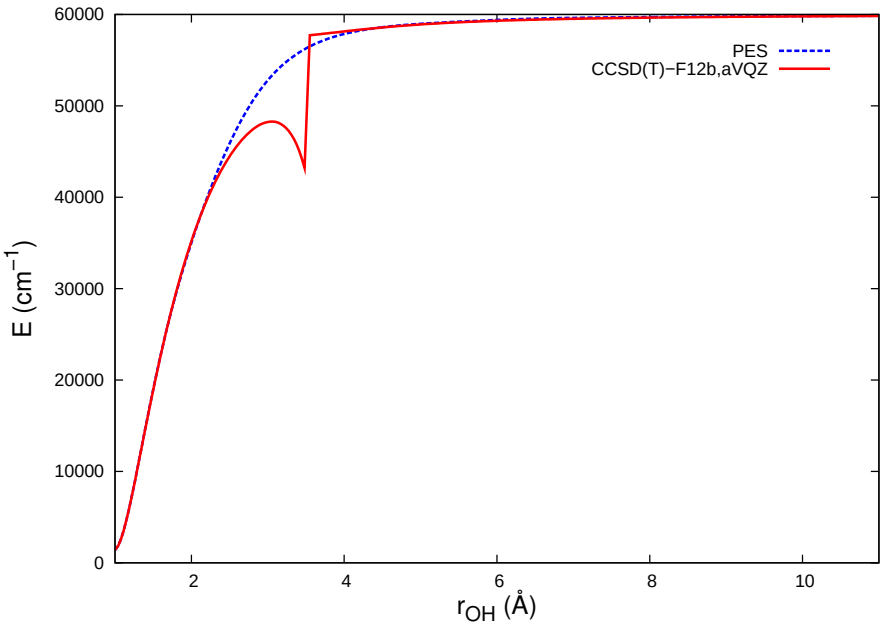

Figure 4.4 Potential cut from the PES including the switch to ion-dipole interaction and direct CCSD(T)-F12/aVQZ energies.

Finally, in the long range the interaction energy of the fragments is essentially ion-dipole. This can be accurately represented by a Coulomb interaction using the ion charge of +1 (in a.u.) and partial charges of H_2O; these are obtained from the accurate dipole moment surface of Tennyson and co-workers.[28] The details of obtaining these partial charges have been given elsewhere.[29] So, the fitted PES is switched beyond

the range of the data set, i.e., 5.2 Å in the OH distance, using a simple switching function to the analytical Coulomb interaction. This is shown in Figure 4.4, which is a comparison of the CCSD(T)-F12b/aVQZ energies and the PES fit, with the switch to Coulomb interaction. As seen the PES cut is very smooth and accurate.

4.3 Hydronium Water 2-body Interaction

The 2-body interaction between H_3O^+ and H_2O, $V^{(2)}_{h,w_i}$, is calculated from previous Zundel PES[30–32] for short $H_3O^+\cdots H_2O$ distance. This Zundel PES uses 48189 CCSD(T) configurations and behaves well both around Zundel minimum and dissociation regions. So considering this Zundel PES is able to describe internal floppy motions and dissociate correctly to H_2O+H_3O^+, we calculate the hydronium water interaction directly from Zundel potential through pulling these two fragments to a significant large distance such that

$$V^{(2)}_{h,w} = V^{(1)}_{\text{zundel}} - V^{(1)}_{h} - V^{(1)}_{w} = V^{(1)}_{\text{zundel}} - V^{(1)}_{\text{dissociated zundel}} \tag{4.9}$$

As to long-range $H_3O^+\cdots H_2O$ interaction, we represent the 2-body energy with charge-dipole interaction that partial charge on each atom in H_3O^+ and H_2O are obtained from their dipole moment surfaces. The long-range $H_3O^+\cdots H_2O$ 2-body energy can then be analytically calculated from Coulomb interaction. Details of the dipole moment surface are in later section. We plot the 2-body energy at two different configurations with change of OO distances in Figure 4.5. It clearly shows that in the long range, the charge-dipole interaction agrees well with *ab initio* calculation and we can safely use the simple Coulomb expression for long-range interaction between H_3O^+ and H_2O. The final $V^{(2)}_{h,w_i}$ is smoothly switched from using Zundel PES to charge-dipole interaction for monomer distances larger than 7 Å.

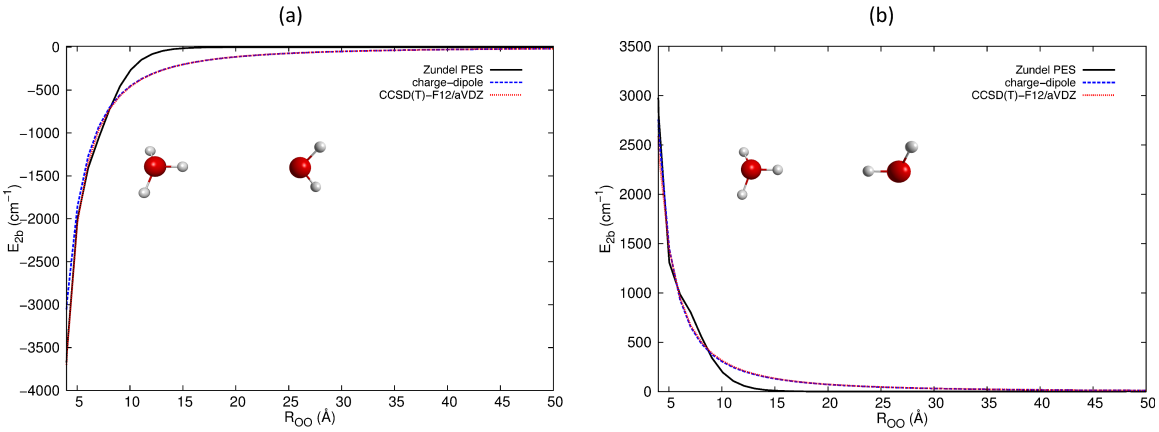

Figure 4.5 h-w 2-body potential cuts along O-O distance at different configurations

4.4 Hydronium Water 3-body Interaction

The hydronium-water-water (h-w-w) 3-body interaction, $V^{(3)}_{h,w,w}$, is defined as

$$V^{(3)}_{h,w,w} = V^{(1)}_{hww} - V^{(1)}_{hw,1} - V^{(1)}_{hw,2} - V^{(1)}_{ww} + V^{(1)}_{h} + V^{(1)}_{w,1} + V^{(1)}_{w,2} \tag{4.10}$$

The first trial work to represent this 3-body term is using an approximate expression stimulated from Skinner and coworker's work on water 3-body interaction. we express the interaction in the following function:

$$\begin{aligned} V(\text{h-w-w}) = & E_a e^{-(r_{\text{oh1}}+r_{\text{oh2}})/k_a} + E_b e^{-(r_{\text{oh1}}+r_{\text{oo3}})/k_b} + E_b e^{-(r_{\text{oh2}}+r_{\text{oo3}})/k_b} + \\ & E_c e^{-(r_{\text{oo1}}+r_{\text{oo3}})/k_c} + E_c e^{-(r_{\text{oo2}}+r_{\text{oo3}})/k_c}. \end{aligned} \tag{4.11}$$

The definition of the variables are given in Figure 4.6. The parameters were obtained from a standard non-linear least-squares fit to roughly 600 3-body CCSD(T)-F12b/aug-cc-VDZ energies. The fit parameters are listed in Table 4.1 and the rms fitting error is 150 cm^{-1} for the data set with a maximum energy of 2100 cm^{-1}.

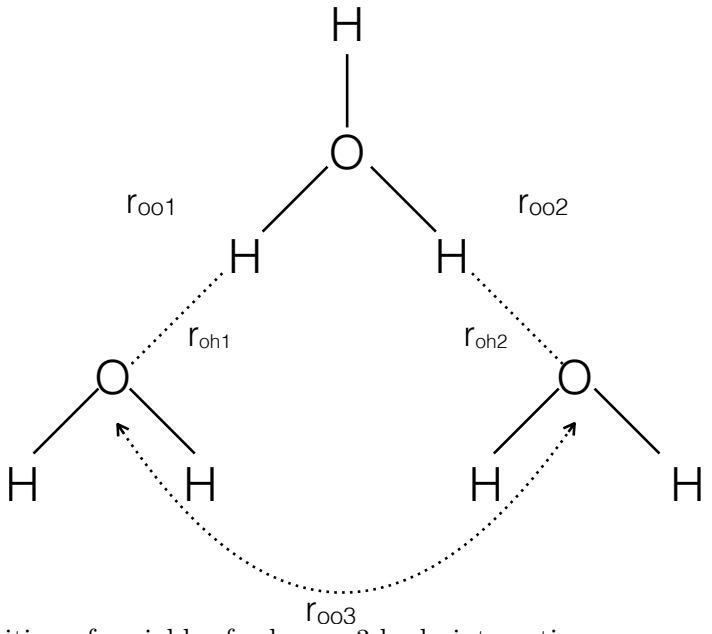

Figure 4.6 Definition of variables for h-w-w 3-body interaction

Table 4.1 Parameters for h-w-w three-body interaction

parameter	E_a	k_a	E_b	k_b	E_c	k_c
value	143.60 Kcal/mol	1.28Å	-129.46 Kcal/mol	1.88Å	118.97 Kcal/mol	1.6Å

This simple expression for the hydronium-water 3-body interaction works mostly for the “Eigen" structures and can not provide accurate predictions for other structures like “Zundel"-like molecules.

To solve this issue, we conducted a more general fit of the hydronium-water 3-body interaction using Monomial Symmetrization method. A total of 107,785 (h-w-w) 3-body electronic energies are generated for fitting this term. This large data set is constructed from (1) (NVE) classical B3LYP/VDZ molecular dynamics trajectories of $H_7O_3^+$. Sets of trajectories are run starting from the minimum structure and saddle point of $H_7O_3^+$ and covering the dissociation region to H_3O^+ and water monomers, (2) (NVE) classical trajectories of the $H_3O^+(H_2O)_4$ isomers and (3) isomers of $H_3O^+(H_2O)_{11}$ and also normal mode sampling of $H_3O^+(H_2O)_{20}$. After sparse sampling of configurations from the trajectories, we subsequently evaluate the 3-body

energies at the CCSD(T)-F12/aVDZ level using Molpro2015.[33]The distribution of all 91043 electronic energies is shown in Figure 4.7. As seen, the h-w-w three-body energy is an important interaction that the sampled data sits in the range of -3500-3500 cm^{-1} with most of the configurations sits around 2000 cm^{-1}. Besides, most of the three-body energies are positive which indicates that the three-body interaction tends to increase the distance between hydronium and water fragments.

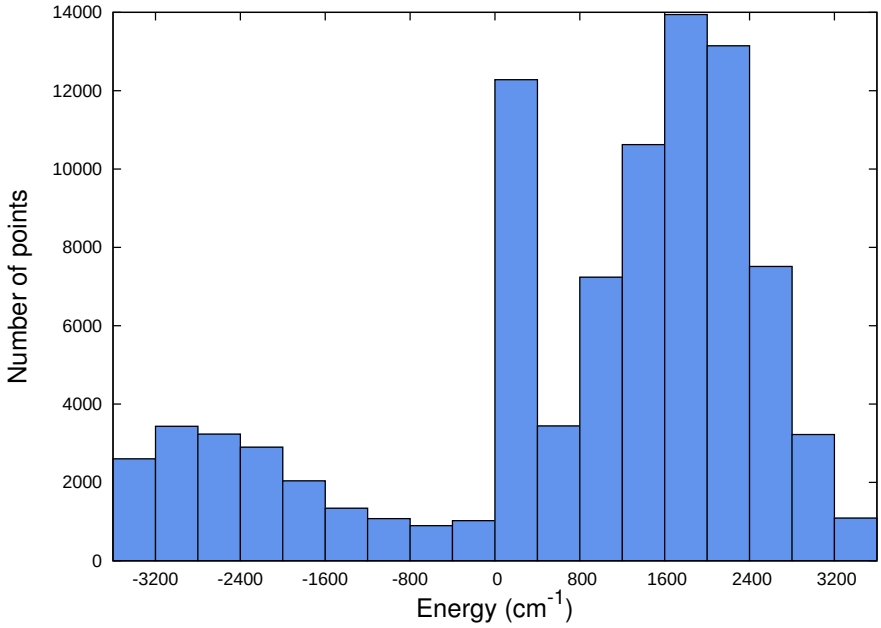

Figure 4.7 Distribution of the h-w-w three-body energies in -3600-3600 cm^{-1}

Considering that there exists a non-negligible Basis Set Superposition Error (BSSE) in computing the 3-body energies with the above basis set, and guided by the present CCSD(T)/CBS binding energies, the calculated energies are uniformly shifted by +0.1 kcal/mol. The whole data set is then fit using the Monomial Symmetrization Approach (MSA)[34] developed by our group with permutationally invariant polynomials, which are functions of Morse variables, $\exp(-r_{ij}/\lambda)$, where r_{ij} is the internuclear distance and λ is a parameter set at 2.5 bohr in this case. For this 10-atom system, the three hydronium hydrogen atoms are equivalent as are the two hydrogen atoms in each water fragment. We use a reduced permutational symmetry that treats the

molecule as $(H_3O)^+(H_4O_2)$ and allows the invariant permutation between the hydronium hydrogen atoms. The water hydrogen atoms are also allowed to interchange. Using this symmetry, there are a total of 4,345 unknown coefficients generated for the least-square fitting and the total rms fitting error over the entire data set was 57 cm^{-1}.

4.5 Hydronium Water 4-body Interaction

To obtain accurate potential energy of hydrated proton, we noticed that a small 4-b correction was needed to improve agreement with the benchmark values. The hydronium-water 4-body interaction, $V^{(4)}_{h,w_i,w_j,w_k}$, is clearly a major challenge to fit using the same approach adopted for fitting the 3-b interactions. Also, given that it is a relatively small and very short-ranged interaction, we followed Skinner and coworkers' work for the water 3-body interaction,[2,3] and used a simple expression for it (see Figure 4.8). As seen in Figure 4.8, five types of 4-body motifs were selected based on the geometry of the optimized isomers of $H_3O^+(H_2O)_3$ and also larger cluster $H_3O^+(H_2O)_{20}$. The corresponding form of the local fit function is also given. For each motif, geometries were generated through randomly changing OO and OH distances and *ab initio* 4-body energies were calculated at the MP2/aVTZ level using Molpro2015.[33] To obtain the variables for each fit for each motif, we use the hydrogen bond length between two monomers as r_i in Fig 4.8 and non-linear least fit is then done. The number of geometries, fitting parameters and rms error are given in Table 4.2

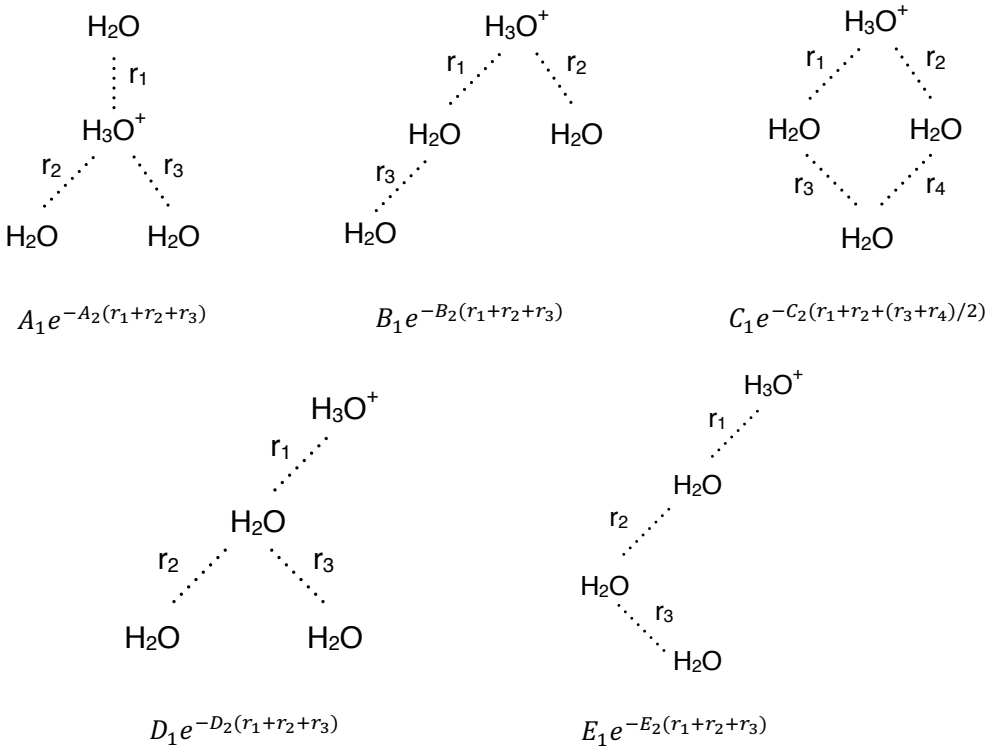

Figure 4.8 Important h-w-w-w 4-body motifs and expression for the 4-body interaction energy

Table 4.2 Fitting details of hydronium-water 4-body interaction

No. of points	Parameter				Fitting rms (cm^{-1})
343	A_1	-0.03102 a.u.	A_2	0.44799 a.u.	14.2
315	B_1	0.01374 a.u.	B_2	0.39063 a.u.	52.3
343	C_1	0.88978 a.u.	C_2	0.70902 a.u.	64.4
343	D_1	0.00281 a.u.	D_2	0.22686 a.u.	38.5
217	E_1	-0.02315 a.u.	E_2	0.49750 a.u.	30.0

There are a total of 1561 data points for the 4-body interaction calculations with an energy range from -600 to 600 cm^{-1} and the total rms error is 42 cm^{-1} for the entire data set. Finally, to obtain the 4-body interaction for a hydronium core and three water monomers, we compute the relevant 4-body energies for all five motifs and each type is assigned a weight. The weight is determined according to the sum of monomer distances, like $r_1+r_2+r_3$ in Fig 4.8. The sum of distances for five types

are denoted as $sr_i, i = 1 - 5$ and the minimum distance among sr_i is sr_{min}. Thus, the weighting function is

$$w(i) = 1 - 10(\frac{sr_i - sr_{min}}{2.0\text{Å}})^3 + 15(\frac{sr_i - sr_{min}}{2.0\text{Å}})^4 - 6(\frac{sr_i - sr_{min}}{2.0\text{Å}})^5, sr_i - sr_{min} < 2.0\text{Å}$$
$$= 0.0, sr_i - sr_{min} > 2.0\text{Å} \tag{4.12}$$

The final 4-body energy is represented through a normalization over all 5 types.

$$E4b_{total} = \frac{\sum_{i=1}^{5} w(i) * E4b_i}{\sum_{i=1}^{5} w(i)} \tag{4.13}$$

4.6 Water Potential

In Equation 4.4, the remaining terms that do not include hydronium are pure water terms. These include the water 1-body, 2-body and 3-body terms. These water interactions are obtained from the WHBB water potential.[35–37]This is also a many-body representation with intrinsic 2- and 3-body terms fitted using roughly 30,000 CCSD(T)/aug-cc-pVTZ and 40,000 MP2/aug-cc-pVTZ electronic energies. The Partridge-Schwenke spectroscopically accurate water monomer potential is used for water 1-body energy.[38] Here, we will not discuss in detail of the WHBB potential and interested reader is referred to references. 35–37

4.7 Dipole Moment Surface

As introduced in Equation 4.5, the dipole moment of hydrated proton can also be expressed in a many-body expansion. Here, we conduct the truncation only at the 2-body level. The hydronium 1-body dipole $\mu_h^{(1)}$ is newly fitted using 48107 configurations. These data points are selected from 96955 data points used in dissociable H_3O^+ PES through setting OH distance shorter than 2.2Å. For each configuration, the dipole moment is calculated at CCSD/aVTZ level using MOLPRO 2015 and fitted using permutationally invariant method with polynomial order to 10. The final

fitting root mean square for the dipole data set is 0.025 Debye. $\mu^{(1)}_{w_i}$ is water monomer dipole moment from LTP2011 DMS.[39] $\mu^{(2)}_{h,w_i}$ is hydronium-water two-body dipole moment obtained using the dissociable Zundel DMS[32] fitting from MP2/aVTZ dipole moment data sets. This intrinsic two-body dipole moment is given by the dipole of the Zundel minus the two monomer dipoles. $\mu^{(2)}_{w_i,w_j}$ is the intrinsic two-body water dipole moment obtained from Wang *et al*'s invariant fits to ∼30,000 MP2/aVTZ dipole moment calculations.[36,37]

4.8 Benchmark electronic structure calculations for $H_3O^+(H_2O)_n$, n=0-5 clusters

We examined the geometries, harmonic frequencies and energetics of the various isomers of clusters of water with the hydronium ion, $H_3O^+(H_2O)_n$, n=0-5. The intent was to investigate the convergence of the results with the level of electron correlation and orbital basis sets in an effort to establish benchmark values for the properties of these systems. The dependence on the level of electron correlation was investigated at the MP2 and CCSD(T) levels of theory, whereas the basis set dependence was probed using Dunning,s aug-cc-pVXZ basis sets[40,41] (X = D, T, Q, 5), hereafter abbreviated as AVXZ. We have chosen to use the regular (as opposed to F12) coupled-cluster approach throughout the calculations for consistency since it was not possible to use the F12 procedure with the larger basis sets for the larger clusters. All calculations were carried out with the NWChem6.6[42] suite of electronic structure codes.

The optimal geometries were obtained as follows: for n=0-2 up to the CCSD(T)/AV5Z level; for n=3 up to the MP2/AV5Z and CCSD(T)/AVTZ levels; for n=4, 5 up to the MP2/AVQZ level. All optimized geometries for H_3O^+ and $H_3O^+(H_2O)$ (1 isomer each), the 2 isomers for n=2, the 4 isomers for n=3, the 5 isomers for n=4 and the 9 isomers for n=5 (22 structures in total, see Figure 4.9) were obtained using the

full number of basis functions (i.e. enforcing zero linear dependencies in the basis by systematically decreasing the number of allowed linear dependencies, one at a time, to zero for cases in which linear dependencies were found). This ensures that the comparison of the relative energies of the various isomers is meaningful.

The harmonic vibrational frequencies were obtained as follows: for n=0 up to the CCSD(T)/ AV5Z level; for n=1 up to the CCSD(T)/AVQZ level; for n=2 up to the CCSD(T)/AVTZ level; for n=3, 4 up to the MP2/AVQZ level. We performed several tests of the step size used in the double numerical differentiation of the CCSD(T) energy with respect to the nuclear coordinates to ensure that the frequencies were real and converged with respect to the step size used. In particular, we performed double numerical differentiations with step sizes of 0.010 (default value in NWChem), 0.015, 0.020, 0.025 and 0.030 a.u. following a geometry optimization step and obtained all positive and six zero frequencies after projection. In all cases, convergence of all positive frequencies was achieved to within ≤ 1 cm^{-1} with a step size of 0.030 a.u.

The binding energies are computed according to:

$$\Delta E = E[\mathrm{H_3O^+(H_2O)_n}] - E[\mathrm{H_3O^+}] - nE[\mathrm{H_2O}]. \tag{4.14}$$

The Basis Set Superposition Error (BSSE) was taken into account using the Boys-Bernardi function counterpoise method, including the deformation energy [43]

$$\Delta E^{def} = \sum_{i=A}^{i=N} [E^i_{A\cdots N}(i) - E^i_i(i)] \tag{4.15}$$

of the individual fragments in the cluster with respect to their geometries in isolation, according to the scheme:

$$\Delta E(BSSE) = E^{\alpha\cup\cdots\cup\nu}_{A\cdots N}(ijk\cdots n) - \sum_{i=A}^{i=N} [E^{\alpha\cup\cdots\cup\nu}_{A\cdots N}(i)] + \Delta E^{def} \tag{4.16}$$

leading to

$$\Delta E(BSSE) = \Delta E - \sum_{i=A}^{i=N} [E^{\alpha\cup\cdots\cup\nu}_{A\cdots N}(i) - E^i_{A\cdots N}(i)], \tag{4.17}$$

where $E^{\alpha\cup\cdots\cup\nu}_{A\cdots N}(i)$ indicates the energy of the ith monomer at its geometry in the cluster with the cluster basis set, and $E^{i}_{A\cdots N}(i)$ indicates the energy of the ith monomer at its geometry in the cluster with only the basis functions centered on the atoms of this monomer, and $E^{i}_{i}(i)$ is the energy of the ith monomer at its equilibrium gas-phase geometry with only the basis functions belonging to this molecule.

The uncorrected and BSSE-corrected binding energies were used for the extrapolation to the Complete Basis Set (CBS) limit. We used two different extrapolation schemes to obtain the CBS estimates as follows:

(A) The scheme suggested recently by us[44] based on the 2/3(uncorrected) + 1/3(BSSE-corrected) weighted sum for the AVDZ and the 1/2(uncorrected) + 1/2(BSSE-corrected) weighted sum for larger basis sets, viz.

$$\begin{aligned} \Delta E_{CBS}(AVDZ) &= 2/3\cdot\Delta E + 1/3\cdot\Delta E(BSSE) \\ \Delta E_{CBS}(AVXZ,\ X=T,Q,5) &= 1/2\cdot\Delta E + 1/2\cdot\Delta E(BSSE) \end{aligned} \tag{4.18}$$

(B) The uncorrected binding energies for the CCSD(T)/AVXZ//CCSD(T)/AVXZ (X=D, T, Q) calculations were extrapolated for n=5 based on the n=1-4 CBS estimated BEs. First, note that we cannot use either an exponential extrapolation or a polynomial extrapolation because in many cases the BEs do not vary monotonically with basis set, thus invalidating the basic assumption of these approaches. Instead, we use the data generated from the results for the n=1-4 cluters to arrive at an approximate trend:

$$\Delta E^{CCSD(T)}_{CBS}(n=5) = \Delta E^{MP2}_{CBS}(n=5) + \langle \Delta E^{CCSD(T)}_{CBS}(n=1-4) - \Delta E^{MP2}_{CBS}(n=1-4).\rangle \tag{4.19}$$

We have found the term $\langle \Delta E^{CCSD(T)}_{CBS}(n=1-4) - \Delta E^{MP2}_{CBS}(n=1-4)\rangle$ to be equal to 0.45 ± 0.2 kcal $\cdot$ mol^{-1} when using the n=1-4 CBS BEs.

The optimized structures of all isomers of the $H_3O^+(H_2O)_n$, n=0-5 clusters are shown in Figure 4.9. Using Scheme (A), the CBS estimates are obtained by combining both the uncorrected and BSSE-corrected numbers as shown in Table S6. The con-

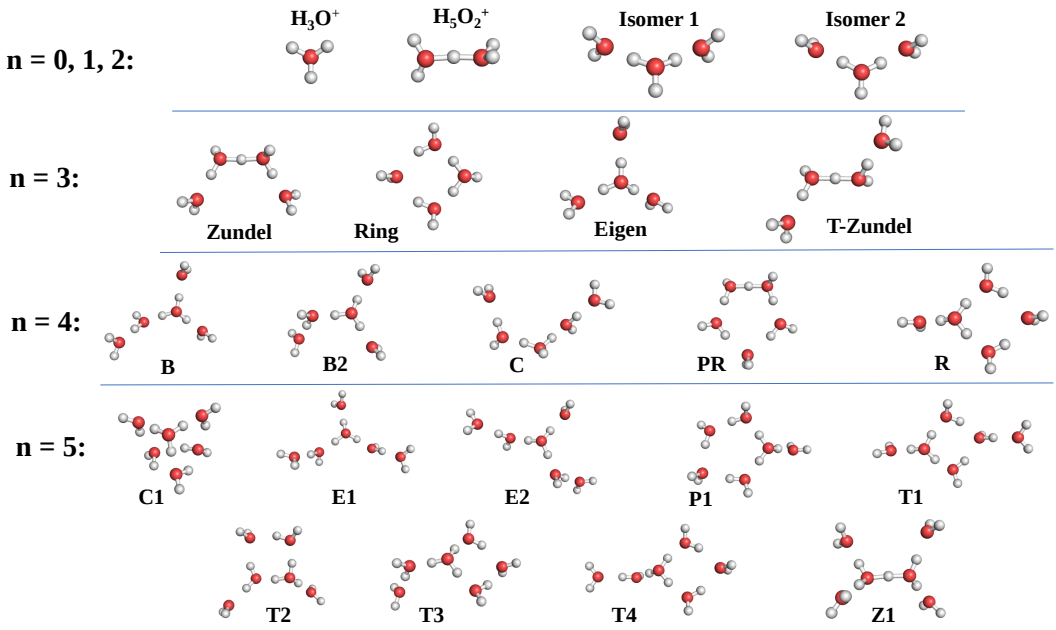

Figure 4.9 Geometries of all isomers of the $H_3O^+(H_2O)_n$ clusters, n=0-5, reported in this study.

vergence to the CBS estimates is first tested with different basis sets for $H_3O^+(H_2O)$ and $H_3O^+(H_2O)_2$. By increasing the basis set during both the geometry optimization and energy calculation, both MP2/CBS and CCSD(T)/CBS binding energies reach convergence. These results guide the path to arrive at the CBS estimates for the larger clusters from the results obtained with the largest basis set; these are listed in Table 1. All MP2/CBS binding energies are calculated directly following Scheme (A). The CCSD(T)/CBS estimates for $H_3O^+(H_2O)$n, n=1-4, were obtained using Scheme (A). To obtain the CCSD(T)/CBS estimates for the larger (n=5) cluster isomers we used Scheme (B) based on the estimates for the smaller n=1-4 CBS estimates. Table 1 also contains the PES binding energies computed at the *ab initio* (PES//ab-initio) and the PES (PES//PES) optimized geometries.

Table 4.3 MP2/CBS, CCSD(T)/CBS and PES binding energies of the $H_3O^+(H_2O)_n$, n=1-5, clusters. All MP2/CBS binding energies are calculated from Scheme (A). The CCSD(T)/CBS binding energies for $H_3O^+(H_2O)_n$, n=1-4, from Scheme (A) and for n=5 from Scheme (B). PES//*ab initio* is the PES result at the *ab initio* geometries optimized at the highest level of theory for each cluster (see text). PES//PES denotes the PES result at the PES optimized geometry.

Cluster	Isomer	Binding Energy (kcal/mol)			
		MP2/CBS	CCSD(T)/CBS	PES//*ab initio*	PES//PES
$H_3O^+(H_2O)$	n/a	-34.1	-33.7	-33.8	-33.8
$H_3O^+(H_2O)_2$	1	-57.5	-57.1	-57.2	-57.2
	2	-57.5	-57.1	-57.2	-57.2
$H_3O^+(H_2O)_3$	Eigen	-77.1	-76.6	-76.7	-76.7
	Ring	-73.0	-73.1	-73.1	-73.2
	cis-Zundel	-73.4	-72.7	-72.8	-72.9
	trans-Zundel	-73.4	-72.6	-72.7	-72.8
$H_3O^+(H_2O)_4$	B	-90.4	-90.0	-89.9	-90.0
	B2	-90.4	-90.0	-89.9	-90.0
	C	-86.9	-86.3	-86.8	-86.8
	R	-91.3	-90.9	-91.0	-91.1
	PR	-87.7	-87.0	-87.5	-87.7
$H_3O^+(H_2O)_5$	T1	-104.1	-103.7	-104.1	-104.4
	P1	-104.1	-103.7	-103.8	-104.0
	T4	-104.0	-103.6	-103.9	-104.3
	T3	-103.9	-103.5	-103.8	-104.3
	T2	-103.7	-103.3	-103.2	-103.7
	C1	-103.3	-102.9	-102.7	-103.7
	E2	-103.2	-102.8	-102.5	-103.0
	E1	-103.0	-102.6	-102.5	-102.9
	Z1	-102.4	-102.0	-102.1	-102.1

As Table 4.3 shows, for the $H_3O^+(H_2O)$n, n=1-4, clusters almost all MP2/CBS binding energies are larger in magnitude than the corresponding CCSD(T)/CBS ones (except for the case of the $H_3O^+(H_2O)_3$ Ring isomer). This finding lends support for the basis that Scheme (B) is based upon and it is used to predict the CCSD(T)/CBS binding energies of n=5 clusters by simply adding 0.45 kcal/mol to the MP2/CBS estimates (the latter obtained using Scheme (A)). The listed PES energies are from two sets of optimized geometries. One set is at the *ab initio* optimized geometries at the highest level of theory for each isomer (CCSD(T) for n=1-3, MP2 for n=4, 5). The other set is the geometry optimized from the PES. The PES binding energies using the two different geometries do not exhibit significant differences. For small clusters (n=1, 2) the PES//*ab initio* and PES//PES binding energies are almost

identical and agree quite well with the CCSD(T)/CBS values. This indicates that the optimized geometries of $H_5O_2^+$ and $H_7O_3^+$ from the PES are very close to the geometries optimized at the CCSD(T) level of theory with a large basis set. It should also be noted that the two isomers of the $H_7O_3^+$ cluster have almost identical binding energies in all different calculations. Isomer 1 has a structure of C_s symmetry while isomer 2 is of C_1 symmetry. The main difference between these two structures is the relative orientation of the two water monomers leading to similar energies. As to the larger clusters, the PES predicts different binding energies using the two different sets of geometries. Generally, the PES optimized geometries have lower BEs by 0.0-0.2 kcal/mol for the n=3, 4 clusters and even a bit more for the n=5 isomers when compared to those using the *ab initio* optimized geometries.

Figure 4.10 shows the percentage difference of the binding energies for various calculations compared to the CCSD(T)/CBS estimates for all cluster isomers. Combining these results with the detailed binding energies listed in Table 4.3, it is clear that for the small clusters, n=1-3, the binding energies predicted from the PES are closer to CCSD(T)/CBS than the MP2/CBS ones. For those clusters, the PES energies using both the *ab initio* and PES optimized geometries are within 0.1-0.25% of CCSD(T)/CBS energies, while MP2/CBS BEs are 0.4-0.8 kcal/mol lower; this corresponds to a 0.7-1.2% deviation from the CCSD(T)/CBS values. Different from the other clusters, the MP2/CBS binding energy of the Ring isomer of $H_3O^+(H_2O)_3$ is 0.1 kcal/mol higher than the corresponding CCSD(T)/CBS value. The PES results using either the optimized *ab initio* or PES geometry, deviate by 0.0-0.2% from the CCSD(T)/CBS value.

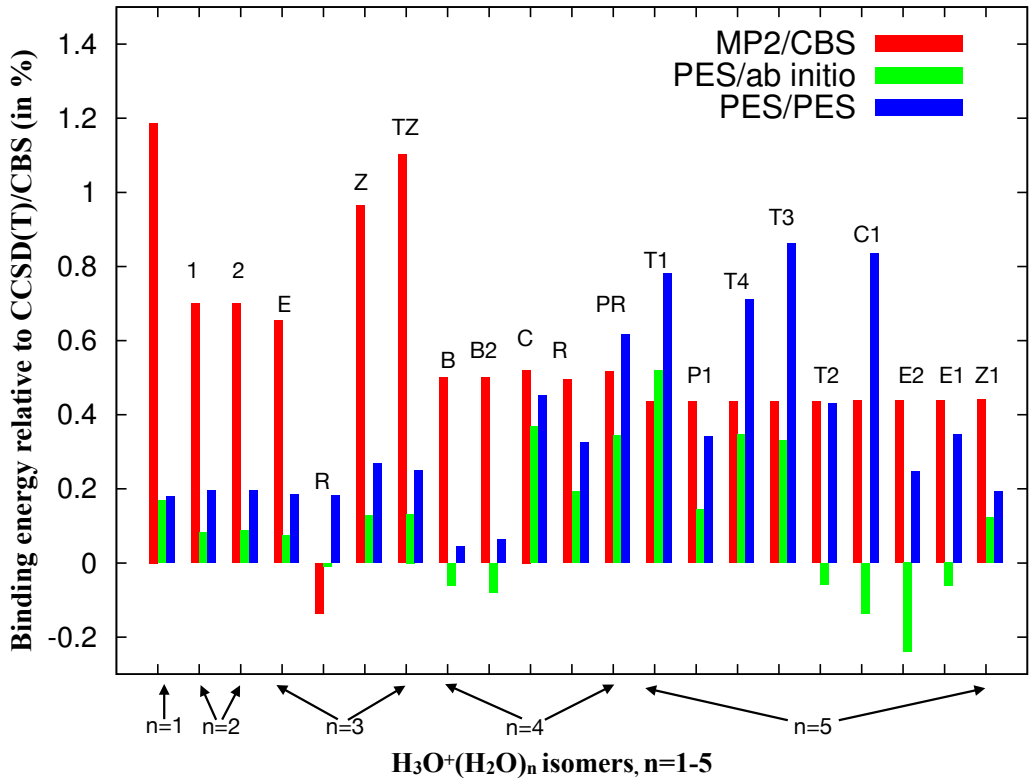

Figure 4.10 Percentage difference of the binding energies of $H_3O^+(H_2O)_n$, n=1-5, for various calculations with respect to the CCSD(T)/CBS estimates. See the caption of Table 1 for information on the CCSD(T)/CBS energies, which are used as references.

For the $H_3O^+(H_2O)_3$ cluster, there are four isomers and their structures are shown in Figure 4.9. The global minimum structure is the "Eigen" configuration, in which the central hydronium core is equally shared by three surrounding water molecules. The next isomer is the Ring, in which the hydronium is shared by two water molecules and another water acts as an acceptor connected with two water hydrogen bonds. The left two isomers display special structures that the proton sits in the middle and is shared by two water molecules. These two isomers are classified as the typical "Zundel" structures. From Table 4.3, we can see that the three high-energy isomers are 4.0 kcal/mol higher than the Eigen minimum and their binding energies are quite close to one another. We have previously discussed in detail the minor, if any, relevance of those high-energy isomers to the cold (20K) experimental IR spectrum

of $H_3O^+(H_2O)_3$.[4]

We investigated five isomers of the $H_3O^+(H_2O)_4$ cluster. The 4-member ring isomer (R) has a binding energy that is 0.9 kcal/mol lower than the two branched isomers (B and B2). The binding energies of the Chain (C) and the 5-member ring (PR) isomers are 3 kcal/mol higher. The difference between the PES and CCSD(T)/CBS energies is increasing for certain isomers. As seen in Table 4.3, the PES predicts very accurate binding energies (within 0.2 kcal/mol) for the B, B2 and R isomers compared to the CCSD(T)/CBS estimates. As regards the C and PR isomers, the PES gives binding energies that are closer to the MP2/CBS values rather than the CCSD(T)/CBS ones. This can also be seen from Figure 4.10, where the relative percentage deviation of the BEs for the C and PR isomers are at the same level with the MP2/CBS values (around 0.5%), while for the three other isomers the PES produces results that are more accurate than the MP2/CBS estimates. The percentage deviations of the B, B2 and R isomers are within $\pm 0.2\%$ of the CCSD(T)/CBS results.

As regards the largest cluster, $H_3O^+(H_2O)_5$, we investigated nine different isomers whose structures are shown in Figure 4.9. The binding energies of these isomers are listed in Table 4.3. Since for that cluster we estimated the CCSD(T)/CBS binding energies using Scheme (B), the CCSD(T)/CBS values are always 0.45 kcal/mol higher than the corresponding MP2/CBS results. Using the MP2/aVQZ optimized geometries, the PES produces reasonable binding energies which are within 0.0-0.4 kcal/mol for most isomers compared to the estimated CCSD(T)/CBS values. The PES optimized structures are naturally associated with larger binding energies (on the negative energy scale) and they are at the same level of accuracy as the MP2/CBS energies, as also seen from Figure 4.10. However, for the Cage isomer the PES//PES binding energy is almost 1.0 kcal/mol different from PES//*ab initio* one. We will discuss this finding later.

Table 4.4 Relative electronic energies ΔE_e (in kcal/mol) of the $H_3O^+(H_2O)_5$ isomers and their ranking from various calculations with electronic structure methods and the PES.

Isomer	MP2/CBS	Rank	CCSD(T)/aVQZ	Rank	PES//MP2/aVQZ	Rank	PES//PES	Rank
T1	0.00	1	0.00	2	0.00	1	0.00	1
P1	0.07	2	-0.01	1	0.39	3	0.45	4
T4	0.12	3	0.13	3	0.28	2	0.17	3
T3	0.23	4	0.21	4	0.40	4	0.12	2
T2	0.46	5	0.47	5	1.00	5	0.76	5
C1	0.86	6	0.54	6	1.48	6	0.76	6
E2	0.99	7	1.18	7	1.68	7	1.45	7
E1	1.13	8	1.25	8	1.70	8	1.55	8
Z1	1.70	9	1.82	9	2.11	9	2.31	9

CCSD(T)/aVQZ energies are calculated at the MP2/aVQZ optimized geometries.

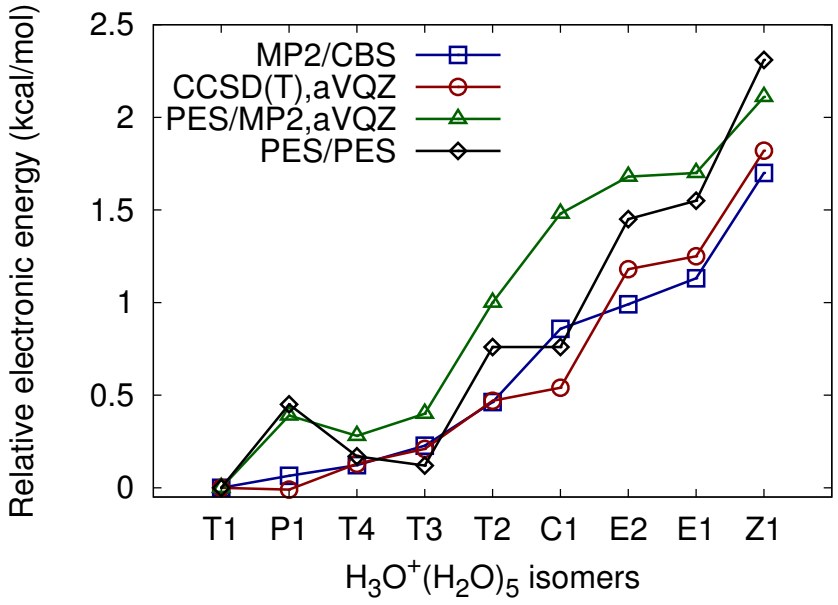

Figure 4.11 Relative electronic energies of the $H_3O^+(H_2O)_5$ isomers from *ab initio* and PES calculations.

Table 4.4 lists the relative electronic energies of these nine isomers and their relative energy rank. The energies are computed at MP2/CBS, CCSD(T)/aVQZ and PES. Since CCSD(T)/CBS estimated energies of these nine isomers are computed using Scheme B which is a constant shift to MP2/CBS energies, the relative electronic energies of nine isomers from CCSD(T)/CBS are the same as MP2/CBS. Thus, we choose the highest-level CCSD(T) energies (CCSD(T)/aVQZ) we compute using op-

timized MP2/aVQZ geometries. The trend of the relative electronic energies is shown in Figure 4.11. First, from Table 4.4, when using the same MP2/aVQZ optimized geometries, the MP2/CBS, CCSD(T)/aVQZ and PES binding energies are in good agreement as regards the isomer relative ranking predictions. Two isomers, T1 and P1, have very similar electronic energies in the MP2 and CCSD(T) calculations, while the PES predicts the T1 isomer to be lower by 0.39 kcal/mol. The other three tetramer-ring isomers (T2, T3 and T4) have higher energies while their differences are within 0.3 kcal/mol from one another in the in *ab initio* calculations. The Zundel structure (Z1 isomer) has the largest binding energy among all isomers. Using the PES optimized geometries, the rankings change little compared to the ones with other methods. The energy difference between the T1, T3 and T4 isomers becomes smaller and thus they have lower electronic energies than the P1 isomer. A large difference is found for the C1 isomer: the PES predicts a ΔE_e of 1.48 kcal/mol when using the MP2/aVQZ optimized geometry and 0.76 kcal/mol with the PES optimized geometry. The large deviation of C1 isomer is also evident from Figure 4.11. The PES therefore provides an overall good agreement with the *ab initio* results, except for the C1 isomer. Actually, the absolute number of these difference is not large. The PES//MP2/aVQZ ΔE_e is 0.62 kcal/mol higher than the MP2/CBS value and even more than the CCSD(T)/aVQZ binding energy, while the PES//PES energies are very close to the CCSD(T)/aVQZ results (the difference is 0.22 kcal/mol). The optimized structure of the C1 isomer from the PES has a slightly different orientation of the water monomers and corresponding hydrogen-bond network. Due to the unavoided error from the fitting of the different components of the PES and our direct truncation of the many-body series in the hydronium-water four-body level, these two structures may result in different binding energies and corresponding relative electronic energies.

Table 4.5 Harmonic frequencies (cm^{-1}) and double harmonic intensities (km/mol, in parentheses) of the HOH bends and OH stretches in $H_3O^+(H_2O)_n$, n=0-2 from different methods.

Mode/H_3O^+	MP2/aV5Z	CCSD(T)/aV5Z	CCSD(T)-F12/aVQZ	PES//PES
Bend-1	1688 (100)	1698	1698	1698 (98)
Bend-2	1688 (100)	1698	1698	1698 (98)
OH-1	**3591** (33)	**3606**	**3605**	**3601** (32)
OH-2	**3702** (493)	**3706**	**3705**	**3708** (461)
OH-3	**3702** (493)	**3706**	**3705**	**3708** (461)
Mode/$H_3O^+(H_2O)$	MP2/aV5Z	CCSD(T)/aVQZ	CCSD(T)-F12/aVTZ	PES//PES
OH-1	**877** (2972)	**825**	**822**	**827** (2936)
Bend-1	1699 (2)	1713	1714	1718 (1)
Bend-2	1759 (988)	1767	1766	1764 (926)
OH-2	3752 (253)	3759	3759	3761 (238)
OH-3	3761 (8)	3766	3767	3766 (4)
OH-4	3858 (254)	3852	3852	3860 (264)
OH-5	3858 (342)	3852	3853	3860 (313)
Mode/$H_3O^+(H_2O)_2$, 1	MP2/aV5Z	CCSD(T)/aVTZ	CCSD(T)-F12/aVTZ	PES//PES
Bend-1	1607 (5)	1623	1625	1635 (9)
Bend-2	1638 (1)	1647	1654	1669 (7)
Bend-3	1683 (17)	1713	1699	1719 (41)
Bend-4	1695 (43)	1713	1709	1746 (17)
OH-1	**2491** (4065)	**2521**	**2551**	**2520** (3934)
OH-2	**2640**(1149)	**2680**	**2702**	**2688** (1254)
OH-3	3812 (135)	3794	3818	3807 (119)
OH-4	3812 (41)	3794	3818	3819 (49)
OH-5	**3830** (205)	**3807**	**3828**	**3839** (209)
OH-6	3921 (3)	3888	3914	3909 (9)
OH-7	3921 (421)	3889	3914	3911 (395)
Mode/$H_3O^+(H_2O)_2$, 2	MP2/aV5Z	CCSD(T)/aVTZ	CCSD(T)-F12/aVTZ	PES//PES
Bend-1	1616 (20)	1633	1634	1651 (28)
Bend-2	1631 (15)	1646	1650	1665 (20)
Bend-3	1683 (14)	1704	1699	1715 (9)
Bend-4	1704 (25)	1731	1721	1751 (20)
OH-1	**2488** (4103)	**2521**	**2552**	**2528** (3918)
OH-2	**2639** (1121)	**2685**	**2705**	**2704** (1216)
OH-3	3808 (90)	3791	3813	3805 (93)
OH-4	3812 (96)	3793	3816	3818 (118)
OH-5	**3826** (193)	**3801**	**3822**	**3825** (178)
OH-6	3916 (186)	3885	3908	3904 (161)
OH-7	3921 (236)	3888	3912	3910 (238)

PES//PES is the PES frequency at the PES optimized geometry. The proton or hydronium stretches are listed in bold.

To further test the accuracy and properties of the new PES/DMS, besides the binding energies of the different clusters, we next investigate the harmonic frequencies and double harmonic intensities of $H_3O^+(H_2O)$n,n=0-4. Tables 3-5 list the frequencies and associated intensities of the HOH bending and OH stretching modes

from various calculations. Overall the PES demonstrates very good accuracy for all these frequencies. The hydronium cation (C_{3v} symmetry) has two degenerate bending modes, one symmetric OH stretch and two degenerate asymmetric OH stretches. All methods properly capture these spectral features. The CCSD(T)/aV5Z harmonic frequencies are ca. 10 cm^{-1} higher than the corresponding MP2/aV5Z ones. We also list the CCSD(T)-F12/aVQZ frequencies, calculated with Molpro 2015,[33] which are very similar to the CCSD(T)/aV5Z ones. This confirms that the reported benchmark frequencies of the bare hydronium are well converged. As seen, the PES//PES frequencies are very close to the benchmark CCSD(T) ones and substantially more accurate than the the MP2/aV5Z frequencies.

The bare Zundel ion, $H_5O_2^+$, has a minimum structure with the proton equidistant between the two water monomers. This gives rise to a large amplitude motion-proton stretch, which carries a large infrared intensity. The MP2/aV5Z level predicts the harmonic frequency at 877 cm^{-1}, while the CCSD(T)/aVQZ frequency is at 825 cm^{-1} and the CCSD(T)-F12/aVTZ at 822 cm^{-1}. Other modes, including the HOH bends and water stretches, are not associated with such a large difference between different *ab initio* calculations. The PES predicts a harmonic proton stretching frequency of 827 cm^{-1}, in excellent agreement with the CCSD(T) value. The new PES yields harmonic frequencies that are in general more accurate than the MP2 level of theory for the smaller clusters. This also holds for the two isomers of $H_3O^+(H_2O)_2$: isomer 1 (C_s symmetry) has three hydronium stretches, which carry most of the IR intensity, namely the asym- and sym-stretches at 2551 and 2702 cm^{-1}, respectively, and one free OH stretch at 3828 cm^{-1} at the CCSD(T)-F12/aVTZ level of theory. Based on previous tests of the harmonic frequencies using these correlated methods,[45] these should be the most accurate results. A careful comparison between the PES//PES and these results shows a close agreement for the highest frequency modes. Again, the MP2/aV5Z frequencies underestimate the hydronium sym- and asym-stretches by

about 50 cm^{-1}, while the PES gives results that are in excellent agreement with the CCSD(T)-F12/aVTZ ones. The same behavior is also observed for the hydronium stretches of isomer 2 (C_1 symmetry).

Table 4.6 Harmonic frequencies (cm^{-1}) and double harmonic intensities (km/mol, in parentheses) of the HOH bends and OH stretches in $H_3O^+(H_2O)_3$ from different methods.

$H_3O^+(H_2O)_3$, Eigen				
Mode	MP2/aV5Z	CCSD(T)/aVTZ	CCSD(T)-F12/aVTZ	PES//PES
Bend-1	1636 (65)	1650	1644	1668 (69)
Bend-2	1636 (66)	1654	1645	1668 (69)
Bend-3	1648 (1)	1669	1654	1686 (5)
Bend-4	1716 (8)	1746	1731	1771 (5)
Bend-5	1718 (9)	1770	1733	1771 (5)
OH-1	**2944** (2927)	**2939**	**2995**	**2984** (3112)
OH-2	**2945** (2935)	**2975**	**2998**	**2984** (3112)
OH-3	**3031** (164)	**3073**	**3089**	**3090** (152)
OH-4	3819 (83)	3775	3856	3818 (79)
OH-5	3819 (84)	3794	3858	3818 (79)
OH-6	3820 (1)	3802	3858	3839 (4)
OH-7	3929 (49)	3891	3955	3919 (37)
OH-8	3930 (37)	3893	3955	3919 (38)
OH-9	3930 (456)	3897	3956	3920 (458)
$H_3O^+(H_2O)_3$, Ring				
Mode	MP2/aV5Z	CCSD(T)/aVTZ	PES//PES	
Bend-1	1609 (30)	1609	1644 (6)	
Bend-2	1626 (22)	1645	1655 (50)	
Bend-3	1633 (100)	1651	1692 (5)	
Bend-4	1659 (31)	1664	1698 (65)	
Bend-5	1815 (187)	1831	1880 (153)	
OH-1	**2329** (2604)	**2367**	**2449** (2624)	
OH-2	**2550** (1851)	**2596**	**2622** (1610)	
OH-3	3638 (241)	3640	3600 (315)	
OH-4	3662 (634)	3661	3610 (693)	
OH-5	3786 (26)	3770	3759 (13)	
OH-6	3816 (208)	3788	3844 (174)	
OH-7	**3882** (362)	**3856**	**3854** (202)	
OH-8	3886 (98)	3857	3882 (191)	
OH-9	3888 (173)	3859	3882 (135)	
$H_3O^+(H_2O)_3$, cis-Zundel				
Mode	MP2/aV5Z	CCSD(T)/aVTZ	PES//PES	
OH-1	**789** (2483)	**751**	**817** (3096)	
OH-2	**1026** (1283)	**1036**	**1025** (1249)	
Bend-1	1646 (25)	1656	1657 (222)	
Bend-2	1646 (190)	1660	1695 (10)	
Bend-3	1723 (6)	1747	1781 (7)	
Bend-4	1764 (722)	1776	1785 (691)	
OH-3	3110 (1036)	3150	3163 (725)	
OH-4	3144 (1968)	3185	3200 (2127)	
OH-5	3818 (64)	3799	3811 (55)	
OH-6	3819 (45)	3799	3812 (116)	
OH-7	3860 (214)	3831	3880 (157)	
OH-8	3862 (146)	3835	3885 (204)	
OH-9	3929 (75)	3894	3929 (28)	
OH-10	3929 (269)	3895	3930 (278)	
$H_3O^+(H_2O)_3$, trans-Zundel				
Mode	MP2/aV5Z	CCSD(T)/aVTZ	PES//PES	
OH-1	**815** (1693)	**794**	**807** (1945)	
OH-2	**1000** (1349)	**1008**	**977** (1682)	
Bend-1	1643 (17)	1657	1656 (180)	

Continued on next page

Continued from previous page

Bend-2	1646 (144)	1660	1683 (4)
Bend-3	1708 (1)	1738	1739 (9)
Bend-4	1757 (765)	1783	1787 (585)
OH-3	3104 (2491)	3143	3181 (2331)
OH-4	3130 (673)	3162	3191 (591)
OH-5	3825 (85)	3798	3823 (56)
OH-6	3825 (28)	3808	3825 (83)
OH-7	3867 (134)	3844	3864 (217)
OH-8	3869 (213)	3845	3884 (169)
OH-9	3937 (180)	3903	3940 (109)
OH-10	3937 (174)	3904	3940 (197)

Notations as in Table 4.5.

Table 4.7 Harmonic frequencies (cm^{-1}) and double harmonic intensities (km/mol, in parentheses) of the HOH bends and OH stretches in $H_3O^+(H_2O)_4$ from different methods.

$H_3O^+(H_2O)_4$, B			
Mode	MP2/aVTZ	MP2/aVQZ	PES//PES
Bend-1	1630 (44)	1630 (38)	1627 (74)
Bend-2	1636 (71)	1638 (72)	1662 (81)
Bend-3	1643 (8)	1645 (7)	1686 (17)
Bend-4	1658 (44)	1658 (51)	1698 (2)
Bend-5	1719 (71)	1712 (26)	1764 (10)
Bend-6	1744 (8)	1735 (8)	1779 (11)
OH-1	**2402** (3403)	**2419** (3367)	**2444** (2842)
OH-2	**3090** (2462)	**3102** (2447)	**3140** (1486)
OH-3	**3130** (850)	**3139** (858)	**3162** (2238)
OH-4	3412 (952)	3424 (951)	3441 (824)
OH-5	3801 (67)	3818 (70)	3822 (78)
OH-6	3801 (25)	3819 (26)	3826 (28)
OH-7	3810 (34)	3827 (35)	3834 (34)
OH-8	3876 (136)	3894 (140)	3889 (119)
OH-9	3911 (52)	3929 (45)	3931 (131)
OH-10	3911 (274)	3929 (290)	3933 (210)
OH-11	3923 (146)	3940 (150)	3955 (110)
$H_3O^+(H_2O)_4$, B2			
Mode	MP2/aVTZ	MP2/aVQZ	PES//PES
Bend-1	1625 (41)	1626 (36)	1633 (87)
Bend-2	1635 (80)	1637 (80)	1660 (76)
Bend-3	1643 (10)	1645 (10)	1689 (20)
Bend-4	1659 (45)	1659 (51)	1710 (13)
Bend-5	1717 (30)	1711 (25)	1759 (2)
Bend-6	1742 (7)	1733 (8)	1786 (8)
OH-1	**2402** (3367)	**2424** (3336)	**2483** (2795)
OH-2	**3090** (2482)	**3093** (2496)	**3118** (2155)
OH-3	**3128** (732)	**3130** (726)	**3161** (1515)
OH-4	3418 (976)	3430 (971)	3457 (774)
OH-5	3801 (66)	3818 (68)	3813 (23)
OH-6	3801 (27)	3819 (29)	3828 (81)
OH-7	3805 (32)	3822 (33)	3841 (45)
OH-8	3871 (143)	3888 (146)	3907 (115)
OH-9	3911 (73)	3929 (85)	3936 (122)
OH-10	3912 (249)	3929 (245)	3937 (90)
OH-11	3918 (147)	3935 (151)	3939 (230)
$H_3O^+(H_2O)_4$, C			
Mode	MP2/aVTZ	MP2/aVQZ	PES//PES
Bend-1	1594 (194)	1592 (179)	1643 (24)
Bend-2	1619 (26)	1617 (24)	1669 (42)
Bend-3	1646 (195)	1647 (129)	1671 (62)
Bend-4	1648 (67)	1649 (114)	1684 (220)

Continued on next page

Continued from previous page

Bend-5	1688 (145)	1685 (115)	1728 (29)
Bend-6	1735 (29)	1728 (29)	1768 (11)
OH-1	**2065** (4715)	**2079** (4777)	**2070** (4469)
OH-2	**2312** (1500)	**2322** (1466)	**2283** (1408)
OH-3	3372 (874)	3386 (843)	3397 (601)
OH-4	3382 (1227)	3395 (1247)	3405 (1275)
OH-5	3804 (36)	3823 (35)	3807 (59)
OH-6	3805 (37)	3823 (42)	3811 (33)
OH-7	3832 (172)	3847 (177)	3882 (166)
OH-8	3865 (135)	3883 (139)	3893 (140)
OH-9	**3870** (160)	**3889** (164)	**3911** (220)
OH-10	3916 (133)	3935 (145)	3933 (102)
OH-11	3917 (159)	3936 (155)	3934 (105)

$H_3O^+(H_2O)_4$, R

Mode	MP2/aVTZ	MP2/aVQZ	PES//PES
Bend-1	1631 (30)	1632 (24)	1651 (149)
Bend-2	1633 (139)	1636 (149)	1659 (22)
Bend-3	1636 (17)	1640 (15)	1669 (4)
Bend-4	1659 (13)	1662 (14)	1687 (42)
Bend-5	1686 (8)	1676 (6)	1762 (4)
Bend-6	1816 (101)	1814 (106)	1858 (92)
OH-1	**2797** (1910)	**2816** (1878)	**2908** (2023)
OH-2	**2906** (2695)	**2921** (2646)	**2994** (1867)
OH-3	**3065** (1013)	**3078** (1030)	**3153** (1767)
OH-4	3647 (246)	3662 (239)	3632 (334)
OH-5	3669 (526)	3684 (536)	3647 (494)
OH-6	3775 (19)	3791 (19)	3771 (10)
OH-7	3804 (49)	3823 (52)	3841 (53)
OH-8	3875 (316)	3893 (327)	3858 (123)
OH-9	3879 (63)	3894 (146)	3893 (56)
OH-10	3879 (179)	3897 (97)	3894 (229)
OH-11	3916 (172)	3935 (177)	3935 (182)

$H_3O^+(H_2O)_4$, PR

Mode	MP2/aVTZ	MP2/aVQZ	PES//PES
OH-1	**867** (2791)	**839** (2749)	**965** (53)
OH-2	**1099** (708)	**1085** (681)	**1219** (2635)
Bend-1	1636 (128)	1641 (132)	1669 (82)
Bend-2	1649 (21)	1650 (22)	1679 (87)
Bend-3	1665 (3)	1667 (2)	1691 (10)
Bend-4	1752 (635)	1748 (644)	1750 (701)
Bend-5	1775 (19)	1770 (20)	1816 (34)
OH-3	3009 (479)	3021 (461)	2847 (1572)
OH-4	3063 (2651)	3074 (2650)	3182 (1385)
OH-5	3637 (453)	3652 (445)	3584 (628)
OH-6	3662 (500)	3676 (503)	3693 (433)
OH-7	3774 (16)	3788 (16)	3760 (35)
OH-8	3832 (190)	3848 (192)	3870 (128)
OH-9	3834 (147)	3851 (155)	3873 (144)
OH-10	3877 (341)	3891 (152)	3882 (320)
OH-11	3877 (169)	3894 (370)	3893 (221)
OH-12	3881 (32)	3898 (27)	3896 (71)

Notations as in Table 4.5.

As shown in Table 4.8, the four isomers of $H_3O^+(H_2O)_3$ display some distinct vibrational features. The Eigen minimum has three hydronium stretches at ∼3000 cm^{-1}: two asymmetric stretches and one symmetric stretch. We reported the CCSD(T)-F12/aVTZ benchmark frequencies of Eigen minimum previously.[4] Using other high-

level *ab initio* method, MP2/aV5Z underestimates the hydronium stretches again by 50 cm^{-1} while the CCSD(T)/aVTZ frequencies are also lower than the CCSD(T)-F12/aVTZ ones. PES gives accurate descriptions of harmonic frequencies for the Eigen cluster especially for the hydronium stretches. The PES hydronium stretches are very close to CCSD(T)-F12/aVTZ calculations, with only 10 cm^{-1} differences. The Ring isomer of $H_3O^+(H_2O)_3$ has different vibration signatures from the Eigen minimum. This isomer has a hydronium core where only two hydrogen atoms are shared by water monomers. Thus, it has similar hydronium stretch signatures to $H_3O^+(H_2O)_2$. The asym- and sym- stretches are at around 2350-2600 cm^{-1} and one free OH stretch is at 3850 cm^{-1}. The hydronium stretches calculated from PES are higher than CCSD(T)/aVTZ results. According to the conclusion from the Eigen case, our PES results may be more accurate since higher-level of *ab initio* calculations should predict higher frequencies of hydronium stretches. The left two isomers, cis- and trans- Zundel isomers, display the typical Zundel signatures. There exists two proton-involved stretches at around 800 and 1000 cm^{-1}. However, these two high-intensity modes differ slightly from the pure proton stretch in bare Zundel case. Actually, in the two Zundel isomers, the proton stretches are motions that involve both proton stretch and water wagging motions. Overall, the current PES describes all the proton and water motions accurately, compared with CCSD(T)/aVTZ results.

Table 4.8 lists the vibrational frequencies of the $H_3O^+(H_2O)_4$ cluster isomers. For this cluster we only have MP2 results with which to compare the PES. So the (sometimes large) differences between MP2 and CCSD(T) frequencies seen for the smaller clusters need to be kept in mind when making comparisons between the MP2 and PES results. The four "Eigen"-like isomers (B, B2, C and R) display the signatures of the "Eigen" frequencies in the 2000-3200 cm^{-1} range. The B and B2 isomers have two hydronium asym-stretches at 2420 and 3100 cm^{-1} and one sym-stretch at 3140 cm^{-1}. The PES yields good predictions of all the hydronium and water bends and

stretches compared to the MP2/aVQZ calculations. Again, the PES frequencies of the hydronium stretches are higher than the MP2 ones by up to 50 cm^{-1}. The C isomer has a chain structure with no branches. Its hydronium core is connected to water through two hydrogen bonds and one free OH exists in its hydronium structure. Thus, in the normal mode analysis, like in $H_7O_3^+$, there exists one asym-OH stretch at 2070 cm^{-1}, one sym-OH stretch at 2322 cm^{-1} and one free-OH stretch at 3847 cm^{-1}. Compared to the same modes in $H_7O_3^+$, the C isomer's two bonded OH stretches have a 500 cm^{-1} red shift. This large shift is again due to the structural features, in which the two OH bond lengths are slightly longer than those in $H_7O_3^+$ due to the water solvation effect. The PES results are in good agreement with the MP2 ones not only in the hydronium stretches but also in the water vibrations like the two H-bonded water stretches at 3400 cm^{-1}, which carry large intensities. The R isomer has also an "Eigen" structure but it forms a tetramer ring. The three hydronium stretches located in the range from 2800 to 3100 cm^{-1}, similar to the MP2/aVQZ predictions. The PES optimized structure has a slight difference from the MP2/aVQZ optimized geometry. As a result, the PES//PES frequencies of the hydronium stretches are associated with ca. 100 cm^{-1} blue shifts. The last isomer of $H_3O^+(H_2O)_4$ is the PR isomer (Pentamer ring) with a "Zundel" structure instead. The harmonic frequencies of this isomer do indeed show the signature of the "Zundel". MP2 predicts two bright proton stretchs at ca. 850 and 1100 cm^{-1} and another signature mode, viz. the Zundel HOH bend at 1750 cm^{-1}. These two modes become the signatures of "Zundel" structure because of their very large infrared intensities that will not show in the Eigen structures. The two intense proton stretches from PES//PES are at 965 and 1219 $cm^{-}1$, upshifted from the MP2 result. It should be noted that the proton motion in these Zundel structures is highly negatively anharmonic and so the harmonic frequencies given here are very sensitive to the details of the anharmonic potential, which in turn is very sensitive to the geometry of the minimum energy structure. Thus, for conducting anharmonic

vibrational calculations, we need a much more extensive grid of points for the whole PES rather than just focusing on the area around the minimum structure.

Table 4.8 Harmonic frequencies (cm^{-1}) of proton-related stretches in $H_3O^+(H_2O)_n$, n=0-3, from *ab initio* calculations and the PES.

Isomer	Mode	CCSD(T)	MP2	PES
H_3O^+	1	3605	-14	-4
	2	3705	-4	3
	3	3705	-4	3
$H_3O^+(H_2O)$	1	822	52	2
	2	3759	-7	2
	3	3767	-6	-1
	4	3852	6	8
	5	3853	5	7
$H_3O^+(H_2O)_2$, 1	1	2551	-60	-31
	2	2702	-62	-14
	3	3828	2	11
$H_3O^+(H_2O)_2$, 2	1	2552	-64	-24
	2	2705	-66	-1
	3	3822	4	3
$H_3O^+(H_2O)_3$, Eigen	1	2995	-51	-11
	2	2998	-53	-14
	3	3089	-58	1
$H_3O^+(H_2O)_3$, Ring	1	2367	-38	82
	2	2596	-46	26
	3	3856	26	-2
$H_3O^+(H_2O)_3$, cis-Zundel	1	751	38	66
	2	1036	-10	-9
	3	3150	-40	13
	4	3185	-41	15
	5	3831	29	49
	6	3835	27	50
$H_3O^+(H_2O)_3$, trans-Zundel	1	794	21	13
	2	1008	-8	-31
	3	3143	-39	38
	4	3162	-32	29
	5	3844	23	20
	6	3845	24	39

The basis set for the *ab initio* calculations is the largest one we used for each cluster, as shown in Tables 3 and 4. The PES results are based on PES optimized geometries. The listed frequencies under the MP2 and PES columns are shifts relative to the CCSD(T) and CCSD(T)-F12 (if available) ones.

To investigate the influences of different methods in describing proton-related stretches, we summarize the proton-related stretches of different clusters from CCSD(T), MP2 and PES in Table 4.8. For smaller clusters, like $H_3O^+(H_2O)$n n=0,1,2 cases,

the CCSD(T) numbers are from CCSD(T)-F12 approach with largest basis set. The numbers of MP2 and PES are shifts in wavenumber as comparing with CCSD(T) ones. As we have discussed before, the MP2 frequencies are generally smaller than CCSD(T) ones for "Eigen" clusters. For "Zundel" clusters, MP2 approach gives higher proton stretches than CCSD(T) results. Using our constructed PES, the calculated frequencies are generally much closer to CCSD(T) frequencies. The differences between PES and CCSD(T) are mostly within 15 cm^{-1} for clusters up to $H_3O^+(H_2O)_3$ Eigen minimum. The difference for other isomers becomes larger but we still expect our PES frequencies are very accurate since that difference should be smaller if we have CCSD(T)-F12 results as references.

A *linear* correlation between the *shifts* in the hydrogen bonded covalent equilibrium OH bond lengths (ΔR) and the corresponding harmonic frequencies ($\Delta\omega$) with respect to the isolated monomer was first discussed in 1993 for water clusters[46] and recently further quantified.[47] In particular, it was found that the linear expression

$$-\Delta\omega = \mathrm{s} \cdot \Delta R \tag{4.20}$$

fit both the MP2 and CCSD(T) harmonic frequency vs. bond length shifts for water clusters, with respect to the isolated monomer bond length and the average of its symmetric and asymmetric frequencies taken as references, with a slope of s=20.18 $cm^{-1}/0.001$Å quite accurately ($R^2 = 0.9735$).[47] The linear relation between frequency shifts and changes in the underlying bond lengths induced by an electric field has also been previously reported for H_2O and OH^-.[48,49] A similar linear correlation was recently reported by one of us for a limited dataset (9 points) of hydronium stretching frequencies / bond lengths in the $H_3O^+(H_2O)_n$ clusters.[50]

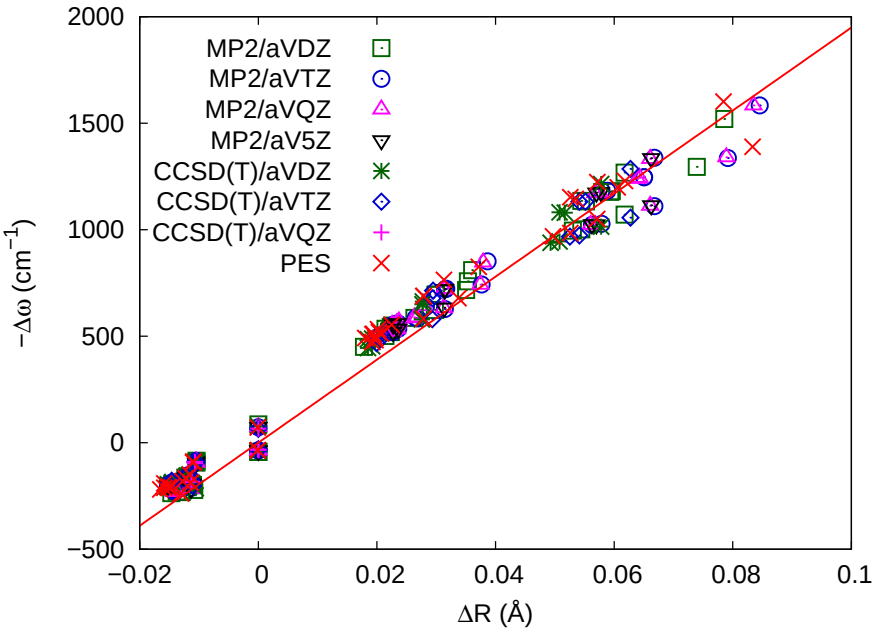

Figure 4.12 Shifts of proton-stretching harmonic vibrations as a function of the elongation of the OH equilibrium bond lengths for the n=0-5 clusters. The shifts are computed with respect to isolated hydronium averages of the sym- and asym-stretches and the OH bond lengths.

The present study offers the opportunity to further investigate the validity of the previously introduced linear correlation (reported for the O-H stretches participating in hydrogen bonds between water molecules) by extending it to a different system (hydronium stretches participating in hydrogen bonds with water molecules) and substantially increasing the number of sampled points with respect to the previous hydronium dataset reported earlier.[50]

Figure 4.12 shows all 260 ($\Delta\omega$, ΔR) pairs for the proton stretching in the n=0-5 clusters, obtained at the MP2/aVDZ (43 pairs), MP2/aVTZ (43 pairs), MP2/aVQZ (43 pairs), MP2/aV5Z (27 pairs), CCSD(T)/aVDZ (27 pairs), CCSD(T)/aVTZ (27 pairs), CCSD(T)/aVQZ (7 pairs) as well as the PES (43 pairs), and their least-mean-squares fit according to Eq. (11), which yields s=19.5 cm^{-1}/0.001Å (R^2 = 0.967). Only the frequencies with intensities larger than 300 km/mol are considered for the clusters. For each case, the shifts are obtained with respect to the isolated

hydronium equilibrium O-H bond lengths and the average of the symmetric and antisymmetric vibrations at that particular level of theory. The fits of the individual points at each level of theory / basis set as well as the PES are listed in Table 4.9. They all produce slopes that are within < 1 cm^{-1} of the overall fit. This further reinforces the previous thesis that errors in the harmonic frequencies arise from the errors in the corresponding bond lengths obtained at the various levels of theory.[47] In addition, the PES was found to be able to capture this effect quite accurately, yielding s=20.1 cm^{-1}/0.001Å ($R^2 = 0.966$) for the 43 pairs (see Table 4.9). Note that the above linear correlation is between the equilibrium bond lengths and the corresponding harmonic frequencies for the proton stretching motion, which is associated with very large anharmonicities.[50]

Table 4.9 Fitting details of shifts of proton-water stretches as a function of the elongation of the OH bond lengths.

$-\Delta\omega = s \cdot \Delta R$			
Method	Number of points	s (cm^{-1}/0.001Å)	R^2
MP2/aVDZ	43	19.7607	0.977
MP2/aVTZ	43	19.1786	0.977
MP2/aVQZ	43	19.3553	0.977
MP2/aV5Z	27	19.3042	0.975
CCSD(T)/aVDZ	27	19.8513	0.971
CCSD(T)/aVTZ	27	19.3750	0.970
CCSD(T)/aVQZ	7	12.7081	0.719
PES	43	20.0578	0.966
Total	260	19.4929	0.967

Bibliography

[1] Yu, Q.; Bowman, J. M. *J. Chem. Phys.* **2017**, *146*, 121102.

[2] Kumar, R.; Skinner, J. L. *J. Phys. Chem. B* **2008**, *112*, 8311–8318.

[3] Tainter, C. J.; Pieniazek, P. A.; Lin, Y. S.; Skinner, J. L. *J. Chem. Phys.* **2011**, *134*, 184501.

[4] Yu, Q.; Bowman, J. M. *J. Am. Chem. Soc.* **2017**, *139*, 10984–10987.

[5] Duong, C. H.; Gorlova, O.; Yang, N.; Kelleher, P. J.; Johnson, M. A.; McCoy, A. B.; Yu, Q.; Bowman, J. M. *J. Phys. Chem. Lett.* **2017**, *8*, 3782–3789.

[6] Esser, T. K.; Knorke, H.; Asmis, K. R.; Schöllkopf, W.; Yu, Q.; Qu, C.; Bowman, J. M.; Kaledin, M. *J. Phys. Chem. Lett.* **2018**, *9*, 798–803.

[7] Heindel, J. P.; Yu, Q.; Bowman, J. M.; Xantheas, S. S. *J. Chem. Theory Comput.* **2018**, *14*, 4553–3566.

[8] Pinski, P.; Csányi, G. *J. Chem. Theory Comput.* **2014**, *10*, 68–75.

[9] Liu, D.-J.; Oka, T. *Phys. Rev. Lett.* **1985**, *54*, 1787–1789.

[10] Liu, D.; Haese, N. N.; Oka, T. *J. Chem. Phys.* **1985**, *82*, 5368–5372.

[11] Gruebele, M.; Polak, M.; Saykally, R. J. *J. Chem. Phys.* **1987**, *87*, 3347–3351.

[12] Okumura, M.; Yeh, L. I.; Myers, J. D.; Lee, Y. T. *J. Phys. Chem.* **1990**, *94*, 3416–3427.

[13] Tang, J.; Oka, T. *J. Molec. Spec.* **1999**, *196*, 120 – 130.

[14] Dong, F.; Uy, D.; Davis, S.; Child, M.; Nesbitt, D. J. *J. Chem. Phys.* **2005**, *122*, 224301.

[15] Dong, F.; Nesbitt, D. J. *J Chem Phys* **2006**, *125*, 144311.

[16] Begemann, M. H.; Gudeman, C. S.; Pfaff, J.; Saykally, R. J. *Phys. Rev. Lett.* **1983**, *51*, 554.

[17] Gerin, M., et al. *A&A* **2010**, *518*, L110.

[18] Huang, X.; Carter, S.; Bowman, J. M. *The Journal of Physical Chemistry B* **2002**, *106*, 8182–8188.

[19] Huang, X.; Carter, S.; Bowman, J. *J. Chem. Phys.* **2003**, *118*, 5431–5441.

[20] RajamÃďki, T.; Miani, A.; Halonen, L. *J. Chem. Phys.* **2003**, *118*, 10929–10938.

[21] Giacomo, F. D.; Schneider, F.; Nikitin, E. *Chem. Phys. Lett.* **2003**, *373*, 258 – 265.

[22] Huang, X.; Braams, B. J.; Bowman, J. M. *J. Chem. Phys.* **2005**, *122*, 044308.

[23] Kendall, R. A.; Dunning, T. H.; Harrison, R. J. *J. Chem. Phys.* **1992**, *96*, 6796–6806.

[24] Adler, T. B.; Knizia, G.; Werner, H.-J. *J. Chem. Phys.* **2007**, *127*, 221106.

[25] Knizia, G.; Adler, T. B.; Werner, H.-J. *J. Chem. Phys.* **2009**, *130*, 054104.

[26] Werner, H.-J. et al. MOLPRO, version 2010.1, a package of ab initio programs.

[27] Braams, B. J.; Bowman, J. M. *Int. Rev. Phys. Chem.* **2009**, *28*, 577–606.

[28] Lodi, L.; Tennyson, J.; Polyansky, O. L. *J. Chem. Phys.* **2011**, *135*, 034113.

[29] Wang, Y.; Bowman, J. M. *Phys. Chem. Chem. Phys.* **2016**, *18*, 24057–24062.

[30] McCoy, A. B.; Huang, X.; Carter, S.; Landeweer, M. Y.; Bowman, J. M. *J. Chem. Phys.* **2005**, *122*, 061101.

[31] Dai, J.; Bačić, Z.; Huang, X.; Carter, S.; Bowman, J. M. *J. Chem. Phys.* **2003**, *119*, 6571–6580.

[32] Huang, X.; Braams, B. J.; Bowman, J. M. *J. Chem. Phys.* **2005**, *122*, 044308.

[33] Werner, H.-J.; Knowles, P. J.; Knizia, G.; Manby, F. R. **2015**,

[34] Xie, Z.; Bowman, J. M. *J. Chem. Theory Comput.* **2010**, *6*, 26–34.

[35] Wang, Y.; Shepler, B. C.; Braams, B. J.; Bowman, J. M. *J. Chem. Phys.* **2009**, *131*, 054511.

[36] Wang, Y.; Huang, X.; Shepler, B. C.; Braams, B. J.; Bowman, J. M. *J. Chem. Phys.* **2011**, *134*, 094509.

[37] Wang, Y.; Bowman, J. M. *J. Chem. Phys.* **2011**, *134*, 154510.

[38] Partridge, H.; Schwenke, D. W. *J. Chem. Phys.* **1997**, *106*, 4618.

[39] Lodi, L.; Tennyson, J.; Polyansky, O. L. *J. Chem. Phys.* **2011**, *135*, 034113.

[40] Dunning Jr, T. H. *J. Chem. Phys.* **1989**, *90*, 1007.

[41] Rick A., K.; Dunning Jr, T. H.; Harrison, R. J. *J. Chem. Phys.* **1992**, *96*, 6796.

[42] Valiev, M.; Bylaska, E. J.; Govind, N.; Kowalski, K.; Straatsma, T. P.; van Dam, H. J. J.; Wang, D.; Nieplocha, J.; Aprà, E.; Windus, T. L.; de Jong, W. A. *Comp. Phys. Chem.* **2010**, *181*, 1477–1489.

[43] Xantheas, S. S. *J. Chem. Phys.* **1996**, *104*, 8821–8824.

[44] Miliordos, E.; Xantheas, S. S. *J. Chem. Phys.* **2015**, *142*, 234303.

[45] Rauhut, G.; Knizia, G.; Werner, H.-J. *J. Chem. Phys* **2009**, *130*, 054105.

[46] Xantheas, S. S.; Dunning, T. H. *J. Chem. Phys.* **1993**, *99*, 8874–8792.

[47] Miliordos, E.; Aprà, E.; Xantheas, S. S. *J. Chem. Phys.* **2013**, *139*, 114302.

[48] Hermansson, K. *J. Chem. Phys.* **1993**, *99*, 861–868.

[49] Hermansson, K. *International Journal of Quantum Chemisry* **1993**, *45*, 747–758.

[50] Fournier, J. A.; Wolke, C. T.; Johnson, M. A.; Odbadrakh, T. T.; Jordan, K. D.; Kathmann, S. M.; Xantheas, S. S. *J. Phys. Chem. A* **2015**, *119*, 9425–9440.

Part III

Vibrational Dynamics of Gas-phase Protonated Clusters

Chapter 5 H_3O^+ PES Validation and Vibrational Analysis

5.1 Fidelity of the Potential and Vibrational Calculations

We now give results of a number of standard tests of the accuracy of the PES. First, in Table 5.1, the optimized geometries of the global minimum and inversion saddle point are given from the PES and directly from CCSD(T)-F12b/aVQZ calculations, along with the energy of the saddle point and the electronic dissociation energy. As seen, the PES accurately reproduces the *ab initio* results. Second, harmonic frequencies at the minimum and inversion saddle point are given in Table 5.2, where again excellent agreement with the direct *ab initio* results is seen.

Table 5.1 Geometry optimization of H_3O^+ C_{3v} minimum and D_{3h} inversion saddle point, barrier height and dissociation energy

	Minimum (C_{3v})		Inversion saddle point (D_{3h})	
	ab initio[a]	PES	*ab initio*[a]	PES
R_{OH}	0.97590Å	0.97588Å	0.96871Å	0.96848 Å
$\angle HOH$	111.87°	111.88°	120.0°	120.00°
Dihedral $\angle OHHH$	31.36°	31.35°	0.0°	0.0°
	ab initio[a]		PES	
barrier	671.8 cm^{-1}		674.3 cm^{-1}	
D_e	171.53 kcal/mol		171.53 kcal/mol	

[a] CCSD(T)-F12/aug-cc-pVQZ

Using the PES, we first performed 1d calculations using the Q_{im} model.[1] In this model, Q_{im} is the normal coordinate of the imaginary-frequency normal mode of the inversion saddle point. $V(Q_{im})$ is the potential along Q_{im}, which is relaxed with respect to the other normal modes of the saddle point. This potential is shown in

Table 5.2 Harmonic frequencies (cm^{-1}) of H_3O^+ at global minimum and inversion saddle point

	Minimum		Inversion saddle point	
Mode	*ab initio*[a]	PES	*ab initio*[a]	PES
Umbrella	886.7	887.0	671.2i	671.2i
Deformation	1698.0	1697.4	1633.5	1633.6
	1698.0	1697.5	1634.0	1633.6
OH sym stretch	3604.8	3601.3	3658.9	3651.6
OH antisym stretch	3705.1	3708.5	3810.3	3811.2
	3705.1	3708.5	3810.3	3811.2

[a] CCSD(T)/aug-cc-pVQZ

Figure 5.1, where, as shown, it spans both global minima and inversion saddle point that have a barrier of 674 cm^{-1}. A numerical solution of the 1-d Schrödinger equation is done using this potential and we show the ground state wavefunction and energies of three states in Figure 5.1 from this calculation. As seen, the ground state energy is about 300 cm^{-1} below the barrier height and the ground state wavefunction has relatively large amplitude at the barrier. Significant tunneling splitting is observed here that the split at ground state is about 71 cm^{-1}. The calculated fundamental energy of umbrella mode (imaginary mode) is then roughly 596 cm^{-1}.

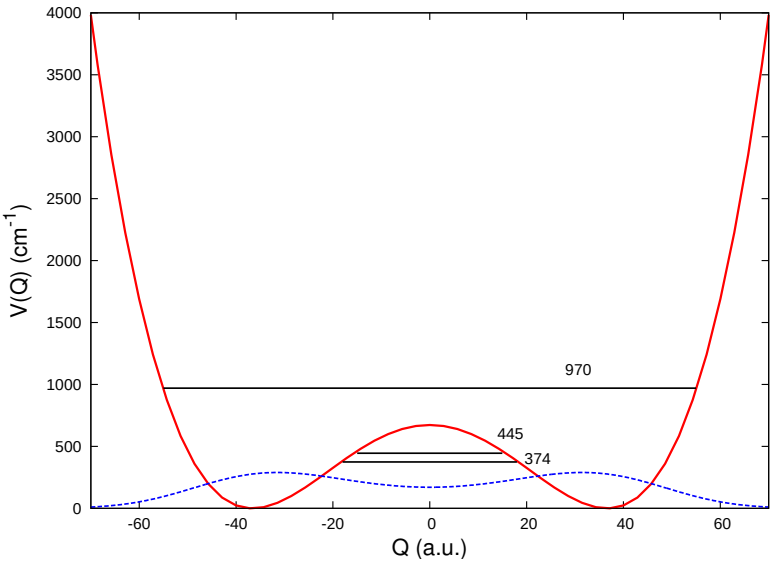

Figure 5.1 Relaxed potential along the imaginary-frequency normal coordinate covering global minimum and inversion saddle point, ground state wavefunction and energies of three states based on 1-d DVR calculation

Table 5.3 contains results of coupled anharmonic calculations of low-lying vibrational states of even and odd parities (with respect to inversion about the saddle point). These have been the focus of numerous experimental and theoretical studies, as noted above. The current variational calculations were done with the latest version of MULTIMODE,[2] which use the saddle-point normal modes with the full-Watson Hamiltonian. This approach was taken in previous calculations,[3,4] however, with an earlier version of MULTIMODE that was limited to fewer than 6-mode coupling in the potential and vibrational angular momentum terms. In those calculations the rigorous degeneracy of deformation mode was achieve numerically, however, not for the OH antisym stretch, where the two modes were split by several wavenumbers. Here that limitation is lifted and an exact 6-mode representation of the potential is used. However, to illustrate the importance of the vibrational angular momentum terms, results for 3-mode and 4-mode representations of these terms (which are often neglected in vibrational calculations using normal modes) are given in the table. As seen those using the 3-mode representation still show a substantial incorrect splitting of the OH antisym stretch modes. However, the 4-mode representation does produce the correct degeneracy to sub wavenumber accuracy. Finally, consider the comparison with experiment. As seen, the agreement is excellent for both parity states, with differences no larger than 3 cm^{-1}. Note the large tunneling splittings, for these states, which indicate both the small barrier for the inversion motion and the effect of the light H-atoms involved in that motion. The infrared spectrum of bare H_3O^+ is further calculated using MULTIMODE and is shown in Figure 5.2

Table 5.3 Anharmonic energies (in cm^{-1}) of H_3O^+ in 1-d DVR, MULTIMODE VCI calculation and experimental results

	1-d DVR		6MR,MC=3[a]		6MR, MC=4[a]		Exp	
Mode	+	-	+	-	+	-	+	- [b]
Umbrella	596.1	1016.6	583.5	952.7	583.8	953.7	581.17	954.40[c]
Deformation			1627.1	1692.0	1626.3	1691.1	1625.95	1693.87[d]
			1627.3	1692.3	1626.3	1691.1		
OH sym str			3445.6	3493.5	3445.4	3492.3	3445.00	3491.17[e]
OH asym str			3534.7	3571.0	3534.3	3571.1	3535.56	3574.29[f]
			3539.7	3579.0	3534.7	3571.8		
Ground state	0.00	71.1	0.00	52.19	0.00	52.48	0.00	55.35[g]

[a] 6MR indicate an exact 6-mode representation of the potential
MC=3,4 indicate a 3 or 4 mode coupled in vibrational angular momentum terms integration
[b] + and - are the parity of each doublet
[c] Refs.[5] [d] Refs.[6] [e] Refs.[7] [f] Refs.[8] [g] Refs.[9]

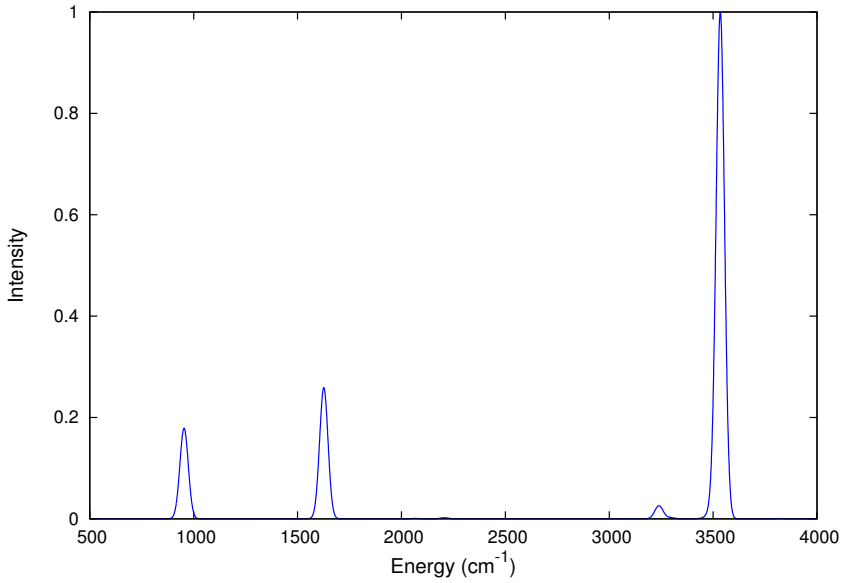

Figure 5.2 Infrared spectrum of H_3O^+

Diffusion Monte Carlo (DMC) calculations were done to rigorously determine the

zero-point energy of H_3O^+. These were done with 40,000 walkers, initiated at one minimum and propagated for 40,000 steps. The DMC zero-point energy is 7459 cm^{-1} with an uncertainty of roughly $\pm 1 cm^{-1}$. This is excellent agreement with the MULTIMODE energy of 7459 cm^{-1}. In addition, the DMC calculation samples large regions of the PES away from the global minimum which indicates the PES has no regions of unphysical behavior as sampled by DMC walkers. Finally, the DMC wavefunction can be visualized as an isosurface and this is done in Figure 5.3

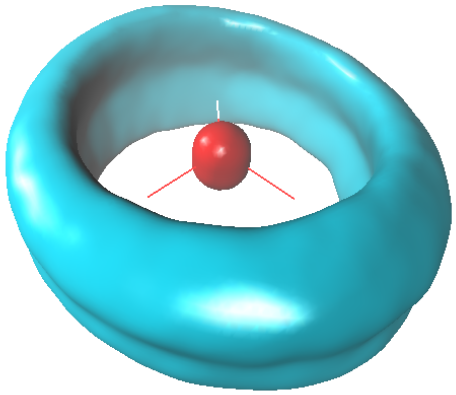

Figure 5.3 Isosurface of ground state wavefunction

5.2 Summary and Conclusions

The H_3O^+ PES is used in converged anharmonic coupled vibrational calculations and results are in excellent agreement with experiment. A diffusion Monte Carlo calculation of the ground state wavefunction demonstrates the delocalization over the two equivalent minima and saddle point separating them. This PES can be also presented as a building block of a many-body representation of the hydrated proton.

Bibliography

[1] Wang, Y.; Bowman, J. M. *J. Chem. Phys.* **2013**, *139*, 154303.

[2] Wang, X.; Carter, S.; Bowman, J. M. *J. Phys. Chem. A* **2015**, *119*, 11632–11640, PMID: 26529348.

[3] Bowman, J. M.; Huang, X.; Carter, S. *Spectrochim. Acta. A.* **2002**, *58*, 839–48.

[4] Huang, X.; Carter, S.; Bowman, J. *J. Chem. Phys.* **2003**, *118*, 5431–5441.

[5] Liu, D.-J.; Oka, T. *Phys. Rev. Lett.* **1985**, *54*, 1787–1789.

[6] Gruebele, M.; Polak, M.; Saykally, R. J. *J. Chem. Phys.* **1987**, *87*, 3347–3351.

[7] Tang, J.; Oka, T. *J. Molec. Spec.* **1999**, *196*, 120 – 130.

[8] Begemann, M. H.; Gudeman, C. S.; Pfaff, J.; Saykally, R. J. *Phys. Rev. Lett.* **1983**, *51*, 554–557.

[9] Liu, D.; Haese, N. N.; Oka, T. *J. Chem. Phys.* **1985**, *82*, 5368–5372.

Chapter 6 Vibrational Dynamics of $H_7O_3^+$ and $H_9O_4^+$

6.1 First Trial of Vibrational Spectra of $H_7O_3^+$ and $H_9O_4^+$

6.1.1 Introduction

The vibrational spectroscopy of the hydrated proton has been investigated both experimentally and theoretically for several decades.[1–15] and a recent review can be found in ref. Fournier2015. In a landmark study of $H^+(H_2O)_n$, n=2-11 clusters, Ar-tagged action spectra were reported,[13] and interpreted as being dominated by the elementary Eigen or Zundel motifs of the hydrated proton.[16–18] In the latter, the proton is equally shared between two water monomers, and in the ideal case of $H_5O_2^+$, it sits midway between them at equilibrium. In the Eigen motif, the proton is closer to one monomer and thus can be considered a perturbed hydronium ion, H_3O^+.

Much detailed spectroscopic information about these motifs has been learned from experiment and theory and much of it has been reviewed recently.[14] In particular, for Eigen clusters, a near linear correlation between the bridging proton OH bond length and the proton stretch fundamental for a variety of such cluster types has been reported.[14] We showed this linear correlation[19] using the bare Zundel, $H_5O_2^+$, potential energy surface, where, as the OO distance increases from equilibrium, the Zundel motif at equilibrium changes to Eigen-like as a result of the development of a barrier that localizes the proton.

These and other studies indicate strong coupling of this stretch mode in these clusters, which presents a major challenge for theory. Ideally, the theoretical analysis of these clusters would follow the approach carried out for $H_5O_2^+$. For this cation,

full-dimensional CCSD(T)-based potential and MP2-based dipole moment surfaces[20] were used in anharmonic, coupled-mode calculations of the IR spectrum. The most rigorous one, using MCTDH methodology, resulted in a near perfect match with experiment.[21] Clearly, this approach is daunting for the next larger clusters, $H_7O_3^+$ and $H_9O_4^+$, as was recently noted.[15] Nevertheless, we report major progress in addressing the computational spectroscopy of the $H_7O_3^+$ and $H_9O_4^+$ clusters using methods that are close to those mentioned above for $H_5O_2^+$.

Using the developed many-body potential and dipole moment surfaces for protonated water clusters. Coupled-mode VSCF/VCI[22,23] calculations of the IR spectrum of these clusters, using the code MULTIMODE, become feasible.[22] Here, we will present some first trial calculations of vibrational spectra of $H_7O_3^+$ and $H_9O_4^+$. The first version of many-body PES was used where the hydronium-water-water 3-body interaction is calculated from a simple expression (As seen in Chapter 4)

6.1.2 Results and Analysis

Table 6.1 Optimized geometry and harmonic frequencies of $H_7O_3^+$ minimum

minimum	MP2	CCSD(T)-F12	PES/no h-w-w	PES/ h-w-w
$R_{OH}(1)$ (Å)	0.967	0.964	0.961	0.963
$R_{OH}(2)$ (Å)	1.038	1.029	1.066	1.040
R_{OO} (Å)	2.487	2.491	2.417	2.480
∠OHO (deg)	174.4	175.1	175.6	174.6
Mode	CCSD(T)-F12	PES/no h-w-w	PES/h-w-w^a	PES/h-w-w^b
1	342	372	389	336
2	366	416	391	364
3	392	443	417	388
4	394	461	426	408
5	479	485	520	490
6	589	675	622	575
7	1054	1235	1080	1036
8	1242	1345	1301	1216
9	1625	1534	1618	1626
10	1654	1617	1645	1660
11	1699	1636	1717	1692
12	1709	1715	1738	1708
13	**2551**	**2013**	**2349**	**2511**
14	**2702**	**2113**	**2466**	**2615**
15	3818	3802	3792	3807
16	3818	3805	3795	3809
17	**3828**	**3865**	**3860**	**3830**
18	3914	3901	3882	3902
19	3914	3901	3886	3903

$R_{OH}(1)$ is the free OH bond length in hydronium core, $R_{OH}(2)$ is the bounded OH bond length in hydronium core, R_{OO} is the distance between hydronium oxygen and water oxygen.

PES/h-w-w^a is the frequencies using PES optimized minimum structure while PES/h-w-w^b is using CCSD(T)-F12 minimum geometry. Basis set for MP2 and CCSD(T)-F12 calculation is aVTZ

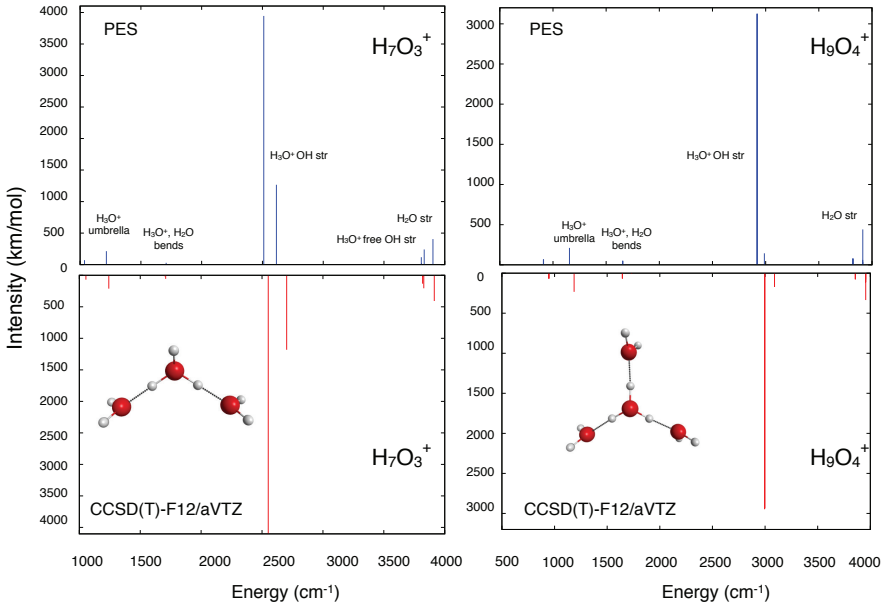

Figure 6.1 Double-harmonic spectra of $H_7O_3^+$ and $H_9O_4^+$ from many-body PES/DMS (upper panels) and CCSD(T)-F12b/aug-cc-pVTZ calculations (lower panels)

Several tests of the accuracy of this version of PES were done against direct CCSD(T)-F12b/aug-cc-pVTZ calculations over $H_7O_3^+$ and $H_9O_4^+$.[24] These are equilibrium structures, normal-mode frequencies (results are in the 6.1) and double-harmonic spectra, shown in Figure 6.1. Before commenting on these spectra, we note that the reference configurations used in all calculations are the *ab initio* ones. These differ slightly from the ones obtained directly from optimizations using the many-body PES. For example, for $H_7O_3^+$, the H_2O-H_3O^+ O-O distance from the PES is 2.48 Å comparing with the direct *ab initio* value of 2.49 Å . This is small difference, but the effect on the perturbed H_3O^+ harmonic frequencies is large (as shown in Table 6.1). This major dependence of these frequencies on this O-O distance was discussed in detail in several recent papers,[14,25] including one from us.[19] With this slight alignment of the PES reference configuration in mind, we see good agreement between the the PES/DMS and direct *ab initio* double-harmonic spectra. The most

intense peak is the perturbed H_3O^+ asymmetric stretch and the frequencies from the PES are downshifted from the *ab initio* ones by 40-100 cm^{-1}. However, these differences do not necessarily indicate the size of systematic errors in an anharmonic coupled-mode calculations, which sample much greater regions of the potential than the curvature of the potential at the minimum. It should also be kept in mind that the monomer components of the PES are based on higher level *ab initio* theory than the present CCSD(T) calculations, which nevertheless are benchmark calculations for these clusters. In summary, these tests do indicate that the many-body approach taken is at least semi-quantitative and these double-harmonic spectra also provide a jumping-off point for the MULTIMODE VSCF/VCI spectra presented next.

The VSCF/VCI calculations use the full Watson Hamiltonian and for $H_7O_3^+$ and $H_9O_4^+$, which have 24 and 33 vibrational modes, respectively, restrictions are necessary in the number of modes that are coupled and in the n-mode representation of the potential and dipole moment surfaces. For the latter, because we have a full-dimensional PES and DMS, we use n=4, a value which typically is needed to obtain results that are converged to a few wavenumbers, for a give number of coupled modes.[26,27] We also did calculations for n equal 2 (a commonly used value) and 3 and results are in 6.2. These underscore the significant mode-coupling in these clusters, especially for the perturbed hydronium stretches, and, as expected, there is less mode coupling in the 2-mode calculations compared to the 3 and 4-mode ones. We use n = 3 for the representation of the DMS.

For $H_7O_3^+$, we selected total 18 modes for calculation with 6 low-frequency modes left. OO stretches, hydronium “frustrated" rotation, umbrella, wagging, bending, OH asym- and sym- stretches and all H_2O bending, stretches are included in MM calculation. The maximum sum of mode excitation is 10, 9, 8, 7 for one-mode, two-mode, three-mode, four-mode expansion. The final matrix size reaches 157790 and Lanczos method is utilized for matrix diagonalization. In the intensity calculation, 3-mode

Table 6.2 Multimode calculation of $H_7O_3^+$ and $H_9O_4^+$ (in cm^{-1})

$H_7O_3^+$	2MR	3MR	4MR
"h" wag	1432	1212	1050
"h" umb	1546	1344	1211
"h" bend,"w" bend	1733,1863,1871 1899,1961,1994	1535,1635,1657 1701,1722,1735	1450,1566,1569 1574,1620,1680
"h" asym str	1529,2988	1535,1765,1841,1848	1450,1838,1870
"h" sym str	1899,1994,3044	1968	1912,1993,2192
"h" free str	3573,3803,3962	3844,3878	3674,3680,3683
"w" str	3984,3926,4074,4079	3754,3776,3854,3856	3635,3654,3743,3745

$H_9O_4^+$	2MR	3MR	4MR
"h" wag	1088	964	908
"h" umb	1309	1165	1112
"h" bend,"w" bend	1733,1738,1753 1784,1800	1621,1624,1669 1691,1693	1559,1560,1597,1612 1613,1638,1639
"h" asym str	2248,2300,2406,2639	2103,2131,2587,2628	2474,2476,2481,2486 2510,2523,2545,2547,2560 2589,2591,2638,2676,2719
"h" sym str	2639	2587,2642	2552,2568,2727
"w" str	3984,3926,4074,4079	3698,3723,3729 3753,3761,3762	3656,3662,3663 3733,3734,3735

"h" is mode in hydronium core and "w" is mode in water fragments

representation of the dipole moment is used and the intensities are obtained through calculating the transition moment with calculated vibrational CI wavefunctions. As for $H_9O_4^+$, all hydronium umbrella, rotation,wagging, bending and stretching modes are involved together with all intramolecular modes in water. Again, 4-mode representation of the potential is used and the sum of mode excitation becomes 11,9,8,7 in VCI calculation. The matrix size is 158503 and intensity calculation also uses 3-mode representation of the dipole moment. The vibrational spectra are for transitions from the ground vibrational state and the potential and dipole transition matrix elements were calculated using standard numerical quadratures. For $H_7O_3^+$ there are 1373 VCI state energies in the range 1000-4000 cm^{-1}. Of these, 309 have intensities larger than 1 km/mol and 81 such states are in the range 1800-2500 cm^{-1}. For the larger clus-

ter, $H_9O_4^+$, additional mode restrictions were needed and so all modes with harmonic frequencies less than 500 cm^{-1} were excluded. Thus, the spectrum is not as complex as $H_7O_3^+$ with around 98 sticks in the range 500-4000 cm^{-1} and 32 sticks with relatively large intensities in the range 2200-2800 cm^{-1} The resulting stick intensities were broadened using a Gaussian function of 10 cm^{-1} FWHM.

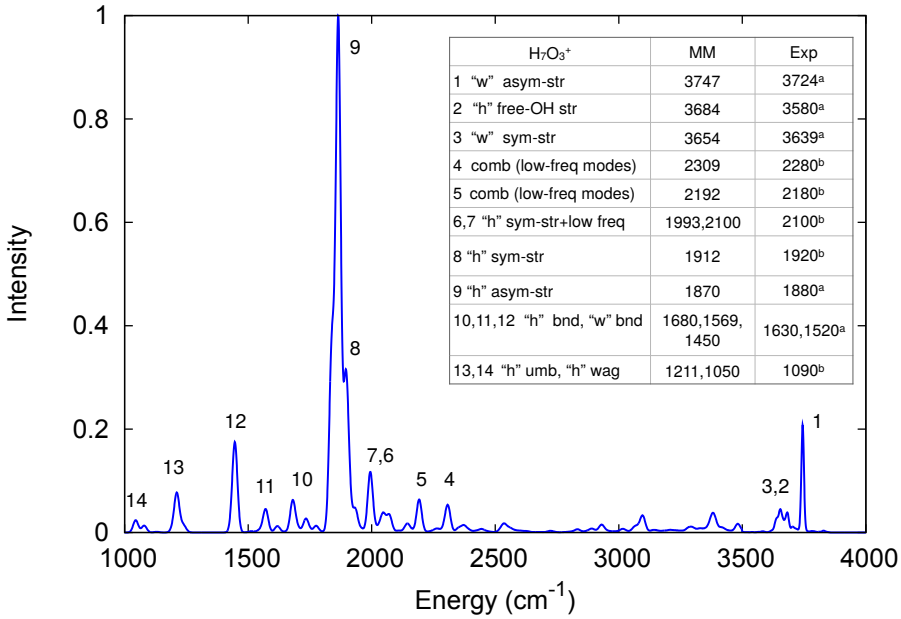

$H_7O_3^+$	MM	Exp
1 "w" asym-str	3747	3724[a]
2 "h" free-OH str	3684	3580[a]
3 "w" sym-str	3654	3639[a]
4 comb (low-freq modes)	2309	2280[b]
5 comb (low-freq modes)	2192	2180[b]
6,7 "h" sym-str+low freq	1993,2100	2100[b]
8 "h" sym-str	1912	1920[b]
9 "h" asym-str	1870	1880[a]
10,11,12 "h" bnd, "w" bnd	1680,1569, 1450	1630,1520[a]
13,14 "h" umb, "h" wag	1211,1050	1090[b]

Figure 6.2 Calculated MULTIMODE (MM) infrared spectrum of $H_7O_3^+$ in the range 1000-4000 cm^{-1} with assignments given in the inset. "h" and "w" denote hydronium and water. See text for more details about peak assignments. Experimental results: ^{a} is from ref. Jorden2005, ^{b} is from ref. Fournier2015

The calculated vibrational spectrum of $H_7O_3^+$ is shown in Figure 6.2, where for convenience the maximum intensity is assigned the value 1.0. A table showing experimental peak positions[13,14] is also given. A comparison to the double-harmonic spectrum, shown in Fig.6.1, reveals a more complex spectrum, however, some features are common to both, e.g., the prominent intense peak labeled 9 at 1870 cm^{-1} is seen in the double-harmonic spectrum, but at 2500 cm^{-1}. The calculated peak position at 1870 cm^{-1} is in good agreement with experiment,[13] which has a strong

band at 1880 cm^{-1}. The breadth of the band at 1870 cm^{-1} results from contributions from eigenstates with large components of H_3O^+ asymmetric stretch and also bending modes and low frequency modes. For example, there is combination state involving the the hydronium frustrated rotation and umbrella modes with some H_3O^+ asymmetric stretch that has significant intensity at 1838 cm^{-1}. The band at 1912 cm^{-1}, labeled 8, is mainly from the perturbed H_3O^+ symmetric stretch and agrees well with experiment, where an intense peak is seen at around 1920 cm^{-1}.[13] In the 2000 to 2500 cm^{-1} range, there are numerous small peaks, labeled 4,5,6,7. This correspond to mixed states involving combination bands of low-frequency modes, labeled that contain small components of perturbed H_3O^+ asymmetric or symmetric stretches. Note, in experiment there does not appear to be an intense peak corresponding to calculated peak 6. There are two bands labeled 13 and 14 below 1400 cm^{-1} which are mainly the H_3O^+ wagging fundamental at 1050 cm^{-1} and H_3O^+ umbrella mode fundamental at 1211 cm^{-1}. These states provide an explanation for the broad feature around 1100 cm^{-1} in the experimental spectrum. The bands labeled 10, 11, 12 correspond to H_2O and H_3O^+ bending fundamental bends. The intense band at 1450 cm^{-1} is mainly the H_2O bend but is coupled with the H_3O^+ asymmetric OH stretch. With this significant coupling, the intensity of this band bend is larger than the bands labeled 10 and 11 at 1569, 1680 cm^{-1}, respectively. (Note this intensity feature is not seen in the double harmonic spectrum.) The vibrational bands in this region are in very good agreement with experiment, where a broad and strong-intensity band is located at 1500 cm^{-1}, with another sharp peak at 1650 cm^{-1}. At energies between 2500 and 3500 cm^{-1} there are several weak bands not labeled. These correspond to several overtones and complicated combination bands The final important features in $H_7O_3^+$ are the water stretches and hydronium free-OH stretch. The H_2O asymnmetric and symmetric stretch peaks, 1, 2, are in good agreement with experiment. However, there is a roughly 100 cm^{-1} difference with experiment for the H_3O^+ free-OH stretch,

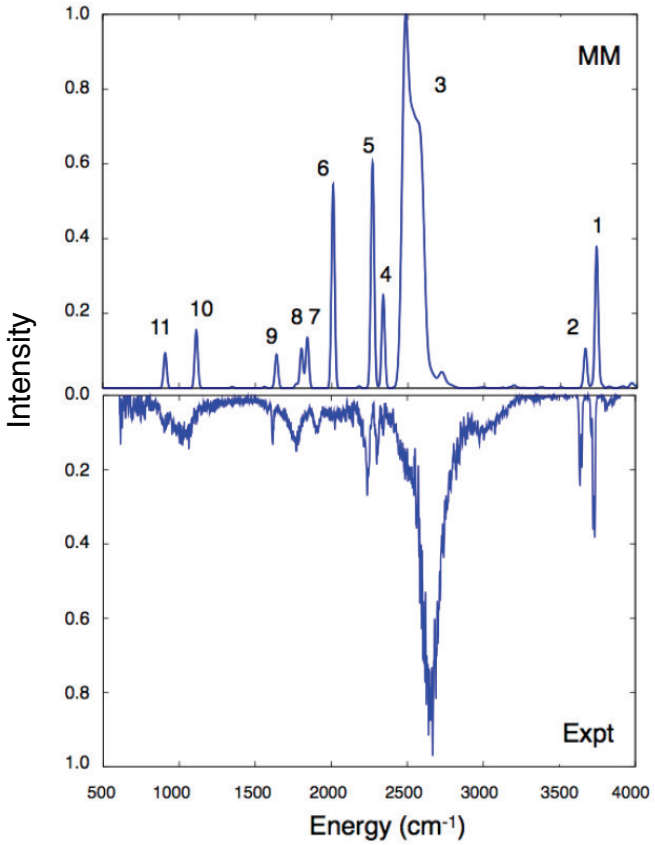

Figure 6.3 Calculated (upper panel) and experimental (lower panel) infrared spectrum of $H_9O_4^+$, experimental data from ref. McCoy2012

labeled, 3.

To conclude this discussion of $H_7O_3^+$, we note the assignments here of prominent bands are in good accord with those made previously from combined experiment and theory, i.e., scaled MP2/aug-ccpVDZ harmonic and 2-mode MP2/aug-ccpVDZ VSCF calculations.[13] However, those calculations give the perturbed hydronium asymmetic stretch at 2381 and 1984 cm^{-1}, respectively, which are roughly 500 and 100 cm^{-1}, respectively, higher than experiment and the present calculations. Next consider the $H_9O_4^+$ cluster, where the hydronium core is fully hydrated. The calculated and Ar-tagged experimental spectra[6] are shown in Figure 6.3, where good correspondence is seen. The largest intensity in the calculations is 692 km/mol at roughly 2500 cm^{-1} and, again, we assign the value of this peak to 1.0 for convenience. This band,

labeled 3, is mainly perturbed hydronium asymmetric stretch(es). These are seen in the double-harmonic spectrum, but at roughly 2920 cm^{-1}. This calculated band, which consists of 14 stick transitions with significant intensity, is broader than the corresponding one in $H_7O_3^+$ and is almost as broad as the corresponding experimental band, which has a peak at around 2650 cm^{-1}. There exits small feature at around 2720 cm^{-1} in the calculated spectrum which is mainly combination band of hydronium umbrella and the bending motion. There is a hint of this in the experimental spectrum at around 2850 cm^{-1}. Note, the calculated peak positions are around 100 cm^{-1} lower than experiment. This *may* be a reflection of the similar difference at the harmonic level seen in the Figure 6.1, or they may be due to the lack of lower-frequency modes in the calculation.

The calculated sharp bands at 3656 cm^{-1} and 3734 cm^{-1}, labeled 2 and 1, are the H_2O symmetric and asymmetric stretches, respectively, are in good agreement with experiment. Bands labeled 4 and 5 around 2300 cm^{-1} are seen experimentally, but, as noted in ref Johnson2016, not in VPT2 calculations. The calculated band at 2264 cm^{-1} is a combination band of the H_3O^+ frustrated rotation and H_3O^+ bending modes. The band at 2336 cm^{-1} is the combination band of H_3O^+ frustrated rotation and the H_2O bending modes. The explanation of why these two combination bands have relatively large intensity is explained nicely by McCoy *et al.*,[6] who stress the importance of electrical anharmonicity for the transition moment of ionic molecules, in this case, the hydrated hydronium ion. From another point of view, we observe strong coupling with hydronium OH asymmetric stretches for both of the two combination bands. In this aspect, the two combination bands can borrow intensity from the hydronium stretches and thus there exits bright signature around 2264 and 2336 cm^{-1}.

The band at 2000 cm^{-1} , 6, and the doublet at 1802 cm^{-1} ,7 and 8, are combination bands. The one at 2000 cm^{-1} is a combination band of hydronium frustrated

rotation and umbrella modes and the 1802 cm^{-1} band is mainly a hydronium wagging and umbrella excitation. Both of these two combination bands have some coupling with the bright perturbed H_3O^+ stretches. We tentatively propose that these bands correspond to the bands labeled "a_{10}" and "a_{11}" in the experimental spectrum of D_2-tagged $H_9O_4^+$.[15] Note, however, that calculated peak 6 is more intense than the experimental band close to it in energy. We do not have a simple explanation for this singular difference; however, it is likely an issue with the calculationsThe calculated band at 1639 cm^{-1} is mainly a bend fundamental, which has the character of a collective bending motion of both H_3O^+ and H_2O. This collective motion results from the near degeneracy of the perturbed H_3O^+ and H_2O harmonic frequencies, in accord with the simple analysis we carried out for the evolution of the perturbed H_3O^+ harmonic frequencies,[19] when applied to $H_9O_4^+$.

Finally, the hydronium frustrated rotation and umbrella fundamentals, 10 and 11, respectively, are at 908 and 1112 cm^{-1}, respectively. In the experiment, a broad band appears in the region 900-1100 cm^{-1}. Probably, inclusion of low-frequency modes would further broaden the calculated bands.

6.1.3 Conclusions

In summary, we reported VSCF/VCI calculations of the vibrational spectra of $H_7O_3^+$ and $H_9O_4^+$, with a 4-mode representation of the potential and 18 coupled modes. The calculations were feasible with the novel many-body representation of the potential and dipole moment surfaces. The calculated spectra do capture, quantitatively or semi-quantitatively, the complex Ar-tagged experimental spectra and the similarities and differences in these two spectra are also captured well by the present calculations.

Bibliography

[1] Woutersen, S.; Bakker, H. J. *Phys. Rev. Lett.* **2006**, *96*, 138305.

[2] Stoyanov, E. S.; Stoyanova, I. V.; Reed, C. A. *J. Am. Chem. Soc.* **2010**, *132*, 1484.

[3] Mandal, A.; Ramasesha, K.; De Marco, L.; Tokmakoff, A. *J. Chem. Phys.* **2014**, *140*, 204508.

[4] Fecko, C. J.; Eaves, J. D.; Loparo, J. J.; Tokmakoff, A.; Geissler, P. L. *Science* **2003**, *301*, 1698.

[5] Loparo, J. J.; Roberts, S. T.; Tokmakoff, A. *J. Chem. Phys.* **2006**, *125*, 194522.

[6] McCoy, A. B.; Guasco, T. L.; Leavitt, C. M.; Olesen, S. G.; Johnson, M. A. *Phys. Chem. Chem. Phys.* **2012**, *14*, 7205.

[7] Begemann, M. H.; Gudeman, C. S.; Pfaff, J.; Saykally, R. J. *Phys. Rev. Lett.* **1983**, *51*, 554.

[8] Yeh, L. I.; Okumura, M.; Myers, J. D.; Price, J. M.; Lee, Y. T. *J. Chem. Phys.* **1989**, *91*, 7319.

[9] Jiang, J.-C.; Wang, Y.-S.; Chang, H.-C.; Lin, S. H.; Lee, Y. T.; Niedner-Schatteburg, G.; Chang, H.-C. *J. Am. Chem. Soc.* **2000**, *122*, 1398.

[10] Yeh, L. I.; Lee, Y. T.; Hougen, J. T. *J. Mol. Spectrosc.* **1994**, *164*, 473.

[11] Douberly, G. E.; Ricks, A. M.; Duncan, M. A. *J. Phys. Chem. A* **2009**, *113*, 8449.

[12] Douberly, G. E.; Walters, R. S.; Cui, J.; Jordan, K. D.; Duncan, M. A. *J. Phys. Chem. A* **2010**, *114*, 4570.

[13] Headrick, J. M.; Diken, E. G.; Walters, R. S.; Hammer, N. I.; Christie, R. A.; Cui, J.; Myshakin, E. M.; Duncan, M. A.; Johnson, M. A.; Jordan, K. D. *Science* **2005**, *308*, 1765.

[14] Fournier, J. A.; Wolke, C. T.; Johnson, M. A.; Odbadrakh, T. T.; Jordan, K. D.; Kathmann, S. M.; Xantheas, S. S. *J. Phys. Chem. A* **2015**, *119*, 9425–9440.

[15] Wolke, C. T.; Fournier, J. A.; Dzugan, L. C.; Fagiani, M. R.; Odbadrakh, T. T.; Knorke, H.; Jordan, K. D.; McCoy, A. B.; Asmis, K. R.; Johnson, M. A. *Science* **2016**, *354*, 1131.

[16] Zundel, G. *Adv. Chem. Phys.* **1999**, *111*, 1.

[17] Zundel, G.; Metzger, H. *Z. Phys. Chem.* **1968**, *58*, 225.

[18] Eigen, M. *Angew. Chem., Int. Ed. Engl.* **1964**, *3*, 1.

[19] Yu, Q.; Bowman, J. M. *J. Phys. Chem. Lett.* **2016**, *7*, 5259–5265.

[20] Huang, X.; Braams, B.; Bowman, J. M. *J. Chem. Phys.* **2005**, *122*, 044308.

[21] Vendrell, O.; Gatti, F.; Meyer, H.-D. *Angew. Chem. Int. Edit.* **2007**, *46*, 6918–6921.

[22] Bowman, J. M.; Carter, S.; Huang, X. *Int. Rev. Phys. Chem.* **2003**, *22*, 533–549.

[23] Christoffel, K. M.; Bowman, J. M. *Chem. Phys. Lett.* **1982**, *85*, 220–224.

[24] others,, et al. MOLPRO, version 2015.1, a package of ab initio programs. 2015; see.

[25] Kulig, W.; Agmon, N. *Nature Chemistry* **2012**, *5*, 29.

[26] Bowman, J. M.; Carrington, T.; Meyer, H.-D. *Molec. Phys.* **2008**, *106*, 2145–2182.

[27] Carter, S.; Culik, J. S.; Bowman, J. M. *J. Chem. Phys.* **1997**, *107*, 10458.

6.2 Vibrational Spectra of the Eigen, Zundel and Ring Isomers of $H^+(H_2O)_4$—Find a Single Match to Experiment

6.2.1 Introduction

The hydrated proton is perhaps the most important and intensively studied hydrated ion.[1] One central issue is the relative importance of the "Eigen" and "Zundel" motifs of the hydrated proton. "Eigen" clusters are hydrated hydronium, whereas "Zundel" ones have the proton roughly equidistant between two water monomers. Gas-phase IR spectroscopy of protonated water clusters has been a vital tool to investigate the structure of various clusters, with the major goal of identifying them as either being "Eigen" or "Zundel".[2–4] Ultrafast 2D IR spectroscopy of protons in water[5] conclude that Zundel plays a key role in proton transfer, based in large part on the observation of bands at 1760 and 3200 cm^{-1}. The former is seen in the classic Zundel cluster, $H_5O_2^+$, while the band at 3200 cm^{-1} is only seen in calculations for larger Zundel clusters[4,6]

The pioneering study of these clusters in the gas phase by the Johnson and Duncan group, using tagged IR spectroscopy, has shown that these IR spectra are quite complex and not always amenable to double-harmonic analysis.[2,4,7,8] The series $H^+(H_2O)$n, n=2,3,4, is particularly important as the expectation is that n = 2 is "Zundel", n = 4 is "Eigen" and n = 3 is something in between. Joint experimental and theoretical (double-harmonic and VPT2 using B3LYP energies) studies concluded that n = 4 is indeed "Eigen"'. However, as noted recently, there are some shortcomings of these calculations, both in the level of electronic structure calculations and the VPT2 treatment of vibrational dynamics.[9] Wang and Agmon reported "AIMD" and VPT2 calculations of the IR spectrum, using a dispersion-corrected DFT Functional and MP2(full)/6-31++G** calculations, respectively. To quote from that paper: "With these issues properly addressed, all theoretical methods generate the

same spectra (at least for the fundamental bands), agreeing with experiment for the Zundel isomer, but not for the Eigen isomer as the sole contributor to the spectrum."[9] At about the same time, Yagi and Thomsen reported a "direct" and very cpu-intensive calculation of the IR spectra of the Eigen and *trans*-Zundel isomers using vibrational quasi-degenerate perturbation theory, however, with limited mode coupling and a mixture of CCSD(T) electronic energies for 1-mode terms and B3LYP for coupled terms.[10] The comparisons with experiments for each isomer were not quantitative and so unfortunately not definitive.

Shortly after these papers appeared, we reported a Communication on the IR spectrum of the Eigen isomer of $H^+(H_2O)_4$,[11] using vibrational self-consistent field/virtual state configuration interaction (VSCF/VCI) calculations, as implemented in the code MULTIMODE[12] with a many-body representation of the potential energy surface (PES) These calculations, although limited to the Eigen isomer, reproduced the experimental spectrum with far greater accuracy than previous ones, and thus allowed us to conclude that the experimental spectrum was consistent with the calculated one for the Eigen isomer. However, the lack of corresponding calculations of the IR spectra for other isomers of $H^+(H_2O)_4$ left open the question of whether these could contribute to the experimental spectrum.

This is now fully addressed in this work, where IR spectra for the Eigen, *cis* and *trans*-Zundel and ring isomers are reported using the above approach, and with a much more extensive fit to the hydronium-water-water 3-body interaction. In addition, in order to describe the Zundel isomers, the above many-body representation was extended by using a weighted sum-of-potentials, in which feasible assignments for the hydronium are made.[13]

6.2.2 Computational Details and Results

To begin we give the MP2/aug-cc-pVTZ electronic energies of the isomers of $H^+(H_2O)_4$, ΔE_{elec}, relative to the Eigen isomer, which is the lowest energy isomer and the energy differences including harmonic zero-point energy, ΔE_0. We also give the absolute energies E_{elec} (in Hartree) of all these isomers in Table 6.3.

The ab initio relative electronic energies (MP2/aVTZ) of Zundel and Ring isomers are in the range of 1233∼1316 cm-1 above Eigen minima. Under low temperature environment (10-20 K in experiment[8,14]), according to Boltzmann distribution, the Eigen minima is most stable and prominent while the ratios of Zundel and Ring isomers are very small. To verify the existence of these isomers, beyond Boltzmann distribution, we need to analysis the detailed spectra for each isomer. Before presenting the VSCF/VCI IR spectra for these isomers, we first show the equilibrium structures and double-harmonic spectra of these isomers from the many-body PES and DMS and direct *ab initio* calculations. (The very good agreement between them is an important validation of the many-body approach.)

Table 6.3 *Ab initio* electronic energy of optimized $H_9O_4^+$ isomers, E_{elec} (absolute energy), ΔE_{elec} (relative electronic energy without ZPE correction), ΔE_0 (relative electronic energy with ZPE correction)

MP2/aVTZ	Eigen	*cis*-Zundel	trans-Zundel	Ring
E_{elec} (Hartree)	-305.7114407	-305.7058241	-305.7056922	-305.7054429
ΔE_{elec} (cm^{-1})	0	1233	1262	1316
ΔE_0 (cm^{-1})	0	776	669	1636

We also mention that the absolute energy of $H_9O_4^+$ Eigen minimum structure optimized in CCSD(T)-F12/aVTZ is -305.8583278 in Hartree

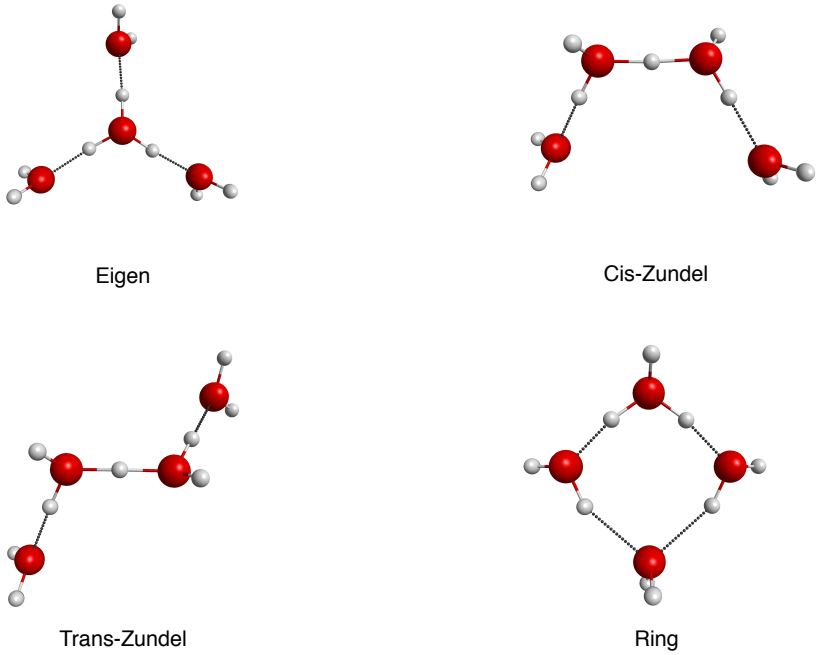

Figure 6.4 Optimized geometry of $H_9O_4^+$ Eigen, *cis*- and *trans*-Zundel and Ring isomers using the current PES.

Table 6.4 Harmonic frequencies (in cm^{-1}) and double harmonic intensity (in km/mol) of $H_9O_4^+$ of the Eigen minimum structure. The text in bold are modes included in the VSCF/VCI calculation and text in italics are hydronium stretches.

Mode	MP2/aVTZ	CCSD(T)-F12/aVTZ	PES
1	64 (0.94)	55	64 (1.43)
2	64 (1.07)	61	64 (1.49)
3	72 (1.31)	63	68 (0.67)
4	104 (0.42)	76	101 (0.71)
5	106 (0.10)	121	102 (0.58)
6	119 (59.79)	130	117 (62.28)
7	241 (68.22)	147	258 (48.24)
8	262 (204.61)	162	277 (170.48)
9	266 (199.67)	175	278 (166.17)
10	286 (12.09)	271	284 (21.17)
11	342 (151.79)	307	335 (132.29)
12	342 (150.90)	308	336 (132.54)
13	**377** (75.37)	**343**	**367** (131.71)
14	**378** (81.57)	**343**	**369** (135.04)
15	**417** (73.68)	**372**	**410** (84.35)
16	**738** (0.18)	**712**	**712** (0.15)
17	**963** (68.61)	**944**	**925** (62.51)
18	**967** (69.08)	**948**	**929** (63.43)
19	**1217** (232.71)	**1186**	**1189** (201.11)
20	**1635** (65.61)	**1644**	**1669** (67.98)
21	**1635** (66.88)	**1645**	**1669** (68.81)
22	**1646** (0.34)	**1654**	**1681**(3.87)
23	**1728** (8.07)	**1731**	**1766** (5.42)
24	**1729** (8.27)	**1733**	**1767** (5.78)
25	***2928*** (2947.69)	***2995***	***2978*** (3095.16)
26	***2932*** (2937.66)	***2998***	***2979*** (3087.25)
27	***3024*** (172.58)	***3089***	***3091*** (145.35)
28	3797 (76.46)	3856	3828 (81.65)
29	3797 (76.82)	3858	3828 (81.12)
30	3798 (6.57)	3858	3836 (2.91)
31	3905 (76.84)	3955	3921 (60.16)
32	3906 (113.12)	3955	3921 (52.42)
33	3907 (335.19)	3956	3922 (423.30)

Table 6.5 Harmonic frequencies (in cm^{-1}) and double harmonic intensity (in km/mol) of $H_9O_4^+$ *cis*-Zundel isomer. The text in bold are modes included in the VSCF/VCI calculation and text in italics are proton stretches.

Mode	MP2/aVTZ	PES
1	25 (0.0)	22 (0.4)
2	50 (0.0)	52 (4.4)
3	85 (35.0)	89 (21.2)
4	114 (26.3)	121 (34.1)
5	138 (10.2)	142 (9.9)
6	215 (403.2)	234 (339.3)
7	270 (1.4)	290 (1.0)
8	287 (179.3)	305 (100.9)
9	308 (104.0)	326 (98.5)
10	309 (87.4)	328 (200.7)
11	353 (138.3)	357(177.0)
12	366 (1.4)	367 (4.2)
13	435 (145.1)	453 (148.5)
14	**611** (11.6)	**600** (56.5))
15	**622** (64.7)	**602** (87.0)
16	**665** (2.8)	**672** (4.1)
17	***824*** (2452.8)	***824*** (2489.0)
18	**971** (9.4)	**969** (12.2)
19	***1047*** (1415.9)	***1018*** (893.1)
20	**1485** (158.7)	**1502** (111.7)
21	**1573** (50.1)	**1613** (67.2)
22	1643 (194.4)	1659(269.5)
23	1643 (20.4)	1674 (14.1)
24	**1732** (5.9)	**1763** (3.7)
25	**1769** (707.4)	**1780** (560.4)
26	**3094** (974.7)	**3140** (884.2)
27	**3128** (2035.9)	**3176** (2084.6)
28	3797 (61.3)	3790 (66.6)
29	3797 (41.8)	3809 (82.1)
30	**3838** (204.7)	**3879** (174.5)
31	**3840** (143.5)	**3893** (208.3)
32	3906 (66.8)	3928 (39.6)
33	3906 (266.5)	3928 (271.5)

Table 6.6 Harmonic frequencies (in cm^{-1}) and double harmonic intensity (in km/mol) of $H_9O_4^+$ *trans*-Zundel isomer. The text in bold are modes included in the VSCF/VCI calculation and text in italics are proton stretches.

Mode	MP2/aVTZ	PES
1	19(0.0)	18 (1.0)
2	60 (22.4)	63 (12.7)
3	68 (0.7)	67 (0.2)
4	99 (33.3)	102 (43.7)
5	105 (1.8)	115 (5.6)
6	194 (191.7)	211 (476.0)
7	195 (167.5)	236 (164.5)
8	197 (770.6)	239 (389.3)
9	301 (58.4)	305 (52.4)
10	326 (158.8)	320 (146.8)
11	337 (8.7)	337(3.0)
12	368 (8.6)	363 (1.3)
13	379 (0.1)	399 (1.0)
14	**595** (18.8)	**583** (31.6))
15	**621** (299.1)	**602** (319.2)
16	**639** (5.8)	**644** (4.8)
17	***840*** (1582.3)	***823*** (1615.0)
18	**1012** (144.1)	**1005** (149.6)
19	***1017*** (1587.8)	***972*** (1216.6)
20	**1468** (262.4)	**1492** (275.4)
21	**1591** (51.3)	**1614** (57.7)
22	1641 (20.4)	1666(8.8)
23	1643 (176.7)	1658 (222.6)
24	**1715** (0.4)	**1730** (6.7)
25	**1763** (717.9)	**1777** (473.6)
26	**3088** (2478.6)	**3156** (2064.6)
27	**3114** (696.6)	**3172** (1031.0)
28	3802 (82.5)	3803 (18.9)
29	3803 (24.0)	3835 (91.4)
30	**3846** (124.3)	**3871** (193.0)
31	**3848** (210.8)	**3891** (206.5)
32	3914 (171.4)	3942 (171.5)
33	3913 (169.8)	3943 (142.9)

Table 6.7 Harmonic frequencies (in cm^{-1}) and double harmonic intensity (in km/mol) of $H_9O_4^+$ Ring isomer. The text in bold are modes included in the VSCF/VCI calculation and text in italics are hydronium stretches.

Mode	MP2/aVTZ	PES
1	52(1.8)	57 (1.5)
2	99 (3.6)	108 (3.5)
3	114 (0.3)	142 (0.6)
4	195 (12.0)	206 (19.2)
5	244 (69.1)	251 (87.1)
6	245 (15.1)	260 (27.3)
7	300 (102.5)	300 (107.3)
8	304 (7.4)	335 (6.6)
9	365 (205.5)	372 (209.4)
10	418 (40.1)	420 (46.8)
11	451 (10.5)	469(119.9)
12	461 (134.8)	479 (1.5)
13	526 (198.2)	546 (221.8)
14	**559** (125.8)	**588** (109.1))
15	**603** (124.1)	**617** (103.8)
16	**682** (39.3)	**722** (54.0)
17	**702** (113.4)	**735** (124.8)
18	**1087** (3.5)	**1097** (4.5)
19	**1301** (231.7)	**1289** (211.9)
20	**1610** (33.1)	**1644** (0.1)
21	**1624** (25.1)	**1656** (57.7)
22	**1630** (100.9)	**1686** (31.5)
23	**1656** (27.0)	**1690** (54.0)
24	**1818** (183.8)	**1889** (175.3)
25	***2316***(2613.9)	***2312*** (2778.4)
26	***2541*** (1874.0)	***2520*** (1735.9)
27	3619 (248.0)	3556 (368.8)
28	3644 (628.9)	3563 (734.0)
29	3768 (25.2)	3752 (34.5)
30	***3798*** (201.7)	***3820*** (274.5)
31	3862 (351.7)	3834 (99.4)
32	3866 (102.2)	3872 (264.5)
33	3869 (164.9)	3880 (67.1)

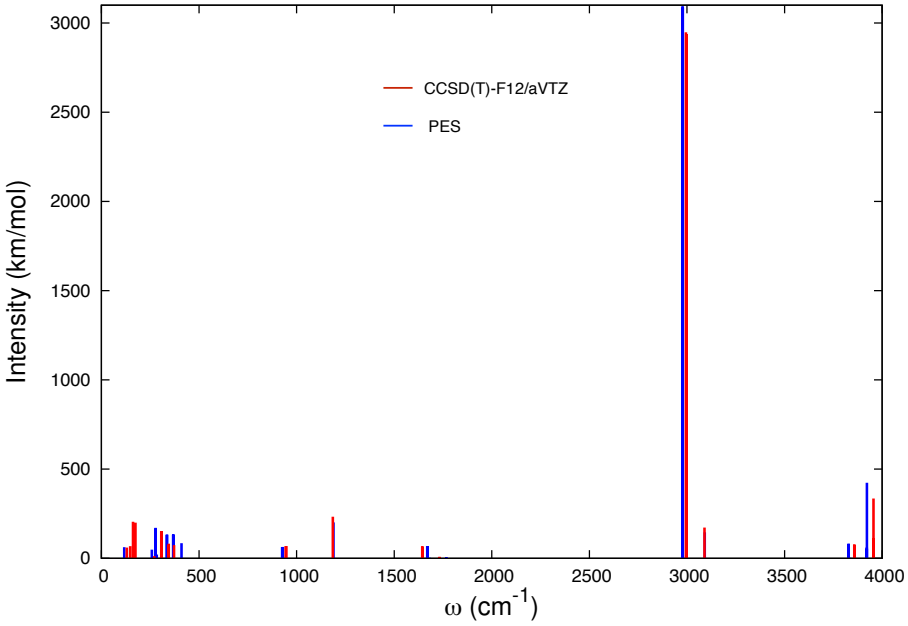

Figure 6.5 Double harmonic spectra of $H_9O_4^+$ Eigen minimum structure using CCSD(T)-F12/aVTZ (intensities are calculated in MP2/aVTZ) and PES

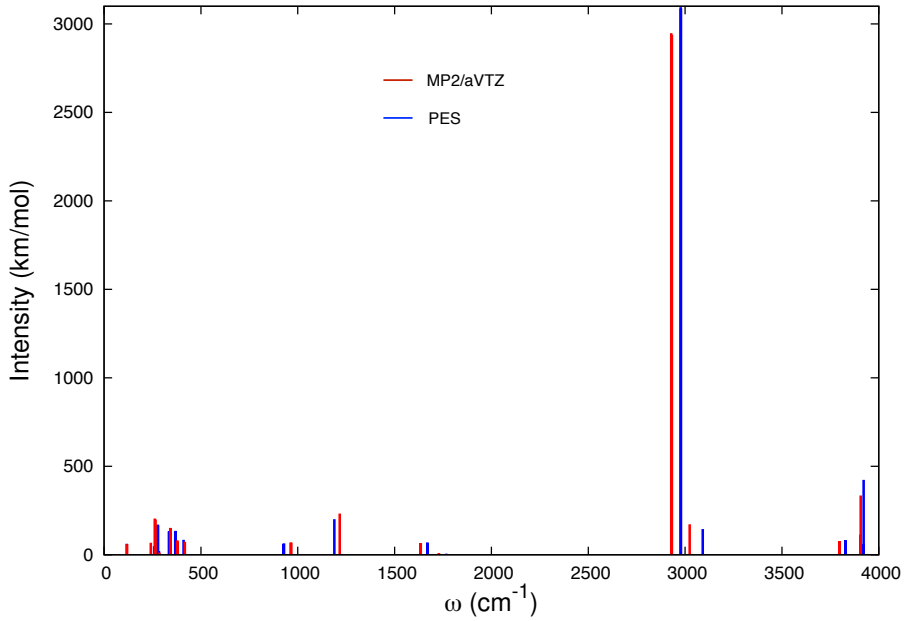

Figure 6.6 Double harmonic spectra of $H_9O_4^+$ Eigen minimum structure using MP2/aVTZ and PES

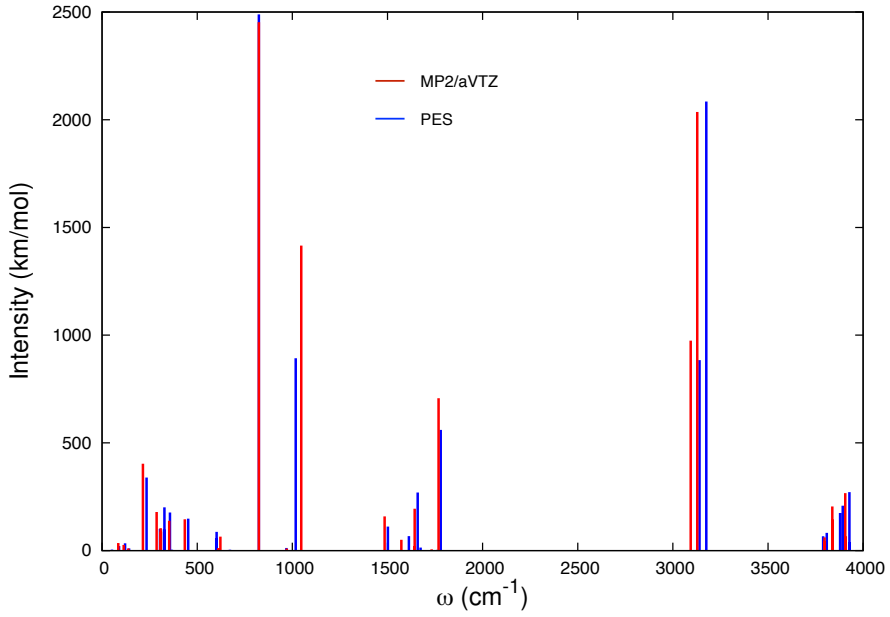

Figure 6.7 Double harmonic spectra of $H_9O_4^+$ *cis*-Zundel isomer using MP2/aVTZ and PES

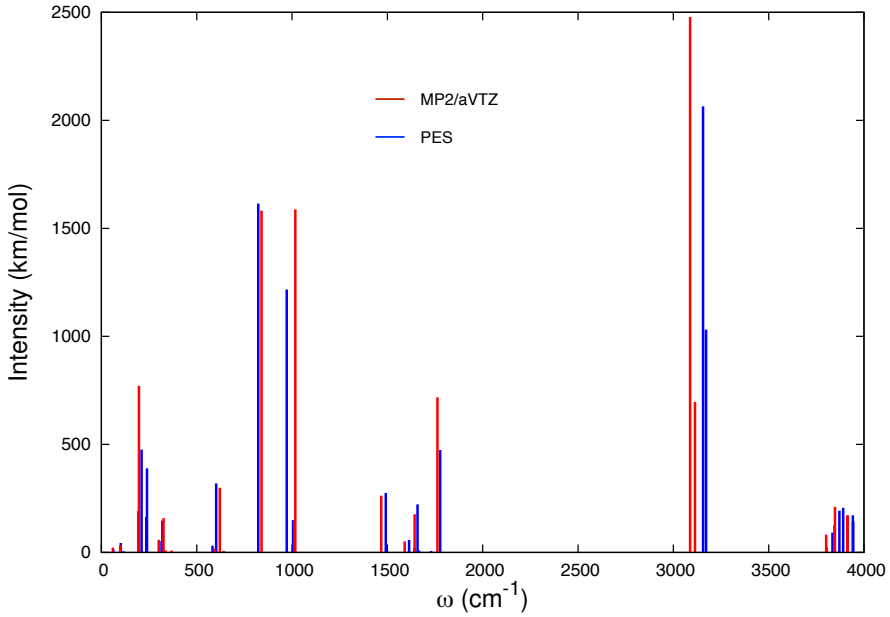

Figure 6.8 Double harmonic spectra of $H_9O_4^+$ trans-Zundel isomer using MP2/aVTZ and PES

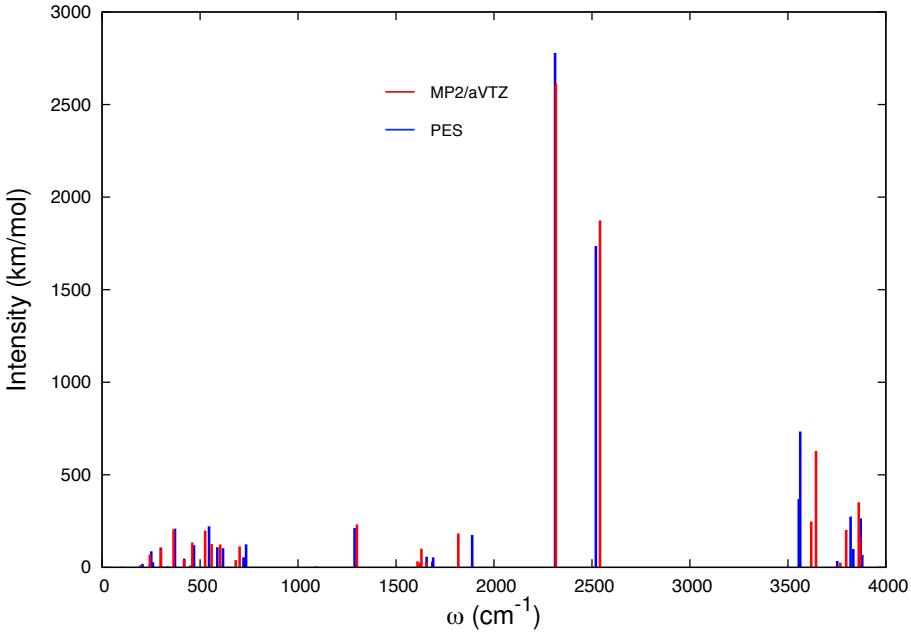

Figure 6.9 Double harmonic spectra of $H_9O_4^+$ Ring isomer using MP2/aVTZ and PES

As seen, there is very good agreement between the PES results and the direct *ab initio* ones. Note especially the ones for the Eigen isomer, where the comparison includes benchmark CCSD(T)-F12/aVTZ results. Zeroing in the hydronium stretches, the PES frequencies are roughly 20 cm^{-1} below the CCSD(T) ones (Interestingly, the MP2 frequencies are downshifted from the CCSD(T) ones by nearly 70 cm^{-1}.) By contrast, the PES intense water bends at around 1670 cm^{-1} are higher than the CCSD(T) ones by nearly 25 cm^{-1}. Turning next to the *trans*-Zundel isomer, we see that the PES frequency for the intense Zundel OH-stretch is roughly 70 cm^{-1} higher than the MP2 frequency. Based on the PES-CCSD(T)-MP2 comparisons for the Eigen isomer for the hydronium stretches, we lean towards the PES frequency as being more accurate than the MP2 one for this Zundel stretch.

The highlights of these approximate IR spectra are the following: for the Eigen isomer, the fundamentals with the largest intensities are two hydronium asymmetric stretches, located at 2978 and 2979 cm^{-1}, while the hydronium symmetric stretch (at 3091 cm^{-1}) has much lower intensity. For the *cis*- and *trans*- isomers, these harmonic

spectra show expected features of Zundel, namely two proton involved stretches at 824,1018 cm^{-1} for *cis*-Zundel isomer and 823, 972 cm^{-1} for *trans*-Zundel isomer. Also, the two Zundel OH stretches at around 3100 cm^{-1} have almost equal strong intensity. Finally, the harmonic spectra for the ring-isomer is much simpler, with the most intense transition corresponding to perturbed hydronium asym- and sym-stretches at 2312 and 2520 cm^{-1}), respectively. As shown next, the coupled mode VSCF/VCI spectra are very different from these double-harmonic ones.

To understand the content of a VSCF/VCI calculation, one equation relating the eigenstates of the Hamiltonian to the underlying basis is given as follows:

$$\psi_J = \sum_{i=1}^{N} C_i^{(J)} \chi_i, \tag{6.1}$$

where ψ_J is the J_{th} eigenstate, $\{\chi\}$ is the expansion basis of N zero-order functions, for example, harmonic-oscillator functions, but in the VSCF/VCI calculations, these are the virtual states[15] of the VSCF ground-state Hamiltonian,[12] and $C_i^{(J)}$ are the "CI" coefficients. Note the sum of the squares of these coefficients equals 1.0 and thus the weight of each term in the above expansion is $|C_I^{(J)}|^2$. If there is one, or perhaps two, dominant "CI" coefficient (say greater than 0.7), then the eigenstate is typically assigned using the character of the associated basis function, for example, an OH-stretch. If this is not the case, and there are many "CI" coefficients of roughly equal weight, then the eigenstate cannot be given a conventional assignment and more sophisticated methods of analysis are required.

Since it is not computationally feasible to couple all 33 vibrational modes, subsets of modes were considered. For Eigen, 15 normal modes (including water bends) are in one group and the second consists of 9 water bends and stretches. For the Zundel isomers, 14 normal modes (without any flanking water modes) are in one group and the second consists of the bends and stretches of the two flanking waters, and for the ring 14 normal modes (including the water bends) are in one group and the second group consists of the nine water modes. For all calculations, a 4-mode representation

of the full-dimensional potential is used and the excitation space consists of singles, doubles, triples and quadruple excitations. The final Hamiltonian matrix is of order 138661 for Eigen (and thus N in Eq. (2) equals 138661). Dipole matrix elements from the ground vibrational state are done numerically using a 3-mode representation of the dipole moment. To plot the spectra, each energy stick is broadened with a Gaussian function of FWHM 10 cm^{-1}.

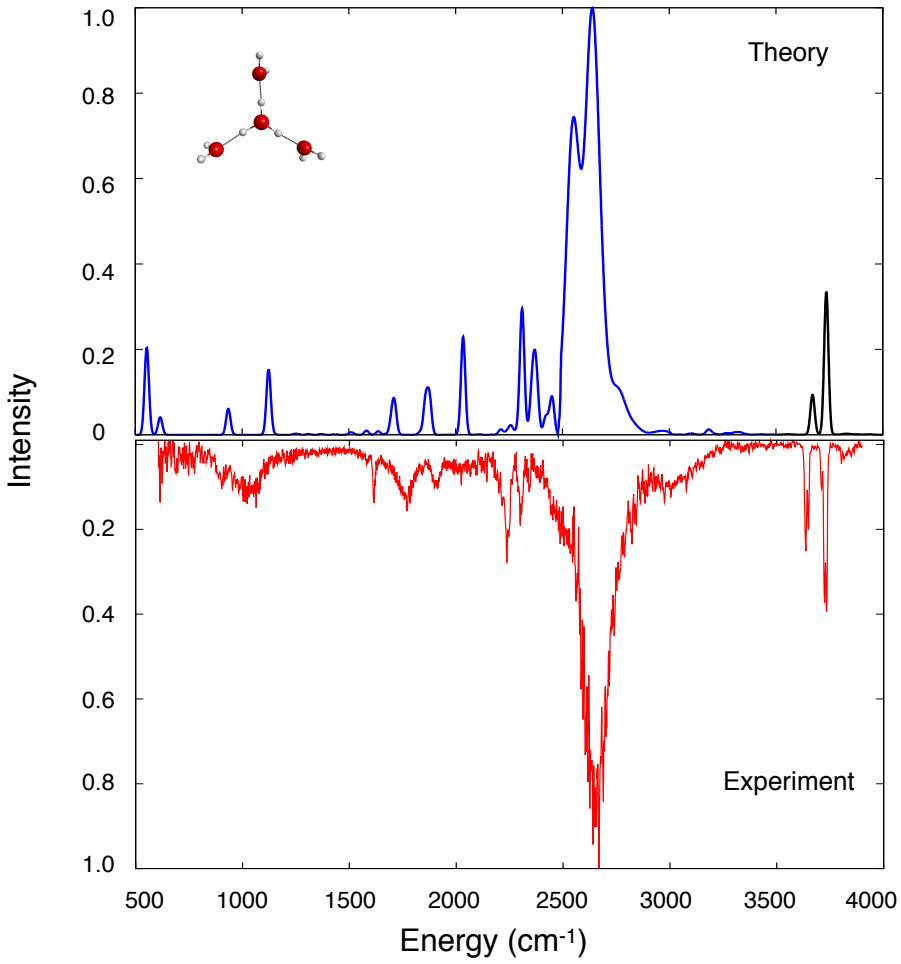

Figure 6.10 Calculated VSCF/VCI (Theory) and experimental[14] (Experiment) vibrational spectrum of the Eigen isomer of $H_9O_4^+$. Black lines are water stretches calculated separately, see text for details.

First, consider the spectrum for Eigen, shown in Fig 6.10, along with the experimental spectrum.[8] As seen, there is very good agreement between them. Note that the peak of the most prominent band is at 2640 cm^{-1} for $H_9O_4^+$, which is downshifted

from the most intense peak in the double-harmonic spectrum by approximately 400 cm^{-1}; this is a very large and atypical downshift. Before discussing the features in these spectra, it is important to note that the calculated IR spectra for the other isomers have little in common with the experimental spectrum and so the conclusion that experiment is indeed giving the IR spectrum of the Eigen isomer, predominantly at least, is secure.

Continuing with the analysis of the $H_9O_4^+$ Eigen spectrum, to further investigate the prominent band at 2640 cm^{-1}, we examined the "CI" coefficients and do not find one that is larger than 0.4, corresponding to a weight of 0.16. Thus, this band cannot be "assigned" in the sense described above. Details of the distribution of the CI coefficients are given in SI; however, the major finding is that for a bright eigenstate in the center of the band, there are roughly 60 basis functions that contribute roughly 90% of the weight of the eigenstate. These involve combinations of the "bright", zero-order hydronium asymmetric stretch fundamental with lower-frequency, frustrated H_3O^+ modes such as the wag, rotation etc. The strong coupling between low-frequency intermolecular modes and the asymmetric stretch, seen here quantitatively, is consistent with recent qualitative analyses showing high sensitivity of the proton stretch harmonic frequency with the position of adjacent water monomers.[8,14,16] These positions change with excitation of the intermolecular modes. The numerous less intense bands downshifted from the main are less strongly mixed and involve hydronium and water bends. The bands seen in theory and experiment at around 1760 cm^{-1} are noteworthy, as there is a feature at this energy in Zundel spectra,[6,9,17,18] which is also confirmed in the calculated Zundel spectra presented here. Since both Eigen and Zundel spectra have the intense band at 1760 cm^{-1}, the use of this feature as spectral marker for Zundel should be used with caution. The sharp bands, upshifted from the main band, are the assignable free water OH-stretches.

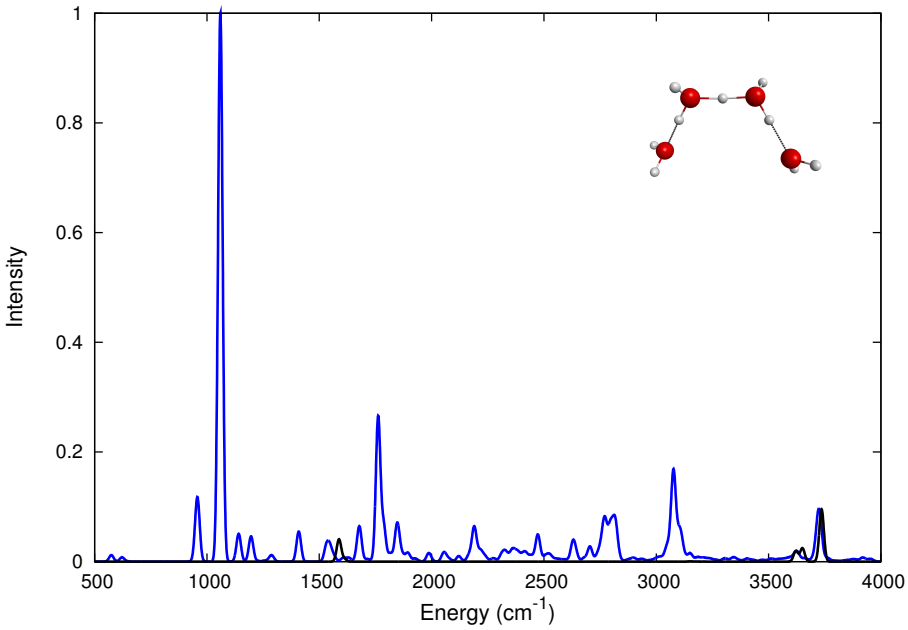

Figure 6.11 Calculated VSCF/VCI vibrational spectrum of the *cis*-Zundel isomer of $H_9O_4^+$, black lines are water bends and stretches calculated separately. See text for details

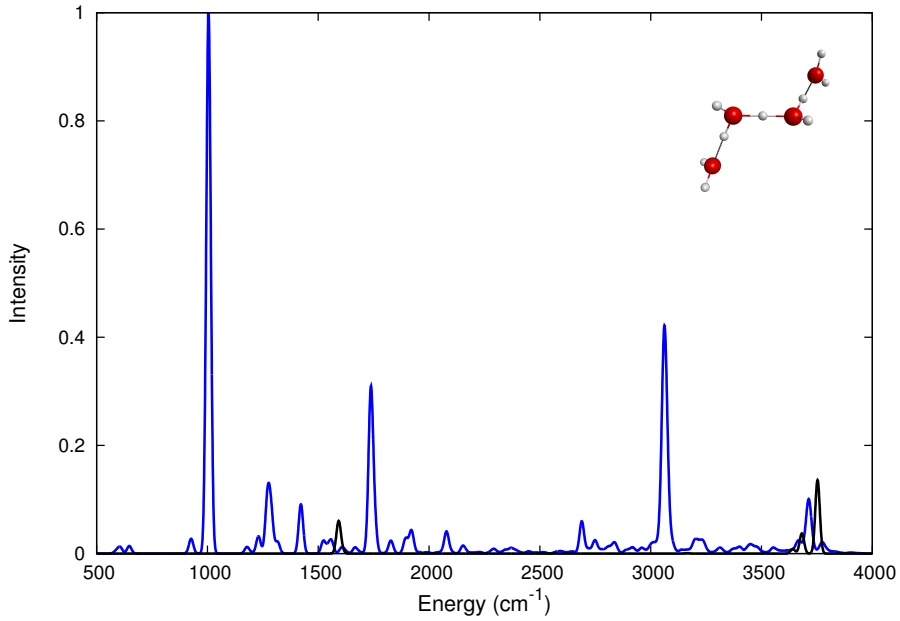

Figure 6.12 Calculated VSCF/VCI vibrational spectrum of the *trans*-Zundel isomer of $H_9O_4^+$, black lines are water bends and stretches calculated separately. See text for details.

Next consider the calculated IR spectra of the Zundel isomers shown in Figure

6.11-6.12. The signature band in these Zundel isomers are all found at around 1000 cm^{-1}, which is also consistent with the bare ($H_5O_2^+$) Zundel spectrum.[17,18] This brightest peak is associated with shared proton stretch, which does not show as strong coupling as the shared proton stretches in Eigen. The next feature of the Zundel isomers is the intense peak at 3100-3200 cm^{-1}. The contributing motions are two Zundel stretches, whose harmonic frequencies are around 3150 cm^{-1}. As seen in Table S3 and S4 in SI, these two Zundel stretches have very large double-harmonic intensity (same level as the proton stretches). However, due to the coupling with other low-frequency modes, in VSCF/VCI spectra, the intensity of this main feature is much lower than those of the proton stretches. Moreover, several states appear from 2500 cm^{-1} to 2800 cm^{-1}. These states do come from the complex combination bands involving low-frequency modes and bending modes, which have significant coupling with Zundel stretches. As to the bending region, Zundel isomers have a strong peak around 1760 cm^{-1} which is the main evidence used to identify Zundel isomers in experiment. However, it should be noted that the intensity of this Zundel bend feature is lower than the shared proton stretch at 1000 cm^{-1}. Thus, it seems that spectral features at around 1000, 1750 and 3200 cm^{-1}, should be used to identify the "Zundel" motif.

We next analyze the calculated spectrum of the ring isomer, shown in Fig 6.13. The structure of this ring isomer can be simply characterized as the H-bonded addition of a water molecule to the $H_7O_3^+$ cluster, forming the ring. Thus, the spectrum should contain signatures of $H_7O_3^+$ and water. Indeed, $H_7O_3^+$ features appear at four major bands at roughly 1450, 1750, 2000 and 3660 cm^{-1}, seen in experiment[4,14] and VSCF/VCI calculations.[11] The peaks at 1450 cm^{-1} and 1750 cm^{-1} are water and hydronium bends, which are mixed with the hydronium asym-stretch. The broad band around 2000 cm^{-1} has contribution from both hydronium asym- and sym- stretches. The peak at 3660 cm^{-1} is the hydronium free OH stretch. We stress that the peaks at

1450, 1750 and 2000 cm^{-1} all have significant contribution from hydronium stretches and their intensities are very sensitive to the corresponding VCI coefficients. Because of the strong coupling with low-frequency modes and bending modes, these states are not very bright comparing with the two hydronium stretches in the double-harmonic spectrum. Thus, the two water stretches at 3350 cm^{-1} become the brightest peaks in the calculated spectrum. It should be noted again that the spectra of ring isomer also has a feature in 1750 cm^{-1}.

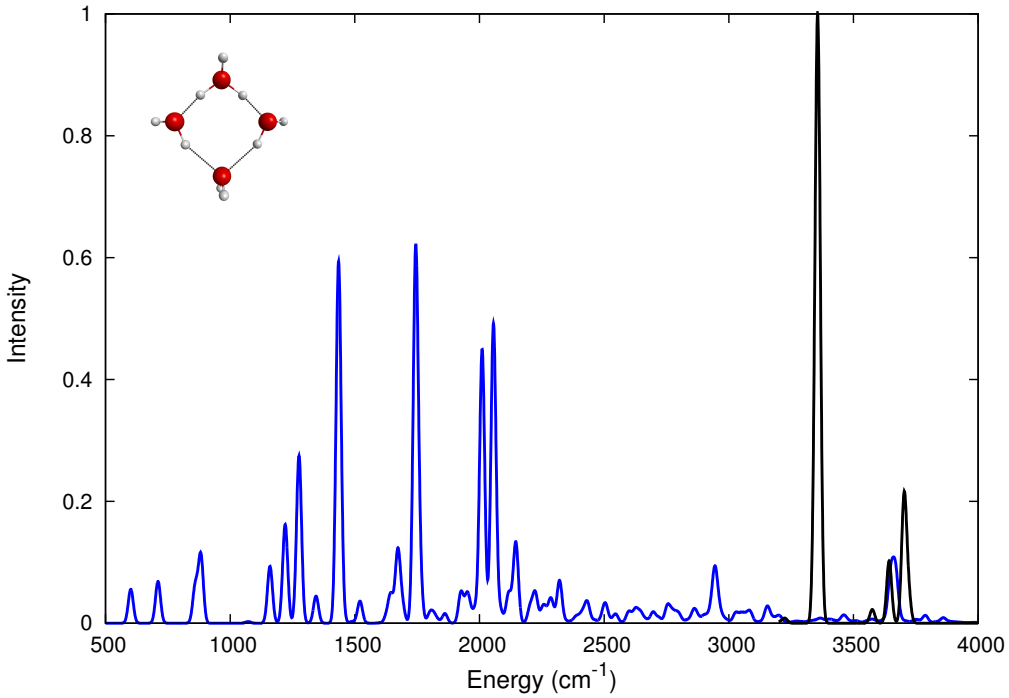

Figure 6.13 Calculated VSCF/VCI vibrational spectrum of the ring isomer of $H_9O_4^+$. Black lines are water stretches calculated separately. See text for details.

Finally, we present a comparison between VSCF/VCI Eigen and the experimental[8] IR spectra of $D_9O_4^+$ in Figure 6.14. Similar to Eigen $H_9O_4^+$, the major band at around 2000 cm^{-1} results from many highly-mixed states involving hydronium stretches, combination bands of frustrated D_3O^+ modes and water/hydronium bending modes. Comparing with the experiment, key features around 1700 cm^{-1} and several bands at 1300-1500 cm^{-1} are also seen in the calculated spectrum. The two

peaks around 1700 cm^{-1} are due to combination bands of hydronium rotation and water/hydronium bend, which are coupled with the bright hydronium asym-stretch. The hydronium and water bend fundamentals appear at 1200 cm^{-1}, in agreement with experiment. Finally, the weak, broad feature at roughly 2300 cm^{-1} is also reproduced by theory.

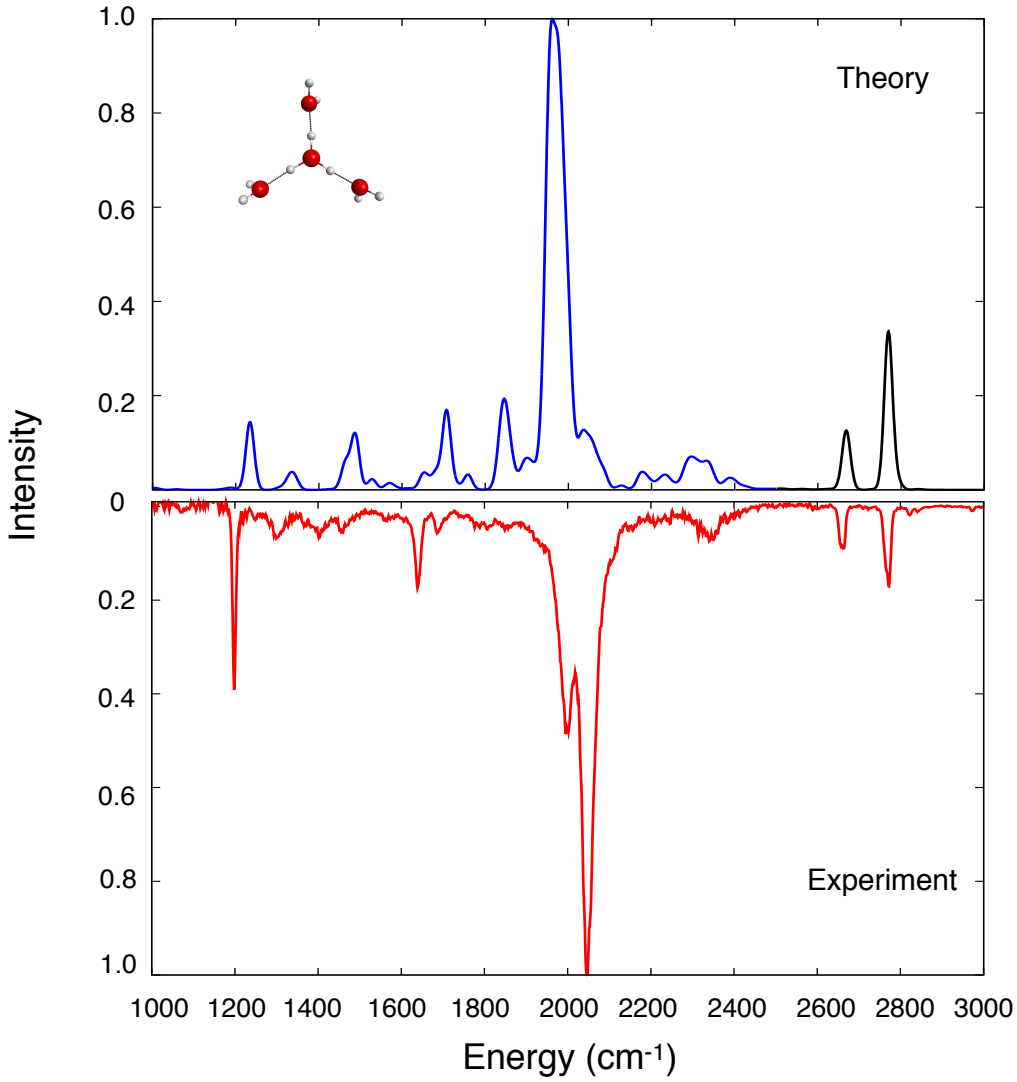

Figure 6.14 Calculated VSCF/VCI (Theory) and experimental[8] (Experiment) vibrational spectrum of the deuterated Eigen isomer of $D_9O_4^+$. Black lines are water stretches calculated separately. See text for details.

6.2.3 Conclusion

To summarize, the IR spectra of Eigen, *cis* and *trans* Zundel and ring isomers of $H_9O_4^+$ were reported, using VSCF/VCI methods and many-body, high-level potential energy and dipole moment surfaces. The calculated Eigen spectrum is in very good agreement with experiment for both $H_9O_4^+$ and $D_9O_4^+$. Spectra for the two Zundel and ring isomers show prominent bands that are not present in experiment, with the exception of an intense band around 1750 cm^{-1} for the Zundel isomers. However this band is also present in the calculated Eigen spectrum and so it alone is not sufficient to distinguish between the two. Distinguishing bands of the Zundel isomer are at roughly 1000 and 3100 cm^{-1} and for the ring isomer at roughly 3350 cm^{-1}. The calculated spectra of the Zundel and ring isomers can guide further experimental studies of this centrally important hydrated proton cluster.

Bibliography

[1] Agmon, N.; J., B. H.; Kramer, C. R.; H., H. R.; Peter, P.; Sylvie, R.; Martin, T.; Ali, H. *Chem. Rev.* **2016**, *116*, 7642–7672.

[2] Shin, J.-W.; Hammer, N. I.; Diken, E. G.; Johnson, M. A.; Walters, R. S.; Jaeger, T. D.; Duncan, M. A.; Christie, R. A.; Jordan, K. D. *Science* **2004**, *304*, 1137.

[3] Yeh, L. I.; Okumura, M.; Myers, J. D.; Price, J. M.; Lee, Y. T. *J. Chem. Phys.* **1989**, *91*, 7319.

[4] Headrick, J. M.; Diken, E. G.; Walters, R. S.; Hammer, N. I.; Christie, R. A.; Cui, J.; Myshakin, E. M.; Duncan, M. A.; Johnson, M. A.; Jordan, K. D. *Science* **2005**, *308*, 1765.

[5] Thämer, M.; De Marco, L.; Ramasesha, K.; Mandal, A.; Tokmakoff, A. *Science* **2015**, *350*, 78–82.

[6] Kulig, W.; Agmon, N. *Nat. Chem.* **2013**, *5*, 29–35.

[7] Douberly, G. E.; Walters, R. S.; Cui, J.; Jordan, K. D.; Duncan, M. A. *J. Phys. Chem. A* **2010**, *114*, 4570.

[8] Wolke, C. T.; Fournier, J. A.; Dzugan, L. C.; Fagiani, M. R.; Odbadrakh, T. T.; Knorke, H.; Jordan, K. D.; McCoy, A. B.; Asmis, K. R.; Johnson, M. A. *Science* **2016**, *354*, 1131–1135.

[9] Wang, H.; Agmon, N. *J. Phys. Chem. A* **2017**, *121*, 3056–3070.

[10] Yagi, K.; Thomsen, B. *J. Phys. Chem. A* **2017**, *121*, 2386–2398.

[11] Yu, Q.; Bowman, J. M. *J. Chem. Phys.* **2017**, *146*, 121102.

[12] Bowman, J. M.; Carter, S.; Huang, X. *Int. Rev. Phys. Chem.* **2003**, *22*, 533–549.

[13] Pinski, P.; Csányi, G. *J. Chem. Theory Comput.* **2014**, *10*, 68–75.

[14] Fournier, J. A.; Wolke, C. T.; Johnson, M. A.; Odbadrakh, T. T.; Jordan, K. D.; Kathmann, S. M.; Xantheas, S. S. *J. Phys. Chem. A* **2015**, *119*, 9425–9440.

[15] Christoffel, K. M.; Bowman, J. M. *Chem. Phys. Lett.* **1982**, *85*, 220–224.

[16] Yu, Q.; Bowman, J. M. *J. Phys. Chem. Lett.* **2016**, *7*, 5259–5265.

[17] Hammer, N. I.; Diken, E. G.; Roscioli, J. R.; Johnson, M. A.; Myshakin, E. M.; Jordan, K. D.; McCoy, A. B.; Huang, X.; Bowman, J. M.; Carter, S. *J. Chem. Phys.* **2005**, *122*, 244301.

[18] Vendrell, O.; Gatti, F.; Meyer, H.-D. *J. Chem. Phys.* **2007**, *127*, 184303.

6.3 Vibrational Spectra of the Protonated Water Trimer $H_7O_3^+$—Combined Experimental and Theoretical Study

6.3.1 Introduction

The vibrational spectra of the small protonated water clusters, $H^+(H_2O)n$, obtained using the messenger "tagging" technique[1] over the past three decades,[2–26] have yielded a microscopic picture of excess proton speciation within H-bonded water networks. One aspect of these spectra that is currently under discussion is the degree to which even the cold cluster spectra reflect large amplitude motions in both the (zero-point) ground and OH stretching vibrationally excited states.[27]In this regard, the smallest clusters, n = 2 to 6, provide the most intimate view of the interplay between the usual spectroscopic properties of H-bonds (red-shifts and intensity enhancement) and the special features associated with excess proton accommodation (vibrationally driven, inter-molecular proton transfer). Here we focus on the protonated water trimer, $H^+(H_2O)_3$, denoted 3H, with the calculated structure displayed in the top of Fig. 6.15. We are particularly interested in this cluster because it represents an intermediate case between the n = 2, $H^+(H_2O)_2$ Zundel ion,[28] which features an equally shared proton between two water molecules in the global minimum structure, and the Eigen form[29] of the n = 4 cluster in which the three water molecules largely play the role of neutral ligands bound to the H3O+ core ion. As such, the protonated trimer presents an interesting case where two protons in the hydronium core bind strongly to the two flanking water molecules with a HOH angle of 115.16° in Fig. 6.15, somewhat distorting them toward the pyramidal structure of the core H_3O^+ ion's 111.86° angle. Vibrational excitation of these H-bonded protons then occurs in a quasi-covalent regime, leading to a scenario where the ν= 1 OH stretch excited states adopt a partial inter-molecular proton transfer character as the shared protons approach the nearby water molecules. Such mechanics would, for example, be expected to result in strongly anharmonic effects in the vibrational spectra, and

indeed, many features in the reported spectra are not recovered at the harmonic level, as indicated by the comparison in Fig. 6.16

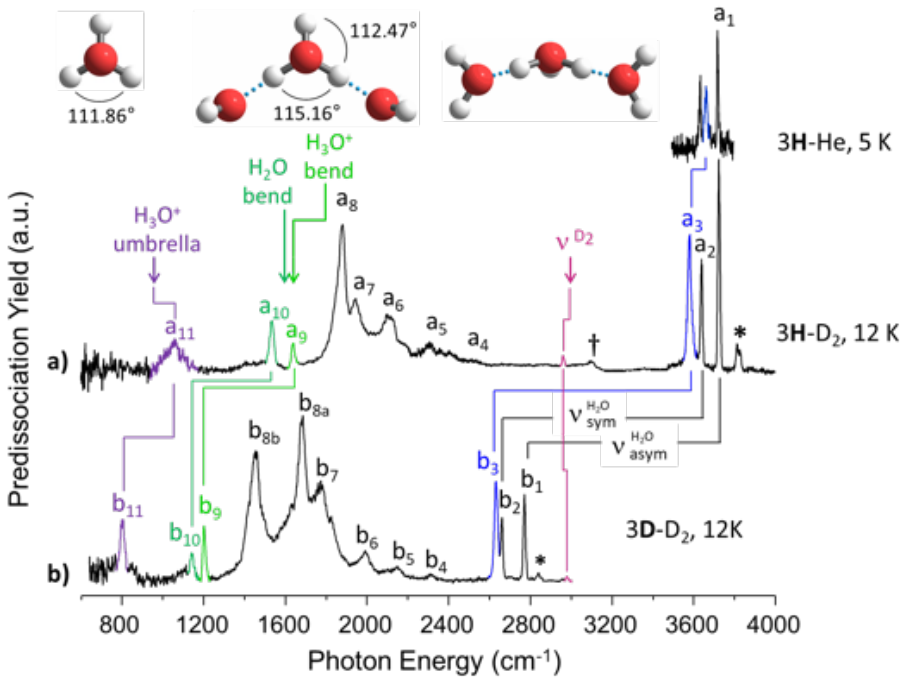

Figure 6.15 Vibrational predissociation spectra of (a) 3H-D_2 and (b) 3D-D_2 with the free OH region of 3H-He on top, where the 3H and 3D denote the $H^+(H_2O)_3$ and $D^+(D_2O)_3$ isotpologues and 3H-X denotes the complexes with X = He or D_2. Colored lines correspond to analogous vibrational modes of the isotopologues. 3H-He presents the least perturbed position of the free hydronium OH (blue). Arrows represent the fundamentals of the bare hydronium umbrella (purple) and bending (green) modes as well as that of the water bending mode (green). Band labels refer to features in the experimental spectra of 3H-D_2 and 3D-D_2, respectively. The minimum energy structure of 3H, computed at the CCSD(T)f12/aVTZ level, is presented in two orientations. A complete list of band positions and assignments is presented in Figure 6.19. $\nu_{sym}^{H_2O}$ and $\nu_{asym}^{H_2O}$ refer to the symmetric and antisymmetric stretches of the OH groups on the flanking water molecules.

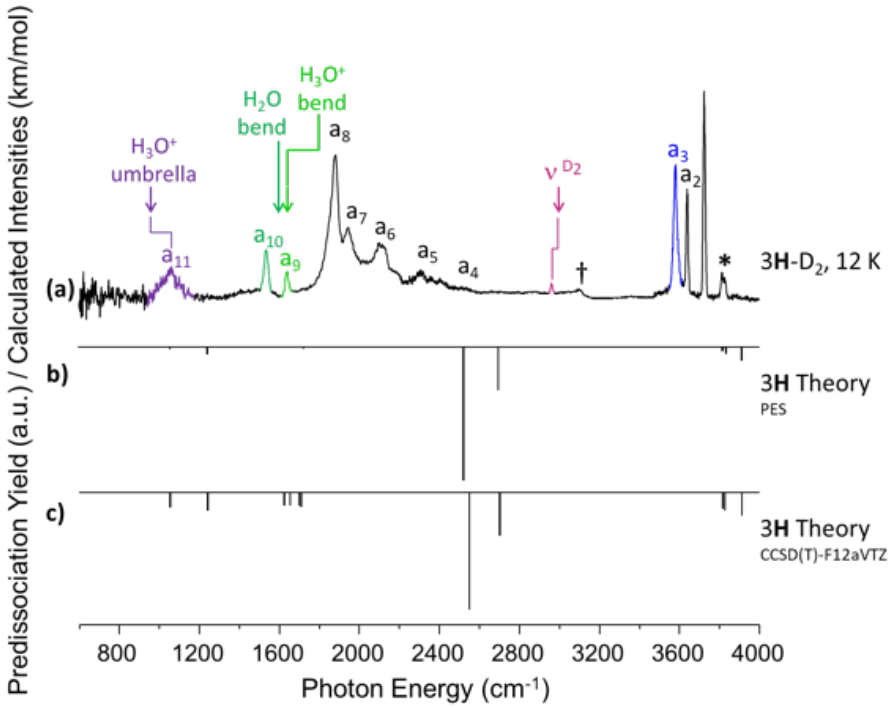

Figure 6.16 A comparison of 3H spectra (a) with harmonic spectra computed using the PES (b) and evaluated at the CCSD(T)-F12/aVTZ (c) levels of theory shown as inverted traces.

We begin this study by extending the previous survey of the spectrum of 3H-Ar,[17,30,31] to include the D_2-tagged spectra of both the $H^+(H_2O)_3$ and $D^+(D_2O)_3$ clusters (denoted 3H-D_2 and 3D-D2, respectively), with the results presented in Fig.6.15a and 1b. The umbrella mode of the embedded hydronium ion (a11) sharpens considerably upon deuteration (b11), similar to the behaviors found in the 4H and 4D spectra by Wolke et al.[9] There are also surprises, however, not anticipated by previous theoretical analysis, as we discuss further below. In particular, the strong band (a8) in the 3H spectrum, long assumed to be assigned to the antisymmetric stretch of the bound OH groups,[9] is replaced by a strong doublet (b8a and b8b) in the 3D spectrum. In addition, both spectra display a series of transitions towards higher energies of the dominant transitions, while strong bands (a10 and b10) appear below the intramolecular HOH bend fundamentals for isolated H2O (Ref. 32) and H3O+

(Ref. 33) (Fig.6.15a green arrows) that are presently unassigned. This behavior is particularly significant as “extra" features near the bending mode have presented a long-standing puzzle in the spectra of the n = 3-6 clusters, where they have been associated with both the bend and the ionic H-bonded OH (IHB) modes based on calculations at the harmonic level with and without inclusion of anharmonicity with a perturbative (VPT2) treatment.[34,35]

Very recently, high level vibrational self-consistent field methods combined with vibrational configuration interaction (VSCF/VCI) calculations have been carried out to map the extended potential energy and dipole moment surfaces associated with the 3H system.[36] These were benchmarked by comparing the spectrum computed from these quantities, displayed in Fig. 6.17.c, with the experimental 3H-Ar spectrum,[9] which is very similar to that obtained here with D_2-tagging. This computational approach indeed recovered the large (400 cm-1) red-shifts in the H-bonded OH stretching fundamentals relative to the CCSD(T)-F12 harmonic values and indicated that, as expected, the dominant band (a8 in Fig. 6.17.a) was primarily due to the antisymmetric stretch of the H-bonded OH groups. The progression of bands a5-a7 were then attributed to combination bands of the antisymmetric stretch with various soft modes, while the a10 feature was attributed to an exterior water bend that is strongly coupled to the H-bonded antisymmetric stretch. Given this relatively straightforward assignment scheme, however, the observation of a strong doublet (b8a and b8b) in the 3D isotopologue is unexpected (Fig. 6.17.f), as anharmonic fundamentals in this energy range typically follow a scaling of 1/1.23 or so upon deuteration.[37,38] Such mass-dependent complexities can arise, however, when modes couple as they become close in energy (e.g., Fermi resonances[39]). To understand the behavior of the 3D-D_2 spectrum, we extended these calculations to 3D using the same PES and dipole surfaces as those used for 3H, with the result presented in Fig. 6.17d. Surprisingly, the calculated pattern is again rather simple, consistent with a dominant band aris-

ing largely from the antisymmetric H-bonded OD (IDB) stretches, in contrast to the dominant doublet character of the observed spectrum. We next address two possibilities for this discrepancy: perturbation by the D2 tag molecules and/or some issues with the 3-body hydronium-water-water (3-b h-w-w) potential energy surface that was used in those VSCF/VCI calculations

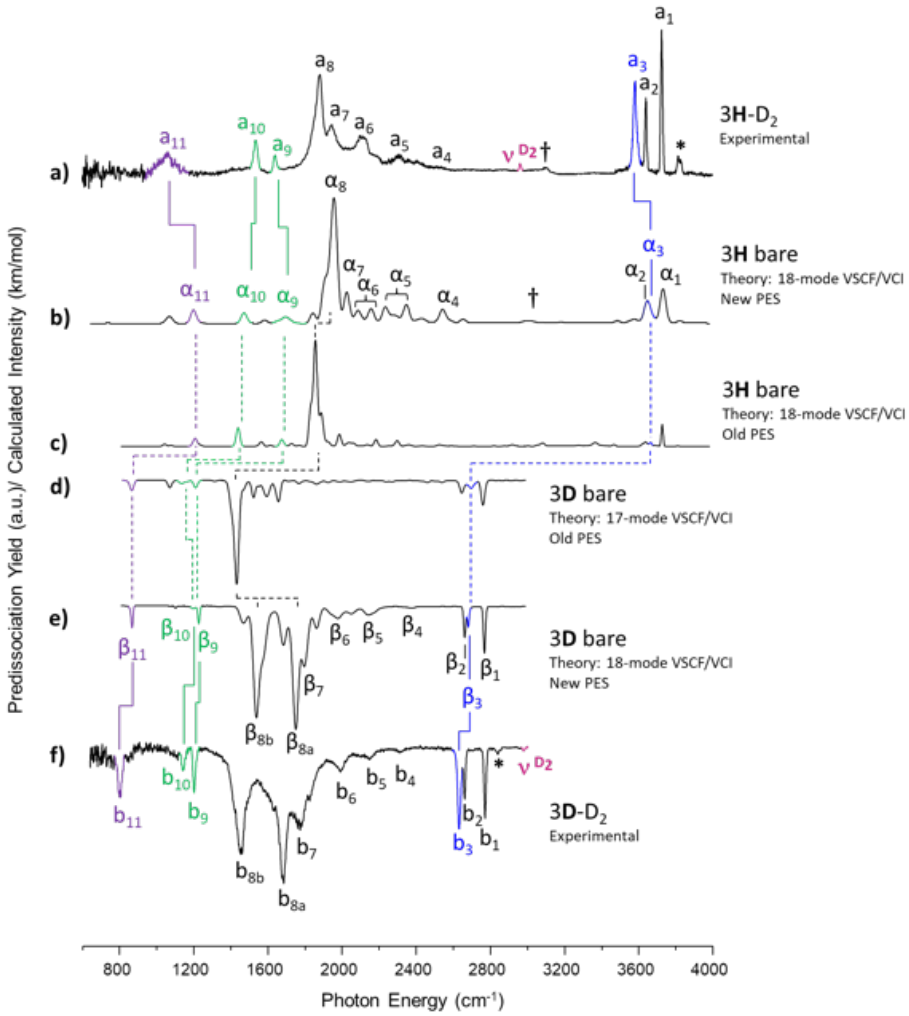

Figure 6.17 D_2 vibrational predissociation spectra of (a) 3H-D_2 and (f) 3D-D_2 with their corresponding anharmonic calculations. Traces (b) and (e) correspond to 18-mode VSCF/VCI calculations on an updated PES (see text), which are compared to 17- and 18-mode calculations (d,c) using the previously reported PES. Greek symbols (αn and βn) refer to significant features in the theoretical spectra after convolution with a standard Gaussian with FWHM of 15 cm-1 (see Figure 6.19). View Fig.6.15 caption for experimental peak labeling scheme.

Because high level calculations of the vibrational quantum structure can only be carried out on the bare protonated trimer, while the experimental results thus far have been reported with the messenger tagging (H_2, Ar and He) technique where the tags could perturb the spectrum, we undertook a study to obtain the spectrum of the cold, bare 3H cluster. The main experimental challenge in obtaining a tag-free spectrum is that the binding energy of the trimer (to $H^+(H_2O)_2 + H_2O$) is about 7000 cm^1,[40] which is much higher than the $<$3700 cm^{-1} energy range of the fundamentals. To observe the linear (e.g., one photon) spectrum of the cold ion, we adopted a variation of the two-color, IR-IR multiple photon dissociation (IR^2MPD) strategy recently reported by Niedner-Schatteburg and co-workers.[41] In particular, we applied it to cryogenically cooled ions prepared in the Yale triple focusing photofragmentation mass spectrometer, described in detail elsewhere.[1] In this application, photodissociation was carried out with selective photodissociation of ions excited with a single photon from a scanning laser h1 by two photons from a second laser fixed at h2 = 2900 cm^{-1} (see level diagram top of Fig. 6.18).

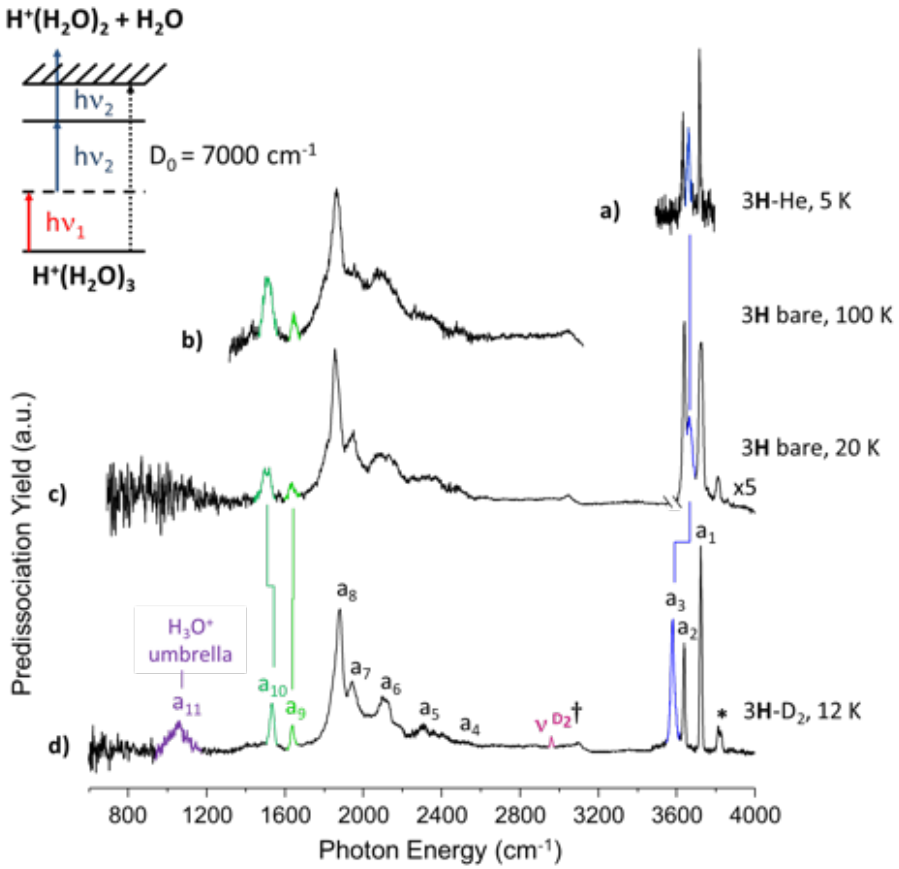

Figure 6.18 Comparison of the IR^{2}MPD spectrum of bare 3H at 100 K (b) and 20 K (c) with 3H-D_2 (d) and 3H-He (a). The level diagram of the IR^{2}MPD scheme used to collect the bare spectra (described in the text), where hÎ¡$_2$=2900 cmâĂŚ1, is top left. Temperatures indicate measurements taken from sensors mounted directly to the trap. See Fig. 6.15 caption for labeling scheme.

The 3H spectrum is compared with that of 3H-D_2 in Fig. 6.18.c and 6.18.d, respectively, along with the He-tagged spectrum of the high energy region in Fig. 6.18.a, reproduced from ref. 42. Most importantly, although the OH stretch of the hydronium bound to the D_2 tag (a3) is strongly shifted by about 90 cm^{-1},[43] the positions of the dominant features from 1400 to 2000 cm^{-1}, which correspond to the key intramolecular bends and H-bonded OH stretches, are not significantly affected by the D_2 tag. Specifically, the features (a7-10) in the 3H-D_2 and 3H spectra are at most displaced by 24 cm^{-1} (a10). Interestingly, the bands in both the D_2 and He-tagged 3H spectra are narrower than those in the IR^{2}MPD spectrum. This suggests

that the 3H ions are not cooled uniformly in the 3D Paul trap, which is expected for such a light ion.[44] Note that the free OH bands are the same in the He-tagged and bare 3H ion, where the disagreement is within the error of our experiment (3668 cm^{-1} $\pm$ 4 cm^{-1} for both the bare 3H-He and 3H), confirming that the weakly bound He tag does not significantly affect the spectroscopic properties of the 3H ion. It is also evident that the umbrella mode (a11) is not well developed in the bare ion spectrum compared to the D2 tag trace, which is consistent with this energy (1000 cm^{-1}) falling below the two-photon threshold for dissociation at h2 = 2900 cm^{-1} (where 1000 cm^{-1} + 2 x 2900 cm^{-1} < D_0). Although it is clear that temperature is only approximate in the current arrangement, we also obtained the spectra for bare 3H at trap temperatures of 20 and 100 K to explore how sensitive the band pattern is to increasing internal energy, with the 100 K results presented in Fig. 6.18.b. Like the $H^+(H_2O)_5$ case discussed earlier, the pattern is preserved, but broadens considerably with increasing temperature. This confirms the expectation that the 3H dynamics occur over a deep minimum in the potential surface at the equilibrium geometry. This is in contrast, for example, to the strongly temperature dependent spectrum of the $I^-(H_2O)_2$ ion, in which the spectra change markedly when the water dimer moiety breaks apart above 125 K.[45]

Application of the IR-IR method to the 3D isotopologue is more challenging because of the lower energies associated with the key ion-bound OD stretches and intramolecular bends. Nonetheless, we were able to obtain a sufficiently resolved spectrum, to establish that the basic doublet structure (b8a and b8b) is intact in the bare 3D ion. This, together with the minimal perturbation of the key bands in 3H by the D_2 tag, indicates that the discrepancy between the 3D spectrum calculated by extending the previous methods[36] (Fig. 6.17.d) and the experimental 3D-D_2 spectrum (Fig. 6.17.f) stems from either the potential surface or the VCI method itself rather than from tag perturbations. We next turn to the sensitivity of the calculated band

pattern to the details of the potential energy and dipole surfaces. The earlier PES was a simple fit to several hundred ab initio 3-b energies. Subsequently, we developed a new fit to 52067 CCSD(T)-F12/aVDZ ab initio 3-b electronic energies and repeated the VCI calculations with the results displayed in Fig. 6.17.b and 2e for 3H and 3D, respectively. Note that, while the character of the 3H spectrum is similar with the new PES, it now recovers the strong doublet in the 3D spectrum.[9]

The agreement with both isotopologues provides compelling evidence that subtle details in the PES are in play in this system, and indeed this raises the important question of what types of motions are actually involved in the observed bands. Of particular importance in this regard are, of course, the strongest bands in the fingerprint region, as well as the features appearing near the intramolecular bends. The latter are of particular interest as the lower energy members (a10 and b10) are suppressed in the 3D-D_2 spectrum. The VCI calculations with the new PES provide an unprecedented picture of the nature of the various absorptions, as it yields a description of the various vibrational eigenstates, $\Psi_\nu(E)$, as superpositions in a normal mode basis:

$$\Psi_\nu(E) = \sum_i C_i^{(\nu)} \prod_{j=1}^{3N-6} \psi^{(k_j)}(Q_j) \tag{6.2}$$

where $\psi^{(k_j)}(Q_j)$ is the normal mode basis for mode Q_j with k_j excitation, $C_i^{(\nu)}$ is the coefficients with i for index of tuples $(k_1, k_2, \cdots, k_{3N-6})$.

The results of this decomposition are included in Figure 6.19, which highlights the contributions to the strong absorptions. It is clear at a glance that the bands calculated to carry significant oscillator strength in the region nominally associated with the ion-bound OH groups are heavily mixed with a variety of background dark states. To emphasize the extent of this mixing, we use a participation number, P_ν, defined as:

$$P_\nu = \frac{1}{\sum_i |C_i^{(\nu)}|^4} \tag{6.3}$$

which ranges from 1.0 for a pure state at the harmonic level and increases as the

state becomes more dilute. Thus, most of the contributing vibrations in key energy regions close to the intramolecular bends involve complex motions distributed around the cluster. These states largely involve combination modes that act to break the H-bond such as rotation of the H_3O^+ ion both in and out of the O-O-O atom plane. In particular, the a8 feature is still dominated by the antisymmetric stretch, but the weight of the zero-order antisymmetric stretch state is only 0.25 for the most intense transition in this band. In both b8a and b8b the antisymmetric stretch is a “bright" contributor, but in b8a the frustrated hydronium rotation and perturbed hydronium bend mix with this state. In b8b, the other relevant modes are the perturbed hydronium wag and umbrella modes. Note that, although the 3H spectrum appears simpler, the strongest band (a8), is also calculated to result from a congested series of transitions to similarly mixed levels, as indicated in Figure 6.19. An important consequence of this analysis is that low order treatments commonly used by perturbation approaches (such as VPT2 as implemented in Gaussian09), will not even qualitatively reproduce the essential physics controlling the vibrational band pattern.

Label 3H-D_2	[a]Exp. 3H-D_2	Theory VSCF/VCI 3H Bare	[b]P 3H	Label 3D-D_2	[a]Exp. 3D-D_2	Theory VSCF/VCI 3D Bare	[b]P 3D	Assignment
*	3814, 3828			*	2840			H_2O antisym. stretch + H_3O^+ torsion[4]
a_1	3726	3748 } α_1	2.9	b_1	2770	2778 } β_1	5.1	Free O-H(D) antisym. $H(D)_2O$ stretch
a_2	3580	3664 } α_2	28	b_2	2631	2688 } β_2	6.7	Free O-H(D) $H(D)_3O^+$ stretch
a_3	3640	3658 } α_3	17	b_3	2660	2670 } β_3	17	Free O-H(D) sym. $H(D)_2O$ stretch
†	3102	3031	37					Complicated comb. band + IHB antisym. stretch
a_4	2410	2554 } α_4	21					O-O stretch + IHB antisym. + IHB symmetric stretch
				b_4	2314	2383 } β_4	NA	Combination band of D_3O^+ bend + water bend
ν^{D2}	2961			ν^{D2}	2978			D_2 stretch
a_5	2307	2364 } α_5	20					H_3O^+ wag + H_3O^+ umbrella + IHB antisym. stretch
				b_5	2149	2181 } β_5	19	Low freq. modes + IDB symmetric and antisym. stretches
a_6	2109	2098, } α_6	11					Low freq. modes + H_3O^+ bend + IHB antisym stretch,
		2166,	13					H_3O^+ rotation + H_2O bend + IHB symmetric stretch,
		2240,	9.7					H_3O^+ rotation + H_2O bend + IHB symmetric stretch,
		2246	5.8					H_3O^+ rotation + H_2O bend + IHB symmetric stretch
				b_6	1991	1980 } β_6	22	Low freq. modes + D_3O^+ rotation + wag + umbrella
a_7	1943	2034 } α_7	7.5					2ν H_3O^+ wag + IHB symmetric stretch
				b_7	1770	1802, } β_7	13	IDB symmetric stretch,
						1821,	2.6	IDB antisym. stretch,
						1868	3.7	IDB antisym. stretch
a_8	1878	1910, } α_8	3.5					3ν H_3O^+ rotation + H_3O^+ rotation + H_3O^+ umbrella + IHB antisym. stretch,
		1923,	5.6					O-O stretch + H_2O bend + IHB symmetric stretch,
		1942,	12					IHB antisym. stretch,
		1959,	5.1					IHB antisym. stretch,
		1960,	10					IHB antisym. stretch + H_3O^+ rotation + H_3O^+ umbrella,
		1974,	9.6					IHB antisym. stretch,
		1976	7.1					IHB antisym. stretch
				b_{8a}	1680	1674, } β_{8a}	3.0	D_3O^+ rotation + D_2O bend + IDB antisym. stretch,
						1690,	16.8	D_3O^+ rot + D_3O^+ bend + IDB antisym. stretch + IDB symmetric stretch,
						1691,	7.9	D_3O^+ rot + D_3O^+ bend + IDB antisym. stretch + IDB symmetric stretch,
						1725,	7.8	IDB antisym. stretch,
						1755,	6.8	IDB antisym. stretch + D_3O^+ rotation + D_3O^+ bend,
						1757,	6.7	D_3O^+ rotation + D_3O^+ bend + IDB antisym. stretch,
						1762	2.5	D_3O^+ rotation + D_3O^+ bend + IDB antisym. stretch,
				b_{8b}	1452	1467, } β_{8b}	2.2	Overtone of D_3O^+ wagging + IDB symmetric stretch,
						1488,	6.0	IDB antisym stretches,
						1541,	6.7	IDB wag + D_3O^+ umbrella,
						1554,	4.4	IDB antisym stretches,
						1578,	15	IDB antisym stretches,
						1584,	5.7	D_3O^+ rotation + D_3O^+ umbrella + IDB symmetric stretch,
						1593	8.7	IDB antisym stretches,
a_9	1639	1688, } α_9	9.3	b_9	1202	1230, } β_9	4.4	$H(D)_3O^+$ bend
		1701	9.9			1229	2.7	$H(D)_3O^+$ bend
a_{10}	1534	1477 } α_{10}	3.1					H_2O bend + IHB antisym. stretch
				b_{10}	1143	1191 } β_{10}	2.4	D_2O bend
a_{11}	1059	1202 } α_{11}	2.2	b_{11}	800	869 } β_{11}	1.8	$H(D)_3O^+$ umbrella
↓	954							Bare H_3O^+ umbrella[55]
↓	1595							Bare H_2O bend [34]
↓	1625.9, 1638.5							Bare H_3O^+ bend[35]
↓	2993.6							Bare D_2 stretch[56]

[a] Experimental frequencies are accurate within ± 4 cm^{-1}.

[b] The participation number P is calculated using the largest 3 coefficients, where $P = \sum \frac{1}{c_i^4}$.

Figure 6.19 Band assignments for tagged and bare 3H and 3D, compared to 18 mode VSCF/VCI calculations of the bare protonated water trimer. Note that IH(D)B refers to the hydrogen bonded OH(D) stretches

6.3.2 Conclusion

Since the detailed descriptions of the various states are rather complex, it is useful to step back and consider the situation from a more general perspective. The main conclusion is that, as the potential surface enables large amplitude motion along the H-bonded stretching degree of freedom, excitation of this motion necessarily couples this mode to bending distortions of both the H3O+ and flanking H2O molecules. Such coupling effectively provides a detailed, molecular level picture of friction associated with translocation of an excess proton. One aspect of this that has caused confusion in the literature, for example, is the origin of âĂIJextraâĂİ features that occur in the region of the intramolecular bends in the n=3-5 clusters,8, as well as the unusually high energy of the bending mode of the flanking water molecules in the Zundel ion, $H^+(H_2O)_2$. These features are most pronounced in the light isotopologues, and the VCI calculation of the 3H spectrum indicates that the a10 band, which falls about 60 cm^1 below the nominal bend fundamental of an isolated water molecule, is traced to a mixed state involving the bound OH stretches and the bends of the flanking water molecules. This effect appears to be amplified when the bound OH stretching frequency approaches the energy of the bend, and points to a mechanism for the activation of similar bands in the 4H and 5H spectra that have caused considerable controversy5,[46–48] in not only the assignments of the bands, but indeed the structures of the clusters. With this new understanding revealed through careful theoretical analysis integrated with experiment, a fruitful direction for further study of these systems will be to experimentally establish the character of the various bands. Extensions of the study to include measurements of the spectroscopic behavior of mixed isotopomers as well as the perturbations caused by increasingly strongly bound tag molecules12 appear likely avenues to accomplish this demanding task.

Bibliography

[1] Wolk, A. B.; Leavitt, C. M.; Garand, M. A., E.and Johnson *Acc. Chem. Res.* **2014**, *47*, 202–210.

[2] Okumura, M.; Yeh, L. I.; Lee, Y. T. *J. Chem. Phys* **1985**, *83(7)*, 3705–3706.

[3] Okumura, M.; Yeh, L. I.; Myers, J. D.; Lee, Y. T. *J. Chem. Phys* **1986**, *85*, 2328–2329.

[4] Fournier, J. A.; Johnson, C. J.; Wolke, C. T.; Weddle, G. H.; Wolk, A. B.; Johnson, M. A. *Science* **2014**, *344*, 1009–1012.

[5] Hammer, N. I.; Diken, E. G.; Roscioli, J. R.; Johnson, M. A.; Myshakin, E. M.; Jordan, K. D.; McCoy, A. B.; Huang, X.; Bowman, J. M.; Carter, S. *J. Chem. Phys.* **2005**, *122*, 244301.

[6] Mizuse, K.; Fujii, A. *Phys. Chem. Chem. Phys.* **2011**, *13*, 7129–7135.

[7] Mizuse, K.; Fujii, A. *J. Phys. Chem. Lett.* **2011**, *2*, 2130–2134.

[8] Mizuse, K.; Fujii, A. *J. Phys. Chem. A* **2012**, *116*, 4868–4877.

[9] Wolke, C. T.; Fournier, J. A.; Dzugan, L. C.; Fagiani, M. R.; Odbadrakh, T. T.; Knorke, H.; Jordan, K. D.; McCoy, A. B.; Asmis, K. R.; Johnson, M. A. *Science* **2016**, *354*, 1131.

[10] Heine, N.; Fagiani, M. R.; Asmis, K. R. *J. Phys. Chem. Lett.* **2015**, *12*, 2298–2304.

[11] Yeh, L. I.; Okumura, M.; Myers, J. D.; Price, J. M.; Lee, Y. T. *J. Chem. Phys.* **1989**, *91*, 7319.

[12] Okumura, M.; Yeh, L. I.; Myers, J. D.; Lee, Y. T. *J. Phys. Chem.* **1990**, *94*, 3416–3427.

[13] Jiang, J.-C.; Wang, Y.-S.; Chang, H.-C.; Lin, S. H.; Lee, Y. T.; Niedner-Schatteburg, G.; Chang, H.-C. *J. Am. Chem. Soc.* **2000**, *122*, 1398.

[14] Lin, C.-K.; Wu, C.-C.; Wang, Y.-S.; Lee, Y. T.; Chang, H.-C.; Kuo, J.-L.; Klein, M. L. *Phys. Chem. Chem. Phys.* **2005**, *7*, 938.

[15] Wu, C. C.; Lin, C. K.; Chang, H. C.; Jiang, J. C.; Kuo, J. L.; Klein, M. L. *J. Chem. Phys* **2005**, *122*, 074315.

[16] Shin, J.-W.; Hammer, N. I.; Diken, E. G.; Johnson, M. A.; Walters, R. S.; Jaeger, T. D.; Duncan, M. A.; Christie, R. A.; Jordan, K. D. *Science* **2004**, *304*, 1137.

[17] Headrick, J. M.; Diken, E. G.; Walters, R. S.; Hammer, N. I.; Christie, R. A.; Cui, J.; Myshakin, E. M.; Duncan, M. A.; Johnson, M. A.; Jordan, K. D. *Science* **2005**, *308*, 1765.

[18] Miyazaki, M.; Fujii, A.; Ebata, T.; Mikami, N. *Science* **2004**, *304*, 1134.

[19] Mizuse, K.; Fujii, A.; Mikami, N. *J. Chem. Phys* **2007**, *126*, 231101.

[20] Mizuse, K.; Mikami, N.; Fujii, A. *Angew. Chem. Int. Ed.* **2010**, *49*, 10119–10122.

[21] Mizuse, K.; Fujii, A. *Chem. Phys.* **2013**, *419*, 2–7.

[22] Douberly, G. E.; Ricks, A. M.; Duncan, M. A. *J. Phys. Chem. A* **2009**, *113*, 8449.

[23] Asmis, K. R.; Pivonka, N. L.; Santambrogio, G.; Brummer, M.; Kaposta, C.; Newmark, D. M.; Woste, L. *Science* **2003**, *299*, 1375–1377.

[24] Fagiani, M. R.; Knorke, H.; Esser, T. K.; Heine, N.; Wolke, C. T.; Gewinner, S.; Schollkopf, W.; Gaigeot, M.-P.; Spezia, R.; Johnson, M. A.; Asmis, K. R. *Phys. Chem. Chem. Phys.* **2016**, *18(38)*, 26743–26754.

[25] Fournier, J. A.; Wolke, C. T.; Johnson, C. J.; Johnson, M. A.; Heine, N.; Gewinner, S.; Schollkopf, W.; Esser, T. K.; Fagiani, M. R.; Knorke, H.; Asmis, K. R. *Proc. Natl. Acad. Sci. USA* **2014**, *111*, 18132–18137.

[26] Heine, N.; Fagiani, M. R.; Rossi, M.; Wende, T.; Berden, G.; Blum, V.; Asmis, K. R. *J. Am. Chem. Soc.* **2013**, *135*, 8266–8273.

[27] Craig, S. M.; Menges, F. S.; Duong, C. H.; Denton, J. K.; Madison, L. R.; McCoy, A. B.; Johnson, M. A. *Proc. Natl. Acad. Sci. USA* **2017**, *114*, E4706–E4713.

[28] Zundel, G.; Metzger, H. *Z. Phys. Chem.* **1968**, *58*, 225.

[29] Eigen, M. *Angew. Chem., Int. Ed. Engl.* **1964**, *3*, 1.

[30] Relph, R. A.; Guasco, T. L.; Elliott, B. M.; Kamrath, M. Z.; McCoy, A. B.; Steele, R. P.; Schofield, D. P.; Jordan, K. D.; Viggiano, A. A.; Ferguson, E. E.; Johnson, M. A. *Science* **2010**, *327*, 308–312.

[31] Fournier, J. A.; Wolke, C. T.; Johnson, M. A.; Odbadrakh, T. T.; Jordan, K. D.; Kathmann, S. M.; Xantheas, S. S. *J. Phys. Chem. A* **2015**, *119*, 9425–9440.

[32] Shimanouchi, T. *National Bureau of Standards.* **1972**, 1–160.

[33] Gruebele, M.; Polak, M.; Saykally, R. J. *J. Chem. Phys.* **1987**, *87*, 3347–3351.

[34] Headrick, J. M.; Bopp, J. C.; Johnson, M. A. *J. Chem. Phys.* **2004**, *121*, 11423.

[35] Diken, E. G.; Headrick, J. M.; Roscioli, J. R.; Bopp, J. C.; Johnson, M. A.; McCoy, A. B.; Huang, X.; Carter, S.; Bowman, J. M. *J. Phys. Chem. A* **2005**, *109*, 571.

[36] Yu, Q.; Bowman, J. M. *J. Chem. Phys.* **2017**, *146*, 121102.

[37] Gorlova, O.; DePalma, J. W.; Wolke, C. T.; Brathwaite, A.; Odbadrakh, T. T.; Jordan, K. D.; McCoy, A. B.; Johnson, M. A. *J. Chem. Phys.* **2016**, *145*, 134304.

[38] Horvath, S.; McCoy, A. B.; Roscioli, J. R.; Johnson, M. A. *J. Phys. Chem. A* **2008**, *112*, 12337–12344.

[39] Robertson, W. H.; Weddle, G. H.; Kelley, J. A.; Johnson, M. A. *J. Phys. Chem. A* **2008**, *106*, 1205–1209.

[40] Magnera, T. F.; David, D. E.; Michl, J. *Chem. Phys. Lett.* **1991**, *182*, 363–370.

[41] Nosenko, Y.; Menges, F.; Riehn, C.; Niedner-Schatteburg, G. *Phys. Chem. Chem. Phys.* **2013**, *15*, 8171–8178.

[42] Johnson, C. J.; Wolk, A. B.; Fournier, J. A.; Sullivan, E. N.; Weddle, G. H.; Johnson, M. A. *J. Chem. Phys.* **2014**, *140*, 221101.

[43] Kelleher, P. J.; Johnson, C. J.; Fournier, J. A.; Johnson, M. A.; McCoy, A. B. *J. Phys. Chem. A* **2015**, *119*, 4170–4176.

[44] Gerlich, D. *Acc. Chem. Res.* **1992**, *82*, 1–176.

[45] Wolke, C. T.; Menges, F. S.; Totsch, N.; Gorlova, O.; Fournier, J. A.; Weddle, G. H.; Johnson, M. A.; Heine, N.; Esser, T. K.; Knorke, H.; Asmis, K. R.; McCoy, A. B.; Arismendi-Arrieta, D. J.; Prosmiti, R.; Paesani, F. *J. Phys. Chem. A* **2015**, *119*, 1859.

[46] Yagi, K.; Thomsen, B. *J. Phys. Chem. A* **2017**, *121*, 2386–2398.

[47] Wang, H.; Agmon, N. *J. Phys. Chem. A* **2017**, *121*, 3056.

[48] Kulig, W.; Agmon, N. *J. Phys. Chem. B* **2014**, *118*, 278–286.

6.4 Deconstructing Prominent Bands in the Terahertz Spectra of $H_7O_3^+$ and $H_9O_4^+$: Intermolecular Modes in Eigen Clusters

6.4.1 Introduction

Recent ultrafast, infrared (IR) spectroscopic studies of excess protons in water have provided new insights into the nature of aqueous proton transfer, in general, and the role of Zundel- vs. Eigen-like motifs, particular.[1,2] The spectral diffusion associated with the characteristic IR absorptions of these local hydration motifs has been disentangled by gas-phase vibrational action spectroscopy on cold protonated water clusters $H^+(H_2O)n$, which directly correlates local distortions of the hydrogen-bonded network with vibrational frequencies in the mid- and near IR spectral regions as a function of the displacement of the transferring proton.[3] However, the characteristic spectral signatures of $H^+(H_2O)n$ clusters in the far-IR or terahertz region (<600 cm-1), namely intermolecular hydrogen-bond stretching and deformation modes[4–7] remain largely ill-characterized. IR photodissociation (IRPD) spectra in this spectral region, which require the intense and widely tunable radiation from an IR free electron laser, have only been reported for some of the larger (n>5) clusters,[8–10] but not for the prototypical Eigen ion, $H_3O^+(H_2O)_3$ itself. Such spectra are reported here for the first time. The IRPD spectra of small protonated water clusters,[3,8,10–20] especially the one for $H_9O_4^+$, have been the subject of numerous theoretical analyses,[3,10,17] 21-24 using VPT2 theory and also “on-the-fly" ab initio molecular dynamics simulations of the IR spectra (both using DFT or MP2 electronic energies) and with conflicting conclusions about whether the experimental spectra are for the Eigen[12,21] or Zundel[22] isomers. Recently, we reported many-body representations of the potential and dipole moment surfaces that are suitable for a variety of post-harmonic analyses.[13,23,24] The representation for the potential is based on the CCSD(T)-level of theory, currently the “gold standard" method. Details of the many-body representations of the poten-

tial energy and dipole moment surfaces and validation are given elsewhere.[13,24] They were recently used in coupled-mode VSCF/VCI quantum calculations, employing the exact Watson Hamiltonian, of the IR spectra of $H_7O_3^+$ and $H_9O_4^+$ to unambiguously confirm the original assignment11 that these ions exhibit Eigen-type (hydronium ion) cores (see Figure 6.20), i.e., they correspond to $H_3O^+(H_2O)_2$ (3E) and $H_3O^+(H_2O)_3$ (4E), respectively.

6.4.2 Computational Details

The IR spectra of $H_7O_3^+$ and $H_9O_4^+$ in the region 0 to 1200 cm^{-1} were calculated using a quasiclassical molecular dynamics (QCMD) approach to obtain the dipole-dipole correlation function, the Fourier transform of which provides the IR spectrum. For both $H_7O_3^+$ and $H_9O_4^+$, 100 trajectories were run for the QCMD spectra. Each trajectory was integrated for 12 ps, and the step size is 0.06 fs. We used a modified normal mode sampling to prepare the initial conditions of the trajectories. Zero-point energy was assigned to all the intermolecular modes as well as the umbrella mode of the H_3O^+, in both cases. We didn't put any energy in other intramolecular modes. The total angular momentum was set to zero. Then the trajectories were propagated using the velocity-Verlet algorithm. The dipole moment was calculated at each step using the instantaneous configuration, and the dipole correlation function was calculated as $C(t) = \langle \mu(t) \cdot \mu(0) \rangle$, where the brackets indicate an average over 100 trajectories of the same total energy. Then C(t) was Fourier transformed to obtain the IR spectra. Note these are not thermal spectra, but microcanonical ones. More details of driven molecular dynamics are given in supporting information in ref. **?**

The QCMD approach we take is a minor modification of the procedure described by Van-Oanh et al.,25 where zero-point energy is given initially to each normal mode of a molecule. This approach is widely used in reaction dynamics, where it is referred to as the quasiclassical approach and so we use that terminology here. It is well-known

that this approach suffers from “zero-point leak", because it is actually an approximate semi-classical quantization procedure and thus mode-mode energy transfer can occur. (This “leak" would in principle be eliminated if exact semi-classical quantization of the zero-point state was done.) The energy transfer from high-frequency intramolecular modes to low-frequency intermolecular ones can result in rapid dissociation of the molecule/complex. To mitigate this rapid dissociation, we apply the approximate quasiclassical quantization to intermolecular modes only and give zero energy initially to the intramolecular modes.

6.4.3 Results and Discussion

Here, we present the IRPD spectra of the cryogenically-cooled, D_2-tagged protonated water trimer, $H^+(H_2O)_3$-D_2, denoted as 3H-D_2, and tetramer, $H^+(H_2O)_4$-D_2 (4H-D_2), in the spectral region 210-2200 cm^{-1}. Tagging is required to probe the linear absorption regime and D_2 was chosen to mitigate well-documented tagging issues. We conclusively assign the spectral features to hydrogen-bond stretching as well as water wagging modes based on anharmonic calculations using the high-level potential and dipole moment surfaces mentioned above. These calculations include the previous VSCF/VCI ones in the spectral range above 1000 cm^{-1} and quasiclassical molecular dynamics (QCMD) calculations, described below, for the spectral range below 1000 cm^{-1}. Unfortunately, in this range the quantum approach becomes prohibitively difficult, as the large-amplitude, torsional motion of the flanking waters is poorly described by the Watson Hamiltonian. Classical MD simulations of IR spectra for low frequency modes are expected to be a substantial improvement over double harmonic oscillator (DHO) ones, as has been amply demonstrated in the literature, and also here. Addition of zero-point energy may also improve MD spectra[24,25] and so that is done here, but only for the intermolecular modes. This approach is essentially the well-known quasiclassical one, used in reaction dynamics calculations and

so we used the term “quasiclassical" molecular dynamics above. Some analysis of the QCMD spectra is done using Driven Molecular Dynamics (DMD), which is the mechanical analog of the classical interaction of an external oscillating electric field with the molecular dipole. Finally, rigorous diffusion Monte Carlo calculations are done for the zero-point wavefunctions for the trimer and tetramer. These are shown, without comment, in Figure 6.20.

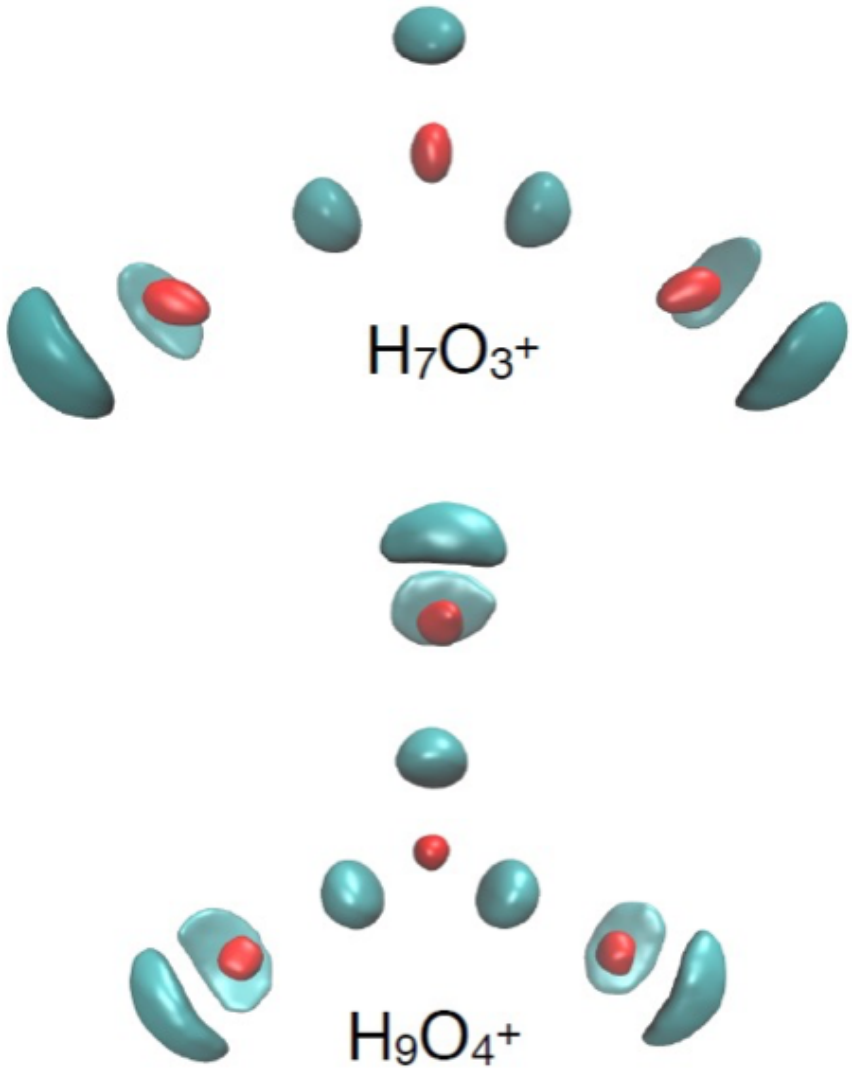

Figure 6.20 Isosurface plots of the ground vibrational wavefunctions of $H^+(H_2O)_3$ (3E) and $H^+(H_2O)_4$ (4E) obtained from diffusion Monte Carlo calculations. Red represents the O nuclei and green the H nuclei.

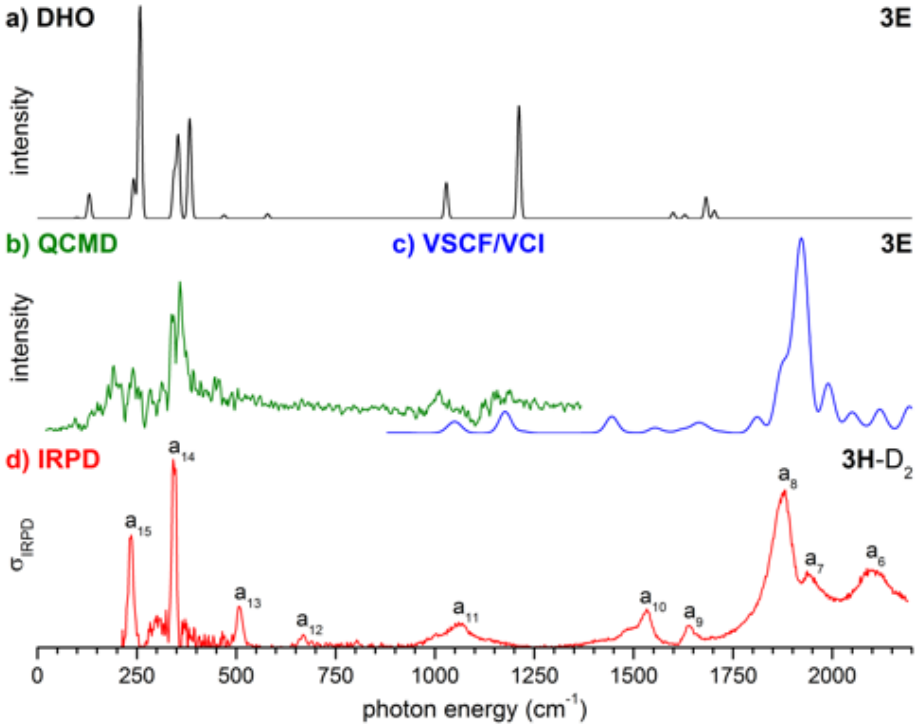

Figure 6.21 Comparison of the calculated (a) double-harmonic (DHO), (b) QCMD and (c) VSCF/VCI vibrational spectra of 3E to the (d) experimental IRPD spectrum of 3H-D_2 in the spectral region from 0 to 2200 cm^{-1}. See Figure 6.22 for band positions and assignments. The calculated DHO and VSCF/VCI spectra were convoluted with Gaussian line shape functions with a fwhm width of 10 and 30 cm^{-1}, respectively

Label	IRPD	IRPD[a]	HO	VSCF/VCI[a]	QCMD	Assignment[b]
a_6	2100	2109		2098-2246		low freq. modes + H_3O^+ bend + IHB antisym. stretch, H_3O^+ frust. rotation + H_2O bend + IHB sym. stretch
a_7	1942	1943	2692	2034		2v H_3O^+ wag + IHB sym. stretch
a_8	1875	1878	2518	1910-1976		IHB antisym stretch, H_3O^+ frust. rotation + H_3O^+ umbrella + IHB antisym. stretch,
a_9	1640	1639	1721,1743	1688,1701		H_3O^+ bend
a_{10}	1533	1534	1636,1666	1477		H_2O bend + IHB antisym. stretch
a_{11}	1060	1059	1240 1051	1202 1081	1176 1015	H_3O^+ umbrella H_3O^+ wag
a_{12}	668		593			H_3O^+ frust. rotation
a_{13}	508		479		456	comb of low freq. modes
a_{14}	344		390 362 351		355	antisym. HB-stretch (H_3O^+ rattle) sym. HB-stretch H_2O rock
a_{15}	234		264 247		241	H_2O wag

Figure 6.22 Experimental IRPD band positions (in cm^1) of 3H-D_2, computed harmonic (HO), VSCF/VCI and QCMD vibrational wavenumbers (in cm^1) of 3E and assignments.

The experimental IRPD spectrum of 3H-D_2 in the spectral range 210 to 2200 cm^{-1} is compared to the DHO, QCMD spectra and previous VSCF/VCI calculations above 900 cm^{-1} of (bare) 3E in Figure 6.21. Experimental band positions and assignments, based on calculations, are listed in Figure 6.22. The IRPD spectrum reveals (at least) ten features, labeled with a6 to a15 (see ref.[13] for bands a1 to a5). Bands a6-a11 agree satisfactorily with the previously published data for 3H-D_2 by Duong et al..[13] Minor discrepancies with respect to relative intensities are observed for a6 and the low-energy shoulder of a10, which may be attributed to the slightly different conditions in the two experiments. Features a12 to a15 have not been previously reported and, in particular, the three prominent bands at 508 cm^{-1} (a13), 344 cm^{-1} (a14) and 234 cm^{-1} (a15) correspond to the first experimental observation of transitions involving the intermolecular water modes in the protonated water trimer.

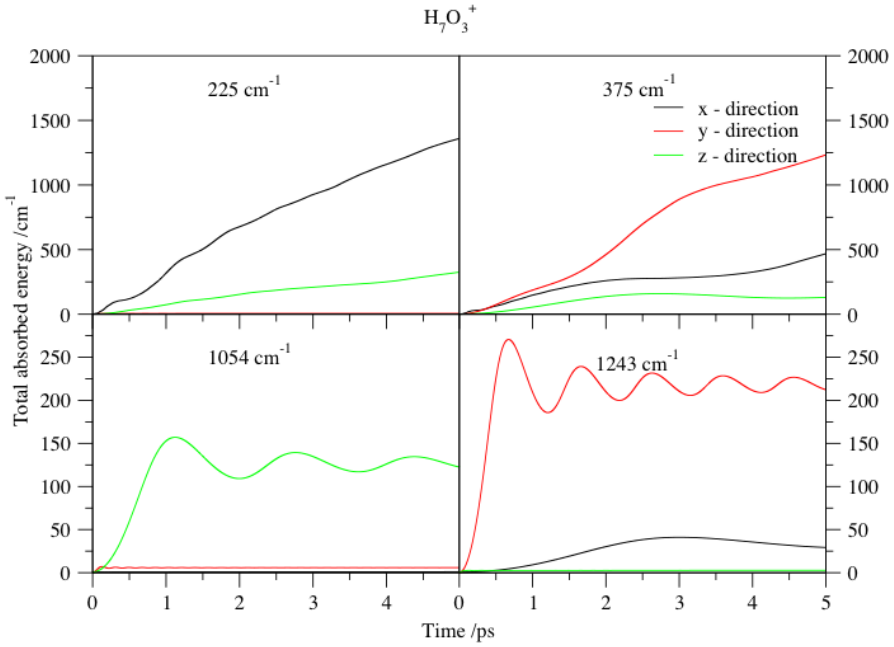

Figure 6.23 Total energy absorbed vs time for H7O3+ at the indicated driving frequencies

As usual, we turn to theory to assign/interpret experiment, with a specific focus on the new experimental bands. First, consider the DHO spectrum, which does have a single intense band and a higher-energy doublet in the range of experimental bands a15 and a14. However, there are other strong bands in the DHO spectrum that are not present in experiment and vice versa. Clearly then, DHO is not reliable, or at least not globally reliable. By contrast, the QCMD spectra are in good agreement with experiment over the expected range of applicability of these spectra and beyond that range the VSCF/VCI spectrum continues the good agreement with experiment. The QCMD spectra was analyzed using DMD and the results, are that for the bands around 241 and 355 cm^{-1} the energy absorption continues monotonically, as seen in Fig. 6.23. This is an indication from DMD that these are intense bands, in agreement with the QCMD results (and also the DHO ones) and experiment. By contrast, the energy absorbed stops for the two intense DHO bands at 1051 and 1240 cm^{-1} (see Figure 6.22), indicating that these are in fact weak absorbers. This agrees with the

QCMD spectrum and also experiment; however, not with the DHO results. Finally, we note that there are no DHO peaks in the spectral range 1750-2200 cm^{-1}, in contrast to experimental and VSCF/VCI spectra.

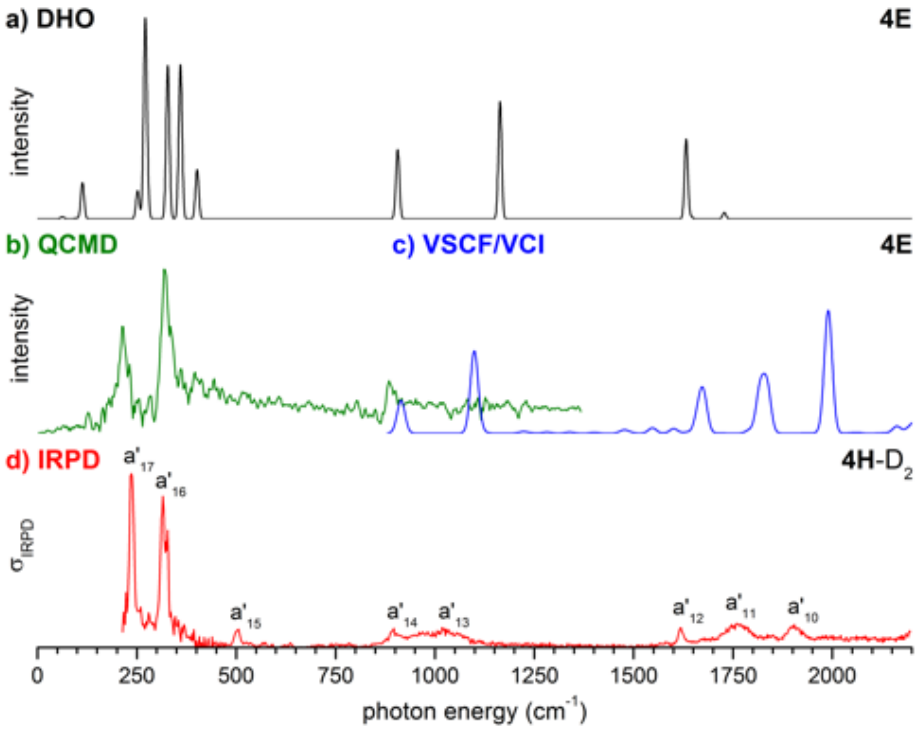

Figure 6.24 Comparison of the calculated (a) double-harmonic (DHO), (b) QCMD and (c) VSCF/VCI vibrational spectra of 4E to the (d) experimental IRPD spectrum of 4H-D_2 in the spectral region from 0 to 2200 cm^{-1}. See Figure 6.25 for band positions and assignments. The calculated DHO and VSCF/VCI spectra were convoluted with Gaussian line shape functions with a fwhm width of 10 and 30 cm^{-1}, respectively

Label	IRPD	IRPD[a]	HO	VSCF/VCI[b]	QCMD	Assignment[c]
a_{10}'	1898	1909		2033		H_3O^+ umbrella + H_3O^+ wag
a_{11}'	1760	1770		1859,1877		overtone H_3O^+ wag, comb 2 H_3O^+ wag
a_{12}'	1615	1615	1669-1768	1712		H_3O^+ and H_2O bends
a_{13}'	1014		1190	1124	1154	H_3O^+ umbrella
a_{14}'	894		928	937	910	H_3O^+ wag
a_{15}'	503					comb of low freq. modes
a_{16}'	316		335-411		331	antisym. HB - stretch (H_3O^+ rattle)
a_{17}'	236		258-284		216	sym. HB - stretch H_2O wag

Figure 6.25 Experimental IRPD band positions (in cm^1) of 4H-D_2, computed harmonic (HO), VSCF/VCI and QCMD vibrational wavenumbers (in cm^1) of 4E and assignments

The experimental IRPD spectrum of 4H-D_2 in the spectral range from 210 to 2200 cm^{-1} is compared to the DHO and QCMD spectra of bare 4E in Figure 6.24. Band positions and assignments are listed in Figure 6.25. The IRPD spectrum shows eight bands (a10'-a17') in total, with two characteristic and intense IR bands and a weaker feature in the far IR region at 316 cm^{-1} (a16'), 236 cm^{-1} (a17') and 503 cm^{-1} (a15'). Bands a10'-a14' agree satisfactorily with the previously reported spectrum of 4H-D_2 by Wolke et al..[3] Minor discrepancies with respect to band maxima (-10 cm^{-1}) of a10' and a11' are observed and due to slightly different band profiles. We first discuss the assignments of the prominent experimental bands labeled a17' and a16'. By examining trajectories that correspond to these, the intensity of band a17' is due to mainly "wagging" motion of the flanking H_2O molecules and for band a16' it is the embedded H_3O^+ hydrogen bond stretching (or "H_3O^+ rattle") mode that is the dominant motion. In both cases there is evidently a large change in the dipole moment. This is worth investigating in detail and this is done in Figure 6.26, where the components of the full dipole moment are plotted along with the component from the above many-body representation of the dipole moment, as a function of the corresponding intermolecular normal mode corresponding closest to the quasiclassical

motion. Even though this normal mode may not be as accurate a description of the QC motion, it suffices for this qualitative explanation of the intensity. In the upper panel, for the wagging motion, we see that the sum of the 1-b water+water dipole tracks the full dipole nearly exactly as a function of Q. The magnitude is less but the derivative is nearly identical and so we are safe in assigning the intensity to the change in the sum of the water monomer dipole moments. The lower panel shows a more complex picture for the dipole moment for band a16'; however, it is clear that change in the 1-body hydronium dipole plus the 2-b hydronium water dipole moment are the main contributors to the intensity. This picture is not as obvious as the one for the wagging of the flanking water; however, it results from coupling of the hydronium and the water intermolecular modes, in this case the H_3O^+ hydrogen bond stretch mode.

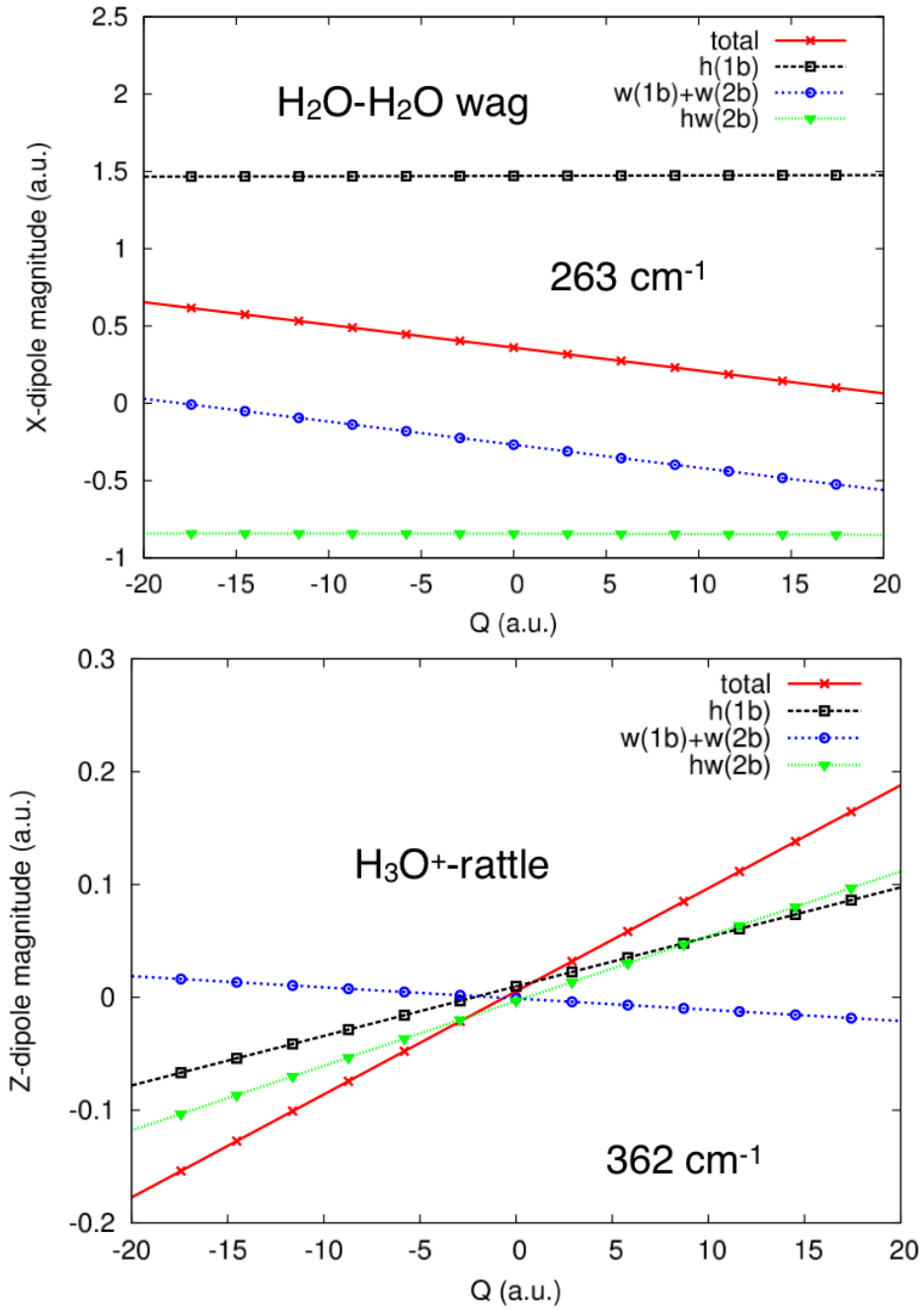

Figure 6.26 Normal mode dependence of the major component of the dipole moment for bands a15 and a14 of 3E. See text for details.

Comparison of the intense bands below 800 cm^{-1} with those observed in-between 800 and 2100 cm^{-1} in the IRPD spectra of 3H-D_2 and 4H-D_2 reveals that the lower frequency bands are considerably narrower, exhibiting fwhm widths of 15 cm^{-1}, similar (a) to the bands found in the free O-H stretching region as well as (b) to the

corresponding bands in the spectra of 5H-D_2 and 6H-H_2. The QCMD results predict broader band profiles for a13/a14 (3E) and a16'/a17' (4E), but these bands from theory do show some sensitivity to the energy of the trajectories; this is typical of MD approaches. We find no evidence that this narrowness originates from multiphoton absorption effects. We employed modest laser pulse energies (<1 mJ below 500 cm^{-1}) and estimates of the dissociation limit, when zero-point and internal energies are considered, support that single photon photodissociation is feasible. Tagging effects should also not alter the band widths dramatically, but probably do contribute to the deviations regarding the band positions and relative intensities. However, because the spectra in the THz region are highly anharmonic and coupled, the numerical values of the shifts should not be taken as accurate. Summarizing, the intermolecular stretching and wagging frequencies appear surprisingly insensitive to the inherent floppiness of these hydrogen-bonded ions.

n	Experiment
3	344
4	316
5[a]	405/298
6[b]	373/279
21[c]	341
∞[d]	~340

Figure 6.27 Evolution of the band positions (in cm^{-1}) of the IR-active hydrogen-bond stretching vibrations associated with the H_3O^+ core in the experimental IR spectra of protonated water clusters $H^+(H_2O)n$ with cluster size n up to the condensed phase limit. a. Ref,[10] b. Ref,[8] c. Ref,[9] d. Ref[7]

Finally, it is of interest to discuss, how the present values for the IR-active low-

frequency modes compare to those in larger protonated water clusters and in solution (see Figure 6.27). The Eigen ion 4E exhibits twelve vibrational normal modes in the terahertz spectral region (<600 cm^{-1}), which correspond to frustrated translations and rotations of the flanking water molecules. These are, in order of decreasing frequency, the three hydrogen bond stretching, three water wagging, three water rocking and three hydrogen bond deformation (bending) modes. Each set consists of a symmetric and a doubly degenerate antisymmetric combination, of which only the antisymmetric hydrogen bond stretching and water wagging modes carry significant IR intensity. These are observed at 316 and 236 cm^{-1}, respectively, in the spectrum of 4H-D_2. Removal of one of the flanking water leads to 3E with only single antisymmetric stretching and wagging modes (3H-D_2: 344 cm^{-1} and 234 cm^{-1}, respectively). While it proves difficult to unambiguously identify the wagging modes of the flanking water molecules in larger water clusters, due to their delocalized nature over an increased number of water molecules, the respective hydrogen-bond stretching modes involving the embedded H_3O^+ can be traced all the way to the solution phase data (see Figure 6.27). The asymmetrically solvated H_3O^+ in 5E and 6E results in a splitting of the IR-active (antisymmetric) hydrogen bond stretches, one that is blue-shifted in the spectra of 5H-D_2 (405 cm^{-1})10 and 6H-D_2 (373 cm^{-1}) and another that is red-shifted (5H-D_2: 298 cm^{-1}, 6H-D_2: 279 cm^{-1}), with respect to their position in the 4H-D_2 spectrum. This yields mean frequencies for these modes of 351 cm^{-1} (n=5) and 326 cm^{-1} (n=6). At n=21, H_3O^+ is more symmetrically solvated again and the 21H-D_2 spectrum9 features a single, prominent broad IR-active band at 341 cm^{-1}, very close to the solution value of 340 cm^{-1}. Summarizing, the mean frequencies of the IR-active hydrogen-bond stretching modes involving the hydronium core in protonated water clusters lie in a narrow spectral window (310-360 cm^{-1}) and seem to have converged close to the bulk value of 340 cm^{-1} (n=∞) already for n=21, suggesting a rather localized nature of these modes.

Bibliography

[1] Thämer, M.; De Marco, L.; Ramasesha, K.; Mandal, A.; Tokmakoff, A. *Science* **2015**, *350*, 78–82.

[2] Dahms, F.; Fingerhut, B. P.; Nibbering, E. T. J.; Pines, E.; Elsaesser, T. *Science* **2017**, *495*, 491–495.

[3] Wolke, C. T.; Fournier, J. A.; Dzugan, L. C.; Fagiani, M. R.; Odbadrakh, T. T.; Knorke, H.; Jordan, K. D.; McCoy, A. B.; Asmis, K. R.; Johnson, M. A. *Science* **2016**, *354*, 1131.

[4] Braly, L. B.; Liu, K.; Brown, M. G.; Keutsch, F. N.; Fellers, R. S.; Saykally, R. J. *J. Chem. Phys.* **2000**, *112*, 10314–10326.

[5] Keutsch, F. N.; Saykally, R. J. *Proc. Natl. Acad. Sci. USA* **2001**, *98*, 10533–10540.

[6] Saykally, R. J.; Wales, D. J. *Science* **2012**, *336*, 814–815.

[7] Decka, D.; Schwaab, G.; Havenith, M. A. *Phys. Chem. Chem. Phys.* **2015**, *17*, 11898–11907.

[8] Heine, N.; Fagiani, M. R.; Rossi, M.; Wende, T.; Berden, G.; Blum, V.; Asmis, K. R. *J. Am. Chem. Soc.* **2013**, *135*, 8266–8273.

[9] Fournier, J. A.; Wolke, C. T.; Johnson, C. J.; Johnson, M. A.; Heine, N.; Gewinner, S.; Schollkopf, W.; Esser, T. K.; Fagiani, M. R.; Knorke, H.; Asmis, K. R. *Proc. Natl. Acad. Sci. USA* **2014**, *111*, 18132–18137.

[10] Fagiani, M. R.; Knorke, H.; Esser, T. K.; Heine, N.; Wolke, C. T.; Gewinner, S.; Schollkopf, W.; Gaigeot, M.-P.; Spezia, R.; Johnson, M. A.; Asmis, K. R. *Phys. Chem. Chem. Phys.* **2016**, *18(38)*, 26743–26754.

[11] Douberly, G. E.; Walters, R. S.; Cui, J.; Jordan, K. D.; Duncan, M. A. *J. Phys. Chem. A* **2010**, *114*, 4570.

[12] Fournier, J. A.; Wolke, C. T.; Johnson, M. A.; Odbadrakh, T. T.; Jordan, K. D.; Kathmann, S. M.; Xantheas, S. S. *J. Phys. Chem. A* **2015**, *119*, 9425–9440.

[13] Duong, C. H.; Gorlova, O.; Yang, N.; Kelleher, P. J.; Johnson, M. A.; McCoy, A. B.; Yu, Q.; Bowman, J. M. *J. Phys. Chem. Lett.* **2017**, *8*, 3782–3789.

[14] Okumura, M.; Yeh, L. I.; Myers, J. D.; Lee, Y. T. *J. Chem. Phys* **1986**, *85*, 2328–2329.

[15] Jiang, J.-C.; Wang, Y.-S.; Chang, H.-C.; Lin, S. H.; Lee, Y. T.; Niedner-Schatteburg, G.; Chang, H.-C. *J. Am. Chem. Soc.* **2000**, *122*, 1398.

[16] Asmis, K. R.; Pivonka, N. L.; Santambrogio, G.; Brummer, M.; Kaposta, C.; Newmark, D. M.; Woste, L. *Science* **2003**, *299*, 1375–1377.

[17] Headrick, J. M.; Diken, E. G.; Walters, R. S.; Hammer, N. I.; Christie, R. A.; Cui, J.; Myshakin, E. M.; Duncan, M. A.; Johnson, M. A.; Jordan, K. D. *Science* **2005**, *308*, 1765.

[18] Mizuse, K.; Fujii, A. *Phys. Chem. Chem. Phys.* **2011**, *13*, 7129–7135.

[19] Mizuse, K.; Fujii, A. *J. Phys. Chem. A* **2012**, *116*, 4868–4877.

[20] Heine, N.; Fagiani, M. R.; Asmis, K. R. *J. Phys. Chem. Lett.* **2015**, *12*, 2298–2304.

[21] Yagi, K.; Thomsen, B. *J. Phys. Chem. A* **2017**, *121*, 2386–2398.

[22] Wang, H.; Agmon, N. *J. Phys. Chem. A* **2017**, *121*, 3056.

[23] Yu, Q.; Bowman, J. M. *J. Chem. Phys.* **2017**, *146*, 121102.

[24] Yu, Q.; Bowman, J. M. *J. Am. Chem. Soc.* **2017**, *139*, 10984–10987.

[25] Van-Oanh, N. T.; Falvo, C.; Calvo, F.; Lauvergnat, D.; Basire, M.; Gaigeot, M. P.; Parneix, P. *Phys. Chem. Chem. Phys.* **2012**, *14*, 2381–2390.

6.5 Revisit of Vibrational Spectra of $H_7O_3^+$ and $H_9O_4^+$: Classical, Thermostatted Ring Polymer, and Quantum VSCF/VCI Calculations

6.5.1 Introduction

The central importance of the hydrated proton in chemistry and biology[1–4] and proton transport[5,6] has stimulated extensive experimental and theoretical research, with much of the recent experimental work focused on 1d and 2d IR spectroscopy of the protonated water clusters[7–11] and the excess proton in liquid water, respectively.[4,12–15] There is currently much interest (and perhaps some controversy) about the dominance of one of two structural motifs of the hydrated proton, namely the Zundel cation $H_5O_2^+$, with the proton located roughly equidistant between two flanking water molecules,[16,17] and the Eigen cation $H_9O_4^+$, with hydronium roughly equally shared by three solvated water molecules.[18] Thus, small protonated water clusters that conform to the Zundel or Eigen structure are important models that help understand the structural, dynamical property and infrared spectroscopy of hydrated proton.[7–11,19–29]

The vibrational spectra of cold protonated water clusters over a large size-range have been investigated both experimentally and theoretically with the aim of identifying signatures of Zundel or Eigen motifs.[8–11,23–25,28,30,31] Post-harmonic theoretical methods to calculate the vibrational spectra of protonated water cluster include vibrational second order perturbation theory (VPT2),[11,31,32] quasi-degenerate VPT2 theory,[33] vibrational self-consistent field/virtual state configuration interaction (VSCF/VCI)[28,34–38] and multiconfiguration time-dependent Hartree (MCTDH) method.[39–41] These quantum methods provide predictions of vibrational states and the corresponding vibrational spectra but come with high computational cost, especially the VSCF/VCI and MCTDH ones. The MCTDH method, which was successfully applied to reproduce and provide an interpretation of the spectrum of

$H^+(H_2O)_2$ [40] and hopefully can be applied to larger clusters such as $H_7O_3^+$ and $H_9O_4^+$. The VPT2 method is comparatively cheaper for vibrational analysis and it has been applied to the spectrum calculation of different sizes of protonated water cluster. [10,11,31] Though many success have been achieved using this method, it cannot fully deal with a very anharmonic system and thus cannot provide explanations to some important regions in spectra. [10,11] Recent VSCF/VCI calculations of the IR spectra of $H_7O_3^+$ and $H_9O_4^+$, based on *ab initio* many-body potential and dipole moment surfaces, are in good agreement with experiment in the spectral range 1000-4000 cm^{-1}. [28,38,42] These are computationally expensive calculations; however, the large degree of mode coupling is captured by them.

In addition to quantum approaches, which are computationally intensive, molecular dynamics (MD) is an efficient and very general approach to obtain the vibrational spectra of protonated water clusters, especially large ones. These simulations can be done "on the fly", using an efficient electronic structure theory, such as density functional theory (DFT). [43] This AIMD approach has been used in several studies of the IR spectra of a variety of protonated water clusters. [31,44] However, because the MD approach is classical, it misses a number of important quantum effects such as zero-point energy and tunneling. Using it with a low-level electronic structure theory, such as DFT, can also be problematic, depending on the application.

Situated between classical MD and quantum approaches are ring polymer approaches. These approaches aim to include some quantum effects, notably zero-point energy, into dynamics calculations, however, quantum coherence is not described. The two major versions of the approach are centroid molecular dynamics (CMD) [21,45] and ring polymer molecular dynamics (RPMD). [46,47] Both methods originate from the imaginary time path integral formalism of quantum statistical mechanics. CMD is

classical MD on a potential of the mean force generated by the thermal fluctuations of ring polymer around its centroid, whereas RPMD is classical MD in the extended phase space of the ring polymer. These two methods have been successfully used to calculate short-time dynamical correlation functions for anharmonic potentials. However, when using RPMD or CMD to simulate the vibrational IR spectra, there can be unphysical results.[48] RPMD suffers from spurious peaks in the spectrum when the frequency of a physical vibration is in resonance with internal modes of the ring polymer.[49] CMD does not have the resonance problem but the high-frequency stretching modes can be coupled with low-frequency angular modes to produce an exaggerated downshift and line broadening; this “curvature" effect is temperature dependent.

To remove the spurious resonances in RPMD calculations, an internal-mode thermostat was added to the dynamics and this is termed thermostatted ring polymer molecular dynamics (TRPMD).[50,51] Two thermostats have been used with RPMD, with the latest one introduced in 2018.[51] These are denoted as path-integral Langevin equation (PILE) and generalized Langevin equation (GLE). Both are options in the i-PI software,[52] and both are used in the TRPMD calculations here. A discussion of the pluses and minuses of these thermostats is given in ref. 51; however, we note that the GLE thermostat is designed to be more accurate for high-frequency modes but may be less accurate for low-frequency ones than the PILE thermostat.

The TRPMD method has been applied to the IR spectrum of the protonated water dimer, $H_5O_2^+$,[50,51] using an accurate *ab initio*, full-dimensional potential energy (PES) and dipole moment (DMS) surfaces.[53] This cluster is not only the smallest protonated cluster that displays the Zundel motif, it is exactly the Zundel, because the proton is shared equally and symmetrically between the two water monomers. Thus, owing to the central importance of this cluster, its experimental spectrum came under intense study. Space does not permit a detailed review of this history; however,

it is important to note that the tagged spectrum of Johnson and co-workers for the cold cluster and theory were finally in good accord.[54] And as noted above, excellent agreement between theory (MCTDH using the *ab initio* PES and DMS mentioned above) and experiment was achieved, including a doublet feature at around 1000 cm^{-1}.[40] This benchmark calculation enables testing of approximate methods and in particular it was used to test the accuracy of the original RPMD approach[55] and more recently the TRPMD approach.[50] The comparisons indicate some limitations of the ring polymer approach. Indeed as stated in ref. 50,"Next, to illustrate the limitations of using any method like RPMD, CMD, or TRPMD to simulate gas phase vibrational spectra, we have considered a significantly more complex test case: the Zundel cation $H_5O_2^+$...". For more details, the interested reader is referred to that paper; however, we note that the this is a challenging problem owing to the large amplitude motion of both the shared proton and the flanking water molecules.

VSCF/VCI calculations (using the rectilinear normal mode Watson Hamiltonian,[56]) of the IR spectra of $H_7O_3^+$ and $H_9O_4^+$ have been reported using a many-body PES and DMS,[28,38,42] and comparisons with experiment show good agreement. These clusters appear much more challenging for theory than $H_5O_2^+$ owing to increasing number of vibrational modes. In fact, the VSCF/VCI calculations used a reduced number of coupled modes (typically 15) and groups of modes. This reduces the computational cost of VSCF/VCI calculation but captures important coupling behavior between essential vibration motions.

The experimental spectra of these clusters (at roughly 20 K) display intense, complex bands that involve the bright proton (hydronium) stretch modes. These bands are of particular interest in that they appear downshifted by several hundred wavenumbers from the double-harmonic prediction of the intense proton (hydronium) stretch band. In addition, there are bands with lower frequencies that are close to the proton stretch of the Zundel isomers of the $H_9O_4^+$ cluster. This has resulted in a lively

discussion in the literature about the possible presence of this isomer in experiment. This issue has largely been settled by recent theoretical and experimental work[28,38,42] and in particular very recent joint experimental/theoretical work on $HD_8O_4^+$.[57]

From the above work, it is clear that theory continues to play an important role in helping interpret complex experimental spectra. As the systems become larger and for spectroscopy of the condensed phase, where quantum calculations become increasingly difficult to perform, methods such as the classical and ring polymer ones may become the only feasible methods to apply. Thus, it is important to continue to test these methods. We do that here for the $H_7O_3^+$ and $H_9O_4^+$ Eigen clusters. Specifically, we performed TRPMD simulations of the IR spectra of the $H_7O_3^+$ and $H_9O_4^+$ clusters at 100 K and compare the results with previous VSCF/VCI calculations at 0 K and the experimental spectra of cold clusters. TRPMD calculations at 20 K are too computationally intensive for us to perform and even the ones presented here for 100 K were cpu intensive but we were able to perform them on our computer cluster. (Details of the computational effort for all the calculations are given below.)

6.5.2 Classical MD and TRPMD IR Spectra Calculation

Classical molecular dynamics (MD) calculations were performed for $H_7O_3^+$ and $H_9O_4^+$ (Eigen) at 20 K and 100 K using the i-PI software.[52] The Langevin thermostat was used in the NVT calculations and for each cluster 10 trajectories were performed. Each trajectory was propagated for 100 picoseconds and the dipole moment was recorded every 0.25 femtoseconds. As to the TRPMD calculations, the temperature was set as 100 K, since a 20-K calculation requires more beads (replicas) and is too computationally intensive. A path integral molecular dynamics (PIMD) calculation was first run for 50-picoseconds to obtain the equilibrium structures that were used as the starting structures for the TRPMD calculations. Two thermostats were used in TRPMD simulations. These are the path integral Langevin equation (PILE)

thermostat[50]and Generalized Langevin equation (GLE) thermostat.[51] For each cluster with one chosen thermostat, 8 independent trajectories were run with the initial structure from previous PIMD simulation. Each TRPMD trajectory was run for 50 picoseconds with 64 beads. As to the dipole moment, we recorded the dipole moment of each bead every 0.25 femtoseconds again and the value for the dipole moment at each step is:

$$\boldsymbol{\mu} = \frac{1}{n}\sum_{i=1}^{n}\boldsymbol{\mu}_i \tag{6.4}$$

where i indicates the i_{th} replica (bead) of the ring polymer.

The IR absorption coefficient $\alpha(\omega)$ is obtained as usual (see e.g.,[48]) by

$$\begin{aligned}\alpha(\omega) &= \frac{\pi\omega}{3\hbar cVn(\omega)\epsilon_0}(1-e^{-\beta\hbar\omega})I_{\mu\mu}(\omega)\\ &\propto \omega(1-e^{-\beta\hbar\omega})I_{\mu\mu}(\omega),\end{aligned} \tag{6.5}$$

where $I_{\mu\mu}(\omega)$ is the Fourier transform of the dipole autocorrelation function:

$$I_{\mu\mu}(\omega) = \int <\boldsymbol{\mu}(0)\cdot\boldsymbol{\mu}(t)> e^{-i\omega t}dt. \tag{6.6}$$

For simplicity we calculated the right hand side of the lower equation for $\alpha(\omega)$ above and do not report absolute absorption intensities.

6.5.3 VSCF/VCI and Quasi-classical MD IR Spectra Calculation

The VSCF/VCI spectra of $H_7O_3^+$ and $H_9O_4^+$ (Eigen)[28,42] were calculated using MULTIMODE software.[58] Specifically for $H_7O_3^+$, 18 normal modes (above 350 cm^{-1}) were selected and they were coupled using a 4-mode representation of the potential. The excitation space in the VCI calculation consists of single, double, triple and quadruple excitations. The Hamiltonian matrix is of the order of 150,000 and was diagonalized using a block-Davidson method. As to $H_9O_4^+$, we carried out 15-mode calculation using a 4-mode representation of the potential and the order of the Hamiltonian matrix was roughly 140,000. For water stretches, we did a separate calculation

that included all water bends and stretches with also 4-mode representation of the potential. More details of these VSCF/VCI calculations are given in our papers.[28,42]

The calculation of the IR spectrum of $H_7O_3^+$ and $H_9O_4^+$ in the range 0 to 1200 cm^{-1} is problematic for the Watson Hamiltonian,[56] which is used in MULTIMODE, because the large amplitude, torsional motion of the flanking waters cannot be accurately described by the rectilinear normal modes used in this Hamiltonian. These modes were not included in the published VSCF/VCI calculations. Instead, we conducted quasiclassical molecular dynamics (QCMD) simulations of the spectra in this range with 100 independent trajectories for each molecule. Each trajectory was run for 12 ps and the step size of 0.06 fs. The zero-point energy was assigned to all intermolecular modes as well as the umbrella mode of H_3O^+ and we did not put any energy in other intramolecular modes. The dipole correlation function was then calculated by averaging over 100 trajectories. After Fourier transformation, the IR spectra of $H_7O_3^+$ and $H_9O_4^+$ in the low-frequency region was obtained. These calculations have been reported in a recent experiment/theory paper[30] and more details are given in that paper. Also, we note that the QCMD approach is the same as the original "semiclassically prepared molecular dynamics" approach[59] which we renamed to the QCMD approach.[60]

Before presenting results, we comment on the computational effort for the MD, TRPMD and VSCF/VCI calculations using the same PES/DMS and the cluster node (Intel® Xeon® CPU E5-2630 v3 @ 2.40 GHz Base Clock Frequency). For $H_9O_4^+$ the MD calculation for a 100-picosecond trajectory took roughly 35 cpu hours using two cores on a single node where one core is used for i-PI solver and another is for the client to evaluate potential and forces. For the TRPMD calculation, a 50-picosecond trajectory with 64 beads, took over 240 cpu hours using 16 cores of a single computer node (one for i-PI solver and 15 for potential/force calculations). Even with the parallel processing feature of the i-PI software to evaluate the potential and forces of

each bead, the 64 bead TRPMD calculation is still much more expensive than the classical MD one. The VSCF/VCI calculations with 15 modes coupled took roughly 150 cpu hours using 8 cores of a single node. This included the time to generate all the n-mode grids, n=1,4 and to set up and diagonalize the Hamiltonian matrix. Clearly, Both TRPMD and VSCF/VCI require more computational cost than the classical MD calculations.

6.5.4 Results and Discussion

In the following sub-sections we present the calculated and experimental IR spectra of $H_7O_3^+$ and $H_9O_4^+$ (Eigen isomer). We also present the distributions of the hydronium O-H bond lengths as well as the O-O distance where one O refers to the hydronium core. These are used to aid in the interpretation of the centrally important intense hydronium stretch band seen in the IR spectra of these clusters.

To begin, we show the minimum energy structures of these clusters in Figure 6.28. The $H_7O_3^+$ structure can be described as a distorted hydronium core hydrated by two water molecules. The lowest energy isomer of $H_9O_4^+$, the Eigen isomer, has the hydronium equally shared by three water molecules.

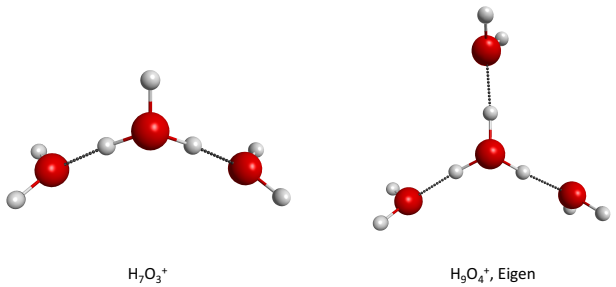

Figure 6.28 Global minimum structure of $H_7O_3^+$ and $H_9O_4^+$(Eigen)

1. $H_7O_3^+$

The calculated and experimental spectra of $H_7O_3^+$ in the range of 0-4000 cm^{-1} are shown in Figure 6.29. Consider first the MD spectrum at 20 K and the double-harmonic stick spectrum shown in Figure.2.a). The double-harmonic one is a 0 K spectrum obtained in the usual harmonic approximations and the frequencies/intensities were reported in tables in ref. 61. As expected, there is good agreement between the MD and double-harmonic spectra, since at such low temperature, classical motion is confined to the region near the global minimum structure. The large sticks and MD bands at around 2600 cm^{-1} correspond to the signature hydrated hydronium proton stretches. The harmonic frequencies at 2520 cm^{-1} and 2688 cm^{-1} are the asymmetric and symmetric O-H stretches of the hydronium. The free hydronium O-H stretch is at 3839 cm^{-1} and is of lower intensity. At the higher temperature of 100 K, the calculated classical MD spectrum shows broader bands, especially for the hydronium stretches. However, the central peaks of different bands remain close to the 20 K bands. A quick comparison with the experimental spectrum,[42] shows a 500-600 cm^{-1} down-shift of the hydronium stretches and 100-200 cm^{-1} down-shift for water stretches. Clearly, the MD simulations do not capture these large down-shifts.

The TRPMD spectra with indicated thermostats are similar in the water stretches region, at around 3750 cm^{-1}, which is downshifted by roughly 100-200 cm^{-1} relative to the harmonic frequencies and are in good agreement with the experimental band positions. The success of TRPMD in simulating the water stretches has been previously noted.[62] As to the hydronium stretches, there is a 200-300 cm^{-1} downshift in the TRPMD spectrum using generalized Langevin equation (GLE) compared with the MD spectrum. However, this hydronium stretch band is still $\sim$300 cm^{-1} higher than experiment. Also, the TRPMD bands are broad, even at 100 K. Using the GLE thermostat does produce a narrower band than using the PILE one, as it was intended to, and does resolve the two hydronium shared O-H stretch bands but with the bands

at around 3750 cm^{-1} not resolved. This general issue of thermostat broadening has been discussed in detail by the developers of the methods and the reader is referred to literature for more details and discussion.[51,62]

Next, consider the VSCF/VCI spectrum, shown in the range 1200-4000 cm^{-1}.[42] As seen, there is good agreement with experiment with respect to band positions and band fine structure. Both VSCF/VCI and experiment spectra predict the intense peak at around 1900 cm^{-1} and the hydronium stretches contribute most to this signature band. As to other less intense bands at around 1950-2500 cm^{-1}, according to VSCF/VCI analyses, the hydronium asymmetric and symmetric stretches have strong coupling with different combination bands. Because of the highly mixing feature, those combination bands borrow intensity from hydronium stretches and show large infrared intensity.[42]

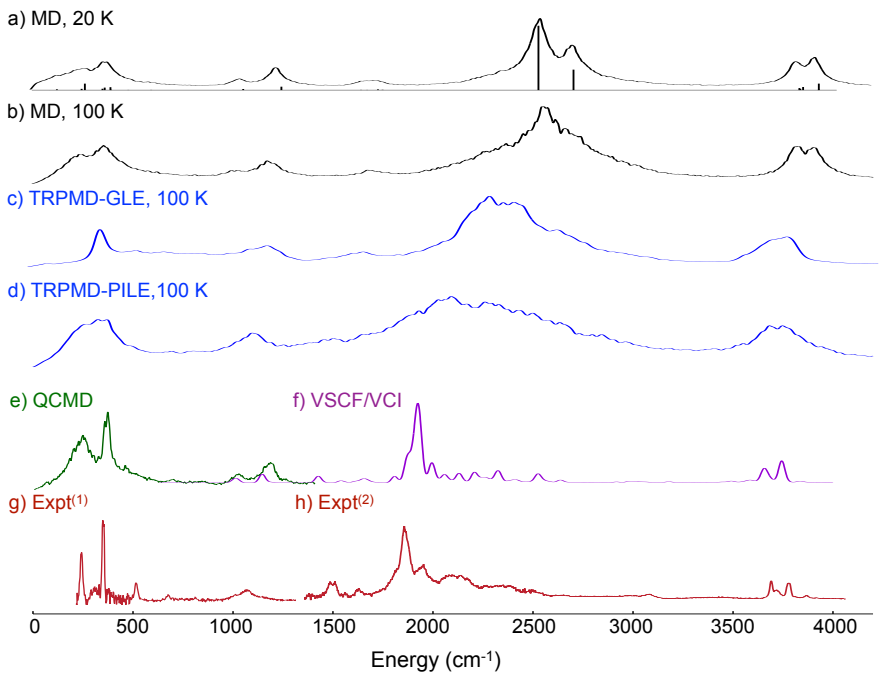

Figure 6.29 Overview of the IR spectrum of $H_7O_3^+$ using the indicated methods. The stick spectrum is from a standard double-harmonic calculation. (1) reference 30 (2) reference 42

Figure 6.29 also shows the spectra in the far-infrared region, 0-1200 cm^{-1}. The experimental spectrum has recently been reported together with quasi-classical molecular dynamics simulation results.[30] As seen, there are two intense peaks below 500 cm^{-1}. The feature around 240 cm^{-1} has been assigned to the flanking water wagging motion, while the embedded H_3O^+ hydrogen-bond stretching mode contributes to the band at around 350 cm^{-1}. Another small feature at 508 cm^{-1} is seen in both experimental and QCMD spectra. This is due to a combination band of low-frequency modes.[30] The MD spectra at 20 K and 100 K, predict both two peaks below 500 cm^{-1}. Thus, these two bands are not affected very much by anharmonic effects and so they are close to the QCMD and experimental bands. A major difference appears in the TRPMD spectrum using the GLE thermostat. The band at 240 cm^{-1} is absent and only the 350 cm^{-1} band is seen below 500 cm^{-1}. With the PILE thermostat, the corresponding TRPMD spectrum has a broad feature in the range 240-400 cm^{-1} whereas from experiment (and the previous QCMD calculations) there are two bands observed. Actually, it was noted that GLE thermostat can cause unphysical results in low-frequency region of vibrational spectrum and this may be the reason for the missing 240 cm^{-1} band in TRPMD-GLE spectrum.[51] Overall, the VSCF/VCI calculated spectra are in the best agreement with experiment above 1500 cm^{-1} and the QCMD spectrum is overall in the best agreement with experiment in the far-IR region.

To delve into the source of the large downshift of the intense hydronium band, we recall that at the harmonic level, a significant change in the average hydronium proton-stretch frequency across a range of protonated clusters has been reported in the literature.[11,61] This change in frequency shows a near liner dependence on the equilibrium hydronium O-H bond length for a given cluster.[11] This is shown in Figure **??** from a variety of calculations over a large range of clusters. The data in this figure are adapted from a recent test of our PES and DMS.[61] In short, as the O-H bond length increases there is a large downshift in the frequency. The correlation

is well-represented by a linear relationship given by ω=a R_{OH}+ b where a=-18362.0 cm^{-1}/Å ,b=21560.2 cm^{-1}. (An even simpler demonstration of this correlation is seen in the bare Zundel cation $H_5O_2^+$, as the distance between the two water monomers changes.[63]) This correlation, together with information about the distribution of the

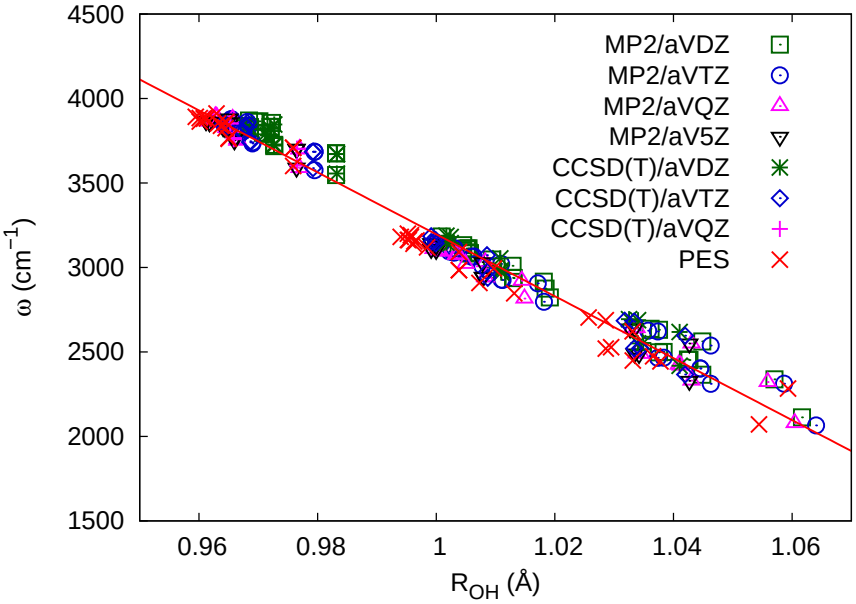

Figure 6.30 Correlation between average proton-stretch harmonic frequency and O-H equilibrium bond lengths for $H_3O^+(H_2O_n)$,n=0-5 clusters from ref. 30 and a linear least-square fit ω=a R_{OH}+ b where a=-18362.0 cm^{-1}/Å , b=21560.2 cm^{-1}

hydronium O-H bond lengths can be used to rationalize the intense proton band position from various calculations. To begin, note that the hydrated O-H equilibrium bond length is 1.029 Å .[61] Using this value in the correlation plot we read off a value of roughly 2600 cm^{-1} for the average proton stretch band. This is in good agreement with the harmonic frequency noted above. The VSCF/VCI (and experimental) band is shifted much below the harmonic estimate, as noted already, and this suggests, according to Figure 6.30, that the quantum shift in the hydrated O-H bond length is to larger values, relative to the equilibrium value. This is verified, semi-quantitatively, using a simple local O-H 1d analysis of the hydronium O-H stretches. As shown in Figure 6.31, 1d potential and corresponding ground vibrational state probability

densities are plotted for the free and two equivalent hydrated O-H stretches. Both distributions have a maximum shifted up from the equilibrium value. This shift is larger for the hydrated O-H stretch, owing to the softer and thus more anharmonic potential. As indicated, the maximum for the hydrated O-H stretch is roughly 1.05 Å . Using bond length we determine a frequency of roughly 2280 cm^{-1}, which is downshifted by 320 cm^{-1} from the equilibrium harmonic frequency. The agreement with the VSCF/VCI (and experimental) band position, which is downshifted by an additional several hundred wavenumbers, is not quantitative. This is not surprising, given the approximation inherent in the 1d analysis. For the free O-H stretch, the maximum is roughly 0.97 Å and the corresponding frequency is 3750 cm^{-1}, which is roughly 100 cm^{-1} downshifted relative to the harmonic frequency of 3839 cm^{-1}. So, the simple 1d analysis captures large downshift of the hydrated hydronium O-H stretch and the small change in frequency of the free O-H stretch. The results are qualitatively in good agreement with the corresponding VSCF/VCI and experimental band positions.

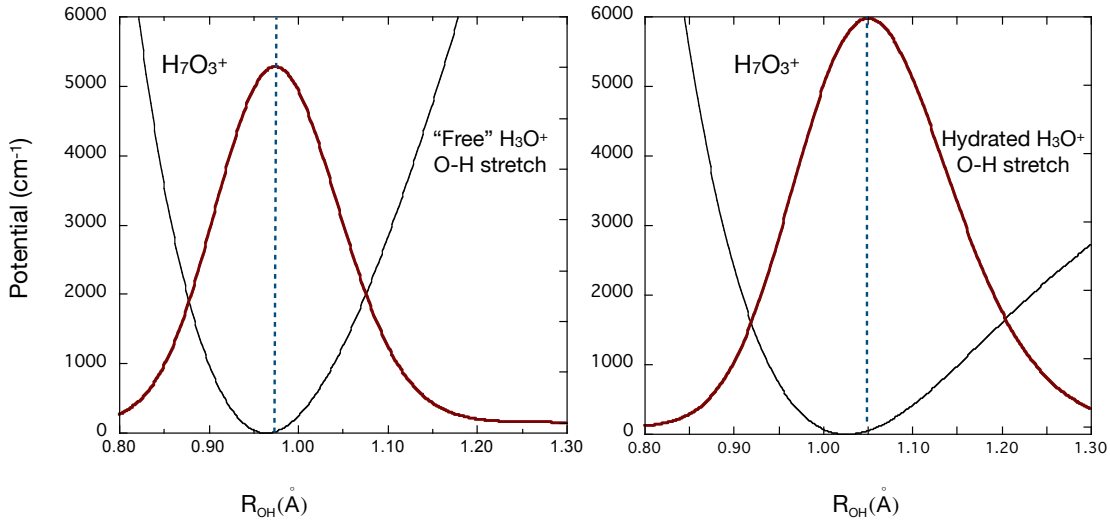

Figure 6.31 Density of the ground vibrational state hydronium O-H bond lengths in $H_7O_3^+$ from 1d DVR calculations

Next, consider the (thermal) distributions of the hydronium O-H stretches ob-

tained from MD and TRPMD calculations; these are shown in Figures 6.32. The distributions from the two TRPMD calculations are very similar, so we only show the one with the PILE thermostat. The MD distribution at 20 K shows relatively sharp maxima, centered around the equilibrium values of 0.964 Å and 1.029 Å, respectively.[61] At 100 K, the MD distribution is broader, as expected; however, the centers of the two peaks are almost unchanged. The corresponding TRPMD distribution at 100 K is broader than the MD one and the peak corresponding to the hydrated O-H stretch is at roughly 1.045 Å . This is significantly longer than the corresponding MD peak, owing to the effect of zero-point motion in the anharmonic potential. However, the peak in the free O-H stretch is slightly shorter than the MD one. This is seen for both thermostats and disagrees quantitatively with the 1d DVR analysis. However, both analyses indicate a rather minor deviation from the equilibrium value of this stretch and thus a relatively minor deviation from the harmonic analysis.

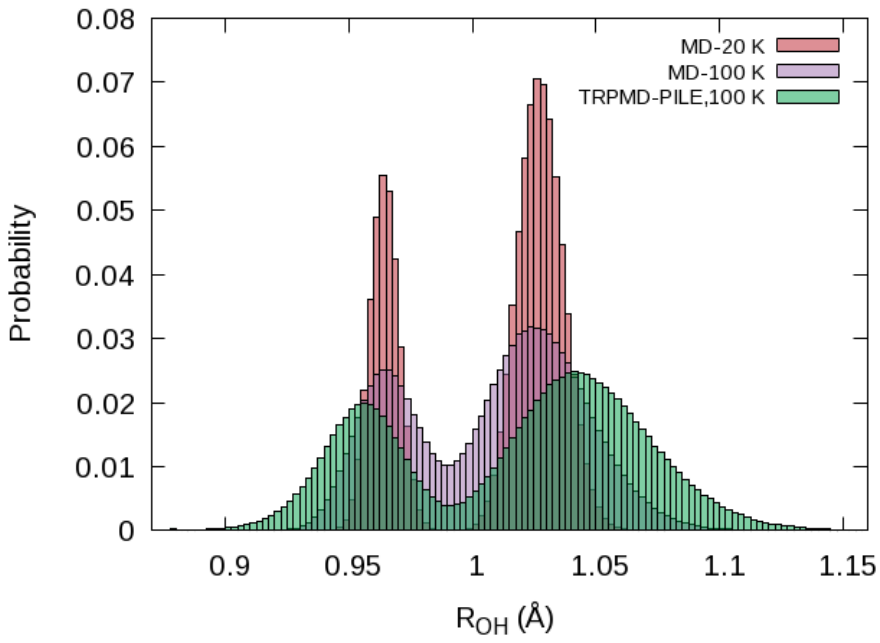

Figure 6.32 Distribution of hydronium OH bond length in $H_7O_3^+$ from indicated methods.

Using these hydronium O-H peak values in the correlation relationship we can

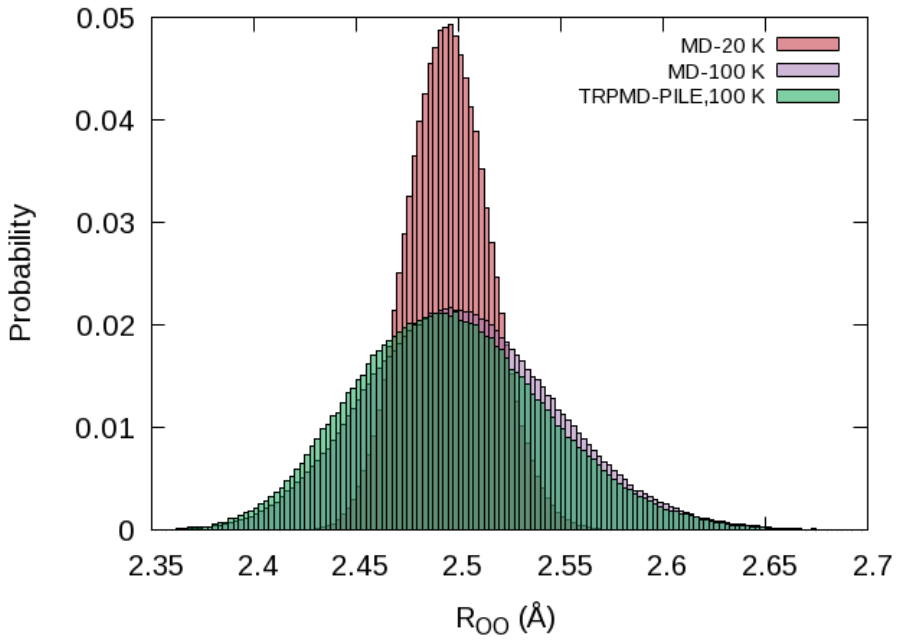

Figure 6.33 Distribution of the O-O distance between the hydronium and water O atoms of $H_7O_3^+$ from indicated methods.

determine the corresponding frequencies. For the MD peak at 1.029 Å the corresponding frequency is roughly 2600 cm^{-1}, in good agreement with the average of harmonic asymmetric and symmetric hydrated O-H stretch frequencies. For the MD peak at 0.964 Å the corresponding frequency is 3859 cm^{-1}, which is in good agreement with harmonic frequency of the free O-H stretch. These are the expected results. For the TRPMD distribution the peak at 1.045 Å corresponds to the hydrated O-H stretch and the corresponding average frequency is ∼2350 cm^{-1}, in good agreement with the intense band maximum in the TRPMD spectra and somewhat closer to the TRPMD-GLE one. This is a 300 cm^{-1} downshift, relative to the harmonic frequency. The second peak, as noted already, is slightly shorter than the MD one and has a corresponding frequency of roughly 4000 cm^{-1}, which is a few percent higher than the harmonic estimate.

We conclude this subsection with a short discussion of the MD and TRPMD distributions of O-O bond length between the hydronium oxygen and the flanking

water oxygen. These are shown in Figure 6.33. As seen, the TRPMD distribution is broader than the MD one; however, both are peaked close to the equilibrium value of 2.491 Å.

Next, we present analogous results and analyses for the $H_9O_4^+$ Eigen cluster, where the hydronium is fully hydrated.

2. $H_9O_4^+$ (Eigen)

The equilibrium of the Eigen isomer of $H_9O_4^+$, shown in Figure **??**, has the hydronium surrounded by three water molecules. The signature experimental band is an intense, broad band centered around 2650 cm^{-1}.[10,11] Similar to $H_7O_3^+$, it was a challenge theoretically to explain the origin of large downshift of this hydronium band relative to a harmonic analyses, which gives the intense hydronium bands at around 3000 cm^{-1} based on CCSD(T)-F12/aVTZ calculations.[61] Thus, there is a roughly 400 cm^{-1} downshift for the anharmonic spectrum. We presented a detailed analysis of this band using VSCF/VCI calculations[28,57] and the interested reader is directed to those papers for details.

The calculated and experimental IR spectra are given in Figure 6.34. Clearly, and not surprisingly, these spectra bear a resemblance to the spectra just discussed for $H_7O_3^+$. As seen, the classical MD simulations at 20 and 100 K are only in qualitative agreement with experiment for the prominent band mentioned above and do not show the large downshift. As expected, and in accord with analogous results for $H_7O_3^+$, the positions of these bands are essentially the same as bands from a double-harmonic analysis. The MD bands are again broad and do not resolve the fine structure in experiment (as was the case for $H_7O_3^+$). The TRPMD spectra successfully reproduce the band positions of the water stretches, which are roughly downshifted from the harmonic bands by 100-200 cm^{-1}. For the intense hydronium proton stretch band the TRPMD-GLE predicts the hydronium stretch band position at ∼2800 cm^{-1} while with TRPMD-PILE band position is at around 2750 cm^{-1}.

While these are significantly downshifted from the MD band, they are not sufficiently downshifted to be in good agreement with experiment. Also, the TRPMD bands are too broad to resolve the fine structure in the experimental spectra in the range from 1500-2400 cm^{-1}, as seen in the Figure 6.34. These features and the band positions are captured by VSCF/VCI calculation. The VSCF/VCI calculation successfully locates the postion of the hydronium stretches at around 2650 cm^{-1}. These stretches are coupled with other vibrational states including several complex combination bands. The VSCF/VCI spectrum also provides explanations of all small featured bands in 1750-2400 cm^{-1}. These bands origin mainly from the important combination bands involving hydronium core frustrated rotation, wagging and umbrella motions. Each combination band has coupling with hydronium stretches (asym- or sym-stretches) and thus they carry significant intensity in the spectrum.

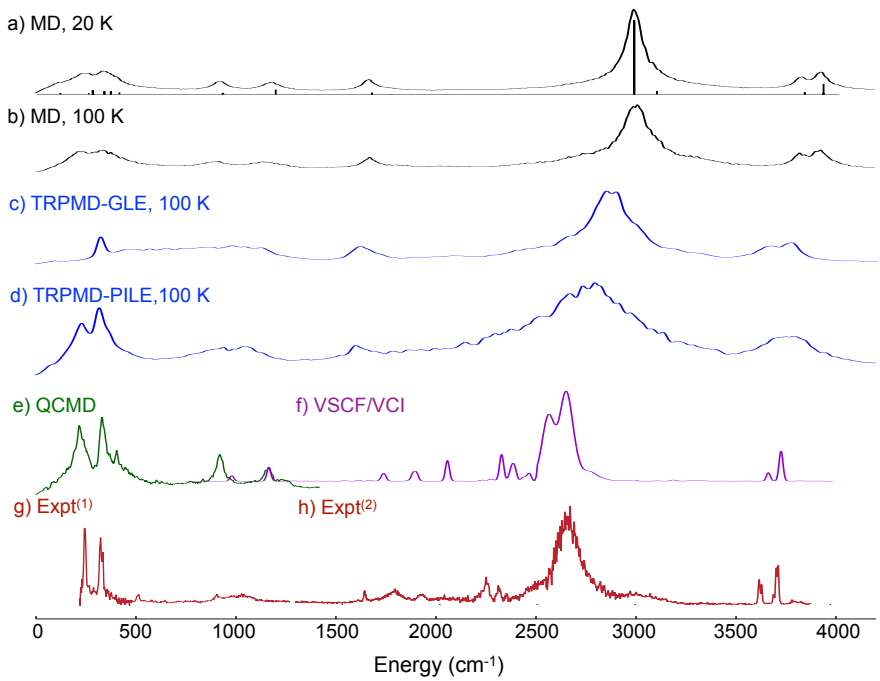

Figure 6.34 Overview of the IR spectrum of $H_9O_4^+$ using the indicated methods. The stick spectrum is from a standard double-harmonic calculation. (1) reference 30 (2) reference 10

Next, consider the spectra in the far-infrared region (0-1250 cm^{-1}). Here, as for $H_7O_3^+$, the QCMD method reproduces the prominent sharp bands below 500 cm^{-1} which are due to the flanking water large amplitude torsional and monomer stretching modes. Details about these bands can be found in a recent joint experimental/theoretical paper.[30] The TRPMD-PILE spectrum does describe these bands, however, with considerable broadening.

We now present the analyses of the intense proton stretch band, analogous to the one done for $H_7O_3^+$. First, note that the equilibrium hydronium O-H distance is 1.005 Å .[61] From the frequency correlation, this corresponds to a harmonic frequency of 3106 cm^{-1}, is good agreement with the stick position and the MD band peak. A 1d DVR calculation of the zero-point state of the hydronium O-H stretch yields a density maximum at 1.022Å . The corresponding frequency is 2794 cm^{-1} and is thus a large downshift relative to the MD band. The MD and TRPMD hydronium O-H distributions are shown in Figure 6.35. Again, the distributions from the two TRPMD simulations are almost superimposable so only one (the PILE one) is shown. As expected, the MD distribution at 20 K gives a narrow O-H distribution centered around the equilibrium value, 1.005 Å . At 100 K, the MD distribution broadens, but remains centered at around 1.005 Å. With quantum zero-point effects included, the TRPMD distribution is shifted up from the equilibrium value and the peak value is roughly 1.018 Å . This correlates with a frequency of 2870 cm^{-1}, which is in good agreement with the TRPMD-PILE band peak. The VSCF/VCI (and experimental) band position is roughly 2650 cm^{-1}, which would correlate with a larger O-H distance than the ones obtained from the 1d DVR and TRPMD distributions.

Overall, the correlation analysis giving the harmonic frequency of the hydronium O-H stretch provides (as with H_7O_3) a simple explanation for the different peak positions of the MD, TRPMD and VSCF/VCI bands.

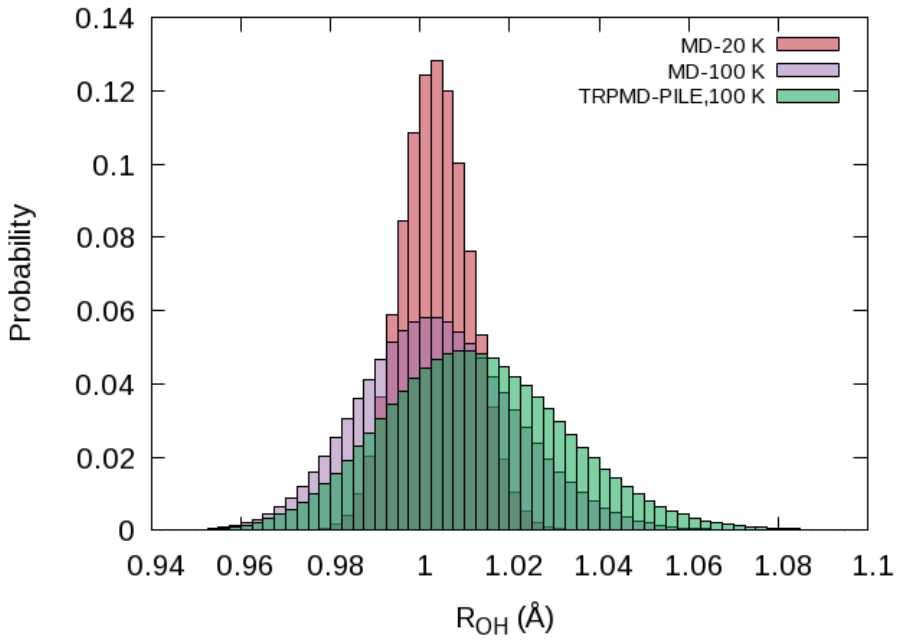

Figure 6.35 Distribution of hydronium OH bond length in $H_9O_4^+$ from various methods

Finally, consider the distribution of O-O distances shown in Figure 6.36. Similar to the situation in $H_7O_3^+$ molecule, the MD distribution at 20 K is narrowly peaked around 2.555 Å. With higher temperature at 100 K, The MD presents broader distribution but still centers around 2.555 Å. Unlike the distribution of R_{OH}, the TRPMD distribution of O-O distance is peaked at the same value as the MD one although the distribution is broader.

Considering now the results for the two clusters, we conclude that the TRPMD approach does capture the large downshift (relative to the harmonic estimates) of the intense proton bands in these clusters. But the band positions are still several hundred wavenumbers upshifted from the VSCF/VCI (and experimental) ones. The explanation for this may lie in the complex coupling with many modes that was shown in the detailed analysis of the VSCF/VCI results.[28,30,38,42] Another source for the difference is perhaps the limited sampling of the anharmonicity from the zero-point motion, which is described in the TRPMD approach. The vibrational transition is of course a quantum event that “starts" in the zero-point state and “ends" in an excited

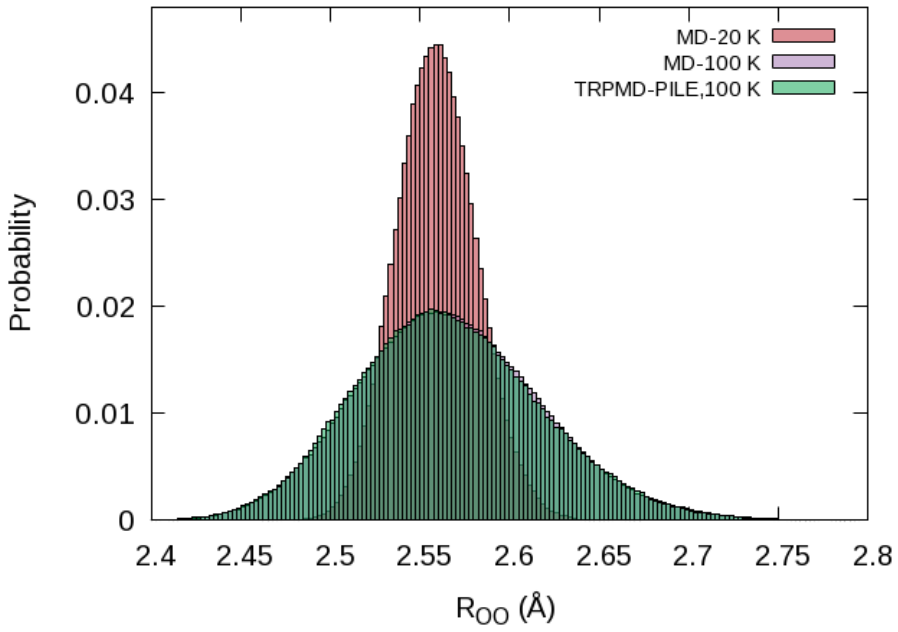

Figure 6.36 Thermal distributions of the O-O distance of $H_9O_4^+$ from indicated calculations

state, which samples more of the potential energy surface than the ground state. This quantum transition is a coherence effect that is not described by TRPMD. Instead, the motion of the ring polymer in the zero-point state accounts for the vibrational resonances seen in the IR spectrum. In general, one could argue that this is an underestimate of the anharmonicty relevant to the vibrational transition. Indeed, from semi-classical theory it has been shown that a trajectory based on the average of the initial and final quantum numbers of a transition produces more accurate results than using the initial quantum number.[64–66]

We conclude this section with some general and somewhat speculative remarks about using MD, TRPMD and (if feasible) VSCF/VCI calculations of the IR spectrum of the hydrated proton in liquid water at room temperature. Recent 2D IR spectra of the proton bands have been reported by two groups with the aim of identifying the dominant motif of the hydrated proton in the liquid.[12,14] In principle the PES and DMS we have developed can be used to obtain corresponding spectra. Such

calculations could be done using the approach we took for calculating the IR spectrum of liquid water.[67,68] Namely, we take "snapshotsâĂİ from a reasonable and efficient MD simulation and then perform calculations of the clusters of the hydrated proton with as many modes as possible coupled in the VSCF/VCI calculations. MD and TRPMD calculations could be done on the same clusters of course.

Aiming at the recent IR spectra reported by the Tokmakoff group,[13] there are broad bands associated with the proton modes (in $H_5O_2^+$, as evidenced in this paper) and so this might be a more reasonable application for the MD and TRPMD approaches. We hope to carry out such calculations in the near future.

Finally, we note the recent success of the Divide-and-Conquer Semiclassical Initial Value Representation, which was recently applied to the vibrational energies of Zundel cation.[69] This is an efficient modification of the original Semiclassical Initial Value Representation approach for IR spectroscopy.[70] It would be interesting to apply this method to larger clusters.

6.5.5 Conclusions

The IR spectra of $H_7O_3^+$ and $H_9O_4^+$ were calculated in the range 0-4000 cm^{-1} using classical and thermostatted ring polymer molecular calculations with *ab initio* many-body potential and dipole moment surfaces. The classical MD spectra at 20 and 100 K are close to the double-harmonic spectrum, although considerably broader. TRPMD calculations done at 100 K successfully produce large downshifts in the water and hydronium O-H stretch bands, relative to the classical MD ones. However, the TRPMD bands are broader than experiment and for the intense proton stretch band the downshift is not sufficient to produce good quantitative agreement with experiment. Such agreement with experiment is seen with VSCF/VCI calculations (using the same PES and DMS).

The downshifting of the proton (hydronium) stretch band was successfully inves-

tigated using a previous linear correlation between the hydronium O-H bond length and harmonic frequency.

Bibliography

[1] Heberle, J.; Riesle, J.; Thiedemann, G.; Oesterhelt, D.; Dencher, N. A. *Nature* **1994**, *370*, 379.

[2] Stowell, M. H. B.; McPhillips, T. M.; Rees, D. C.; Soltis, S. M.; Abresch, E.; Feher, G. *Science* **1997**, *276*, 812–816.

[3] Luecke, H.; Richter, H.-T.; Lanyi, J. K. *Science* **1998**, *280*, 1934–1937.

[4] Rini, M.; Magnes, B.-Z.; Pines, E.; Nibbering, E. T. J. *Science* **2003**, *301*, 349–352.

[5] Agmon, N. *Chem. Phys. Lett.* **1995**, *244*, 456.

[6] de Grotthuss,; T., C. J. *Ann. Chim.* **1806**, *58*, 54.

[7] Yeh, L. I.; Lee, Y. T.; Hougen, J. T. *J. Mol. Spectrosc.* **1994**, *164*, 473.

[8] Shin, J.-W.; Hammer, N. I.; Diken, E. G.; Johnson, M. A.; Walters, R. S.; Jaeger, T. D.; Duncan, M. A.; Christie, R. A.; Jordan, K. D. *Science* **2004**, *304*, 1137.

[9] Headrick, J. M.; Diken, E. G.; Walters, R. S.; Hammer, N. I.; Christie, R. A.; Cui, J.; Myshakin, E. M.; Duncan, M. A.; Johnson, M. A.; Jordan, K. D. *Science* **2005**, *308*, 1765.

[10] Wolke, C. T.; Fournier, J. A.; Dzugan, L. C.; Fagiani, M. R.; Odbadrakh, T. T.; Knorke, H.; Jordan, K. D.; McCoy, A. B.; Asmis, K. R.; Johnson, M. A. *Science* **2016**, *354*, 1131.

[11] Fournier, J. A.; Wolke, C. T.; Johnson, M. A.; Odbadrakh, T. T.; Jordan, K. D.; Kathmann, S. M.; Xantheas, S. S. *J. Phys. Chem. A* **2015**, *119*, 9425–9440.

[12] Thämer, M.; De Marco, L.; Ramasesha, K.; Mandal, A.; Tokmakoff, A. *Science* **2015**, *350*, 78–82.

[13] Fournier, J. A.; Carpenter, W. B.; Lewis, N. H. C.; Tokmakoff, A. *Nat. Chem.* **2018**, *10*, 932–937.

[14] Dahms, F.; Fingerhut, B. P.; Nibbering, E. T. J.; Pines, E.; Elsaesser, T. *Science* **2017**, *495*, 491–495.

[15] Biswas, R.; Carpenter, W.; Fournier, J. A.; Voth, G. A.; Tokmakoff, A. *J. Chem. Phys.* **2017**, *146*, 154507.

[16] Zundel, G.; Metzger, H. *Z. Phys. Chem.* **1968**, *58*, 225.

[17] Zundel, G. *Adv. Chem. Phys.* **1999**, *111*, 1.

[18] Eigen, M. *Angew. Chem., Int. Ed. Engl.* **1964**, *3*, 1.

[19] Begemann, M. H.; Gudeman, C. S.; Pfaff, J.; Saykally, R. J. *Phys. Rev. Lett.* **1983**, *51*, 554.

[20] Yeh, L. I.; Okumura, M.; Myers, J. D.; Price, J. M.; Lee, Y. T. *J. Chem. Phys.* **1989**, *91*, 7319.

[21] Jiang, J.-C.; Wang, Y.-S.; Chang, H.-C.; Lin, S. H.; Lee, Y. T.; Niedner-Schatteburg, G.; Chang, H.-C. *J. Am. Chem. Soc.* **2000**, *122*, 1398.

[22] Douberly, G. E.; Ricks, A. M.; Duncan, M. A. *J. Phys. Chem. A* **2009**, *113*, 8449.

[23] Douberly, G. E.; Walters, R. S.; Cui, J.; Jordan, K. D.; Duncan, M. A. *J. Phys. Chem. A* **2010**, *114*, 4570.

[24] Asmis, K. R.; Pivonka, N. L.; Santambrogio, G.; Brummer, M.; Kaposta, C.; Newmark, D. M.; Woste, L. *Science* **2003**, *299*, 1375–1377.

[25] Heine, N.; Fagiani, M. R.; Rossi, M.; Wende, T.; Berden, G.; Blum, V.; Asmis, K. R. *J. A. Chem. Soc.* **2013**, *135*, 8266–8273.

[26] Xantheas, S. S. *Nature* **2009**, *457*, 673.

[27] Berkelbach, T. C.; Lee, H. S.; Tuckerman, M. E. *Phys. Rev. Lett.* **2009**, *103*, 238302.

[28] Yu, Q.; Bowman, J. M. *J. Am. Chem. Soc.* **2017**, *139*, 10984–10987.

[29] Agmon, N.; Bakker, H. J.; Campen, R. K.; Henchman, R. H.; Pohl, P.; Roke, S.; Thämer, M.; Hassanali, A. *Chem. Rev.* **2016**, *116*, 7642–7672.

[30] Esser, T. K.; Knorke, H.; Asmis, K. R.; Schöllkopf, W.; Yu, Q.; Qu, C.; Bowman, J. M.; Kaledin, M. *J. Phys. Chem. Lett.* **2018**, *9*, 798–803.

[31] Wang, H.; Agmon, N. *J. Phys. Chem. A* **2017**,

[32] Nielsen, H. H. *Rev. Mod. Phys.* **1951**, *23*, 90–136.

[33] Yagi, K.; Thomsen, B. *J. Phys. Chem. A* **2017**, *121*, 2386–2398.

[34] Bowman, J. M. *J. Chem. Phys.* **1978**, *68*, 608.

[35] Carter, S.; Culik, J. S.; Bowman, J. M. *J. Chem. Phys.* **1997**, *107*, 10458.

[36] Christoffel, K. M.; Bowman, J. M. *Chem. Phys. Lett.* **1982**, *85*, 220–224.

[37] McCoy, A. B.; Huang, X.; Carter, S.; Landeweer, M. Y.; Bowman, J. M. *J. Chem. Phys.* **2005**, *122*, 061101.

[38] Yu, Q.; Bowman, J. M. *J. Chem. Phys.* **2017**, *146*, 121102.

[39] H. D. Meyer, U. M.; Cederbaum, L. S. *Chem. Phys. Lett.* **1990**, *165*, 73.

[40] Vendrell, O.; Gatti, F.; Meyer, H. D. *Angew. Chem. Int. Ed.* **2007**, *46*, 6918–6921.

[41] Vendrell, O.; Gatti, F.; Meyer, H. D. *Angew. Chem. Int. Ed.* **2009**, *48*, 352–355.

[42] Duong, C. H.; Gorlova, O.; Yang, N.; Kelleher, P. J.; Johnson, M. A.; McCoy, A. B.; Yu, Q.; Bowman, J. M. *J. Phys. Chem. Lett.* **2017**, *8*, 3782–3789.

[43] Thomas, M.; Brehm, M.; Fligg, R.; VÃČÂűhringer, P.; Kirchner, B. *Phys. Chem. Chem. Phys.* **2013**, *15*, 6608–6622.

[44] Kulig, W.; Agmon, N. *J. Phys. Chem. B* **2014**, *118*, 278–286.

[45] Cao, J.; Voth, G. a. *J. Chem. Phys.* **1994**, *100*, 5093.

[46] Craig, I. R.; Manolopoulos, D. E. *J. Chem. Phys.* **2005**, *123*, 034102.

[47] Habershon, S.; Manolopoulos, D. E.; Markland, T. E.; Miller, T. F. *Annu. Rev. Phys. Chem.* **2013**, *64*, 387–413.

[48] Witt, A.; Ivanov, S. D.; Shiga, M.; Forbert, H.; Marx, D. *J. Chem. Phys.* **2009**, *130*, 194510.

[49] Habershon, S.; Fanourgakis, G. S.; Manolopoulos, D. E. *J. Chem. Phys.* **2008**, *129*, 074501.

[50] Rossi, M.; Ceriotti, M.; Manolopoulos, D. E. *J. Chem. Phys.* **2014**, *140*, 234116.

[51] Rossi, M.; Kapil, V.; Ceriotti, M. *J. Chem. Phys.* **2018**, *148*, 102301.

[52] Ceriotti, M.; More, J.; Manolopoulos, D. E. *Computer Physics Communications* **2014**, *185*, 1019 – 1026.

[53] Huang, X.; Braams, B. J.; Bowman, J. M. *J. Chem. Phys.* **2005**, *122*, 044308.

[54] Hammer, N. I.; Diken, E. G.; Roscioli, J. R.; Johnson, M. A.; Myshakin, E. M.; Jordan, K. D.; McCoy, A. B.; Huang, X.; Bowman, J. M.; Carter, S. *J. Chem. Phys.* **2005**, *122*, 244301.

[55] Huang, X.; Habershon, S.; Bowman, J. M. *Chem. Phys. Lett.* **2008**, *450*, 253 – 257.

[56] Watson, J. K. G. *Mol. Phys.* **1968**, *15*, 479.

[57] Duong, C. H.; Yang, N.; Kelleher, P. J.; Johnson, M. A.; DiRisio, R. J.; McCoy, A. B.; Yu, Q.; Bowman, J. M.; Henderson, B. V.; Jordan, K. D. *J. Phys. Chem. A* **2018**, *x*, xxx.

[58] Bowman, J. M.; Carter, S.; Huang, X. *Int. Rev. Phys. Chem.* **2003**, *22*, 533–549.

[59] Van-Oanh, N.-T.; Falvo, C.; Calvo, F.; Lauvergnat, D.; Basire, M.; Gaigeot, M.-P.; Parneix, P. *Phys. Chem. Chem. Phys.* **2012**, *14*, 2381–2390.

[60] Chen, M.; Zheng, L.; Santra, B.; Ko, H.-Y.; DiStasio Jr, R. A.; Klein, M. L.; Car, R.; Wu, X. *Nat. Chem* **2018**,

[61] Heindel, J. P.; Yu, Q.; Bowman, J. M.; Xantheas, S. S. *J. Chem. Theory Comput.* **2018**, *14*, 4553–3566.

[62] Rossi, M.; Liu, H.; Paesani, F.; Bowman, J.; Ceriotti, M. *J. Chem. Phys.* **2014**, *141*, 181101.

[63] Yu, Q.; Bowman, J. M. *J. Phys. Chem. Lett.* **2016**, *7*, 5259–5265.

[64] Wardlaw, D. M.; Noid, D. W.; Marcus, R. A. *J. Phys. Chem.* **1984**, *88*, 536–547.

[65] Garcia, A., Ayllon; Martens, C. C.; Santamaria, J.; Ezra, G. S. *J. Chem. Phys.* **1987**, *87*, 6609–6617.

[66] Heisenberg, W. *The Physical Principles of the Quantum Theory*; Dover, New York, 1949.

[67] Liu, H.; Wang, Y.; Bowman, J. M. *J. Chem. Phys.* **2015**, *142*, 194502.

[68] Liu, H.; Wang, Y.; Bowman, J. M. *J. Phys. Chem. B* **2016**, *120*, 2824–2828.

[69] Di Liberto, G.; Conte, R.; Ceotto, M. *J. Chem. Phys.* **2018**, *148*, 014307.

[70] Kaledin, A. L.; Miller, W. H. *J. Chem. Phys.* **2003**, *118*, 7174–7182.

Part IV

Vibrational Spectra of the Aqueous Proton

Chapter 7 High-Level VSCF/VCI Calculations Decode the Vibrational Spectrum of the Aqueous Proton

7.1 Introduction

The aqueous proton is a fundamental cationic species whose transport process is ubiquitous and plays an important role in biological and chemical systems.[1–4] Due to the strength and flexibility of the hydrogen bond (H-bond) network, the aqueous proton system exhibits unique properties such as ultrafast proton mobility. The Grotthuss mechanism is used to explain this ultrafast rearrangement process, whereby a series of sequential transfers of individual protons resulting in overall charge transport.[5–7] Both experimental and theoretical efforts have been made in investigating the structures and ultrafast dynamics of the hydrated proton complex, from gas phase protonated water clusters[8–16] to the hydrated proton in the condensed phase.[7,17–26] The vibrational spectra of acidic solutions provide essential information on the ultrafast dynamics and various structures of the excess proton.[21,22,24,26–28] In the linear infrared[28–30] and Raman[24,31] spectra of acidic solutions, the “proton continuum" presents as a broad continuous absorption spanning the mid-IR from below 1000 cm^{-1} up to 3000 cm^{-1}. Even though rich information about the structure, H-bonding environment, and dynamics of aqueous species can be obtained from vibrational spectroscopy,[18] the broad featureless spectrum of the excess proton eludes straightforward interpretation.

To address this issue, gas-phase vibrational spectroscopy of small protonated water clusters has provided invaluable insight on the fundamental geometries and motions of the excess proton. By carefully analyzing IR spectra of clusters ranging from hy-

dronium H_3O^+ to larger clusters $H^+(H_2O)_n, n = 2-28$,[10–12,14,32] researchers have described the structure of the aqueous proton within the framework of two idealized structures. On one end, the excess proton localizes on one water to form a hydronium ion with a particularly tight first solvation shell, known as the Eigen species $H_9O_4{}^+$.[33,34] On the other extreme, the proton is equally shared between two flanking waters, behaving collectively as the Zundel complex $H_5O_2^+$.[31] In the gas phase, the spectra of these two species display distinguishable sets of resonances that reflect the complexes' inherent molecular symmetries, and thus have been used to broadly categorize clusters of differing sizes as corresponding to Eigen-like or Zundel-like geometries. In particular, the protonated water hexamer $H^+(H_2O)_6$ is the smallest cluster for which both two structural motifs coexist at low temperature. In the experiment conducted by Asmis and coworkers, the IR spectra of these two isomers were decomposed via double-resonance spectroscopy, revealing distinct Eigen and Zundel forms whose resonances were significantly broadened and coupled due to anharmonicity in their nuclear potentials, as revealed by *ab initio* molecular dynamics (AIMD) simulations.[32]

Within the last few years, multiple simulation studies have begun to provide insight into the broad features in the aqueous-phase proton spectrum. With the aid of molecular dynamics simulations using the Multi-State Empirical Valence Bond (MS-EVB) force field,[35,36] the spectrum of the aqueous proton was modelled at the harmonic level, revealing spectral trends with the geometry of the hydrated proton complex, the extent of vibrational delocalization, and the mixture of stretching and bending character in the normal modes.[30] Even at the harmonic level, the study uncovered that the vibrations of the excess proton are highly mixed and delocalized, requiring a careful interpretation of the vibrational bands. Another landmark study combined linear IR and Raman spectroscopies with anharmonic local-mode spectral calculations on protonated clusters drawn from *ab initio* simulations.[29] This study

treated the stretching motions of the excess proton one-dimensionally, applying a discrete variable representation (DVR) of the Schrödinger equation to the proton stretch with potential energy also calculated with DFT at the B3LYP level. This study predicted the presence of asymmetric “Zundel-like" species in solution, similar to Zundel's original conception and later supported by ultrafast IR experiments.[24,26,37] Despite the contributions these studies have played in illuminating the nature of the aqueous excess proton, the multidimensional anharmonic nature of the vibrational potential was not addressed, which have been investigated in small gas-phase protonated water clusters.[13,16,38]

Recently, the 2D IR spectrum of the aqueous excess proton was measured to investigate the vibrational potentials of the various modes and to directly observe the effects of anharmonic mode mixing.[24,26] Excitation of the proton stretch mode at 1200 cm^{-1} produces an excited state absorption between the first and second vibrational excited states at higher frequency than the ground state bleach.[24] This indicates that the vibrational potential of the excess proton is strongly confined by two waters with Zundel-like vibrational behavior, rather than associating with solely with one water as predicted for a hydronium species. A subsequent 2D IR study spanning the entire mid-IR found that cross peaks between every main feature imply that one predominant motif describes the aqueous proton complex.[26] The polarization-dependent cross peaks between all of the main features can be self-consistently explained by a persistent Zundel-like core around the aqueous proton. However, the relationship between the molecular configurations of aqueous proton complexes and the vibrational potentials of their highly anharmonic modes has yet to be understood. Thus, to capture the essentials of the vibrational spectrum of the hydrated proton complex, more rigorous theoretical tools should be applied for analysis.

Calculating the vibrational anharmonicity and mode mixing has previously been more successful in small protonated water clusters. Vendrell, Meyer and coworkers

applied multiconfiguration time-dependent Hartree (MCTDH) method to decipher the spectrum of $H^+(H_2O)_2$ successfully.[13] For larger gas-phase clusters, the vibrational self-consistent field/virtual state configuration interaction (VSCF/VCI) approach was successfully applied to reproduce the IR spectra of $H^+(H_2O)_3$ and $H^+(H_2O)_4$.[16,38,39] These high-level quantum calculations are based on highly accurate *ab initio* potential energy surfaces and dipole moment surfaces (PES/DMS) of protonated water clusters that some of us developed.[40–42] The VSCF/VCI approach and accurate PES/DMS have enabled access to the anharmonic and multi-dimensional nuclear potentials to disentangle the complicated spectra of protonated water clusters. However, as the size of clusters gets larger, such as in the cases of $H^+(H_2O)_6$ or aqueous proton complexes, it becomes unfeasible to conduct full-dimensional vibrational analysis due to the high dimensionality and cost of potential calculation.

To overcome the dimensionality limitations, the local monomer approximation was developed to calculate the IR spectra of larger systems.[43] This approximation reduces computational cost by breaking a large system into smaller local monomer subgroups and discarding the coupling constants between vibrational modes on different local monomers. The spectrum of the whole system is a sum of contributions of vibrations from each defined monomer. This approximation has proved to be useful and accurate for calculating the IR spectra of the liquid and ice forms of H_2O and D_2O, capturing broad, anharmonic features such as the bend-libration combination band at 2200 cm^{-1} in H_2O.[44–47] Thus, it becomes natural to apply the local monomer approximation on the structures of the aqueous proton and efficiently generate accurate anharmonic vibrational spectra for the multiple possible configurations in the liquid phase.

In this study, we extend the local monomer approximation to VSCF/VCI calculations of hydrated proton clusters as a technique to analyze and interpret the IR spectrum of the aqueous proton. Hydrated proton configurations were drawn from 800 $H^+(H_2O)_6$ geometries accessed from aqueous-phase MS-EVB trajectories. As

mentioned above, protonated hexamers constitute the smallest cluster that incorporates Eigen-like and Zundel-like species, providing a workable trade-off between calculation cost and incorporation of many-body effects from the solvation environment. $H^+(H_2O)_6$ can be rewritten as $[H^+(H_2O)_2](H_2O)_4$, where we define the local monomers as the central $H^+(H_2O)_2$ and four remaining water monomers. The vibrational spectrum of the aqueous proton can be approximated as the spectral contribution from central $H^+(H_2O)_2$ in those $[H^+(H_2O)_2](H_2O)_4$ clusters. To benchmark the local monomer approximation, we first compare our calculations of the gas-phase Eigen and Zundel isomers of the protonated water hexamer to the experimental spectra mentioned above, finding excellent agreements with peak position and intensity, even for subtler features. We then present the IR spectrum obtained from the VSCF/VCI calculations on protonated hexamer geometries drawn from aqueous MS-EVB simulations.[30] We also find agreement with the experimental aqueous-phase linear spectrum, and we decompose the spectrum based on vibrational character to assign the various regions across the mid-IR. The difference with the harmonic spectrum underscores the importance of taking into account the full anharmonicity in the vibrational potentials of the aqueous proton. We then correlate shared proton stretch frequency with various structural parameters and decompose the full spectrum by geometry to uncover spectral trends as proton configurations transition from behaving more Zundel-like to more Eigen-like. This information can aid the interpretation of the experimental infrared spectrum in each IR frequency range. The high-level treatment of the anharmonicity in these calculations also reveals substantial mode mixture of different proton-associated vibrations, in particular the proton stretching and bending modes of Zundel-like complexes.

7.2 Computational Details

To analyze the spectrum of the aqueous proton, we made use of 800 clusters extracted from the snapshots of MS-EVB simulations performed in Ref. 30. The molecular dynamics simulations were performed using 256 SPC/Fw water molecules and one excess proton in the presence of a chloride ion. This reactive MD simulation was based on MS-EVB 3.2 model. The system was equilibrated in constant NVT ensemble for 1 ns with density 1.0 gm/cm^3 and room temperature 298 K. The time step was set as 0.5 fs with Nosé-Hoover chain thermostats. 1 ns constant NVE trajectories were run afterwards for generating small clusters. We used the same criteria in identifying the proton position as in Ref. 30: from instantaneous configurations of the MS-EVB trajectory, we extracted clusters of molecules centered on a H atom that participates in an O_1-H$\cdots O_2$ hydrogen bond, selecting them on the basis of the proton sharing parameter $\delta R_{OH} = |r_{O_1H}\text{-}r_{O_2H}|$. Among the three protons of the hydronium moiety, the proton with the lowest δR_{OH} was chosen as the excess proton. We selected 800 clusters from the MS-EVB trajectory snapshots with all waters whose oxygen atoms were within 5Å to the defined proton, written as $H^+(H_2O)_n$, $n \approx 16-18$. From each $H^+(H_2O)_n$ cluster, we further decreased the cluster size to $H^+(H_2O)_6$ which only included the proton and its closest six water molecules. We identified the central $H^+(H_2O)_2$ structure with the proton and two closest water monomers for all 800 $H^+(H_2O)_6$ clusters and 800 $H^+(H_2O)_n$, $n \approx 16-18$ clusters. The $H^+(H_2O)_n$, $n \approx 16-18$ clusters were used for harmonic analysis to compare with the previously calculated harmonic spectra.[30] The $H^+(H_2O)_6$ clusters were used for both harmonic analysis and VSCF/VCI calculation based on local monomer approximation. The distribution of 800 clusters according to proton asymmetry coordinate (seen in Table 7.1) was kept the same as that in total data set. More details about the MD simulations are referred to ref 30.

Table 7.1 Population distribution of 800 chosen protonated water clusters from MS-EVB trajectory

δR_{OH} (Å)	Number	Population (%)	MS-EVB population(%)
0.0-0.1	184	23	23
0.1-0.2	240	30	30
0.2-0.3	248	31	31
0.3-0.4	112	14	14
0.4-	16	2	2
R_{OH} (Å)	Number	Population (%)	MS-EVB polulation(%)
1.00-1.05	82	10	11
1.05-1.10	278	35	35
1.10-1.15	290	36	36
1.15-1.20	142	18	17
1.20-	8	1	1
Zundel-like	424	53	53
Eigen-like	376	47	47

Examples of the two sizes of clusters, $H^+(H_2O)_n$ and $H^+(H_2O)_6$ are shown in the right panel of Figure 7.4 along with their central $H^+(H_2O)_2$ structure encircled in red. This central $H^+(H_2O)_2$ can be identified as proton with two water monomers or the hydronium H_3O^+ with its closest water according to different proton positions. We classified all cluster structures according to the proton asymmetry δR_{OH}, with the criterium of $\delta R_{OH} = 0.2$ Å to identify Zundel-like (< 0.2Å) and Eigen-like (≥ 0.2Å) species. As shown in Table 7.1, among those 800 $H^+(H_2O)_6$ clusters, we obtain 53% Zundel-like clusters and 46% Eigen-like clusters which agrees with previous results.[29,30] Further decomposition by δR_{OH} of the total trajectory and the 800 analyzed configurations is presented in the SI and indicates that the clusters are representative of the trajectory.

For each $H^+(H_2O)_6$ cluster, we located the central $H^+(H_2O)_2$ as describe above. This central $H^+(H_2O)_2$, denoted as the "special pair,"[48,49] is the smallest structure to that includes both Zundel-like and hydronium-like geometries and is the largest local monomer that we can apply in VSCF/VCI calculations. Larger structures like $H^+(H_2O)_3$ require much more computational cost mainly because of the increasing

number of normal modes. In the local $H^+(H_2O)_2$ monomer analysis, we conducted normal mode analysis on the central $H^+(H_2O)_2$ structure with all remaining water monomers fixed at their geometries. For all 800 $H^+(H_2O)_6$ clusters, we conduct VSCF/VCI calculation using normal vectors in the local Zundel monomer analysis. For each cluster, we choose all vibrational modes from local Zundel monomer analysis with harmonic frequency larger than 700 cm^{-1}, resulting in 12-15 modes for each cluster. Here, we did not add any imaginary frequencies because it has been demonstrated that the imaginary frequencies do not contribute much to the total vibrational spectra.[30] We apply 4-mode representation of the potential (4MR) and generate the excitation space with maximum sum of singles, doubles, triples and quadruple excitations as 9, 8, 7, 6. The final size of the Hamiltonian matrix for each cluster is around 10,000 $\times$ 10,000. After obtaining the vibrational wavefunction and associated vibrational energies for all ground and excited VCI states, we calculate the quantum expectation values of OH and OO distances in the central $H^+(H_2O)_2$ structure using the ground state wavefunction. For the two isomers of gas phase $H^+(H_2O)_6$ cluster, to obtain the total spectra, we also conduct the local water monomer analysis of each isomer and then VSCF/VCI calculations of each water molecules separately. The spectra of each isomer include the contribution from central $H^+(H_2O)_2$ structure and also all remaining water molecules. All the above VSCF/VCI calculations are finished using code MULTIMODE which can conduct calculations using exact normal-coordinate Watson Hamiltonian. The local monomers for these two isomers include (1) central $H^+(H_2O)_2$ which is a proton with two water monomers for the Zundel isomer and hydronium with the closest water monomer for the Eigen isomer (2) each of four remaining water monomers. The VSCF/VCI spectrum of each isomer is sum of contributions from all above local monomers.

Both harmonic analysis and VSCF/VCI calculations were done based on accurate *ab initio* many-body PES/DMS. This PES/DMS has already been verified to be

highly accurate in describing the structures, energies, and vibrational properties of different sizes of protonated water clusters.[16,38,41,42,50,51]

7.3 Vibrational Spectra of Two Isomers of $H^+(H_2O)_6$

Before we show the vibrational spectra of aqueous proton, we first illustrate the accuracy of the local monomer VSCF/VCI calculations with two important isomers of the gas-phase protonated water hexamer $[H^+(H_2O)_2](H_2O)_4$, known as the Zundel and Eigen isomers. The Zundel isomer consists of the symmetric “Zundel" core with four solvating water molecules, while the Eigen isomer has the standard “Eigen" core with additional two waters accepting H-bonds from the waters in hydronium's first solvation shell. Their calculated spectra and comparisons with experiment[32] are shown in Figure 7.1. Their double harmonic spectra are also plotted in Figures 7.2 and 7.3. The harmonic spectra appear qualitatively different from the experimental spectra with peak position inaccuracies of several hundred wavenumbers for some features. However, upon including anharmonicity and mode coupling, the VSCF/VCI spectra achieve excellent agreement with experiment in terms of frequency positions and relative intensities, even with the local $H^+(H_2O)_2$ monomer and local water monomer approximation. Additionally, the agreement between the calculated and experimental spectra for the Eigen isomer demonstrate that the choice of a local $H^+(H_2O)_2$ monomer can also be applied for Eigen-like configurations.

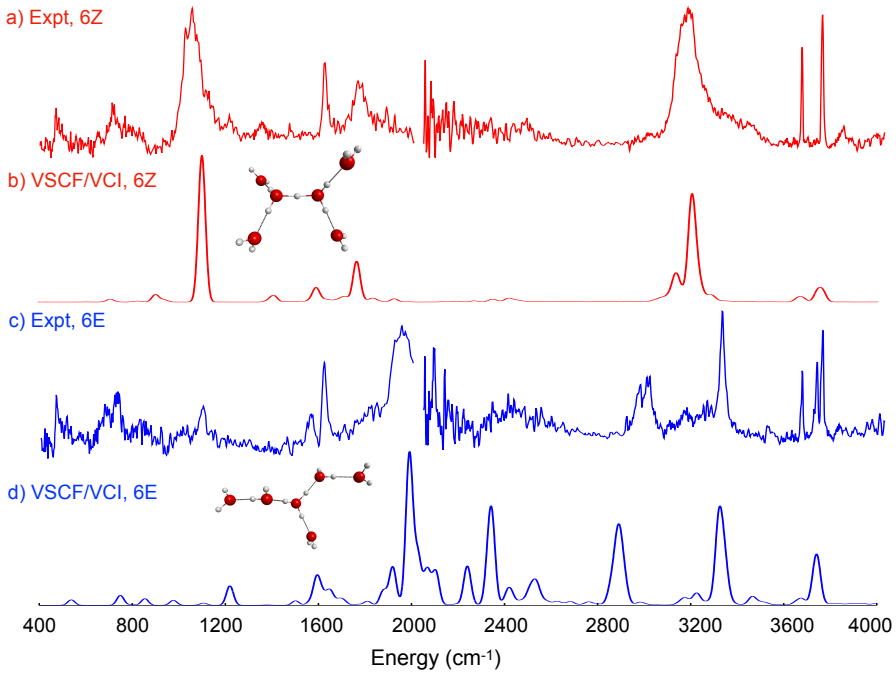

Figure 7.1 Vibrational spectra of (a)-(b) Zundel (6Z) and (c)-(d) Eigen (6E) isomers of protonated water hexamer from experiment[32] and VSCF/VCI calculations.

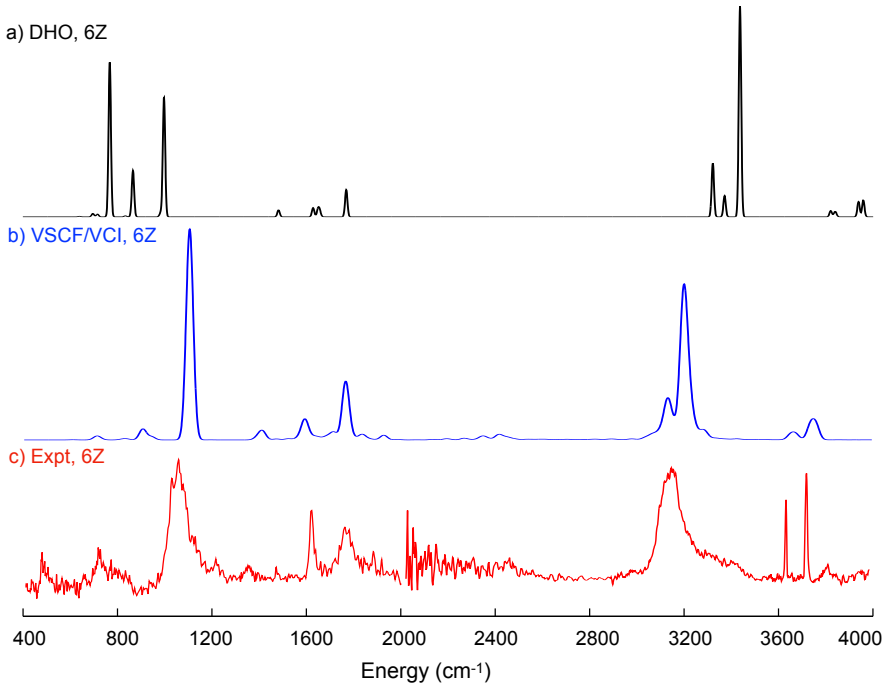

Figure 7.2 Calculated spectra of Zundel isomer of $H^+(H_2O)_6$

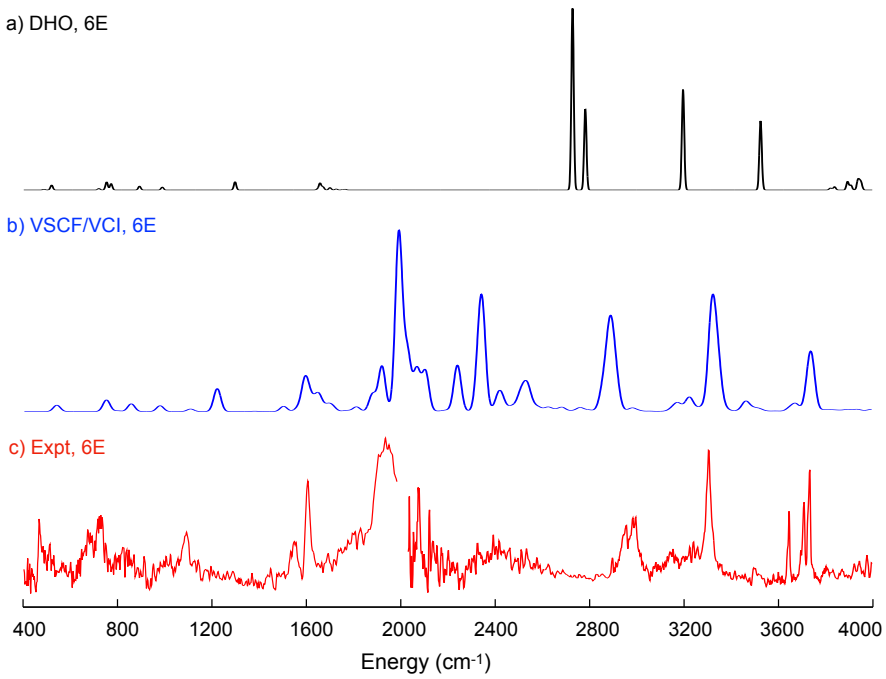

Figure 7.3 Calculated spectra of Eigen isomer of $H^+(H_2O)_6$

Detailed peak frequencies and assignments from experiment, VSCF/VCI, and harmonic analysis are listed in Table 7.2. Briefly, from the VSCF/VCI calculation, the Zundel isomer displays a strong proton stretch band at 1102 cm^{-1} which is more than 100 cm^{-1} blue shifted from its harmonic frequency. Another signature band of the Zundel isomer is the bending mode of the proton's hydration waters at around 1760 cm^{-1}, which has relatively large intensity due to coupling with the proton stretch. The band at 3167 cm^{-1} from experiment is verified as the OH stretch of the two flanking water monomers within the central $H^+(H_2O)_2$. The harmonic analysis predicts the frequency at around 3350 cm^{-1} which is almost 200 cm^{-1} higher than both experiment and VSCF/VCI calculations. The shift of important signature bands relative to their harmonic predictions is even larger in the Eigen isomer, as seen in Figure 7.3 and Table 7.2. Harmonic analysis produces three hydronium stretches at 3197, 2783 and 2728 cm^{-1}, but experiment demonstrates three strong and broad bands at 3007, 2425 and 1951 cm^{-1}. With the VSCF/VCI approach, we successfully reproduce these three important bands and verify their origins. The hydronium stretches are

redshifted 200-700 cm^{-1} from their harmonic counterparts due to the anharmonicity of the system and extensive mode coupling within the local monomer. As introduced before, this phenomenon has been seen in vibrational analyses of other protonated water clusters, $H^+(H_2O)_3$ and $H^+(H_2O)_4$, where the VSCF/VCI approach works very well while harmonic and some post-harmonic approaches (like VPT2) cannot fully explain the experimental spectra.[16,38]

Table 7.2 Peak positions (cm^{-1}) of two isomers of $H^+(H_2O)_6$in the experimental spectra and calculated (harmonic and VSCF/VCI) values along with detailed assignments based on VSCF/VCI spectrum

Zundel isomer of $H^+(H_2O)_6$			
Exp. (cm^{-1})	Theory, VSCF/VCI (cm^{-1})	Theory, harmonic (cm^{-1})	Assignment
3737	3739, 3762	3938, 3958	w free O-H asym-str
3651	3655, 3677	3844, 3856	w free O-H sym-str
3167	3128, 3136	3353, 3371	z O-H str
1759	1765	1796	z proton bend
1618	1633, 1643	1671, 1692	w bend
1050	**1102**	**964, 765**	z proton str
Eigen isomer of $H^+(H_2O)_6$			
Exp. (cm^{-1})	Theory, VSCF/VCI (cm^{-1})	Theory, harmonic (cm^{-1})	Assignment
3738	3744, 3750	3939, 3953	w free O-H asym-str
3714	3730	3895	w free O-H str
3651	3650, 3677	3825, 3840	w free O-H sym-str
3312	3319	3525	w H-bonded O-H str
3007	**2895**	**3197**	h O-H str
∼2425	**2345**	**2783**	h O-H str
1951	**1991**	**2728**	h O-H str
1618	1587,1619	1656,1669	w bend
1097	1219	1297	h umbrella

bold font are frequencies of proton stretch/hydronium stretch. Experimental data are from refs. 32

7.4 Vibrational Spectra of 800 $H^+(H_2O)_6$ clusters

Before presenting the anharmonic spectrum of the aqueous proton, we briefly summarize the features of the harmonic spectra from local $H^+(H_2O)_2$ monomer analysis of two sizes of clusters, $H^+(H_2O)_n$, $n \approx 16-18$ and $H^+(H_2O)_6$ (Figure 7.4). For both sizes of clusters, the spectrum of their central $H^+(H_2O)_2$ consists of a broad con-

tinuum from below 1000 cm^{-1} to above 3000 cm^{-1}. This spectral shape agrees with the previously calculated difference spectral density for aqueous proton at the B3LYP level (Figures 3.e and 3.f in Reference 30). Even though the spectrum in Figure 7.4 is the spectral contribution from central $H^+(H_2O)_2$, the spectrum in the previous study was calculated from the difference spectral density between protonated water clusters and bulk water clusters.[30] The harmonic spectrum includes contributions from both Zundel-like $H^+(H_2O)_2$ cores and Eigen-like structures' central H_3O^+ and its closest water, which already produces the IR continuum of absorption. There are only small differences between the spectrum of the central $H^+(H_2O)_2$ moiety embedded in the $H^+(H_2O)_n$ and $H^+(H_2O)_6$ clusters, which implies that the central $H^+(H_2O)_2$ spectrum is more influenced by its first solvation shell and the excess proton than by the solvation water beyond the first four hydration molecules. These observations indicate that calculating the vibrational spectrum with a central $H^+(H_2O)_2$ in a $H^+(H_2O)_6$ cluster instead of in a $H^+(H_2O)_n$ cluster is a qualitatively reasonable approximation. Additionally, since the broad continuum is recovered using a local $H^+(H_2O)_2$ monomer, the VSCF/VCI calculation of these structures should also be able to recover the main features of the aqueous excess proton spectrum. To emphasize the local $H^+(H_2O)_2$ monomer strategy, we will denote the clusters as $[H^+(H_2O)_2](H_2O)_4$ rather than $H^+(H_2O)_6$ in the following text.

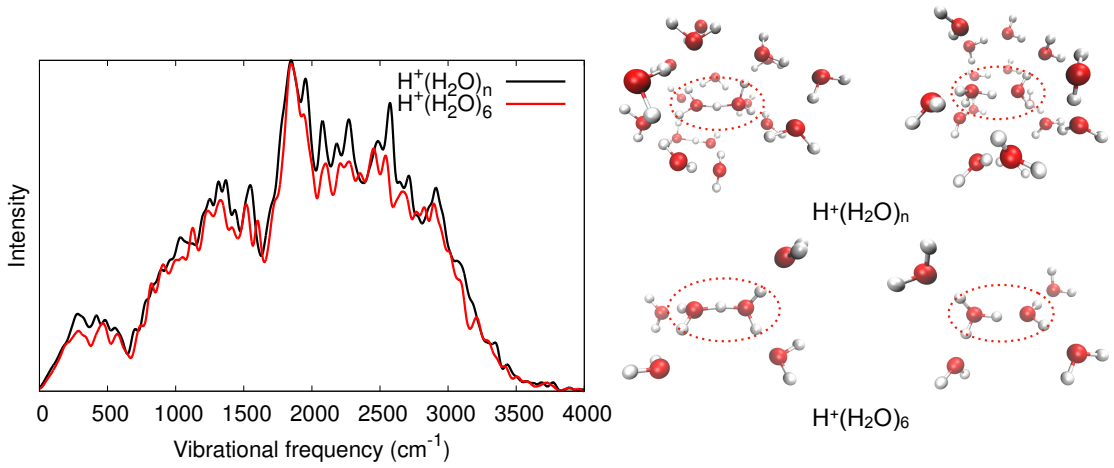

Figure 7.4 Double harmonic spectra of $H^+(H_2O)_2$ structure in 800 protonated water clusters with different sizes. $H^+(H_2O)_n$ has 16-18 water molecules and $H^+(H_2O)_6$ has proton with 6 water molecules. The harmonic frequencies are calculated from local $H^+(H_2O)_2$ monomer analysis where central $H^+(H_2O)_2$ structures are circled in the right panel for different clusters.

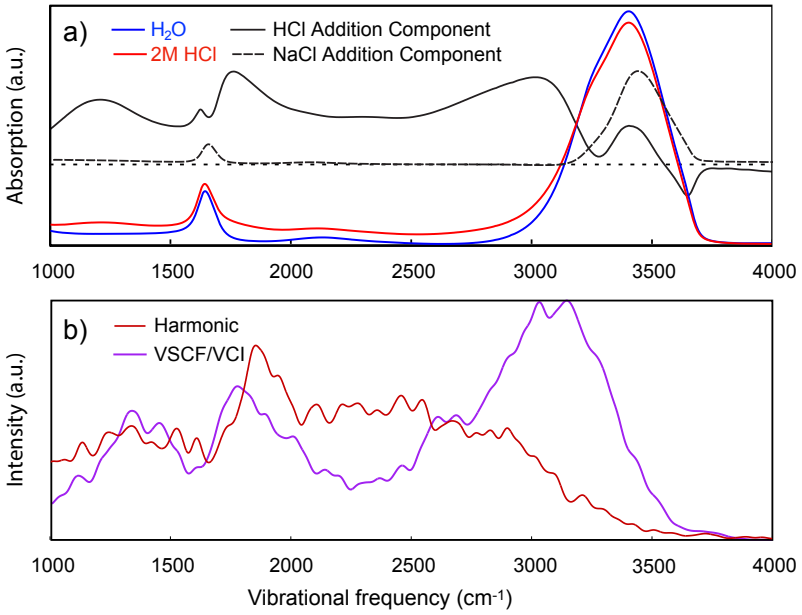

Figure 7.5 Infrared spectrum of the aqueous proton from experiment and VSCF/VCI calculations. The experimental spectra include neat water (blue), 2 M HCl (red) and the maximum entropy difference component (black). The theoretical (VSCF/VCI) spectrum is spectra contributed from central $H^+(H_2O)_2$ part of 800 $[H^+(H_2O)_2](H_2O)_4$ clusters.

To analyze the aqueous proton spectrum, we begin with an introduction to the experimental linear IR spectral features that grow in upon introduction of strong acid. The experimental spectrum associated with aqueous HCl solution is presented as the second spectral component derived from the maximum entropy analysis of the acid concentration series. We find that the component resembles an acid-water difference spectrum consisting of broad features centered around 1200 cm^{-1}, 1750 cm^{-1}, 3000 cm^{-1}, with continuous absorption between each of these maxima and also a small positive peak around 3500 cm^{-1}. Since the maximum entropy analysis cannot extract components due to solvation of the H^+ or the Cl^- individually, we also present the results of the same maximum entropy analysis on a NaCl concentration series, which shows features centered at 1640 cm^{-1} and 3470 cm^{-1}. The 3470 cm^{-1} peak in both the HCl and NaCl spectra are centered at the same frequency in the ATR spectrum, but it is nontrivial to directly interpret these spectral contributions

in highly-congested spectral regions.

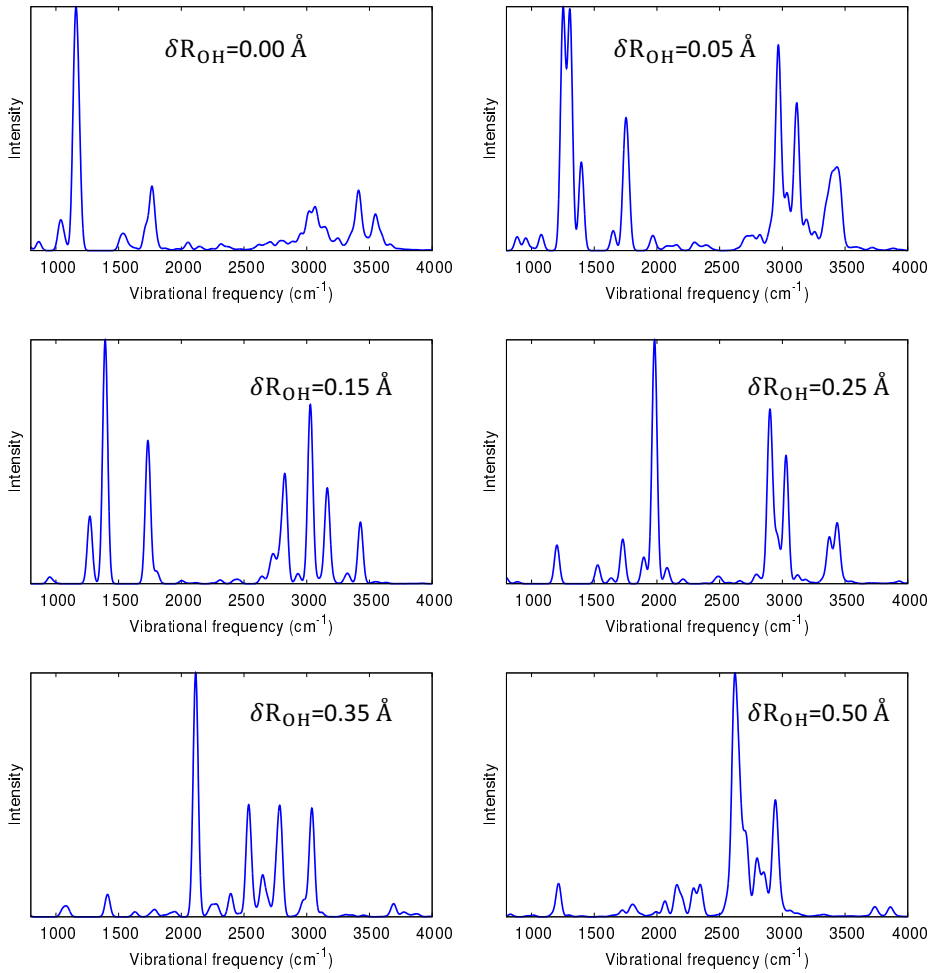

Figure 7.6 Decomposition of the calculated spectra of aqueous proton according to different $\langle \delta R_{OH} \rangle$ values.

The calculated VSCF/VCI spectrum of the $H^+(H_2O)_2$ local monomers summed over 800 $[H^+(H_2O)_2](H_2O)_4$ configurations (Figure 7.5b) consists of a continuum and three broad bands, consistent with experiment. Examples of VCI spectra for individual clusters are presented in Figure 7.6. The first signature band spans 1000-1500 cm^{-1} with center frequency at 1200 cm^{-1} in experiment but is blueshifted to 1300 cm^{-1} in the VSCF/VCI calculations. According to previous analyses, the feature has been assigned to both asymmetric proton stretches in Zundel-like configurations [13,30] and umbrella modes in Eigen-like configurations. [52] The second signature band is centered at 1750 cm^{-1} in both the harmonic and VSCF/VCI and harmonic calculations,

but the bandwidths and relative intensities of the 1750 cm^{-1} and 1200 cm^{-1} features are better captured by the anharmonic calculations. The 1750 cm^{-1} band has been assigned to bending motions of the waters flanking the excess proton,[10,22,24,30] but other studies have demonstrated that highly redshifted hydronium OH stretches in gas-phase $H^+(H_2O)_{21}$ clusters are also located at this frequency.[14]

Between 1900 and 3000 cm^{-1} lies the proton continuum, which has been assigned to both hydronium stretches in Eigen-like configurations[53] and OH stretches of the flanking waters in Zundel-like configurations.[26,29] The third signature band is around 3000 cm^{-1} both in experiment and in our calculations. This band in the VSCF/VCI spectrum is more prominent than in the harmonic calculation. This feature has also been associated with Zundel-like configurations, arising from OH stretches of the two flanking waters around the central excess proton.[10,13,22] To assess the various assignments across the mid-IR and to explore the influence of anharmonic mode-coupling, we will decompose this spectrum by geometric variables and vibrational character below.

The improved accuracy of the VSCF/VCI spectrum over the harmonic spectrum underscores the importance of anharmonic effects on the IR spectrum of the aqueous proton complex. The most apparent difference between the two methods is the intensity of the continuum across 1900-3000 cm^{-1}. According to harmonic analysis, this continuum is assigned as both hydronium-like OH stretches in different distorted Eigen-like clusters and OH stretches in flanking waters. However, the extremely large harmonic intensity and broad bandwidth of the hydronium-like stretches dominate over the flanking water stretches in this region. In the VSCF/VCI spectrum, strong anharmonicity and mode mixing make hydronium stretches undergo significant redshifts and decreases in intensity, as in the cases of smaller gas-phase clusters.[50]

While the VSCF/VCI method is a great improvement over a harmonic treatment, the difference between the anharmonic calculation and the experimental spectrum

indicates that the special pair local monomer spectrum does not fully represent the experimental aqueous proton spectrum. For instance, the experimental band at 1200 cm^{-1} is blueshifted to 1300 cm^{-1} in the VSCF/VCI spectrum. Besides the lack of mode coupling to other low-frequency modes (O$\cdots$O stretches for example) within the local monomer, there may be some uncertainty associated with the MS-EVB model in providing correct statistics of aqueous protons structures. The MS-EVB model reproduces the experimental radial distribution functions better than other methods,[54] but there is still some slight over-structuring that may influence the accessible configurations. We also expect the VSCF/VCI spectra can be further improved with more normal modes included in the calculation. Finally, the intensity of the 3000 cm^{-1} feature is larger than in experiment, but there is variability in the literature on the measured intensity of this feature,[29,30] subject to details of experimental collection. Even with the above caveats, this approach is cost-effective and reliable for calculating highly anharmonic IR spectra and analyzing the aqueous proton spectrum.

7.4.1 Decomposition of Spectrum by Vibrational Character

To assess the various assignments outlined above, we determined the spectral contributions from different vibrational components. For this analysis, the 800 clusters were binned into Zundel-like and Eigen-like configurations based on the proton asymmetry parameter δR_{OH}.[29,30] Due to the quantum delocalization of the proton in the VSCF/VCI calculations, the quantum expectation value, $\langle \delta R_{OH} \rangle$, with cutoff of 0.2 Å was used. As seen in Figure 7.7a), the spectrum of Zundel-like ($\langle \delta R_{OH} \rangle < 0.2$Å) clusters display three intense and broad bands: 1300 cm^{-1}, 1750 cm^{-1} and 3000 cm^{-1}, whereas the spectrum due to Eigen-like configurations appears as a broad continuum from 1000-3500 cm^{-1} with maxima around 2000 cm^{-1} and 2600 cm^{-1}. We next used geometric cutoffs in normal mode displacements to identify the vibrational character. Normal modes with OH stretching displacements greater than 0.01Å were counted as

either proton stretching or flanking water stretching modes, depending on location of the H atom in the local monomer. Bending modes consisted of normal modes where both flanking waters changed angle by at least 1.0°, and umbrella modes consisted of normal modes where all three HOH angles of H_3O^+ changed by more than 0.8° with the same phase. Modes that consisted of both proton stretch and flanking bend character were also considered. After identifying the vibrational character of the normal mode basis in each cluster, for each VSCF/VCI state we multiplied the square of each of its normal mode's VCI coefficients with their respective harmonic intensities. The results of this procedure summed over clusters are presented in Figure 7.7b-d. Multiplying the square of VCI coefficient with normal mode's harmonic intensity is a good approximation to identify the spectrum contribution from different normal mode basis, which has been used to simulate the vibrational spectrum of the formic acid dimer.[55]

The vibrational character decomposition is shown for all configurations in Figure 7.7b), with Zundel-like and Eigen-like decompositions in Figure 7.7c) and d), respectively. For Zundel-like configurations, the proton stretch has a significant contribution from 800-1600 cm^{-1} and 1700-2000 cm^{-1} while the flanking water OH stretch mainly contributes to the region in 2500-3500 cm^{-1}. Modes with primarily flanking water bend character and proton stretch-bend mixed character overlap strongly at 1750 cm^{-1}. Umbrella modes do not make significant contributions to the spectrum Zundel-like complexes. In Eigen-like configurations (Figure 7.7d), the proton stretches span a broad region from 1500-2600 cm^{-1} with a maximum at 2000 cm^{-1}, whereas the flanking water stretches span 2500-3500 cm^{-1}. The spectral distribution of flanking waters in Eigen-like complexes is broader than those in Zundel-like configurations since the OH stretches on the hydronium and nearest water differ.[29] There are bending modes of Eigen-like complexes at 1750 cm^{-1}, but they are weaker than those from Zundel-like complexes and there is less mixing with the proton stretch. Finally, there

is weak umbrella mode character at 1200 cm^{-1}.

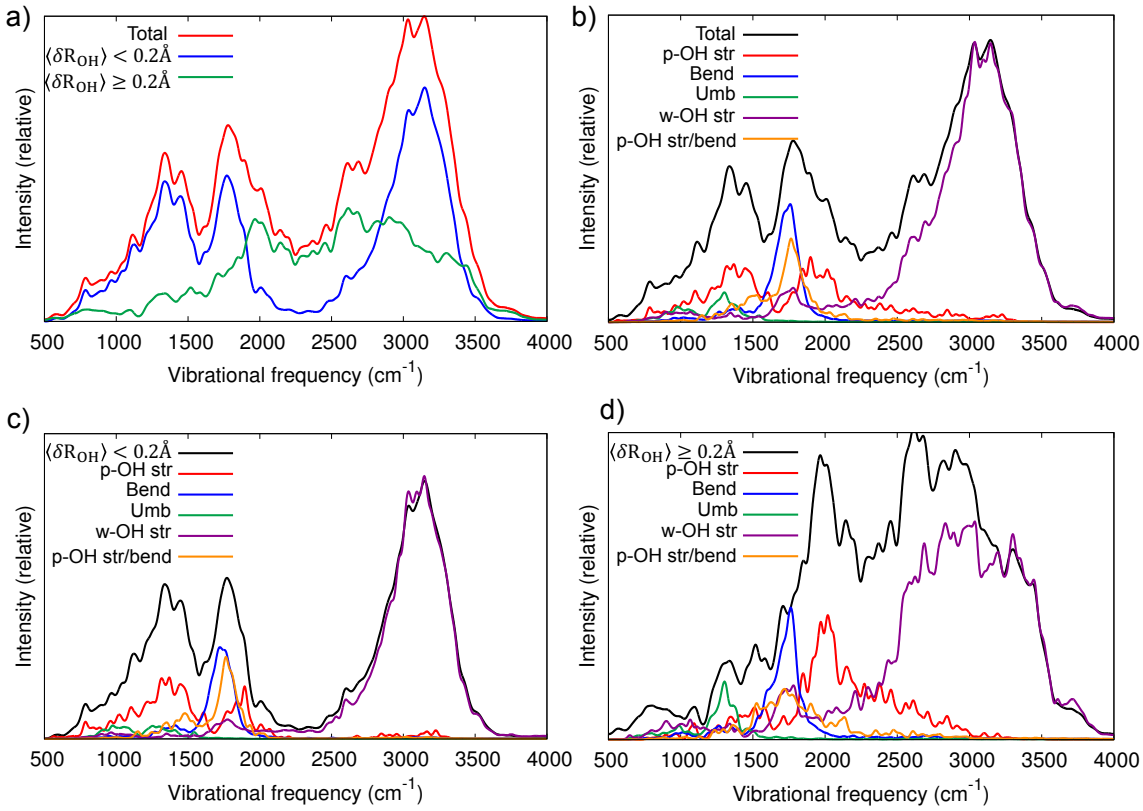

Figure 7.7 a) Calculated spectra of the aqueous proton from all 800 clusters, $\langle \delta R_{OH} \rangle < 0.2$Å (Zundel-like) clusters, and $\langle \delta R_{OH} \rangle \geq 0.2$Å (Eigen-like) clusters. b) Decomposition of the total spectra into different components, with p-OH str as proton stretch, bend as flanking water bend, Umb as hydronium umbrella motion, w-OH str as flanking water stretch, p-OH str/bend as motion which has both proton stretch and flanking water bend character. c)-d) Decomposition results for (c) Zundel-like and (d) Eigen-like configurations.

This decomposition assists in clarifying the various assignments presented above from the literature. At 1200 cm^{-1} in the total spectrum (Figure 7.7b), the proton stretch of Zundel-like configurations dominates, with little contribution from umbrella modes of Eigen-like geometries. The intense and broad band from 1600-2000 cm^{-1} comes from multiple sources, listed in order of highest to lowest importance: flanking water bends and mixed stretch-bend modes in Zundel-like configurations, proton stretches in Zundel-like and Eigen-like clusters, and bending modes in Eigen-

like configurations. This heterogeneity explains why there has been controversy in the assignment of this region, but all of these contributions should be taken into account when analyzing this region of the IR spectrum. The continuum from 2000-2700 cm^{-1} consists of contributions from Eigen-like proton stretches and flanking water stretches, while flanking water stretches in both Eigen-like and Zundel-like complexes are found at frequencies higher than 2700 cm^{-1}. In general, flanking water stretches do not show strong mixing with the other modes and therefore do not donate their high intensity to those modes. As a result, the flanking water stretches become distinguishable on top of the continuum.

7.4.2 Influence of Structural Parameters on Proton Stretch Frequency

To disentangle structural information encoded in the calculated vibrational spectrum, we conduct a statistical analysis of several important proton-related structural parameters (R_{OO}, R_{OH}, δR_{OH}) and the associated proton stretch vibration in each chosen $[H^+(H_2O)_2](H_2O)_4$ cluster. In each local $H^+(H_2O)_2$ monomer, δR_{OH} is the previously defined proton asymmetry parameter, R_{OO} is the distance between the oxygen atoms of the two flanking waters, and R_{OH} is the shortest distance between the excess proton and one of the oxygens. Previous studies have demonstrated that the proton stretch frequency is highly sensitive to its local environment,[24,56,57] and these local parameters may each be useful for characterizing the relationship between proton stretch frequency and local monomer configuration. Recently, some of us analyzed the distribution of hydronium R_{OH} in $H_7O_3^+$ and $H_9O_4^+$ from classical MD and thermostatted Ring Polymer MD (TRPMD) at 100 K.[50] It was found that the hydronium OH distance significantly lengthens in TRPMD calculations, which reflects the strong nuclear quantum effects of the proton and is the main reason for large shifts in anharmonic vibrational spectra. To appropriately account for quantum delocalization of the proton, we also calculated the expectation value of each structural parameter

using the VCI ground state wavefunction for every cluster.

Figures 7.8a) and 7.8b) show the value of R_{OO} and δR_{OH} drawn from the classical simulation frames, and their expectation values from VSCF/VCI calculations. As seen in Figure 7.8a), there exists high correlation between R_{OO} and its expectation value, $\langle R_{OO} \rangle$, which indicates that the nuclear quantum effects do not have significant impact on the central oxygen atoms. On the other hand, Figure 7.8b) shows that the quantum expectation value of δR_{OH} decorrelates substantially from the values in its associated cluster's initial structure, owing to a much larger nuclear quantum effect of the proton. A similar decorrelation is observed between R_{OH} and $\langle R_{OH} \rangle$ (Figure 7.9). In the VSCF/VCI calculation, the proton delocalizes and explores a large region around the anharmonic potential energy surface, rather than remaining fixed at the initial structure. For flat, highly anharmonic potentials such as the proton stretch, the VSCF/VCI calculation therefore more accurately represents the delocalization of the proton in the vibrational ground state. In Table 7.3, we list the numbers of clusters in different δR_{OH} intervals based on initial structures and VSCF/VCI expectation values. From the nuclear quantum effects of the proton, the distribution of expectation values of δR_{OH} is skewed more to the extremes of δR_{OH} (specially to low $\langle \delta R_{OH} \rangle$, Figure 7.10) than the distribution of initial structures.

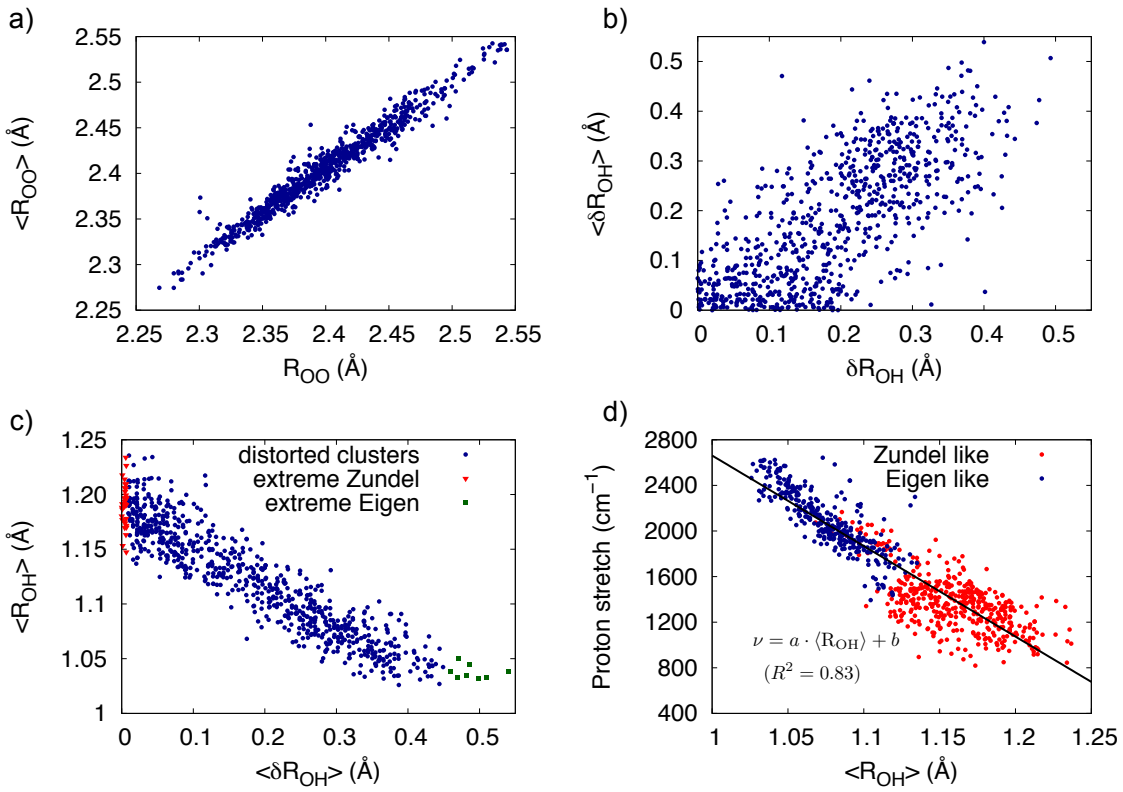

Figure 7.8 a) Distribution of R_{OO} and quantum expectation values $\langle R_{OO}\rangle$ from 800 clusters. b) Distribution of δR_{OH} and quantum expectation values, $\langle \delta R_{OH}\rangle$. c) Correlation between $\langle \delta R_{OH}\rangle$ and $\langle R_{OH}\rangle$. Extreme Zundel structures ($\langle \delta R_{OH}\rangle = 0.0$Å) are indicated in red triangles and extreme Eigen structures ($\langle \delta R_{OH}\rangle > 0.45$Å) are in green squares. d) Relationship between anharmonic proton stretch frequency and $\langle R_{OH}\rangle$ with linear least-squares fit (solid red line), $\nu = a \cdot \langle R_{OH}\rangle + b$ where $a = -7941.2$ cm^{-1}/Å , $b = 10603.0$ cm^{-1}. Red points are from Zundel-like ($\langle \delta R_{OH}\rangle < 0.2$Å) structures and blue points are from Eigen-like ($\langle \delta R_{OH}\rangle \geq 0.2$Å) structures.

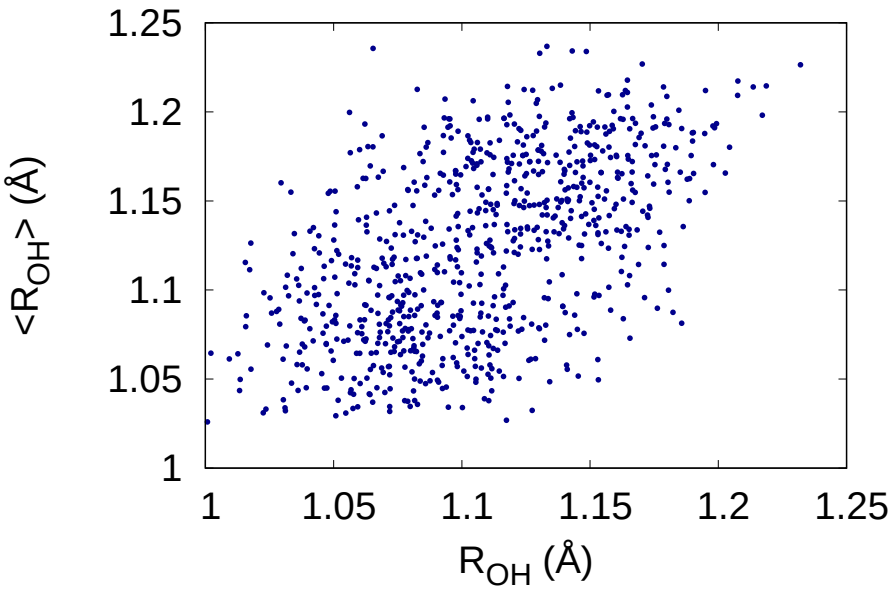

Figure 7.9 Scatter plot of R_{OH} in clusters and their expectation values $\langle R_{OH}\rangle$ from VSCF/VCI calculations

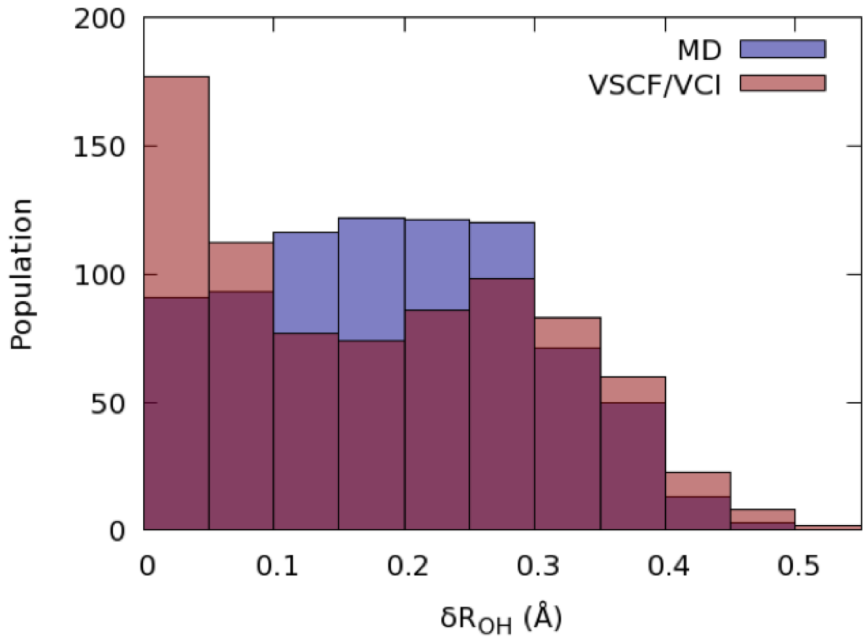

Figure 7.10 Distribution of δR_{OH} from 800 MS-EVB MD structures and their expectation values $\langle \delta R_{OH} \rangle$ from VSCF/VCI calculations

Table 7.3 Population distribution of 800 chosen protonated water clusters from inital structures in MS-EVB MD trajectory and VSCF/VCI calculations

MS-EVB MD					
δR_{OH} (Å)	0.0-0.1	0.1-0.2	0.2-0.3	0.3-0.4	0.4-
Number	184	240	248	112	16
VSCF/VCI					
$\langle \delta R_{OH} \rangle$ (Å)	0.0-0.1	0.1-0.2	0.2-0.3	0.3-0.4	0.4-
Number	287	152	185	143	33

Taking into account the strong quantum effects on proton positions, we next explore the relationship between structural parameters and proton stretch frequency. From Figure 7.11-7.14, we show the scatter plots for all three parameters separately. Generally, the initial values of R_{OH} or δR_{OH} only weakly correlate with anharmonic proton stretch frequency, but the frequency correlations show significant improvement with $\langle R_{OH} \rangle$ and $\langle \delta R_{OH} \rangle$. As to the parameter R_{OO} or $\langle R_{OO} \rangle$, from Figure 7.13, it can be seen that in Zundel-like structures, the anharmonic proton stretch decreases with longer $\langle R_{OO} \rangle$ while proton stretch frequencies in Eigen-like structures are less

sensitive to changes in $\langle R_{OO} \rangle$. Finally, among the initial and quantum expectation values of all three parameters, we find the best correlation between proton stretch frequency and $\langle R_{OH} \rangle$ (Figure 7.8d). Previous studies have raised issues with using δR_{OH} as a descriptive coordinate for the entire aqueous proton complex[29,57,58] due to the additional dependence of the proton potential on R_{OO} and the arbitrariness of δR_{OH} as a cutoff on a continuum of structures. Alternatively, R_{OH} has successfully been used to predict the red-shift of proton-related stretches in Zundel-like and Eigen-like protonated water clusters $H^+(H_2O)_n$, $n = 2-4$.[42,50,56] Even more recently, vibrationally averaged R_{OH} values were successfully analyzed to provide a unifying picture for predicting OH stretch frequencies in bulk water, flanking waters in aqueous proton complexes, and waters in the first solvation shell of halide anions.[59] As shown in Figure 7.8c), $\langle R_{OH} \rangle$ correlates well with $\langle \delta R_{OH} \rangle$ but comparison with Figure 7.11 illustrates that $\langle R_{OH} \rangle$ correlates better with proton stretch frequency. Interestingly, the correlation is weaker between $\langle R_{OH} \rangle = 1.1$ and $\langle R_{OH} \rangle = 1.2$, which suggests that incorporating other coordinates is necessary to better describe the proton stretch frequency for Zundel-like configurations. This likely arises from anharmonic coupling to other degrees of freedom such as bending modes, which are known to strongly couple to the proton stretch in the gas phase.[10,13]

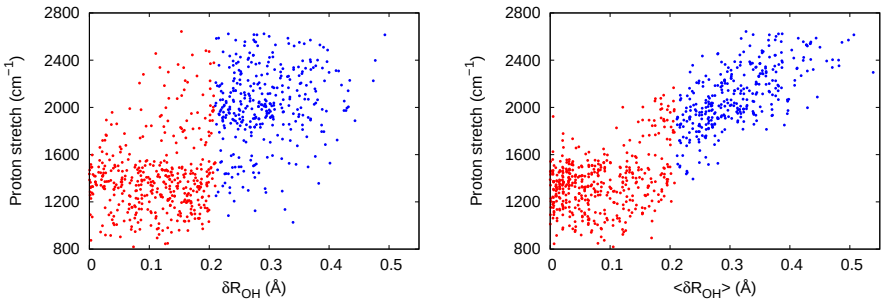

Figure 7.11 Relationship between proton stretch and δR_{OH}(left) and its expectation values (right). Red points are from structures with δR_{OH}<0.2Å. Blue points are from structures with $\delta R_{OH} \geq 0.2$Å.

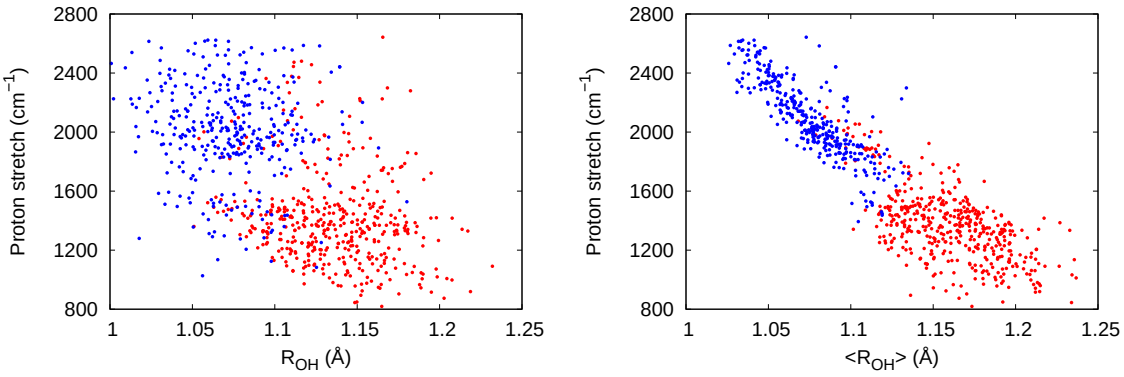

Figure 7.12 Relationship between proton stretch and R_{OH}(left) and its expectation values (right). Red points are from structures with δR_{OH}<0.2Å. Blue points are from structures with $\delta R_{OH} \geq 0.2$Å. Linear least square fit for red points: $\nu = a \cdot \langle R_{OH} \rangle + b$, a=-5220.1, b=7422.6, R_2=0.42, RMS=187.6 cm^{-1}. Linear least square fit for blue points: $\nu = c \cdot \langle R_{OH} \rangle + d$, c=-9018.0, b=11794.0, R_2=0.70, RMS=142.1 cm^{-1}. Linear least square fit for all 800 points: $\nu = e \cdot \langle R_{OH} \rangle + f$, e=-7941.2, f=10603.0, R_2=0.82, RMS=183.5 cm^{-1}.

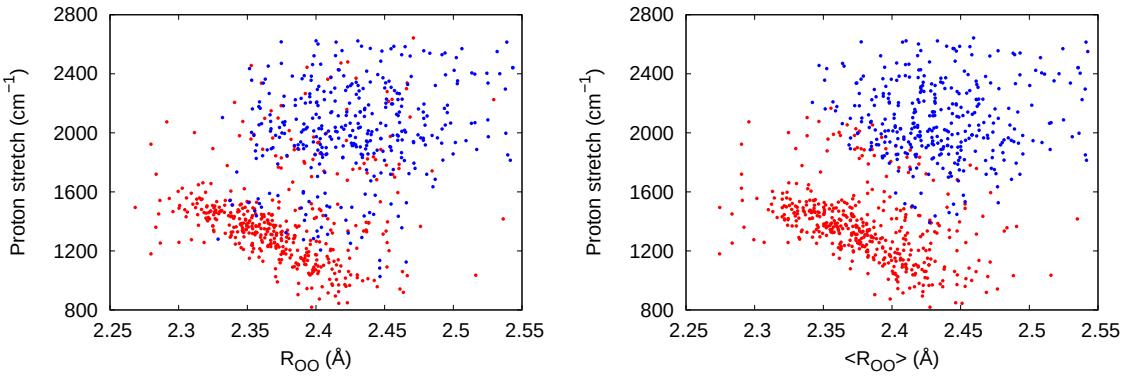

Figure 7.13 Relationship between proton stretch and R_{OO}(left) and its expectation values (right). Red points are from structures with δR_{OH}<0.2Å. Blue points are from structures with $\delta R_{OH} \geq 0.2$Å. Linear least square fit for red points: $\nu = a \cdot \langle R_{OO} \rangle + b$, a=-2342.0, b=6944.0, R_2=0.15, RMS=226.3 cm^{-1}.

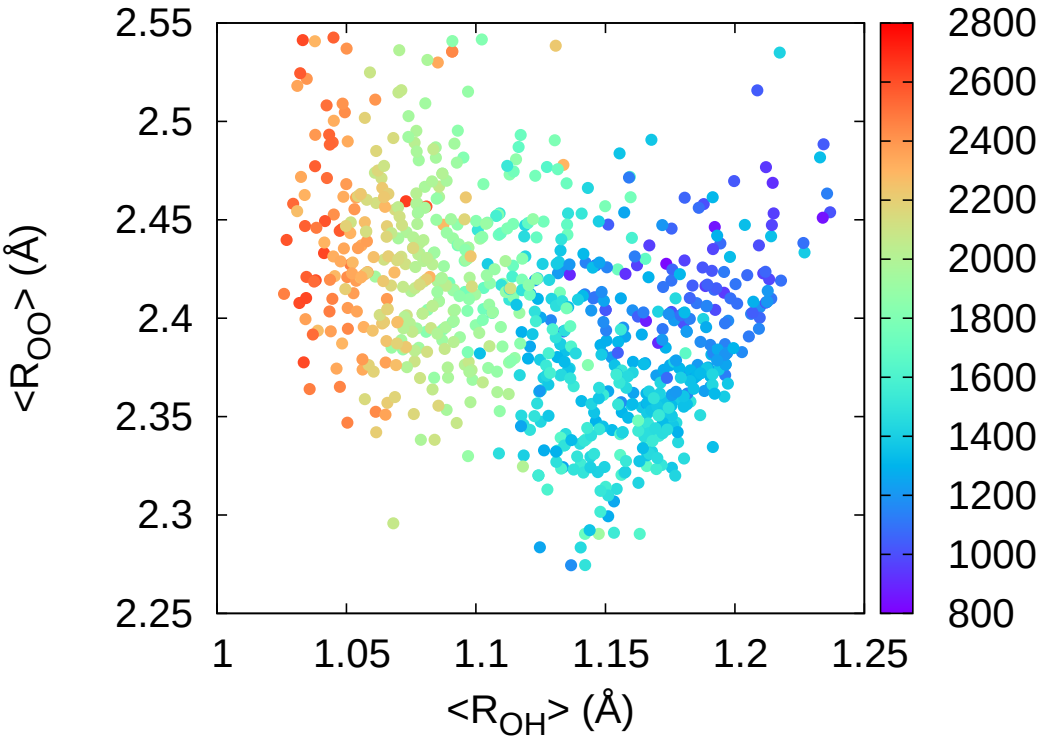

Figure 7.14 Relationship between $\langle R_{OO} \rangle$, $\langle R_{OH} \rangle$ and proton stretch frequency in cm^{-1} (color bar).

7.4.3 Decomposition of Spectrum by $\langle R_{OH} \rangle$

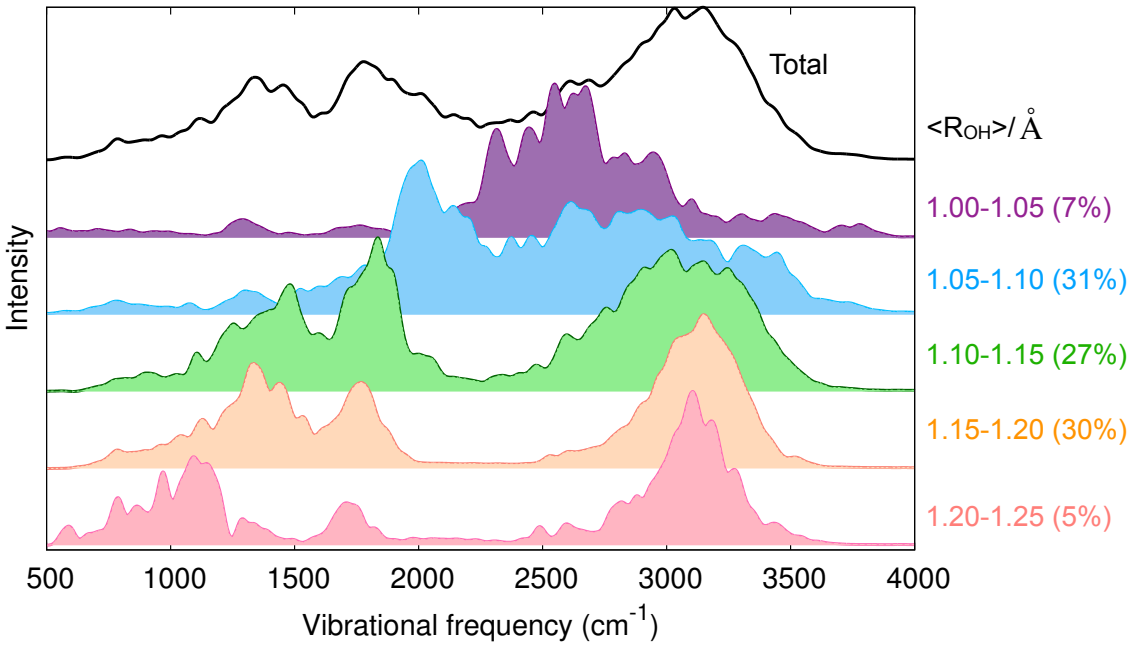

Figure 7.15 Decomposition of the calculated spectra of aqueous proton according to different $\langle R_{OH} \rangle$ values. The percentage of clusters in each group is included in parentheses.

To examine how the various vibrations shift with $\langle R_{OH} \rangle$, we present the full mid-IR spectrum decomposed by $\langle R_{OH} \rangle$ (Figure 7.15). Decomposition by $\langle \delta R_{OH} \rangle$ is also presented in Figure 7.16. For $\langle R_{OH} \rangle$ between 1.00-1.05 Å (extreme Eigen configurations), the spectrum displays intense hydronium stretches at 2500-2700 cm^{-1} and a weak umbrella mode around 1250 cm^{-1}. When $\langle R_{OH} \rangle$ lengthens to 1.05-1.10 Å, the continuum begins to bifurcate into two broad features centered around 2000 cm^{-1} and 2800 cm^{-1}. Comparing with Figure 7.7d), the split reflects the symmetry breaking between the three hydronium protons, resulting in a "special pair" OH stretch at 2000 cm^{-1} and flanking OH stretches at higher frequencies. The extreme breadth of the higher-frequency feature may reflect that the flanking OH stretches of the central

hydronium and the OH stretches in the adjacent water of the local monomer interact differently with the excess proton.[29]

As $\langle R_{OH} \rangle$ increases above 1.10 Å($\langle \delta R_{OH} \rangle < 0.2$Å), the spectral signatures of the aqueous proton complex appear more Zundel-like. As the proton stretch redshifts with $\langle \delta R_{OH} \rangle$, spectral overlap with the bending modes increases, resulting in stronger anharmonic mode mixing. At 1800 cm^{-1}, there is significant stretching and bending character, and the bending modes gain intensity as a result. The stretching modes of the shared proton are centered at 1400 cm^{-1}, while the flanking OH stretch band blueshifts to 3000 cm^{-1} and narrows somewhat as the two flanking waters share the excess proton more equitably. For $\langle R_{OH} \rangle > 1.15$Å, the spectrum appears even more Zundel-like with three bands at 1400 cm^{-1}, 1750 cm^{-1}, and 3100 cm^{-1} and negligible intensity between 2000 and 2500 cm^{-1} (like the Zundel isomer of $H^+(H_2O)_6$ in Figure 7.1).

These trends illustrate how the various frequency regions report on different instantaneous configurations. First, because the small populations of the extreme configurations $\langle R_{OH} \rangle < 1.05$Å and $\langle R_{OH} \rangle > 1.20$Å, the vast majority of spectra are best described as among a range of distorted Eigen-like to asymmetric Zundel-like vibrational spectra. The 1000-1500 cm^{-1} region primarily reports on proton stretches in Zundel-like configurations, whereas umbrella modes in Eigen-like configurations do not contribute significantly to the overall feature in the experimental spectrum. The intensity of the bending feature at 1750 cm^{-1} is largest for 1.10Å$< \langle R_{OH} \rangle < 1.20$Å, where the intensity is borrowed via anharmonic coupling with proton stretching motions. In distorted Eigen-like configurations, the stretch-bend coupling is reduced (Figure 7.7d) and so bend features are less apparent on top of the continuum. For these distorted Eigen-like complexes, the bend also blueshifts to 1800 cm^{-1}, which has been observed in the gas phase[32] and more recently in contact ion pairs between $H^+(aq)$ and $NO_3^-(aq)$.[60] The continuum is only seen in Eigen-like configurations,

but a strongly blue-shifted OH stretch involving the hydronium proton that donates an hydrogen bond to the closest water is present at 2000 cm^{-1}. There are multiple overlapping contributions between 1500 and 2000 cm^{-1}, where stretching and bending motions of both Zundel-like and Eigen-like complexes contribute. This ambiguity may be responsible for the counterintuitive polarization response in the 2D IR cross peak between the stretch and bend of the proton hydration complex.[26]

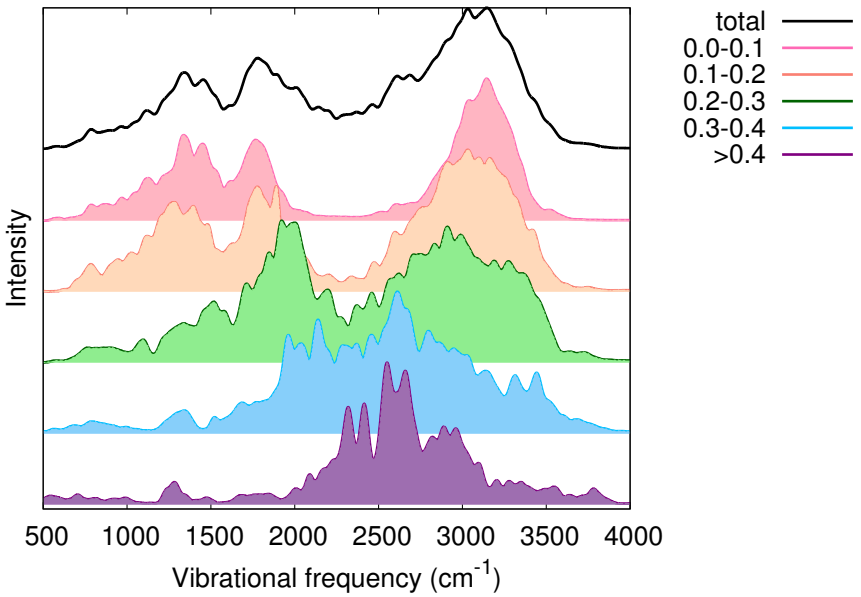

Figure 7.16 Decomposition of the calculated spectra of aqueous proton according to different $\langle \delta R_{OH} \rangle$ values.

7.4.4 Challenges and Outlook

The results here have been useful for disentangling assignments for aqueous proton vibrations, but there are still some areas that require further study. As we mentioned above, the VSCF/VCI spectra presented here are calculated from static structures of local $H^+(H_2O)_2$ monomers drawn from MS-EVB frames, which altogether leave out various characteristics of the aqueous proton spectrum. In addition, recent 2D IR spectra of the aqueous proton demonstrated that all of the main features displayed cross peaks between each other, implying strong anharmonic mixing between every

vibrational mode.[26] However, the spectral decomposition in Figure 7.7 would imply that coupling between Eigen-like and Zundel-like complexes would be missing cross peaks. This might be reconciled with experiment by taking into account the spectral dynamics associated with sub-100-fs proton rattling[19,48] that may blur the distinctions between Eigen-like and Zundel-like configurations.

Regardless, the anharmonic calculations here provide an exciting opportunity to interpret linear IR and also 2D IR spectrum of the aqueous excess proton. Excited state and combination band energies are calculated by the VSCF/VCI method, which can be directly compared to excited state absorptions and cross peaks in the 2D IR spectrum. Additionally, transition dipoles from various excitations are calculated, which can be related to measured 2D anisotropy measurements and could possibly bring clarity to the heterogeneity of vibrations in the 1500-2000 cm^{-1} region. The multi-dimensional nuclear potential for the anharmonic proton stretch can also be compared to its 2D lineshape to more accurately determine structure-frequency trends and to interpret low-dimensional projections of the potential. These tools may even be useful for benchmarking classical trajectories, which would help generate frequency and dipole trajectories needed for capturing spectral dynamics and reproducing the 2D spectrum of the excess proton.

7.5 Summary and Conclusions

We report the anharmonic spectrum of the aqueous proton calculated from the VSCF/VCI approach using 800 $H^+(H_2O)_6$ clusters. The accuracy of the theoretical scheme is verified in the Zundel and Eigen isomers of gas-phase $H^+(H_2O)_6$. The calculated vibrational spectrum of the aqueous proton improves in agreement to experiment compared to the harmonic spectrum, even though the spectrum consists of local $H^+(H_2O)_2$ monomers in hexamer clusters. By decomposing the spectrum into different normal mode components, we successfully verify and make assignments

of proton stretch, flanking water stretch, and bending motions across the spectrum. The strong mixing between proton stretch and bending motion is also observed, particularly for Zundel-like snapshots. Further analysis finds strong nuclear quantum effects of the proton and also strong correlation between excess proton-oxygen distance $\langle R_{OH} \rangle$ and associated anharmonic proton stretch. We finally decompose the anharmonic spectrum by $\langle R_{OH} \rangle$ to dissect the spread of IR response over a distribution of possible configurations. By comparing the trends based on $\langle R_{OH} \rangle$ and on normal mode decomposition, we discuss how one can interpret different frequency regions of the total spectrum in terms of geometry and vibrational character. We look forward to harnessing these anharmonic calculations for in-depth interpretation of the 2D IR spectrum of the aqueous proton and investigation of the strong anharmonic mixing between different vibrational modes.

Bibliography

[1] Heberle, J.; Riesle, J.; Thiedemann, G.; Oesterhelt, D.; Dencher, N. A. *Nature* **1994**, *370*, 379.

[2] Stowell, M. H. B.; McPhillips, T. M.; Rees, D. C.; Soltis, S. M.; Abresch, E.; Feher, G. *Science* **1997**, *276*, 812–816.

[3] Luecke, H.; Richter, H.-T.; Lanyi, J. K. *Science* **1998**, *280*, 1934–1937.

[4] Rini, M.; Magnes, B.-Z.; Pines, E.; Nibbering, E. T. J. *Science* **2003**, *301*, 349–352.

[5] de Grotthuss,; T., C. J. *Ann. Chim.* **1806**, *58*, 54.

[6] Agmon, N. *Chem. Phys. Lett.* **1995**, *244*, 456.

[7] Marx, D.; Tuckerman, M. E.; Hutter, J.; Parrinello, M. *Nature* **1999**, *397*, 601.

[8] Yeh, L. I.; Okumura, M.; Myers, J. D.; Price, J. M.; Lee, Y. T. *J. Chem. Phys.* **1989**, *91*, 7319.

[9] Jiang, J.-C.; Wang, Y.-S.; Chang, H.-C.; Lin, S. H.; Lee, Y. T.; Niedner-Schatteburg, G.; Chang, H.-C. *J. Am. Chem. Soc.* **2000**, *122*, 1398.

[10] Asmis, K. R.; Pivonka, N. L.; Santambrogio, G.; Brummer, M.; Kaposta, C.; Newmark, D. M.; Woste, L. *Science* **2003**, *299*, 1375–1377.

[11] Shin, J.-W.; Hammer, N. I.; Diken, E. G.; Johnson, M. A.; Walters, R. S.; Jaeger, T. D.; Duncan, M. A.; Christie, R. A.; Jordan, K. D. *Science* **2004**, *304*, 1137.

[12] Headrick, J. M.; Diken, E. G.; Walters, R. S.; Hammer, N. I.; Christie, R. A.; Cui, J.; Myshakin, E. M.; Duncan, M. A.; Johnson, M. A.; Jordan, K. D. *Science* **2005**, *308*, 1765.

[13] Vendrell, O.; Gatti, F.; Meyer, H. D. *Angew. Chem. Int. Ed.* **2007**, *46*, 6918–6921.

[14] Fournier, J. A.; Wolke, C. T.; Johnson, M. A.; Odbadrakh, T. T.; Jordan, K. D.; Kathmann, S. M.; Xantheas, S. S. *J. Phys. Chem. A* **2015**, *119*, 9425–9440.

[15] Wolke, C. T.; Fournier, J. A.; Dzugan, L. C.; Fagiani, M. R.; Odbadrakh, T. T.; Knorke, H.; Jordan, K. D.; McCoy, A. B.; Asmis, K. R.; Johnson, M. A. *Science* **2016**, *354*, 1131.

[16] Yu, Q.; Bowman, J. M. *J. Am. Chem. Soc.* **2017**, *139*, 10984–10987.

[17] Tuckerman, M. E.; Marx, D.; Parrinello, M. *Nature* **2002**, *417*, 925.

[18] Fecko, C. J.; Eaves, J. D.; Loparo, J. J.; Tokmakoff, A.; Geissler, P. L. *Science* **2003**, *301*, 1698.

[19] Berkelbach, T. C.; Lee, H. S.; Tuckerman, M. E. *Phys. Rev. Lett.* **2009**, *103*, 238302.

[20] Day, T. J. F.; Schmitt, U. W.; Voth, G. A. *J. Am. Chem. Soc.* **2000**, *122*, 12027.

[21] Kulig, W.; Agmon, N. *Nat. Chem.* **2013**, *5*, 29.

[22] Thämer, M.; De Marco, L.; Ramasesha, K.; Mandal, A.; Tokmakoff, A. *Science* **2015**, *350*, 78–82.

[23] Agmon, N.; Bakker, H. J.; Campen, R. K.; Henchman, R. H.; Pohl, P.; Roke, S.; Thämer, M.; Hassanali, A. *Chem. Rev.* **2016**, *116*, 7642–7672.

[24] Dahms, F.; Fingerhut, B. P.; Nibbering, E. T. J.; Pines, E.; Elsaesser, T. *Science* **2017**, *495*, 491–495.

[25] Chen, M.; Zheng, L.; Santra, B.; Ko, H.-Y.; DiStasio Jr, R. A.; Klein, M. L.; Car, R.; Wu, X. *Nat. Chem* **2018**,

[26] Fournier, J. A.; Carpenter, W. B.; Lewis, N. H. C.; Tokmakoff, A. *Nat. Chem.* **2018**, *10*, 932–937.

[27] Kundu, A.; Dahms, F.; Fingerhut, B. P.; Nibbering, E. T. J.; Pines, E.; Elsaesser, T. *J. Phys. Chem. Lett.* **2019**, *10*, 2287–2294.

[28] Stoyanov, E. S.; Stoyanova, I. V.; Reed, C. A. *J. Am. Chem. Soc.* **2010**, *132*, 1484.

[29] Daly, C. A.; Streacker, L. M.; Sun, Y.; Pattenaude, S. R.; Hassanali, A. A.; Petersen, P. B.; Corcelli, S. A.; Ben-Amotz, D. *J. Phys. Chem. Lett.* **2017**, *8*, 5246.

[30] Biswas, R.; Carpenter, W.; Fournier, J. A.; Voth, G. A.; Tokmakoff, A. *J. Chem. Phys.* **2017**, *146*, 154507.

[31] Zundel, G.; Metzger, H. *Z. Phys. Chem.* **1968**, *58*, 225.

[32] Heine, N.; Fagiani, M. R.; Rossi, M.; Wende, T.; Berden, G.; Blum, V.; Asmis, K. R. *J. Am. Chem. Soc.* **2013**, *135*, 8266–8273.

[33] Wicke, E.; Eigen, M.; Ackermann, T. *Z. für Phys. Chem.* **1954**, *1*, 340.

[34] Eigen, M. *Angew. Chem., Int. Ed. Engl.* **1964**, *3*, 1.

[35] Biswas, R.; Tse, Y.-L. S.; Tokmakoff, A.; Voth, G. A. *The Journal of Physical Chemistry B* **2016**, *120*, 1793–1804.

[36] Schmitt, U. W.; Voth, G. A. *J. Phys. Chem. B* **1998**, *102*, 5548.

[37] Carpenter, W. B.; Fournier, J. A.; Lewis, N. H.; Tokmakoff, A. *J. Phys. Chem. B* **2018**, *122*, 2792.

[38] Duong, C. H.; Gorlova, O.; Yang, N.; Kelleher, P. J.; Johnson, M. A.; McCoy, A. B.; Yu, Q.; Bowman, J. M. *J. Phys. Chem. Lett.* **2017**, *8*, 3782–3789.

[39] Yu, Q.; Bowman, J. M. *J. Chem. Phys.* **2017**, *146*, 121102.

[40] Huang, X.; Braams, B. J.; Bowman, J. M. *J. Chem. Phys.* **2005**, *122*, 044308.

[41] Qu, C.; Yu, Q.; Bowman, J. M. *Annu. Rev. Phys. Chem.* **2018**, *69*, 6.1–6.25.

[42] Heindel, J. P.; Yu, Q.; Bowman, J. M.; Xantheas, S. S. *J. Chem. Theory Comput.* **2018**, *14*, 4553–3566.

[43] Wang, Y.; Bowman, J. M. *J. Chem. Phys.* **2011**, *134*, 154510.

[44] Liu, H.; Wang, Y.; Bowman, J. M. *J. Phys. Chem. Lett.* **2012**, *3*, 3671–3676.

[45] De Marco, L.; Carpenter, W.; Liu, H.; Biswas, R.; Bowman, J. M.; Tokmakoff, A. *J. Phys. Chem. Lett.* **2016**, *7*, 1769–1774.

[46] Liu, H.; Wang, Y.; Bowman, J. M. *J. Chem. Phys.* **2015**, *142*, 194502.

[47] Liu, H.; Wang, Y.; Bowman, J. M. *J. Phys. Chem. B* **2016**, *120*, 2824–2828.

[48] Markovitch, O.; Chen, H.; Izvekov, S.; Paesani, F.; Voth, G. A.; Agmon, N. *J. Phys. Chem. B* **2008**, *112*, 9456–9466.

[49] Tuckerman, M.; Laasonen, K.; Sprik, M.; Parrinello, M. *J. Chem. Phys.* **1995**, *103*, 150.

[50] Yu, Q.; Bowman, J. M. *J. Phys. Chem. A* **2019**, *0*, null.

[51] Esser, T. K.; Knorke, H.; Asmis, K. R.; Schöllkopf, W.; Yu, Q.; Qu, C.; Bowman, J. M.; Kaledin, M. *J. Phys. Chem. Lett.* **2018**, *9*, 798–803.

[52] Napoli, J. A.; Marsalek, O.; Markland, T. E. *J. Chem. Phys.* **2018**, *148*, 222833.

[53] Xu, J.; Zhang, Y.; Voth, G. A. *J. Phys. Chem. Lett.* **2011**, *2*, 81–86.

[54] Biswas, R.; Tse, Y. L. S.; Tokmakoff, A.; Voth, G. A. *J. Phys. Chem. B.* **2016**, *120*, 1793–1804.

[55] Houston, P.; Van Hoozen, B. L.; Qu, C.; Yu, Q.; Bowman, J. M. *Faraday Discuss.* **2018**, *212*, 65–82.

[56] Yu, Q.; Bowman, J. M. *J. Phys. Chem. Lett.* **2016**, *7*, 5259–5265.

[57] Marx, D. *ChemPhysChem* **2006**, *7*, 1848.

[58] Swanson, J.; Simons, J. *J. Phys. Chem. B* **2009**, *113*, 5149.

[59] Boyer, M. A.; Marsalek, O.; Heindel, J. P.; Markland, T. E.; McCoy, A. B.; Xantheas, S. S. *J. Phys. Chem. Lett.* **2019**, *10*, 918.

[60] Lewis, N. H.; Fournier, J. A.; Carpenter, W. B.; Tokmakoff, A. *J. Phys. Chem. B.* **2018**, *123*, 225–238.